

University of Alberta

**Subsurface Geophysical Characterization of the Crystalline Canadian
Shield in Northeastern Alberta: Implications for Geothermal Development**

by

Judith Sin Hang Chan

A thesis submitted to the Faculty of Graduate Studies and Research
in partial fulfillment of the requirements for the degree of

Master of Science

in

Geophysics

Department of Physics

©Judith Sin Hang Chan

Fall 2013

Edmonton, Alberta

Permission is hereby granted to the University of Alberta Libraries to reproduce single copies of this thesis and to lend or sell such copies for private, scholarly or scientific research purposes only. Where the thesis is converted to, or otherwise made available in digital form, the University of Alberta will advise potential users of the thesis of these terms.

The author reserves all other publication and other rights in association with the copyright in the thesis and, except as herein before provided, neither the thesis nor any substantial portion thereof may be printed or otherwise reproduced in any material form whatsoever without the author's prior written permission.

Abstract

In northern Alberta, existing heat flow and geothermal gradient studies suggest that using geothermal heat in oil sands processing would require deep drilling of the crystalline Canadian Shield. Using a 2.36 km deep borehole located near Fort McMurray, the goal of this study is to investigate the presence of any geological features that could act as fluid pathways for the development of an engineered geothermal system in the basement rocks. This is done by integrating the results from a comprehensive suite of geophysical borehole logs, seismic reflection surveys, zero-offset and walk-away vertical seismic profiles. The final results provide useful information on the *in-situ* physical properties of the rocks, depths to fracture zones and seismic reflectors, types of fractures, stress directions, and the acoustic responses of rock properties. Significant P-wave velocity anisotropy is also observed from the walk-away vertical seismic profile.

Acknowledgement

I would like to thank my supervisor, Dr. Doug Schmitt, for giving me the opportunity to work on this unique project. I am very grateful for the invaluable learning opportunities on the types of logging and seismic data sets that I got to work with, for the field experiences in Idaho, Fort McMurray, and Milk River, and for the opportunities to present my project at numerous conferences. Thank you for reaching out to me when I was contemplating about pursuing graduate studies, and for the continuous encouragement and guidance during my studies here.

This project was made possible under the funding support of Helmholtz-Alberta Initiative (HAI), and the borehole owner (Mr. Charles Warren Hunt) for permitting U of A researchers to gain access to the borehole for scientific research purposes. Borehole logging and seismic data acquisition were made possible under the assistance of ICDP-OSG, members of the Experimental Geophysics Group, and Greg Nieuwenhuis for organizing the field logistics. Thank you to Jochem Kück from ICDP-OSG for guiding me through the processing of some of the logging data. Furthermore, I am grateful for Randy Kofman's assistance in the laboratory measurements, and Gautier Njiekak for his geological inputs. I would also like to acknowledge GEDCO for providing the VISTA[®] seismic data processing software package, Schlumberger for Petrel[™], IHS for AccuMap[®] and Petra, Senergy for Interactive Petrophysics[™], Dr. Mirko van der Baan for lending out his SeisWare[™] license key for the initial seismic interpretation and his advices on 2D seismic data processing.

Thank you to my mom and brother, for always believing in me and supporting me through every step. Last but not least, I would like to thank all my wonderful friends for their support, through rants and laughters over many coffees and gatherings, especially during the last few months of my studies. Thank you, all!

Table of Contents

Chapter 1: Overview.....	1
Chapter 2: Introduction.....	5
2.1. Geothermal Development in Northeastern Alberta.....	5
2.2. Study Area.....	9
2.3. Geothermal Exploration Using Seismic Methods.....	12
2.3.1. Active Seismic Methods.....	13
2.3.1.1. Seismic Refraction Surveys.....	13
2.3.1.2. Seismic Reflection Surveys.....	14
2.3.1.3. Vertical Seismic Profiles.....	16
2.3.2. Passive Seismic Methods.....	17
2.3.2.1. Natural Microearthquakes.....	18
2.3.2.2. Induced Microseisms.....	19
2.3.2.3. Others.....	19
2.4. Deep Borehole Study.....	20
2.5. Regional Stress Field and Borehole Failures.....	24
2.6. Physical Properties of Crystalline Basement Rocks.....	29
2.7. Summary.....	31
Chapter 3: Geological Framework.....	36
3.1. Tectonic Setting of the Canadian Shield.....	36
3.2. Depositional Setting and Stratigraphy.....	39
3.3. Summary.....	44
Chapter 4: Geophysical Well Logging.....	45
4.1. Borehole Logging.....	46
4.1.1. Natural Gamma Ray (GR).....	46
4.1.2. Spectral Gamma Ray (SGR).....	48
4.1.3. Caliper (CALI, C).....	50
4.1.4. Self Potential (SP).....	51
4.1.5. Resistivity (R).....	52
4.1.6. Litho-Density.....	54
4.1.7. Neutron Porosity (NPOR, NPHI).....	56
4.1.8. Sonic (DT).....	58

4.1.9. Full Waveform Sonic (FWS).....	59
4.1.10. Dipole Shear Sonic Imager (DSI™).....	61
4.1.11. Formation MicroImager (FMI™).....	62
4.1.12. Magnetic Susceptibility (MSUS).....	63
4.1.13. Temperature (T).....	64
4.2. Data analysis.....	65
4.2.1. Precambrian Unconformity.....	65
4.2.2. Rock Characterization.....	66
4.2.3. Heat Generation.....	71
4.2.4. Fracture Detection Using Indirect Methods.....	71
4.2.5. Fracture Detection Using Direct Methods.....	78
4.2.6. Acoustic Properties.....	85
4.2.7. Thermal Logging.....	89
4.3. Summary.....	91
Chapter 5: Seismic Reflection Profiles.....	94
5.1. Seismic Overview.....	94
5.2. Data Acquisition.....	98
5.3. Pre-Stack Processing.....	101
5.3.1. Geometry Setup.....	104
5.3.2. Vibroseis Correlation.....	104
5.3.3. Trace Editing.....	106
5.3.4. First Arrivals Picking.....	106
5.3.5. Gain Application.....	108
5.3.6. Frequency Analysis.....	110
5.3.7. Elevation and Refraction Statics.....	111
5.3.8. Noise Attenuation.....	112
5.3.8.1. Frequency-Wavenumber (F-K) Filtering.....	113
5.3.8.2. Radial-Trace (R-T) Transform Filtering.....	114
5.3.9. Predictive Deconvolution.....	116
5.3.10. Time-Variant Bandpass Filtering.....	118
5.3.11. Common Midpoint (CMP) Sort.....	118
5.3.12. Velocity Analysis.....	122
5.3.13. Normal Moveout Correction.....	125
5.3.14. Residual Statics.....	125

5.3.15. CMP Stacking.....	126
5.4. Post-Stack Processing.....	127
5.4.1. F-X 2D Prediction.....	128
5.4.2. Finite Difference Migration.....	128
5.5. Data Analysis.....	133
5.5.1. Synthetic Seismograms.....	133
5.5.2. Horizon Interpretations.....	134
5.5.3. Dipping Reflectors.....	135
5.6. Summary.....	136
Chapter 6: Zero-Offset Vertical Seismic Profile.....	143
6.1. Overview.....	143
6.2. Data Acquisition.....	144
6.3. Data Processing.....	145
6.3.1. Data Quality.....	146
6.3.2. Wavefield Separation.....	149
6.3.3. Deconvolution.....	155
6.3.4. Corridor Stack.....	158
6.4. Data Analysis.....	160
6.4.1. Velocity Profile.....	160
6.4.2. Tube Waves.....	164
6.5. Summary.....	165
Chapter 7: Walk-Away Vertical Seismic Profile.....	167
7.1. Overview.....	167
7.2. Data Acquisition.....	170
7.3. Data Processing.....	172
7.3.1. Component Separation and Orientation.....	172
7.3.2. Plane-Wave Decomposition.....	175
7.4. Data Analysis.....	181
7.5. Summary.....	183
Chapter 8: Conclusions.....	185
8.1. Contributions of This Thesis.....	186
8.2. Unresolved Issues and Directions for Future Work.....	190

8.3. Implications for Geothermal Exploitation.....	192
Bibliography.....	193
Appendix.....	211
A. History of Hunt Well.....	211
B. ICDP-OSG Logging List.....	214
C. Logs Measured in Hunt Well To-Date.....	216
D. Swab Report.....	217
E. Seismic Anisotropy of Metamorphic Core Sample from the Hunt Well.....	219
F. Thin Sections.....	241
G. Photos of Hunt Well.....	242

List of Figures

2-1	Outlines of the oil sands area in Alberta.....	7
2-2	Mean magnitude ranges of permeability of different rock types.....	8
2-3	Schematic of an engineered geothermal system in a low-permeability crystalline basement rock setting.....	9
2-4	Locations of the Hunt well and seismic surveys.....	11
2-5	Location of a geothermal injection well in Boise, Idaho projected onto a seismic reflection survey.....	15
2-6	Schematics of the deep borehole (Hunt well).....	22
2-7	Variation of vertical stress magnitudes with depth in the deep borehole of Fort McMurray.....	25
2-8	Illustration of stress-induced borehole deformation.....	27
2-9	Horizontal stress trajectories in the Western Canada Sedimentary Basin.....	28
2-10	Log responses of igneous and metamorphic rock types from deep boreholes in the continental basement.....	33
2-11	Density values of some igneous and metamorphic host rocks.....	34
2-12	Intrinsic compressional- and shear- wave velocities for common igneous and metamorphic rocks.....	34
2-13	Electricity resistivity values of some common rock types.....	35
3-1	The total magnetic and Bouguer gravity maps of Alberta.....	37
3-2	Tectonic domains and shear zones for the subsurface basement of Alberta....	38
3-3	Surficial geology of Alberta.....	42
3-4	Generalized stratigraphic column of northeastern Alberta.....	43
3-5	Precambrian basement surface of the Western Canada Sedimentary Basin....	44
4-1	Distribution of gamma ray energies from the three radiogenic elements in the Earth's crust as measured by the spectral gamma ray tool.....	48
4-2	Schematic diagram of elastic scattering between neutron and nuclei of atoms in the formation.....	57
4-3	Sample waveforms from a sonic array tool showing the compressional, shear, and Stoneley arrivals	60
4-4	Image display of the Formation MicroImager™ log revealing the image of the borehole in the presence of the bedding and fracture planes.....	63

4-5	Plot of gamma ray, neutron porosity, and sonic logs.....	67
4-6	Formation MicroImager™ static log display near the sediment-basement boundary.....	68
4-7	Enlarged FMI™ mage of the sediment-basement interface at 541.3 m.....	69
4-8	Log display of gamma ray, density, photoelectric factor, density correction, magnetic susceptibility, total magnetic field and interval transit time.....	70
4-9	Major geophysical logs for the 600 to 1880 m depth interval.....	74
4-10	Display of full waveform sonic data for the far-receiver in variable density format and resistivity laterologs between the 1020 to 1390 m depth intervals.....	75
4-11	Display of waveform attenuation of full waveform sonic data in wiggle format between 1140 to 1220 m depth.....	76
4-12	Quality comparison of processed Formation MicroImager™ logs of the Hunt well. FMI™ logs in the upper section of the Precambrian basement.....	79
4-13	Interpreted fractures in the Hunt well between 541 to 600 m depth displayed in the form of Rosette diagram and lower hemispheric equal-area projection.....	80
4-14	Interpreted fractures in the Hunt well between 1400 to 1500 m depth displayed in the form of Rosette diagram and lower hemispheric equal-area projection.....	81
4-15	Examples of natural fractures of Formation MicroImager™ logs between depth intervals of 1410 to 1423 m and 1461 to 1468, and of drilling induced tensile fractures at 1638 to 1643 m in the Precambrian basement.....	82
4-16	Dipmeter log display shows the borehole breakouts between 1652 to 1740 m depth.....	84
4-17	Orientations of drilling-induced tensile fractures and natural fractures of the Hunt well in a borehole cross-section.....	85
4-18	Processing and interpretation of full waveform sonic data.....	87
4-19	Results of the compressional and shear wave velocities from full waveform sonic and dipole-shear sonic™ imager logs.....	88
4-20	Temperature profile at the Hunt well.....	90
4-21	A composite of all logs acquired at the Hunt well in the Precambrian basement.....	93
5-1	Diagram illustrating the principle of reflection and refraction at an interface.....	95

5-2	Illustration of ray paths and wavefronts at a velocity interface.....	97
5-3	Example of uncorrelated and correlated shot gathers of Tower Road survey.....	105
5-4	Types of events on a shot gather in the Thickwood 2D seismic survey.....	107
5-5	Types of events on a shot gather in the Tower Road 2D seismic survey.....	108
5-6	An example of the raw shot gather of the Tower Road seismic survey without any gain application and a processed shot gather with noisy traces removed.....	109
5-7	Frequency spectral analysis of Tower Road and Thickwood 2D seismic surveys in linear and decibel formats.....	111
5-8	Frequency-wavenumber filtering to attenuate linear noise.....	115
5-9	Comparison of shot gathers before and after predictive deconvolution.....	117
5-10	Common midpoint fold and binning for Tower Road 2D seismic profile.....	120
5-11	Common midpoint fold and binning for Thickwood 2D seismic profile.....	121
5-12	Interactive velocity analysis using semblance plot and common velocity stack.....	123
5-13	Result of velocity analysis for Tower Road Survey.....	124
5-14	Comparison of stacked seismic sections of Thickwood survey using different offset distances.....	127
5-15	Original and re-processed stacked section of Thickwood seismic survey.....	130
5-16	Comparison of Thickwood seismic section before and after finite-difference migration.....	131
5-17	Stacked section of Tower Road seismic survey with time-variant Ormsby filter applied followed by F-X predictive deconvolution with interpreted horizons.....	132
5-18	Synthetic seismograms generated using wavelet extraction from Thickwood and Tower Road seismic surveys.....	134
5-19	The stacked profile of the Tower Road 2D seismic survey with F-X prediction applied.....	137
5-20	The interpreted stacked profile of the Tower Road 2D seismic survey with F-X prediction applied.....	138
5-21	The stacked profile of the Thickwood 2D seismic survey generated using offset distances between 70 to 1000 m.....	139
5-22	The stacked profile of the Thickwood 2D seismic survey generated using	

	offset distances between 70 to 1000 m with interpretations.....	140
5-23	The stacked profile of the Thickwood 2D seismic survey generated using offset distances between 100 to 3000 m.....	141
5-24	The stacked profile of the Thickwood 2D seismic survey generated using offset distances between 100 to 3000 m with interpretations.....	142
6-1	The basic components of a vertical seismic profile.....	144
6-2	Frequency spectrum of the zero-offset vertical seismic profile at various depths.....	148
6-3	Display of zero-offset vertical seismic profile after stacking traces at the common depth and applying an automatic gain function.....	151
6-4	The concept of frequency-wavenumber filtering.....	152
6-5	Separation of downgoing and upgoing waves in VSP data using median filtering method and arithmetic subtraction.....	153
6-6	Wavefield separation of zero-offset VSP data collected at the Hunt well using the vertical component.....	154
6-7	Upgoing wavefield after deconvolution in two-way travel time.....	156
6-8	Upgoing wavefield after deconvolution in two-way travel time in the cased hole section.....	157
6-9	Outside corridor stacks of a zero-offset VSP containing mostly primary reflections.....	158
6-10	The 25 ms outside corridor zone selected for corridor stacking of the zero-offset VSP.....	159
6-11	Display of velocity profiles generated from zero-offset vertical profile using different averaging methods.....	163
6-12	Outlines of downgoing and upgoing primary and multiple tube waves in the zero-offset vertical seismic profile.....	166
7-1	Hypothetical wave surface in x - z space and hypothetical phase slowness surface in a plane of an anisotropic material.....	169
7-2	Field geometry for the walk-away VSP at the Hunt well.....	171
7-3	Acquisition of the walk-away VSP data along the straight segment of Tower Road.....	171
7-4	First arrival picks of the walk-away VSP data.....	173
7-5	The three components of the walk-away vertical seismic profile at 797 m depth after geometry setup, trace editing and component separation.....	174

7-6	First rotation of the X and Y components at 1777 m depth.....	178
7-7	Second rotation of the Hmax (horizontal radial) and Z' (SV) components...	179
7-8	Relationship between the τ -p and x-t space.....	180
7-9	Display of intercept time and horizontal slowness for the walk-away VSP data at 797 m depth.....	180
7-10	P-wave phase and group velocities measured and calculated from the two levels of the walk-away VSP at the Hunt well.....	181
A-1	The relationship between group (ray) and phase velocities when energy propagates in the shape of an elliptical wave surface.....	223
A-2	Symmetry of a transversely isotropic medium where elastic properties are symmetric about the z-axis.....	225
A-3	Dimensions of metamorphic rock sample for velocity measurement.....	226
A-4	A schematic diagram of the experimental setup.....	229
A-5	Variable-area wiggle displays of P- and S-waves propagating along foliation plane, across foliation plane, and at 45° to foliation plane.....	230
A-6	Comparison of P- and S-wave velocities as a function of confining pressure ranging from 0 to 60 MPa.....	233
A-7	Comparison of anisotropic parameters and elastic constants assuming transversely isotropic medium as a function of confining pressure.....	236
A-8	Plane and cross-polarized light images of Hunt well sample at 2350.3 to 2350.5 m depth.....	241

List of Tables

2-1	Rock samples from Hunt well characterized by Walsh (2013).....	30
4-1	Density and photoelectric factor values for common minerals found in metamorphic rocks.....	56
4-2	Results of heat generation measurement in the Precambrian rocks near the study area.....	73
4-3	Geometry of fractures interpreted from FMI TM and dipmeter logs.....	83
5-1	Acquisition parameters for 2D seismic reflection surveys along Tower Road by the Hunt well.....	100
5-2	Processing sequence and parameters for Thickwood 2D seismic line.....	102
5-3	Processing sequence and parameters for Tower Road 2D seismic line.....	103
6-1	Acquisition parameters of the zero-offset vertical seismic profile.....	145
6-2	Processing sequence for the zero-offset vertical seismic profile.....	147
A-1	Parameters used for velocity and elastic constant calculations.....	237
A-2	Measured velocities calculated elastic constants and anisotropic parameters during the pressurization cycle.....	238
A-3	Measured velocities, calculated elastic constants and anisotropic parameters during the de-pressurization cycle.....	239

List of Symbols and Abbreviations

3-C	Three-component
2D	Two-dimension
3D	Three-dimension
ϕ	Porosity
λ	Elastic modulus
μ	Shear modulus
ρ	Density
ρ_b	Bulk density
ρ_e	Electron density
ρ_{gr}	Grain density
ρ_w	Density of pore fluid
τ	Intercept time or zero-offset arrival time
θ	Angle of dip (dip direction of planar feature) in FMI TM log
θ	Phase propagation angle
A	Anisotropy
A	Heat generation
AI	Acoustic impedance
AGC	Automatic gain control
API	American Petroleum Institute
BS (sonic log)	Borehole sonic
BS (caliper log)	Bit size
BS (swabbing)	Base sediments
CALI (or C, CAL)	Caliper
CAPP	Canadian Association of Petroleum Producers
CMP	Common midpoint

CNL	Compensated neutron log
CVS	Constant velocity stack
d	Diameter of the borehole
DIP	Dipmeter
DITF	Drilling-induced tensile fracture
DLL	Dual laterolog
DLS	Dominion land survey
DSI TM	Dipole Sonic Imager TM
DST	Drill stem test
DT (DT4P)	Sonic (delta-time)
DTCO	Sonic compressional slowness
DTSM	Sonic shear slowness
EGS	Engineered (or enhanced) geothermal system
FAC40	Televiewer, acoustic images
FFT	Fast Fourier Transform
F-K	Frequency-wavenumber
FD	Finite-difference
FMI TM	Formation MicroImager TM
FTOT	Total magnetic field strength
FWS	Full waveform sonic
F-X	Frequency-offset
g	Gravity
Ga	Billion years
GFZ	German Research Center for Geoscience (GeoforschungZentrum)
GIS	Geographic information system
GR	Gamma ray
h	Overburden depth

h	Height of the sinusoidal curve in FMI TM log interpretation
HAI	Helmholtz-Alberta Initiative
HAZI	Hole azimuth
Hmax	Horizontal radial component
H _{mc}	Mud cake thickness
Hmin	Horizontal transverse component
URLA	High-resolution laterolog array
ICDP-OSG	International Continental Scientific Drilling Program Operational Support Group
IFFT	Inverse fast Fourier transform
K	Potassium
KB	Kelly bushing
LDT	Litho-density tool
LLD	Deeper laterolog measurement of the dual laterolog tool
LLS	Shallow laterolog measurement of the dual laterolog tool
masl	Meters above sea level
MSFL	Micro-spherically focused log
MSUS (or MS)	Magnetic susceptibility
NE	Northeast
NGT	Natural gamma ray spectrometer
NMO	Normal moveout
NPOR/NPHI	Neutron porosity
NW	Northwest
p	Horizontal phase slowness
P1AZ	Pad 1 azimuth of caliper logging tool
PEF, P _e	Photoelectric factor
ppm	Parts per million
q	Vertical slowness

R	Resistivity
R_a	Apparent resistivity
RC	Reflection coefficient
RHOB	Bulk density
R_{mc}	Resistivity of mud cake
RMS	Root mean square
R_t	True formation resistivity
R-T	Radial trace
R_{xo}	Resistivity of the invaded zone
SE	Southeast
SGR	Spectral gamma ray
SH	Horizontally-polarized shear wave
SH_{max}	Maximum horizontal stress
SH_{min}	Minimum horizontal stress
SI	International system of units
S/N	Signal-to-noise ratio
SP	Self (or spontaneous) potential
STC	Slowness time coherence
SV	Vertically-polarized shear wave
S_v	Vertical stress
SW	Southwest
t	Travel time
T	Temperature
T_f	Transit time in the pore fluid
Th	Thorium
TI	Transverse isotropy
t_{ma}	Transit time of the rock matrix

TLD	Three-detector lithology density
TR	Tower Road (2D seismic reflection survey)
TS	Telemetry including GR
TW	Thickwood (2D seismic reflection survey)
TVD	True vertical depth
U	Uranium
v	Magnitude of phase velocity
V_m	Velocity in rock matrix
V_p	P-wave velocity
V_s	S-wave velocity
VSP	Vertical seismic profile
x	Offset distance
WCSB	Western Canada Sedimentary Basin

Chapter 1

Overview

This thesis contributes to the feasibility study of geothermal development in northern Alberta as part of the Helmholtz-Alberta Initiative (HAI). In order to use geothermal energy to heat water for oil sands processing, existing geothermal gradient studies have suggested that deep drilling into the crystalline basement rocks is required in northeastern Alberta to reach the target temperature. There are, however, additional considerations that must be met for geothermal energy extraction to be viable. These relate to the state of fracturing of the rock mass, its permeability, and the nature of the *in-situ* fluids. Using a combination of geophysical methods and downhole logs acquired in a deep borehole (Hunt well), the focus of this thesis is to provide a detailed subsurface characterization of these metamorphic basement rocks toward future geothermal exploitation in Alberta.

Between 1994 to 2003, the Anhydride Oil Corporation, operated by Mr. Charles Warren Hunt, drilled a deep borehole located west of Fort McMurray, Alberta, which extended deep into the basement rocks. As such, this provides a unique opportunity to study the *in-situ* metamorphic rocks via an extensive borehole logging programme. Currently, the Hunt well is believed to be the deepest borehole drilled into the metamorphic Canadian Shield in Western Canada.

In total, there are 8 chapters in this thesis. Each geophysical method used in the project has its own chapter for the detailed discussion on its data acquisition, processing, and interpretation workflow.

To introduce all relevant background information regarding this project, **Chapter 2** begins with the context of geothermal energy development in Alberta, and how the current study area was selected on the basis of the existing studies and the available data. A comprehensive literature review on the various seismic methods for geothermal exploration is included in the chapter, *e.g.* reviews on seismic reflection survey, vertical seismic profile, and induced microseisms. Such reviews

demonstrate how seismic data have been utilized successfully for the development of geothermal energy in other parts of the world. The chapter continues with providing background information on the deep borehole (Hunt well) used in this study. Since this borehole penetrates into the metamorphic rocks of the Canadian Shield, literature reviews on deep borehole logging in the metamorphic rocks are also included. Next, a section is included on the regional stress field and borehole failures toward optimizing the development of a subsurface reservoir after it has been properly characterized. The chapter concludes with the physical properties of crystalline rocks and the general parameters measured for different rock types.

To assist with the interpretation of the geophysical data, **Chapter 3** presents the underlying geological framework of the study area, at least as currently understood. The first section includes the tectonic setting of the Canadian Shield and the corresponding tectonic domain in which the study area is located. The assembly of the Canadian Shield has been widely studied via a number of geoscience techniques developed over the years including the use of total magnetic and Bouguer gravity anomaly methods. The chapter ends with the stratigraphic column of northeastern Alberta and a map of the Precambrian basement surface. Knowledge of the local stratigraphy is useful in identifying the geological formations in the processed seismic sections.

Chapter 4 is the first chapter that discusses the geophysical data in this project. This chapter focuses on the geophysical borehole logs acquired in the Hunt well. A total of 13 downhole logging techniques are discussed in separate sections with their relevant applications to the characterization of the basement rocks and geothermal reservoirs. Data analysis is divided into seven separate sections according to the geological features and physical properties determined from the logs. The first two sections provide information on the depth of the Precambrian unconformity and rock characterization using the physical properties extracted from a number of wireline logs. Since geothermal energy development requires an understanding of heat generation from the subsurface rocks, a calculation of heat generation was performed in the next section to compare with the existing

reported values. To optimize fluid flow in the geothermal reservoir, it is also important to have a good understanding of fractures in the rocks. Both direct and indirect methods are discussed to identify the potential fracture zones in the deep borehole. The final two sections focus on the acoustic and thermal properties. Direct measurements from the acoustic logs provide velocity information for other types of geophysical data processing. Thermal measurements allow one to determine the target depth needed for geothermal exploration.

Surface seismic reflection data are acquired near the deep borehole studied in Chapter 4. **Chapter 5** describes the field acquisition and the processing procedures of two 2D seismic profiles. The chapter begins with an overview of the seismic theory that is also applicable to other seismic methods discussed in the later chapters. The final goal of the processing workflow is to generate a proper image of the subsurface for the interpretation of geological structures relevant for the development of a geothermal reservoir. Using the sonic and density logs from Chapter 4 and stratigraphic framework information from Chapter 3, the seismic horizons (geological formations) have been interpreted after correlating the seismic data to the Hunt well.

Besides surface seismic methods, borehole seismic data are also available in this project and are addressed in Chapters 6 and 7. **Chapter 6** discusses the zero-offset vertical seismic profile. Similar to the previous chapter, the beginning of the chapter provides information on the field acquisition and processing routine. The purpose of this profile is three-fold: to generate a time-depth relationship of seismic data, to identify multiples in the final processed seismic sections, and to identify fracture zones from the upgoing tube waves. This chapter serves to assist with the seismic interpretation in Chapter 5 with increased confidence.

The second type of borehole seismic methods discussed in this thesis is the walk-away vertical seismic profile in **Chapter 7**. A stacking velocity analysis in the common seismic processing routine generally does not account for any directional variations in seismic velocities. This chapter focuses on determining the degree of seismic velocity anisotropy from the walk-away vertical seismic profile using a τ -

p transform. The exact cause of anisotropy is unknown with the absence of cores, but it is commonly related to the presence of fractures and textures in the metamorphic rocks. The calculated value of seismic velocity anisotropy is then compared with the value measured from the laboratory measurements.

Chapter 8 is the final chapter of this thesis and will summarize all the interpretations from the aforementioned borehole logging and geophysical methods. Also included in this chapter are recommendations for further investigations and implications for geothermal exploitation based on the data interpretations.

A compilation of the drilling and logging history of the Hunt well and a detailed list of logs measured to date are included in the **Appendices** of this thesis. This data is compiled from the daily drilling reports, well completion and workover reports as archived by the Energy Resources Conservation Board (ERCB) (succeeded by Alberta Energy Regulator (AER) as of June 17, 2013), and also from the Phase 1 environmental site assessment report produced by Worley Parsons. A copy of the term paper submitted toward the completion of the GEOPH 620 course (Fall 2011) is also attached. The paper contains laboratory measurements and analysis of a rock sample from the bottom of the Hunt well to obtain information on the seismic velocity anisotropy. The last two pages contain photos of the thin sections from the same rock sample and of the logging campaign in July 2011.

Chapter 2

Introduction

The Helmholtz-Alberta Initiative (HAI) is a partnership between the Helmholtz Association of German Research Centres and the University of Alberta seeking solutions to some of the pressing environmental concerns facing energy projects. The development of geothermal energy, with a focus on the oil sands region is a form of clean, sustainable and renewable energy resources currently being investigated. This falls under the “renewable energy sources” category of the HAI projects and it is divided into different sub-projects to evaluate the feasibility of geothermal systems in the sedimentary basin and/or the crystalline basement rocks in Alberta. These sub-projects include focuses on geothermics, magnetotellurics, thermal studies, geology, reservoir modeling, magnetics, regional seismic and stress studies, and a deep borehole study (this thesis). This chapter aims to provide background information on the intent of geothermal energy development in Alberta, the study area of this thesis, the choice of geophysical methods used for this study, literature review on seismic methods related to the development of geothermal systems, the concept of regional stress field and borehole failures, and the relevant physical rock properties in the metamorphic basement.

2.1. Geothermal Development in Northeastern Alberta

Traditionally, geothermal energy has been exploited near the tectonic plate boundaries where high temperature resources are available closer to the surface. Conventional steam plants (flash technology) or closed-loop configuration (*e.g.* enhanced geothermal system, EGS) has been globally employed for extracting high temperature geothermal resources for power generation. Recent development of binary plant technology allows lower temperature resources (<100°C) to also be exploited for electricity generation. This form of heat is generally used for heating buildings and homes, aquaculture, horticulture and industrial processes

(Guerrero-Lemus and Martínez-Duart, 2013). In Western Canada, direct usage of warm or hot water in British Columbia currently include space heating, agriculture (greenhouses), recreation (spas), medical, and industry use (process heating) (Ghomshei and Sadlier-Brown, 1996). In Alberta, because of the relatively low thermal gradients, the ongoing geothermal research focuses on the extraction of heat for oil sands processing rather than electricity generation.

Oil sands extraction and processing requires large quantities of hot water that currently is heated by burning natural gas. In Alberta, this accounts for about 6.9 percent of Canada's overall greenhouse gas emissions, and is considered as the fastest growing source of greenhouse gas pollution in Canada (Canadian Association of Petroleum Producers (CAPP), 2009). As such, there is pressure at the international level to reduce the environmental footprint of bitumen recovery, thus prompting new sources of renewable heat energy to be developed. One potential source is geothermal heat extracted from beneath the Earth's surface (Majorowicz and Moore, 2008; Grasby *et al.*, 2011; Majorowicz *et al.*, 2012). Presently, little is known about the extent or the economic viability of geothermal heat in the areas where geothermal energy might be needed.

The temperature gradient in the Earth's crust is approximately 30°C/km globally, but it can also reach above 100°C/km in areas of active volcanism (Tiwari and Mishra, 2012; Guerrero-Lemus and Martínez-Duart, 2013). Comparatively, Alberta exhibits a lower geothermal gradient ranging between 20 to 30°C/km, and such low enthalpy can be developed through enhanced geothermal systems (Grasby *et al.*, 2011). In July 2011, a temperature gradient of 21.2°C/km was measured in a deep borehole in Fort McMurray (Unsworth *et al.*, 2012). This borehole is one of the focuses in this thesis and will be discussed in Section 2.4. The desired temperature needed for EGS electrical power production via binary plants (*e.g.* organic Rankine cycles mainly) is greater than 80°C. Thus, 80°C was set as the optimal temperature needed for heat extraction toward oil sands processing in northeastern Alberta (Majorowicz *et al.*, 2012).



Figure 2-1. Outlines of the oil sands area in Alberta. The Athabasca oil sands area is currently known as the largest oil sands deposit in the world suitable for surface mining and is the focus area of this study (Wikipedia public domain data, accessed on April 4, 2013).

One of the largest known oil sands reservoirs in the world is in the Athabasca region of northeastern Alberta, Canada (Figure 2-1). The sedimentary succession in this area is only a few hundred meters thick and thins toward the northeastern part of the province. As such, existing heat flow and geothermal gradient studies suggest that deep drilling into the crystalline basement rocks is needed to reach the sufficient temperature for use as a heat source. Besides the low enthalpy resources in Alberta, the metamorphic crystalline basement rocks are known to have low porosity and permeability. Therefore, the subsurface must be engineered to allow heat extraction from the otherwise low permeability rocks. Typical permeability values for un-fractured metamorphic and igneous rocks fall in the

range of 10^{-21} to 10^{-17} m² (10^{-6} to 10^{-2} md) (Schön, 2011) (Figure 2-2). Permeabilities for fractured and intact crystalline rocks, such as those in California near the San Andreas Fault, were measured to be 10^{-18} and 10^{-15} m² (10^{-3} to 1 md) respectively at 15 km depth (Manning and Ingebritsen, 2010). The concept of engineered geothermal system (EGS) development (also known as hot dry rock technology) in Alberta was first introduced by an industry consortium – GeoPOS (Geopower in the Oil Sands) in 2006 to 2008. Using the EGS concept, the target reservoir is ‘engineered’ to produce geothermal energy that was originally not deemed economical due to the lack of fluid and/or permeability. To further increase the productivity of a reservoir, hydraulic stimulation can be performed by inducing artificial fractures through fluid injection (Blöcher *et al.*, 2010). The natural fracture system within the impermeable crystalline basement is subsequently enhanced and heat extraction is performed by circulating water through the fractures at target depth (Figure 2-3).

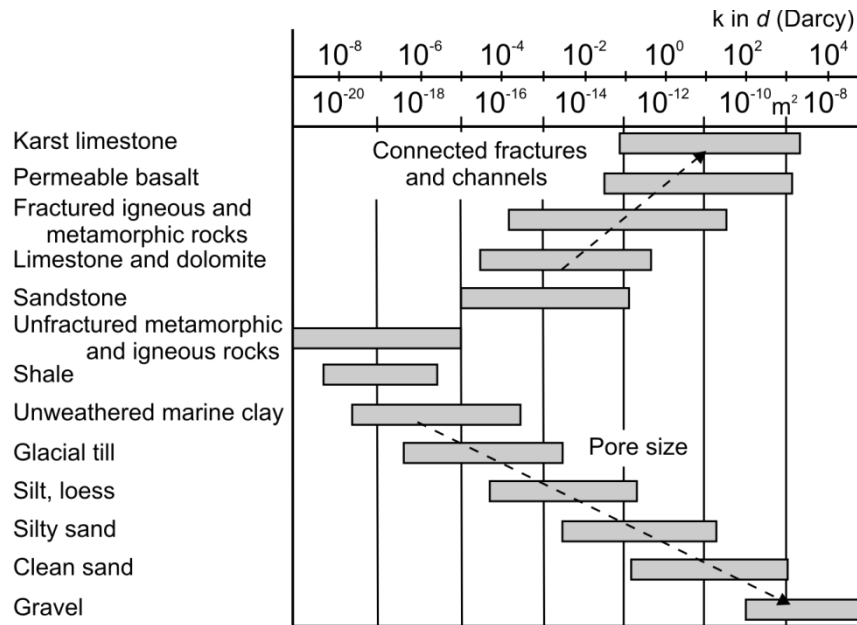


Figure 2-2. Mean magnitude ranges of permeability of different rock types (Schön, 2011)*.

* Reprinted from Handbook of Petroleum Exploration and Production, Volume 8, Schön, J. H. (ed.), Physical Properties of Rocks – A Workbook, Pg. 35, Copyright Elsevier (2011), with permission from Elsevier.

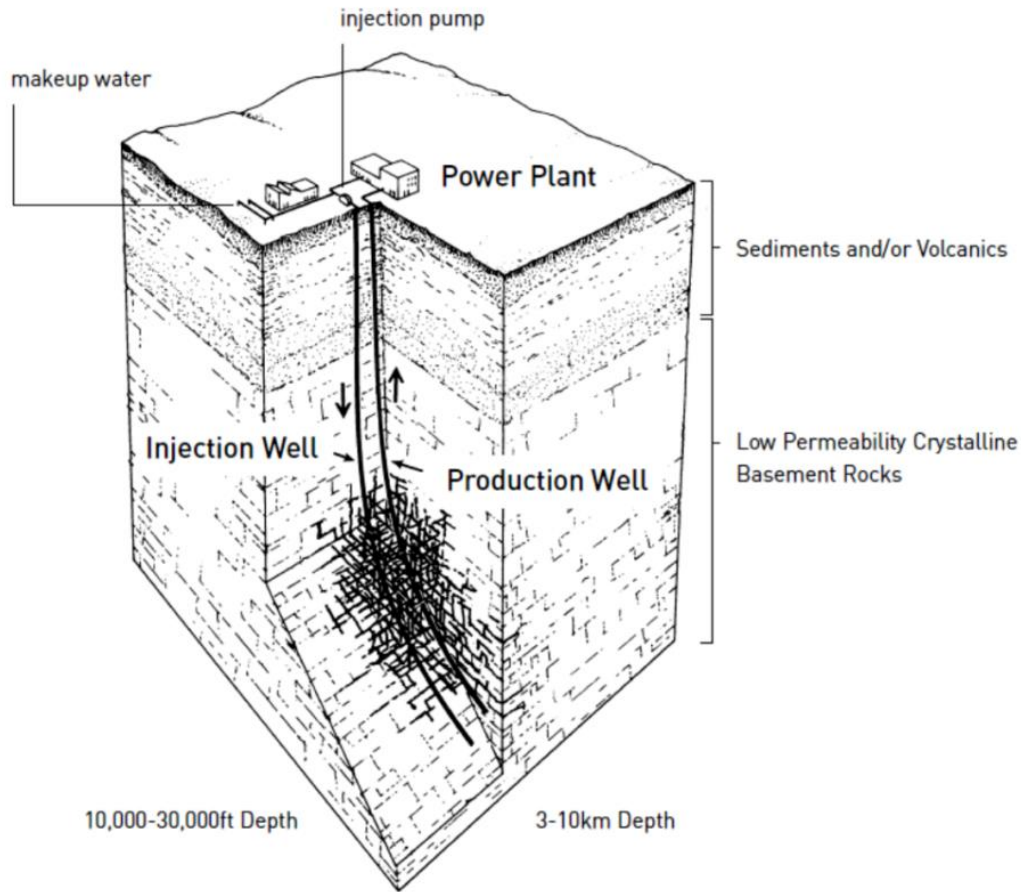


Figure 2-3. Schematic of an engineered geothermal system in a low-permeability crystalline basement rock setting (Tester *et al.*, 2006) ^{*}.

2.2. Study Area

The study area of this project encompasses the deep borehole located west of Fort McMurray, Alberta, Canada. Borehole AOC GRANITE 7-32-89-10 W4M (latitude 56°45'N, longitude 111°33'W) was drilled by Anhydride Oil Corporation under the operation of Mr. Charles Warren Hunt to test alternative hypotheses related to the origins of hydrocarbons in northeastern Alberta (Figure 2-4a). This vertical borehole will be hereafter referred to as the Hunt well in recognition of its operator. The borehole was completed to a depth of 2363.3 m

^{*} Reprinted from Tester, J. W. *et al.*, The future of geothermal energy: Impact of enhanced geothermal systems (EGS) on the United States in the 21st Century, pg. 1-11. Copyright Massachusetts Institute of Technology (2006).

with reference to the Kelly bushing (KB) at an elevation of 409.3 m in 2004. It is located 4.4 km in the western suburb of Fort McMurray, easily accessible via Tower Road. Its location offers an exceptional opportunity to study the *in-situ* conditions of the basement rocks beneath the Athabasca oil sands deposit area in the Canadian Shield. Through agreements with Mr. Hunt, the University of Alberta currently has access to this deep borehole for scientific research purposes.

Three separate 2D seismic surveys have been acquired close to the Hunt well along Tower Road in the past 35 years. The nearest part of the road is located approximately 165 m southwest of the Hunt well. The first survey (Line: MSE-407) was acquired in 1978 and brokered to the project by Sigma Explorations. This was the oldest survey available which focused on imaging the Cretaceous strata for oil sands exploration. Despite attempts at reprocessing this survey, it will not be discussed further due to its short record length which provided only subsurface imaging in the upper 250 m of the sedimentary succession. We note that at the writing of this thesis modern 3D geophysical data is being recorded near this site in order to evaluate the oil sand potential.

The second survey (Line: Thickwood PH-101 or TW survey) was conducted in 1993 by the Anhydride Oil Corporation along the entire Tower Road as outlined in Figure 2-4b. It has a profile length of approximately 24 km, and was used for imaging the crystalline basement in advance of the drilling of the Hunt well. This was intended to gain support for Mr. Hunt's hypothesis regarding the deep sources of hydrocarbon deposits (Hunt *et al.*, 1992). However, it is unique relative to the standard industrial practice with a long recording length of 12 seconds (approximately 35 km in depth). This allows for subsurface imaging of the basement rocks well beneath the thin sedimentary cover and deep into the metamorphic crust.

As part of the Helmholtz-Alberta research initiative, the shortest and newest survey (Line: Tower Road or TR survey) was acquired in July 2011 by the University of Alberta together with the ICDP Operational Support Group. This survey follows a ~2 km straight section of Tower Road adjacent to the Hunt well

(Figure 2-4b). This was to allow for a more precise determination of the near surface ‘static’ time shift corrections following the methodology of Schijns *et al.* (2012). The goal of the survey was to image the crystalline basement for any geological features relevant for EGS development with higher resolution than the TW survey. To ensure a higher spatial resolution and seismic fold coverage of the subsurface, closer geophone spacing was used to allow proper imaging of the sedimentary cover and the upper section (approximately 600 m) of the crystalline basement. The TW and TR surveys have been (re-) processed for the purpose of this project and will be discussed in Chapter 5 of this thesis.

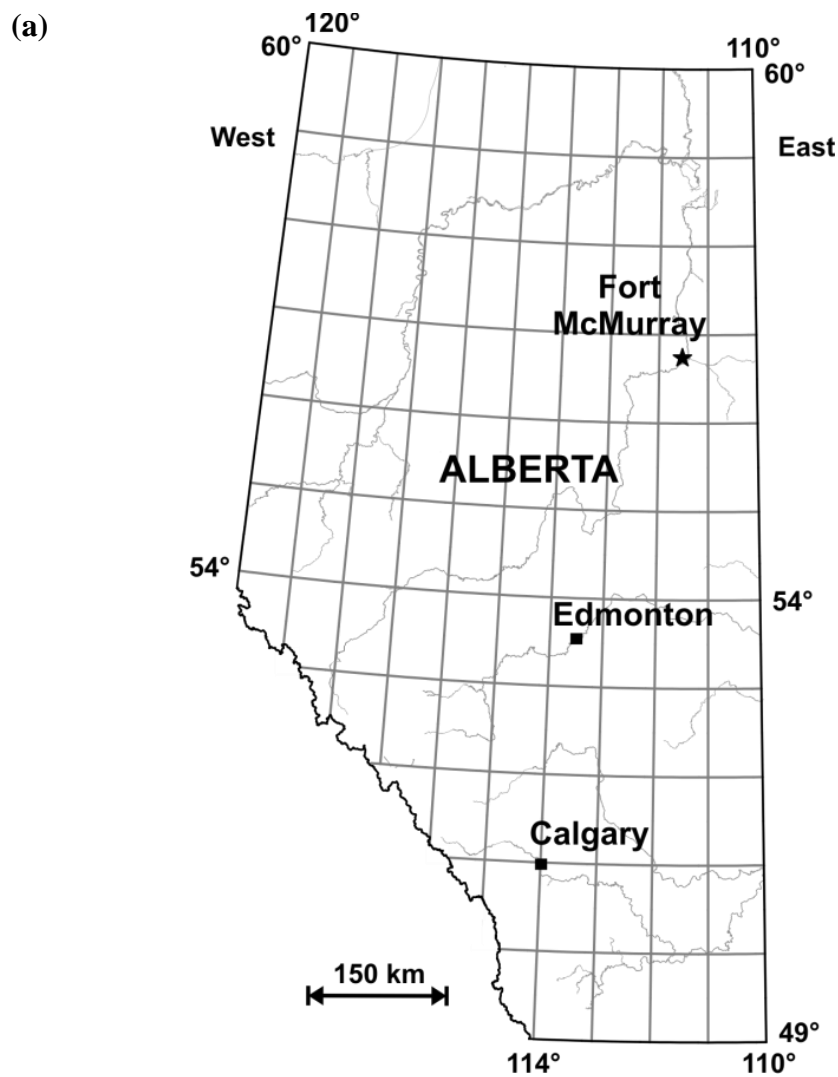


Figure 2-4. (a) The location of the Hunt well is marked with a star on the map. The map is displayed in the geographic coordinate system.

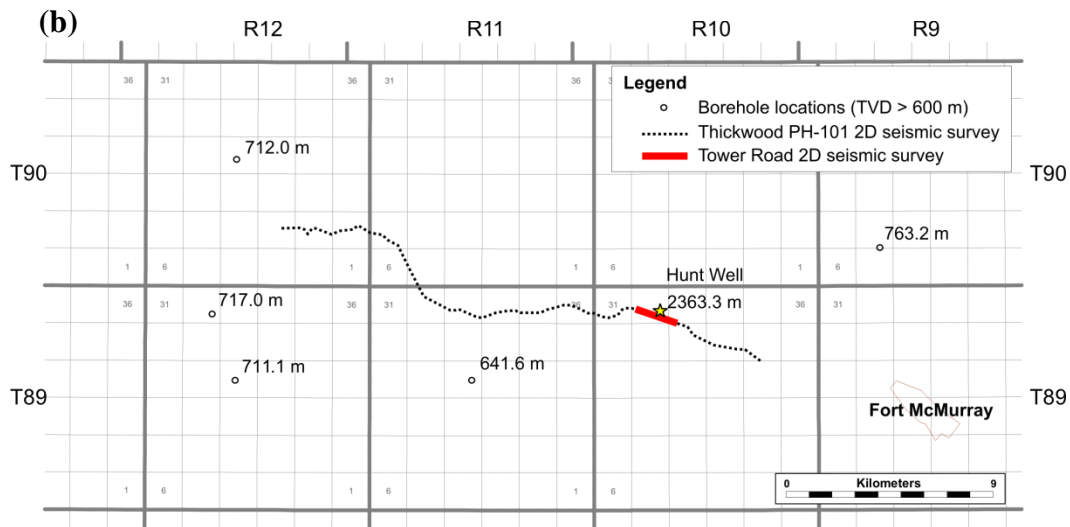


Figure 2-4. (b) The location of the Hunt well (star) and 2D seismic surveys in the Dominion Land Survey (DLS) system of Alberta west of the 4th Meridian. Other circles and numbers indicate nearby wells that have total vertical depths greater than 600 m.

2.3. Geothermal Exploration Using Seismic Methods

Geophysical methods are employed in existing geothermal exploration to understand the subsurface conditions of the basement rocks. Common geophysical methods include gravity, magnetic, electrical, thermal, radiometric, and seismic surveys. Borehole geophysical surveys serve as an important complement to the surface techniques. Geophysical surveys provide a means of delineating deep subsurface features and covering larger areas in a short time period without the exponentially greater costs of borehole drilling. They could provide important information relevant to geothermal exploration including the source and areal extent of the subsurface heat reservoir, the existence of structures such as faults that could be associated with permeable zones, and assessment of geothermal energy potential of the thermal resources (Gupta and Roy, 2007). Not all geophysical surveys are appropriate for the potential reservoirs as they are dependent on the geological, tectonic, and hydrological settings. The two types of geophysical data sets available for the study area in Fort McMurray are seismic surveys and borehole geophysical logs.

Seismic methods are broadly classified as active or passive (Pálmason, 1975; Iyers, 1978; Manzella, 2000; Gupta and Roy, 2007). The next few sections review the applications of active and passive seismic methods in existing geothermal fields around the world.

2.3.1. Active Seismic Methods

Active methods make use of seismic signals generated by an artificial source and have been successfully used in oil and gas exploration. These methods include seismic refraction and reflection surveys. In the development of engineered geothermal systems (EGS), active seismic methods can provide information about the mechanical properties, location, and presence of fractures of the geothermal reservoir (Niitsuma *et al.*, 1999).

2.3.1.1. Seismic Refraction Surveys

Seismic refraction surveying involves long source-to-receiver offset distances to allow geologic structural mapping using head waves. Generally, seismic refraction techniques are used mainly as a reconnaissance tool for mapping velocity distributions in the upper few kilometers of the crust. Structural features including faults, fracture zones, intrusions, and rock types can be inferred from the velocity variations useful for geothermal exploration programmes. In the Coso geothermal field, modelling of seismic refraction data revealed a possible correlation between high velocity regions with un-fractured or low porosity regions (Malin, 1994; Wamalwa *et al.*, 2013). In areas with complex topography and high velocity heterogeneity, such as the Lipari Island's low-enthalpy geothermal field in Southern Italy, seismic refraction surveys have been used to provide topographic corrections for seismic reflection data (Bruno *et al.*, 2000). Other studies also have demonstrated the use of refraction profiles to update their crustal velocity model, to associate surface geothermal phenomena, and to investigate lateral variation in compressional wave velocity and attenuation (Hill, 1976; Combs and Hadly, 1977; Majer and McEvilly, 1979). Traditionally, the seismic refraction method is not as commonly used as seismic reflection surveys for geothermal exploration due to the effort required for acquiring data in the deep

subsurface, and also the potential problems encountered by the generally high degree of complexity of geological structures in areas likely to host geothermal systems.

2.3.1.2. Seismic Reflection Surveys

The seismic reflection method has been an integral part of conventional oil and gas exploration and is a key structural and stratigraphic mapping tool. This method has also been widely used in geothermal exploration to investigate structural features that may control the production rate of a geothermal reservoir. Proper subsurface characterization applying seismic reflection data is used as an integrative study with geological mapping, well results and other geophysical data sets toward a complete resource capacity assessment (Melosh *et al.*, 2010). The heterogeneous nature of geothermal reservoirs, due to their complex fractured system, has proven to be a challenge for seismic imaging in the past (Gritto *et al.*, 2003). One of the biggest challenges of using seismic reflection data is the poor resolution due to the attenuation, scattering and absorption of seismic waves for deep subsurface imaging and characterization. Despite the challenges, seismic reflection surveys are still commonly used as a form of subsurface imaging due to their capabilities to resolve horizontal and shallow-dipping layered structures at greater depths. With the extensive use of seismic reflection surveys for oil and gas exploration in Alberta, these surveys are commonly acquired in existing exploration areas that could be (re-) interpreted for geothermal studies.

Proper processing workflow and advanced seismic imaging techniques developed in recent years have also led to an improved success rate of reservoir assessment for geothermal exploration. Nakagome *et al.* (1998) used long offset distance in a seismic reflection survey to image the fractured geothermal reservoirs in the Kakkonda geothermal field in Japan. Liberty (1998) used seismic reflection profiles to estimate the depth of geothermal aquifers at shallow depths and the continuity of a volcanic sequence in Boise, Idaho (Figure 2-5). Cameli *et al.* (2000) verified a statistically high correspondence between fractured systems and strong seismic reflectors in the metamorphic basement for geothermal exploration

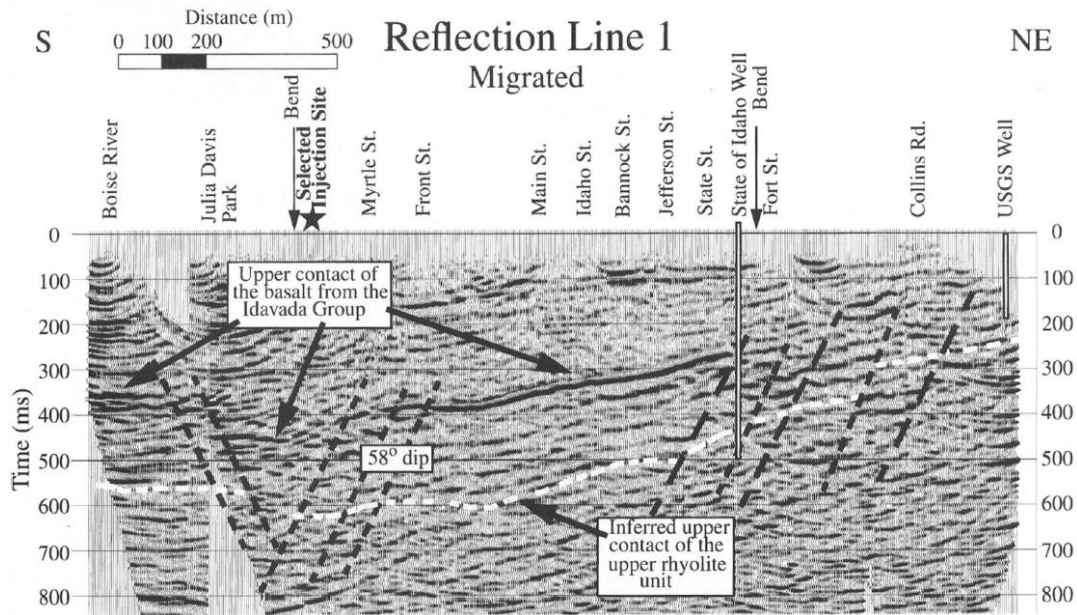


Figure 2-5. Location of a geothermal injection well in Boise, Idaho projected onto the seismic reflection survey. The seismic reflection technique was used to determine the depth to rocks associated with the geothermal reservoir (Liberty, 1998)*.

in southern Tuscany, Italy. The same area was also studied by Brogi *et al.* (2005) who reported a decrease in reflectivity when the seismic profile intersects the crustal shear zones along the strike. At the Coso geothermal field in California, the two producing areas in the crystalline rocks have been imaged as low velocity zones using improved seismic imaging methods. These low velocity zones were interpreted to contain pervasive fracturing and/or hydrothermal alteration associated with localized hydrothermal circulation demonstrating subsurface permeability (Unruh *et al.*, 2006). Melosh *et al.* (2010) interpreted faults from seismic reflection data based on reflector offsets and apparent fault surface reflectors in Nevada. Their interpretations were found to correlate with fluid entries at the intersected boreholes. Subsequent well locations based on the interpretations resulted in drilling success for geothermal development. Louie *et*

* Reprinted from Geophysics, 63(4), Liberty, L., Seismic reflection imaging of a geothermal aquifer in an urban setting, 1285-1294, Copyright Society of Exploration Geophysicists (1998), according to the fair use of publications outlined by SEG.

al. (2011) used advanced seismic reflection imaging to improve the resolution of seismic reflection data for fault characterization and geometry constraints of the reservoir structures in the geothermal fields of Nevada.

2.3.1.3. Vertical Seismic Profiles

Surface seismic surveys offer substantial coverage of the subsurface when no existing boreholes are available in the study area. However, the complex structures of fractured reservoirs in the crystalline basement cannot always be properly resolved at the reservoir scale (*e.g.* Schutter, 2003; Luthi, 2005; Al-Ali *et al.*, 2009; Place *et al.*, 2011). Borehole geophysical surveys such as the vertical seismic profile (VSP) are utilized to minimize the ambiguity in the interpretation of seismic reflection surveys. By placing the receivers directly into the borehole, versus surface-planted geophones in a seismic survey, and its higher frequency content, VSP imaging overcomes hurdles of seismic attenuation and reveals reflectors that could not always be resolved by surface seismic data. These reflectors have proven to associate with dipping geological structures and flow anomalies that could affect the development of a geothermal reservoir (Nakagome *et al.*, 1998; Melosh *et al.*, 2010; Place *et al.*, 2011). Many important reflectors detected by several VSPs recorded in the metamorphic basement could be attributed to the change in petrophysical characteristics of the rocks, particularly changes in fracture density, rather than contrasts in lithology (Cameli *et al.*, 1995). Interval velocities extracted from the VSP data are used to determine the variation of seismic velocity with depth with possible geological significance. Besides using the VSP data for reflectivity and velocity analysis, they can be interpreted separately for fracture analysis and toward an understanding of the degree of seismic anisotropy in a borehole (*e.g.* Schijns *et al.*, 2012). Such information is useful for the development of a geothermal reservoir and provides input parameters for the fracturing and reservoir simulation of a geothermal system.

At the Larderello geothermal field in central Italy, Cameli *et al.* (1995) analyzed VSP data with other geological and geophysical information to help identify important seismic reflectors inside the metamorphic basement. These sub-

horizontal reflectors were found to correlate with a producing fracture zone that intersected a borehole in the geothermal reservoir (Cameli *et al.*, 1995). At the Kakkonda geothermal reservoir in Japan, VSP imaging shows an up-dip pattern which was associated with the slope of an anticline. This interpretation was used to constrain the positioning of seismic reflectors deduced from the poor quality seismic reflection survey and revealed geological structures that were not apparent in the surface seismic surveys (Nakagome *et al.*, 1998). At the Rye Patch geothermal field in Nevada, Gritto *et al.* (2003) used multiple VSP surveys to obtain information on the velocity structure and the reflectivity of the subsurface. The goal was to explore the structural features that may control geothermal production in the area. Based on the velocity changes and strong seismic reflectivity, it was suggested that localized geological heterogeneity is present in the area as a result of hydrothermal alteration and volcanic deposition. Despite the uncertainty in the identification and mapping of faults in this area, the VSP surveys still suggested the existence of at least one fault. A 3D seismic reflection survey was later acquired to provide structural constraints of the geothermal reservoir by accurately imaging the regional trend of the faults and understanding the localized velocity heterogeneities.

2.3.2. Passive Seismic Methods

Passive methods involve the use of natural sources such as earthquakes, microseisms, and seismic noise to obtain information on parameters that may be influential to the development of a geothermal system (Gupta and Roy, 2007; Georgsson, 2010). Since it is a by-product of the subsurface phenomena and does not directly represent the physical property of the geothermal reservoir, understanding the meaning of such responses is essential in assessing the development of a geothermal reservoir and potential risks encountered. Passive seismic monitoring has been used for the *in-situ* monitoring of hydraulic fracturing and circulation tests in the development of engineered geothermal systems. Such monitoring can provide information about the size of the reservoir,

locations of fractures, and whether the reservoir volume is expanding during reservoir circulation (Niitsuma *et al.*, 1999).

2.3.2.1. Natural Microearthquakes

The identification of microearthquakes (Richter magnitude range: 1 to 3) in a prospective geothermal area is a means to investigate and characterize modern tectonic activity and volcanic areas. Such activity is frequently related to major hydrothermal convection systems including active faulting and fracturing in the subsurface, and also the base of the brittle/ductile transition above a heat source (Ward, 1972; Wright *et al.*, 1985; Manzella, 2000). Detailed compressional and shear wave velocities may be retrievable from microearthquake surveys aside from using seismic refraction surveys. The velocity information can help to locate and monitor the precise microearthquake hypocenters in order to estimate the depth of fluid circulation in a hydrothermal system (Gupta and Roy, 2007). Another use of velocity information is to understand the spatial variations in the mechanical properties of a geothermal reservoir by tomographic inversions of compressional and shear wave velocities (*i.e.* microearthquake travel time tomography) (Niitsuma *et al.*, 1999; Gritto *et al.*, 2003). Furthermore, information about the presence and alignment of fractures in a reservoir can be understood by analysing the wave scattering (Malin, 1994; Verdon *et al.*, 2009). It was also suggested that the Poisson's ratio determined from microearthquake activity can be used to distinguish between water- and vapor-dominated reservoirs (Gupta and Roy, 2007).

Ward and Jacob (1971) reported microearthquake activity in the Ahuachapan geothermal area of El Salvador due to the circulation of hot water to the surface in the presence of a fault plane. Similarly, Combs and Hadly (1977) used microearthquake locations to infer the presence of a fault in the East Mesa geothermal area of California. Gupta *et al.* (1982) derived regional compressional and shear wave velocities by analyzing of the microearthquake data. Majer and McEvilly (1979) and Gupta *et al.* (1982) reported a lowered Poisson's ratio in the geothermal production zone relative to the area outside the production zone as a

relation to the decrease in compressional wave seismic velocity at the Geysers geothermal field in California.

2.3.2.2. Induced Microseisms

Microseismicity can also be induced during geothermal exploration by hydrofracturing and fluid injection in addition to being naturally induced (Majer *et al.*, 2007). In order to enhance the permeability in a subsurface geothermal reservoir, engineered geothermal systems (EGS) require fracture stimulation at the target reservoir to allow water to circulate through the reservoir rocks. Induced seismicity has been documented in a number of EGS operations worldwide and has been hypothesized to be attributed to the increase in pore pressure, decrease in temperature, volume change, chemical alteration of fracture surfaces during the fluid injection stage (Majer *et al.*, 2007). Such reservoir stimulation can generate microseismic events and critically small earthquakes that exceed local limits leading to public concerns (Dyer *et al.*, 2008).

At the Geysers geothermal field in California, induced seismicity has been monitored for a number of years. These processes involve the mechanisms of reservoir cooling and pore pressure changes as a result of water injection and steam extraction. It was suggested that by varying the rate of increase of fluid injection, sufficient time exists for the geothermal system to equilibrate and reduce the initial seismicity in the geothermal reservoir (Majer and Peterson, 2005). At Soultz-sous-Forêts hot dry rock site in France, microseismicity was also found to have a strong dependence on the variations of the injection rate which led to the change of the velocity structure, the number and magnitude of microseismic events (Cuenot *et al.*, 2008). More examples of induced seismicity associated with EGS development can be found in Majer *et al.* (2007).

2.3.2.3. Others

Besides natural and induced microseismicity, other applications of passive seismic data include imaging fractures and sedimentary fabrics using shear wave splitting measurements (Verdon *et al.*, 2009), identifying stress tensor and joint distribution from the alignments of structures in the patterns of microseismic

events (Green *et al.*, 1987), characterizing the number, energy, and source mechanism of seismic events during reservoir development (Nagano *et al.*, 1994; Scotti and Cornet, 1994; Niitsuma *et al.*, 1999), characterizing the reservoirs using waveforms of microseismic events influenced by reservoir structure (*e.g.* velocity tomography) (Nishizawa *et al.*, 1983; Block *et al.*, 1994; Sato and Fehler, 1997; Gunasekera *et al.*, 2003), and locating hot bodies beneath geothermal system by interpreting the delay times of compressional wave arrivals (*i.e.* teleseisms) (Steeple and Iyer, 1976a; Steeples and Iyers, 1976b; Robinson and Iyer, 1981). Fehler *et al.* (1987) developed a method that determined the locations and orientations of discrete planes where many of the microearthquakes occurred. These planes of slip were further investigated by Fehler (1989) to estimate the *in-situ* stress field at the Fenton Hill hot dry rock geothermal energy site in New Mexico during numerous hydraulic fracturing experiments. More detailed explanations about the usage of each passive seismic method and relevant examples can also be found in Niitsuma *et al.*, (1999).

2.4. Deep Borehole Study

As Canada's largest oil and natural gas producer and home to vast deposits of oil sands, there are over 489,000 boreholes drilled in Western Canada up till 2011 (Canadian Association of Petroleum Producers (CAPP), 2013). However, the availability of a borehole drilled deep into the crystalline basement rocks in Alberta is scarce since basement rocks with their low porosity and permeability are not considered as prospective for hydrocarbons. As such, the Hunt well provides an unparalleled opportunity to study the conditions within the Canadian Shield underlying the Western Canada Sedimentary Basin (WCSB). In this section, some of the history of this unique borehole according to the TOUR reports publicly available from the Energy Resources Conservation Board (succeeded by Alberta Energy Regulator (AER) as of June 17, 2013) is mentioned. As noted, the borehole was originally drilled to investigate the Precambrian granite as a potential hydrocarbon source.

Drilling of the borehole to its current total depth occurred in two stages; the chronological details are listed in Appendix A. Briefly, the borehole was first spudded on September 1st, 1994 and was completed on October 8th, 1994 to a depth of 1649 m by Anhydride Oil Corporation. The first steel casing was set at 94 m on September 1st, 1994 and the second one set at 598 m on September 10th, 1994. Logging was also run by Schlumberger on October 8th, 1994. Bridge plugs were drilled out on September 27th to 28th, 2002.

In the second stage, the borehole was taken to a depth of 2363.3 m, spudded on December 17th, 2002 and was completed on January 9th, 2003. This was the last drilling session of the borehole with 1821 m of coverage in the crystalline basement rocks (Figure 2-6). The primary objective of this second drilling was to reach an approximate 3000 m depth in order to investigate strong seismic reflectors identified in the nearby 2D seismic section (see Chapter 5). The 3rd steel casing was set at 1005.7 m on February 28, 2003. During the well completion and workover stage (including tubing installation), it was reported that the junk mill and tubing string were stuck in hole at 1187 m. A power swivel was used to drill out the tight spot in the hole between 1187.48 m to 1216.16 m. Borehole geophysical logging was again run by Schlumberger beneath the Paleozoic and Cretaceous sediments on January 7, 2003 (Refer to Appendix C). The borehole was completed with production tubings down to the bottom in early 2003 through which extensive swabbing tests produced 67 m³ of fluids with 0.2% oil show (Refer to Appendix D).

The borehole was re-entered for temperature measurements by the GeoPos consortium during its existence in 2004 to 2008 but these proprietary data are not accessible. Dr. Jacek Majorowicz, as part of the HAI geothermal project, gained access to perform temperature logging in the borehole from December 7th to 9th 2010. Temperature logging was also repeated on June 14th to 15th, 2011.

From July 12th to 16th, 2011, a collaborative effort between the Operational Support Group of the International Continental Scientific Drilling Program (ICDP-OSG) from the GeoforschungZentrum (GFZ) Potsdam and the University

of Alberta acquired additional geophysical logs to measure the natural radioactivity, electrical, magnetic, and acoustic properties of the rocks. This logging campaign focused on open hole (*i.e.* sections with no steel casings) measurements from the bottom of the casing collar (1005.7 m) to a depth of 1880 m, restricted by the cable length available at the time. Attempts in recording ultrasonic borehole televiewer data were unsuccessful due to a partial blockage of the borehole at 1360 m and problems with tool centralization. Prior to this logging campaign, the production tubing that were previously installed in the borehole were removed in order to perform geophysical logging in an open hole environment.

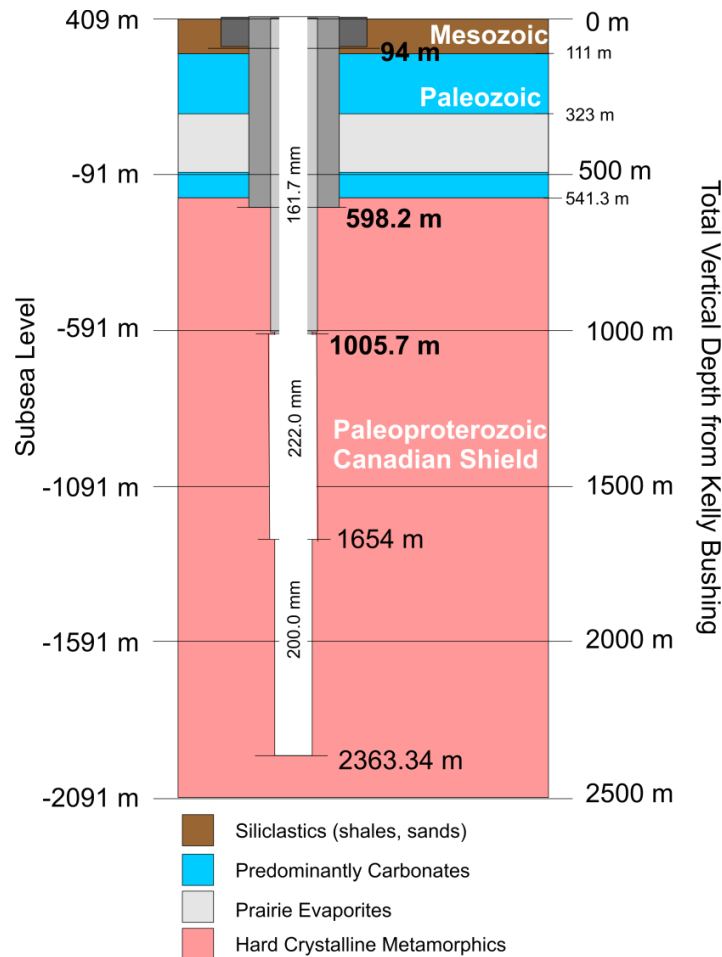


Figure 2-6. Schematics of the deep borehole (Hunt well). Bold numbers indicate the shoe depth of casing set in the borehole (Image courtesy of Dr. Douglas R. Schmitt).

A complete list of all logs acquired from 1993 to 2011 at the Hunt well is included in Appendices B and C. The uppermost 541.3 m of the geological column consists of Paleozoic and Cretaceous sediments which are well sealed behind three different casings. The open hole section is directly exposed to the crystalline basement rocks from a depth of 1005.7 m down to the bottom of the borehole.

Log responses in the metamorphic rocks are poorly constrained since the development of the technical and interpretation methods have primarily been driven by the petroleum industry with a central focus on the sedimentary layers (Bartetzko *et al.*, 2005). Deep borehole logging in the metamorphic rocks were mainly conducted for scientific research purposes such as the KTB pilot hole (German Continental Deep Drilling Program) in Germany, Cajon Pass borehole (Cajon Pass Scientific Drilling Project) in the United States, or CCSD-MH (Chinese Continental Scientific Drilling) in China (Pezard and Luthi, 1988; Lüschen *et al.*, 1996; Luo and Pan, 2010). Although there are over 4000 exploratory wells that penetrated the metamorphic Precambrian basement in Western Canada, logging into the basement rocks is almost exclusively limited to the sedimentary successions for exploration purposes (Pană, 2003). Furthermore, the boreholes that do cross the Precambrian unconformity only penetrate at most a few meters into the basement. While the core and cutting materials obtained from these boreholes has provided key information in developing the age and radioactivity of the rocks, there is insufficient core or well log information in the basement on the geophysically important properties (Burwash and Culbert, 1976; Burwash and Cumming, 1976; Burwash, 1979; Drury, 1988). Moreover, there are no data of which we are aware of that provides indication of the *in-situ* fluids, state of stress, or fracture permeability of the basement.

We are not aware of any public release of geophysical logging in the Precambrian basement in Alberta. Some examples of work in the Canadian Shield rocks outside of Alberta are discussed in publications by Davis and Tammemagi (1982), Paillet and Hess (1986), and Mwenifumbo *et al.* (2004). The nearest known

borehole (JXWS) with geophysical logs recorded deep into the basement section is located approximately 650 kilometers southeast of the Hunt well close to the Saskatchewan-Manitoba border for the investigation of the Reynard Lake Pluton (Davis and Tammemagi, 1982). This borehole was drilled from 1965 to 1966 and geophysical logs, including caliper, sonic, gamma and dipmeter logs, revealed an apparent increase in fractures at depth. The paucity of core samples restricts the possibility of verifying the presence of fractures in that borehole.

In Alberta, the availability of the Hunt well for geophysical logging permits the compilation of a comprehensive suite of logs to study the physical properties and conditions of the Precambrian basement. This allows characterizing zones of interest in the basement that are of importance for any potential development of geothermal heat resources in the Athabasca oil sands area. Borehole logs can also provide useful information for the design of seismic surveys including achievable vertical resolution, desirable seismic bandwidth, and average crustal velocities for common midpoint stacking, and time-to-depth conversion (Milkereit and Eaton, 1998).

2.5. Regional Stress Field and Borehole Failures

Engineered geothermal system (EGS) development requires an understanding of the regional stress field to optimize fluid flow between injection and production wells. Furthermore, an understanding of the *in-situ* stress fields, confining pressure, and their relation to rock mechanics, helps to predict the geometry of induced fractures and the amount of pressure needed for fracture propagation (Tester *et al.*, 2006). *In-situ* stresses are the present-day natural stresses present in the Earth's crust as a result of gravitational stresses, current tectonic stresses, and remnant/residual stresses (Ameen, 2003). Gravitational stresses are due to the weight of the overburden while current tectonic stresses are related to present-day tectonic forces. Lastly, remnant/residual stresses are locked in rocks during past episodes of tectonic and gravitational stresses (Ameen, 2003). *In-situ* stress is characterized by the maximum horizontal stress (S_{Hmax}), minimum horizontal stress (S_{Hmin}), and vertical stress (S_v).

Vertical stress (S_v) is often assumed to be equivalent to the overburden weight by integrating the densities of overlying rocks:

$$S_v(h) = - \int_0^h \rho(h)g dh \quad (2-1)$$

where h is the overburden depth, ρ is the average density value and g is the acceleration of gravity. The vertical stresses expected in the Hunt well (Figure 2-7) have been calculated by integrating the density (RHOB) log to be discussed in Chapter 4. The negative stress sign convention assumes that both g and h are positive numbers with the compressional stress increasing with depth (Schmitt *et al.*, 2012). It was found that the magnitude of S_v increases towards the western margin of the basin, where denser materials are present at shallower depths (Bell and Grasby, 2012).

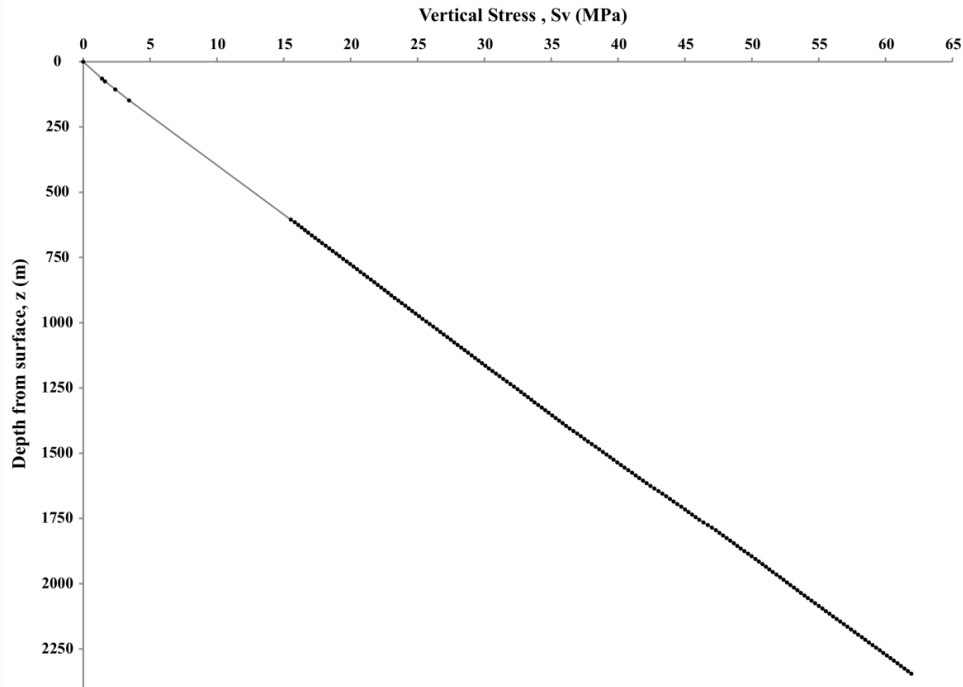


Figure 2-7. Variation of vertical stress magnitudes (black points) with depth in the deep borehole of Fort McMurray under the assumption that the borehole is vertical. Density values are obtained from the bulk density log and no data is available between 148 to 605 m depth. A grey line connecting the available data points is added to facilitate the interpretation across the missing data gap.

In the Western Canada Sedimentary Basin (WCSB), axes of maximum (S_{Hmax}) and minimum (S_{Hmin}) horizontal stresses have been derived from borehole breakouts using borehole image logs and 4-arm dipmeter logs with the majority identified using the latter method (Babcock, 1978). Borehole failures are reliable stress indicators which include the identification of breakouts and drilling-induced tensile fractures (DITF) from the borehole images. Borehole breakouts are stress-induced enlargements that occur on opposite sides of a borehole wall due to the symmetry of stress concentrations around a borehole (Bell and Gough, 1979). This is due to the stress concentration in the surrounding rock exceeding the required stress to cause compressive failure of the borehole wall (Bell and Gough, 1979; Zoback *et al.*, 1985; Bell, 1990; Reinecker *et al.*, 2003). The borehole is then enlarged due to the development of intersecting conjugate shear planes that promotes caving aligned with the axis of S_{Hmin} (Figure 2-8) (Gough and Bell, 1982). S_{Hmax} trajectories are perpendicular to the breakout long axes where the shear failure zone is developed symmetrically about S_{Hmax} . DITFs are formed at right angles to borehole breakouts when the stress concentration in the surrounding rock exceeds that required to cause tensile failure of the borehole wall. They are formed as narrow, sharply-defined features with minimal borehole enlargement in the fracture orientation aligned with S_{Hmax} (Tingay *et al.*, 2008). The 4-arm dipmeter tool contains caliper pads which record the extension of opposite pairs of pads and the compass azimuths of one of the pads. The unequal extension of the pairs of pads and the cessation of tool rotation can also be indicators of borehole breakouts with one of the pad pairs confined to the breakout interval.

In the Western Canada Sedimentary Basin (WCSB), the maximum horizontal stress trajectories are generally found to be aligned along the northeast-southwest direction using the methods discussed above (Bell *et al.*, 1994; Bell, 1996a). These trajectories were mapped in the Mesozoic and Paleozoic rocks by Bell *et al.* (1994) and in the uppermost part of the Precambrian basement using three wells by Bell (1996b). Figure 2-9 shows the S_{Hmax} and S_{Hmin} trajectories in the WCSB that are largely inferred from breakouts (Bell and Grasby, 2012). In the figure,

S_{Hmin} trajectories are aligned with the orientation of borehole breakouts whereas S_{Hmax} trajectories are drawn at right angles to the S_{Hmin} trajectories. The consistent orientation of S_{Hmax} in the WCSB was found to follow the same orientation as the northwestern part of the mid-continental stress province of North America. It was suggested by Fordjor *et al.* (1983) to be associated with the absolute motion of the Earth's tectonic plates ascribed to northeastward flow in the underlying mantle (Bell and Grasby, 2012).

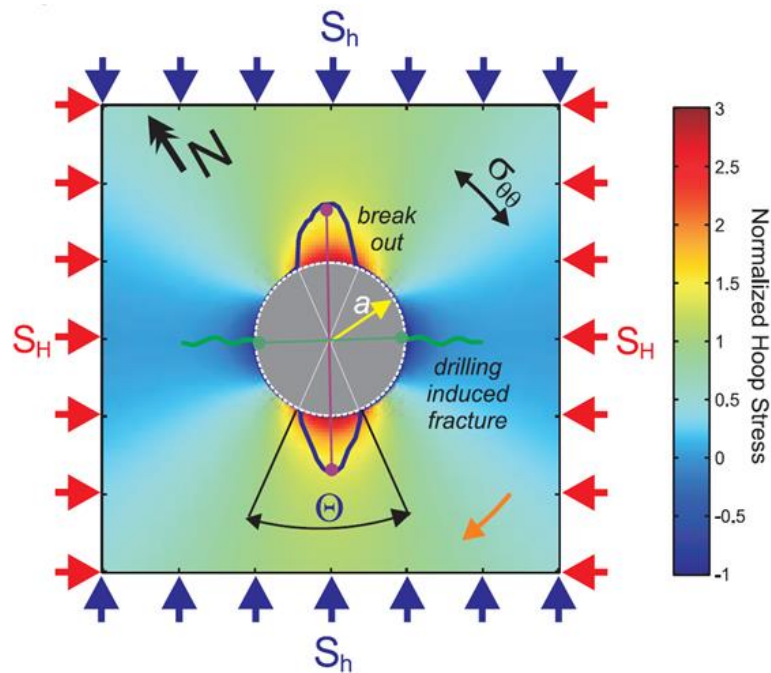


Figure 2-8. Illustration of stress-induced borehole deformation including borehole breakouts, drilling-induced tensile fractures, and their corresponding horizontal stress orientations ($S_H = S_{Hmax}$, $S_h = S_{Hmin}$) (Schmitt *et al.*, 2012)*.

Geothermal exploration requires drilling wells that may involve creating new *in-situ* fractures by hydraulically fracturing the subsurface rocks, or by opening up an existing fracture network via inducing shear motion on the existing discontinuities in the rock mass (*i.e.* hydro-shearing). Engineered geothermal system (EGS) development in the WCSB can be optimized by drilling horizontal

* Reprinted from Tectonophysics, 580, Schmitt, D. R., C. A. Currie, and L. Zhang, Crustal stress determination from boreholes and rock cores: Fundamental principles, 1-26, Copyright Elsevier (2012), with permission from Elsevier.

wells in the direction in which the rate of fluid flow is enhanced. Conventional fluid flow pathway studies have suggested that preferential flow is parallel to the maximum *in-situ* horizontal stress direction with the least degree of closure. Alternatively, it has also been suggested that fractures have less resistance to fluid flow when they are oriented in the direction with high ratio of shear to normal stress (*i.e.* minimum *in-situ* horizontal stress) (Heffer and Lean, 1993; Barton *et al.*, 1995; Rogers, 2003).

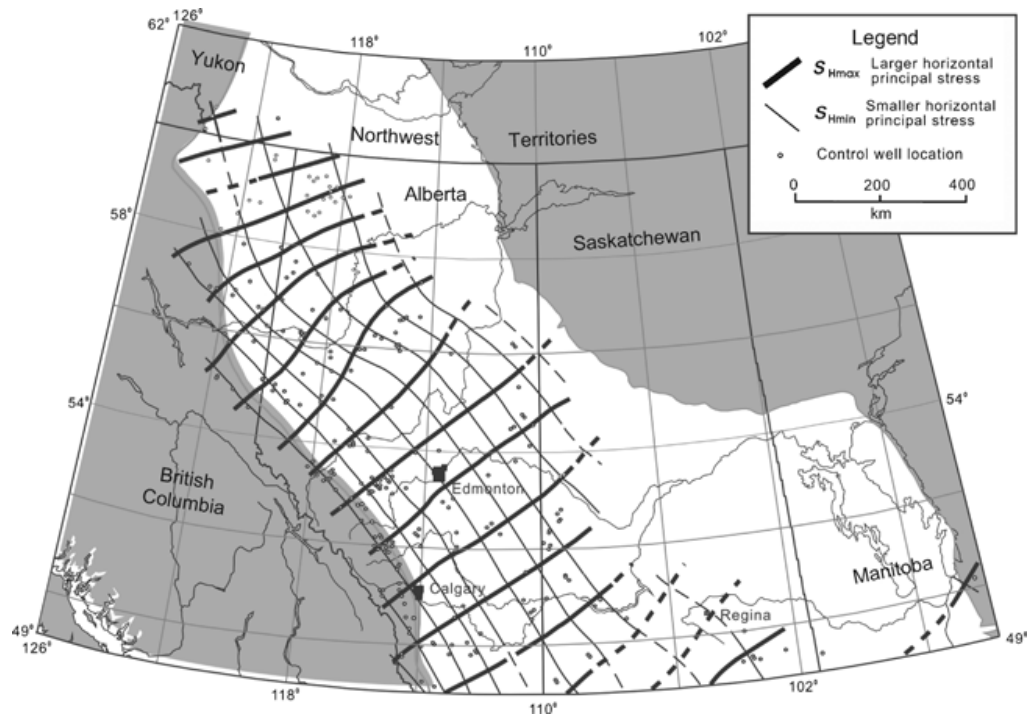


Figure 2-9. Horizontal stress trajectories in the Western Canada Sedimentary Basin largely inferred from borehole breakouts (Bell and Grasby, 2012)*.

There are no known natural phenomena that can record the subsurface horizontal stress field with great precision (Schmitt *et al.*, 2012). The most accurate subsurface determination of *in-situ* S_{Hmin} is obtained by carrying out a ‘micro-frac’ test by initiating a hydraulic fracture in a borehole. This is costly to run and few of them are known to have been made in western Canada. The detail of this

* Reprinted from Geofluids, 12, Bell, J. S. and S. E. Grasby, The stress regime of the Western Canadian Sedimentary Basin, 150-165, Copyright John Wiley and Sons (2012), with permission from John Wiley and Sons.

process is beyond the scope of this thesis and will not be discussed further, but additional details can be found in many references including Fordjor *et al.* (1983), Rutqvist *et al.* (2000), Haimson and Cornet (2003), and Schmitt *et al.* (2012). New stress mapping of the WCSB is also currently being investigated under one of the sub-projects in the geothermal energy research group of Helmholtz-Alberta Initiative. One of the research goals is to update the *in-situ* stress mapping previously done by Bell and Gough (1979), Bell and Babcock (1986), Bell and Price (1989), Bell (1990), and Bell and McCallum (1990). True stress states are also being updated to be as quantitative as possible which could benefit the development of EGS. However, despite these accelerating efforts, the Hunt well will remain, to the best of our knowledge, the only borehole allowing access to deeper rocks of the metamorphic Canadian Shield.

2.6. Physical Properties of Crystalline Basement Rocks

A significant portion of this thesis investigates the log responses in the deep Canadian Shield metamorphic rocks. As such, one must first have some understanding of what physical properties might be encountered in such materials.

Crystalline rocks cover a spectrum of igneous, metamorphic and some sedimentary rocks where recrystallization processes play a role in their formation (Harvey *et al.*, 2005). Geochemistry and geochronology analysis reveal rock types of both igneous and metamorphic origins from the basement cores of the Hunt well. Igneous rocks are formed through the cooling and solidification of magma whereas metamorphic rocks are formed by the alteration of pre-existing sedimentary or igneous rocks in response to increased pressure and temperature, a process referred to as metamorphism (Skinner *et al.*, 2006). Only limited cores were collected at the Hunt well during the drilling operations. The available samples were analyzed to be hercynite biotite garnet gneiss of metasedimentary origin (samples from 1656.5 to 1657.5 m depth) and orthopyroxene granite at 2350 to 2364 m depth (Walsh, 2013) (Table 2.1). Walsh (2013) also dated the crystallization age of the Hunt well samples to be approximately 2400 Ma at the bottom of the borehole.

In crystalline rocks, wireline logs mainly respond to lithology, petrophysical properties of the microfractured rock matrix and macrofractures (Bremer *et al.*, 1992). The term “petrophysics” pertains the study of the physical properties of rock to the pore and fluid distribution (Archie, 1950). Studies of the crystalline rocks in deep boreholes revealed complex geological conditions with low porosity and permeability particularly for metamorphic rocks due to their varying compositional and structural variations. As such, there is no systematic interpretation or classification charts available for the crystalline rocks (Pechnig *et al.*, 2005).

Table 2.1. Rock samples from Hunt well characterized by Walsh (2013).

Depth (m)	Rock Type	Major Minerals	Minor mineral	Accessory minerals	Alteration	Foliation	Comments
1656.7 – 1657.5	Hercynite biotite garnet gneiss	Quartz, potassium feldspar, plagioclase feldspar, garnet	Biotite, hercynite	Zircon, monazite	None	Gneissosity	-
2350 – 2364	Orthopyroxene granite	Quartz, potassium feldspar, garnet	Biotite, orthopyroxene, clinopyroxene, hematite, magnetite, ilmenite,	Zircon, monazite, apatite	none	Minor	Some display schlieren texture

Pechnig *et al.* (2005) compiled a figure displaying the log responses of selected deep boreholes of igneous and metamorphic rock types (Figure 2-10). This figure includes the comparison of log responses of gamma ray, density, compressional velocity, neutron porosity, resistivity, and potassium concentration from boreholes drilled into the continental basement. Gamma ray values were reported to cover a range of 40 to 550 API within the plutonic rocks and gneisses with gneisses typically in the lower gamma-ray range of < 210 API. Acoustic

impedances (Z) between lithologies are defined by compressional-wave (P-wave) velocity (V_p) and density (ρ):

$$Z = V_p \rho \quad (2-2)$$

Difference in acoustic impedance has an effect on the strength of reflectors in seismic surveys. Most metamorphic rocks are an aggregate of minerals that have density values in the range of 2.3 to 3.3 g/cm³ with gneissic rock types revealing broader value ranges (Figures 2-10 and 2-11). Despite laboratory measurements of density and P-wave velocities, they may not necessarily be fully representative of the measured rock samples due to the *in-situ* presence of fractures, formation damage, and ambient stress (Schmitt *et al.*, 2003). Hence, density and sonic logging in a borehole can provide *in-situ* constraints on the elastic properties of the rocks (Eaton *et al.*, 2003). Electrical resistivity values are typically above 10³ ohm-m for massive igneous and metamorphic rocks (Pechnig *et al.*, 2005; Schön, 2011) (Figures 2-10 and 2-13). Zones of lower resistivity values in the massive rock can be attributed to factors such as fracture density, presence of pore fluids, connectivity of pores, or clay content (Pechnig *et al.*, 2005; Schön, 2011).

2.7. Summary

Geothermal energy has the potential of providing a sustainable solution to minimize greenhouse gas emissions in the Alberta oil sands area. An existing deep borehole in the area offers a unique opportunity to study its *in-situ* rock properties for the development of an engineered geothermal system in the crystalline basement rocks of Alberta. Geophysical methods have been widely used in the development of other geothermal sites around the world depending on their tectonic, geological, and hydrological settings. Subject to the availability of geophysical data available near the Hunt well, this project focuses on the interpretation of surface seismic data, borehole seismic data and wireline logs that have been acquired to-date. Regional stress field and an understanding of borehole failure were also reviewed. When an ideal location of the geothermal reservoir has been identified, the regional stress field helps to determine the proper positioning of geothermal wells for the optimal fluid flow direction from

the injection to the production well. Typical physical rock properties for crystalline basement rocks were mentioned for correlation with the measured log responses in Chapter 4. The goal of this study is to provide an integrative approach in understanding the crystalline basement rocks in the current research and development phase of geothermal energy under the Helmholtz-Alberta Initiative.

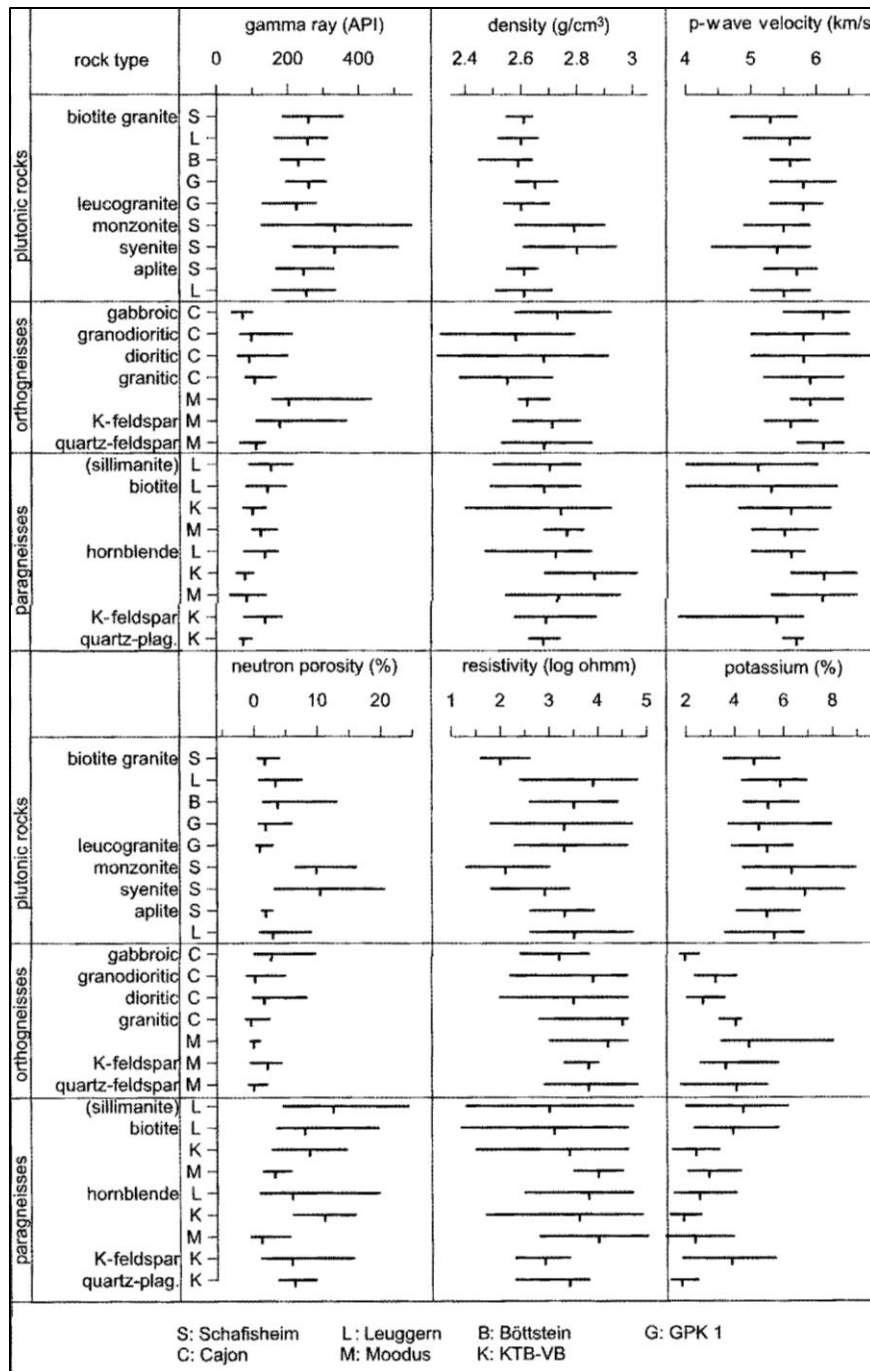


Figure 2-10. Log responses of igneous and metamorphic rock types from deep boreholes in the continental basement (Pechnig *et al.*, 2005)*.

* Pechnig, R., H. Delius, and A. Bartetzko (2005), Effect of compositional variations on log responses of igneous and metamorphic rocks. II: acid and intermediate rocks, in *Petrophysical Properties of Crystalline Rocks*, edited by P. K. Harvey, T. S. Brewer, P. A. Pezard and V. A. Petrov, pp. 279-300, Geological Society Special Publications, London, UK.

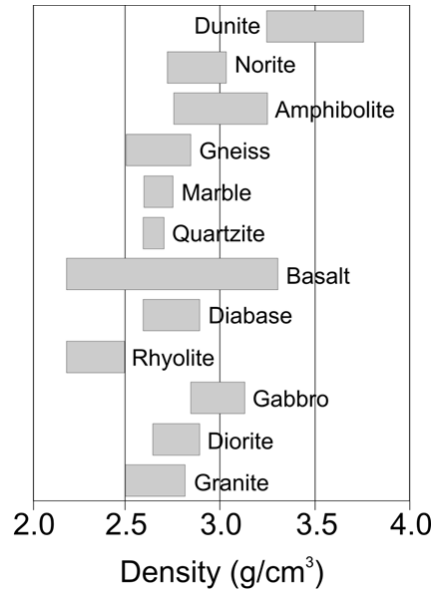


Figure 2-11. Density values of some igneous and metamorphic host rocks (compiled from Hallenborg (1984) and Olhoeft and R. (1989) by Schmitt *et al.* (2003)).*

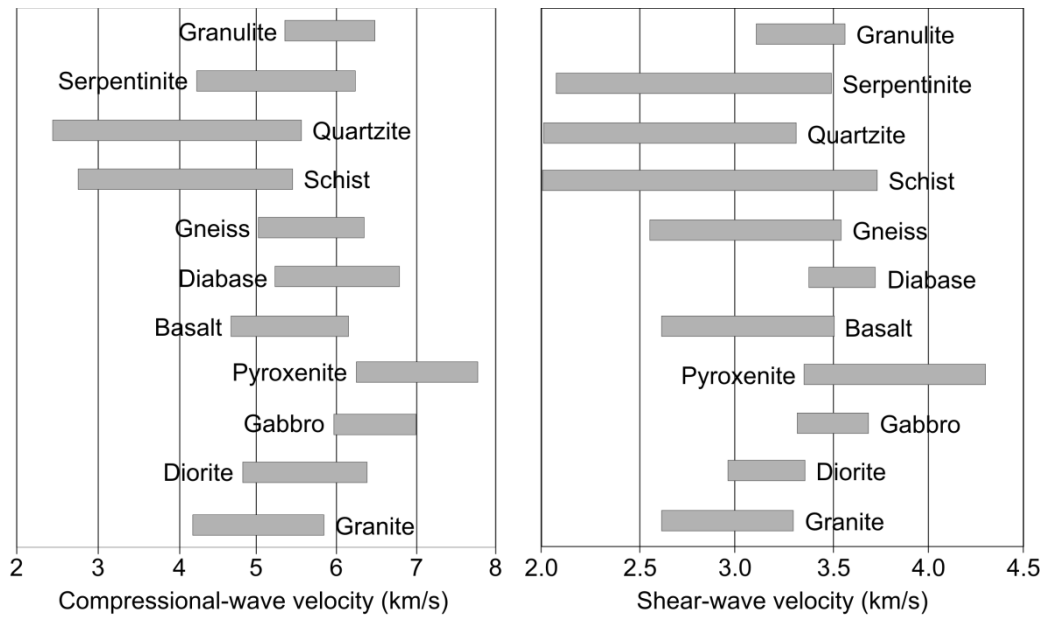


Figure 2-12. Intrinsic compressional- and shear- wave velocities for common igneous and metamorphic rocks (compiled from Schon (1996) by Schmitt *et al.* (2003)).*

* Reprinted from Geophysical Developments, 10, Eaton, D. W., B. Milkereit, and M. Salisbury (eds.), Hardrock Seismic Exploration, Pg. 23-24, Copyright Society of Exploration Geophysicists (2003), according to the fair use of publications outlined by SEG.

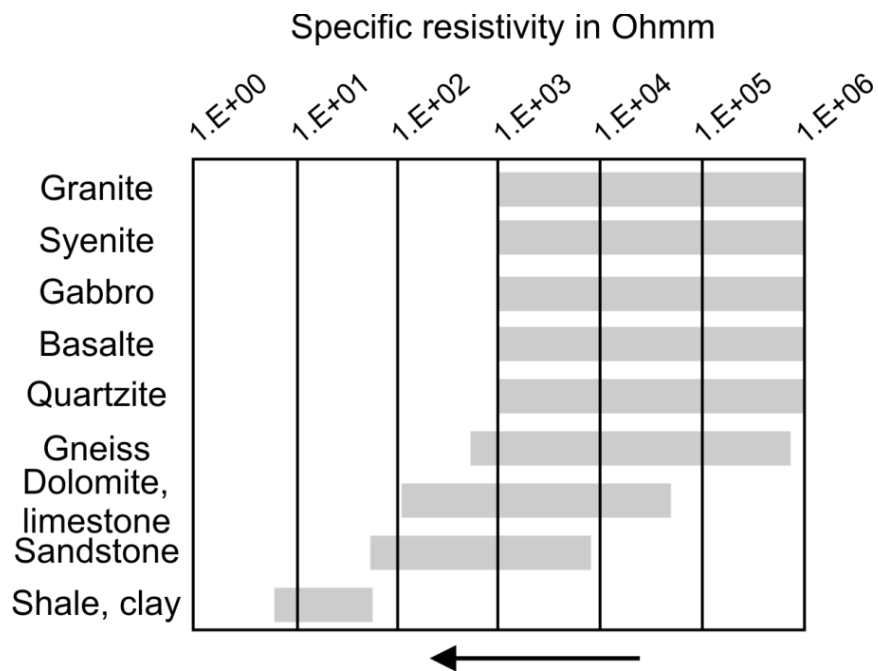


Figure 2-13. Electricity resistivity values of some common rock types. The arrow indicates the effect of water-filled pores and fractures (Schön, 2011) ^{*}.

^{*} Reprinted from Handbook of Petroleum Exploration and Production, Volume 8, Schön, J. H. (ed.), Physical Properties of Rocks – A Workbook, Pg. 280, Copyright Elsevier (2011), with permission from Elsevier.

Chapter 3

Geological Framework

An understanding in the underlying geological framework of the study area is important in proper geophysical data interpretation. This chapter presents background geological information on the tectonic setting of the Canadian Shield, followed by the depositional and stratigraphic setting of the overlying sedimentary successions in the Fort McMurray area. This information is necessary in order to set the geological context for the geophysical interpretations to follow.

3.1. Tectonic Setting of the Canadian Shield

The assembly of the Canadian Shield is the result of tectonic accretionary and collisional processes of pre-existing Proterozoic and Archean cratons during the 2.0 to 1.8 Ga time period (Hoffman, 1989; Pană, 2003). Many of the orogenic belts involved the closure of oceanic basins and consumption of oceanic lithosphere that produced magmatic rocks with the presence of magnetite as an accessory mineral phase (Henderson *et al.*, 1987; Meyer *et al.*, 1992; Ross, 2002). Distinct tectonic settings and boundaries of the Canadian Shield can be understood via geological mapping, geochronological studies, geophysical signatures on potential field maps (Figure 3-1), and geochemical and isotopic database from drill cores (*e.g.* Ross *et al.*, 1991; Burwash *et al.*, 1994; Chacko *et al.*, 2000; Hope and Eaton, 2002; Lyatsky *et al.*, 2005). The crustal structure of the basement beneath Alberta has been identified from gravity and magnetic maps (Hoffman, 1989; Pilkington *et al.*, 2000). An anomaly in the geophysical field map is an indirect indication of some perturbation in the geometric distribution of a particular physical property of underlying rocks (Lyatsky and Pană, 2003). Crustal seismic data in Alberta reveals the complex internal structural fabrics and the non-homogeneous nature of the subsurface rocks in the basement domains (Ross and Eaton, 1999).

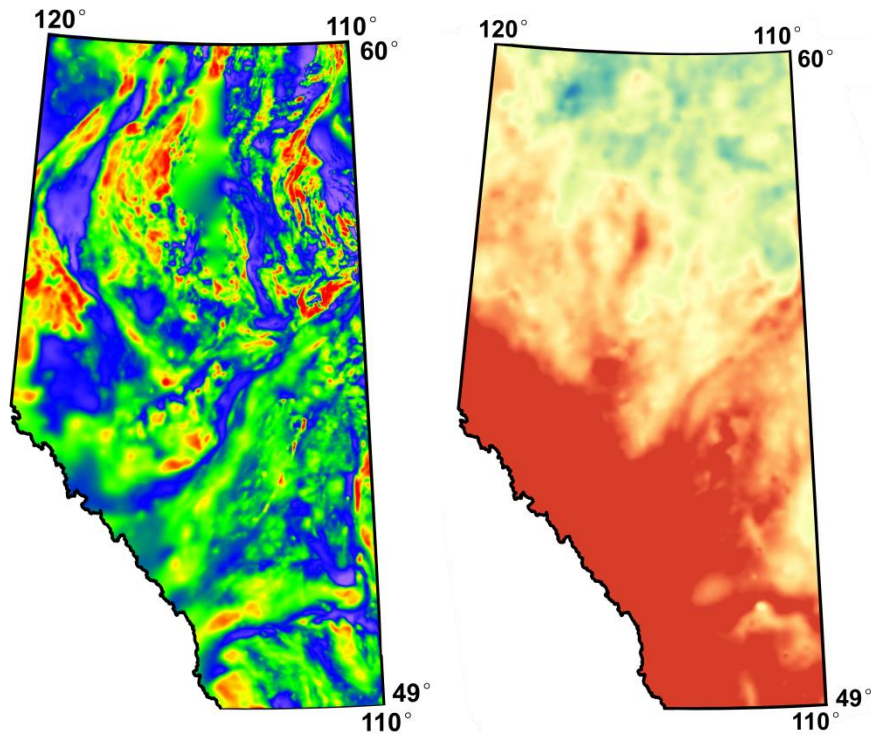


Figure 3-1. The total magnetic (**left**) and Bouguer gravity anomaly (**right**) maps of Alberta. Tectonic domain boundaries can be interpreted from these maps to infer crustal structure as outlined in Figure 3-2. Anomalies in gravity and magnetic data are used to indicate the lateral variations in rock densities and the total magnetization of rocks, respectively (Data from Geoscience Data Repository, 2012a, 2012b)*.

The Fort McMurray area lies within the Taltson magmatic zone (TMZ) (Figure 3-2), a 500 km north-trending Paleoproterozoic orogenic belt that is the southern continuation of the Thelon-Taltson orogens. Magmatic rocks in TMZ were generated during the eastward subduction of oceanic crust beneath a continental margin, followed by direct collision between formerly separated crustal rocks at

* Geoscience Data Repository (2012), Aeromagnetic Data, Retrieved on April 10, 2013 from http://gdrdap.agg.nrcan.gc.ca/geodap/index_e.html.

* Geoscience Data Repository (2012), Gravity Data, Retrieved on April 10, 2013 from http://gdrdap.agg.nrcan.gc.ca/geodap/index_e.html.

1.9 to 2.0 Ga (Ross and Eaton, 1999). To the west of TMZ is the older magmatic belt of the Buffalo Head Terrane (2.0 to 2.3 Ga) and to the east lies the Rae Province (2.6 to 2.8 Ga) (Ross *et al.*, 1991). TMZ extends southward along the western edge of the exposed margin of the Precambrian Shield rocks from Great Slave Lake shear zone and is truncated to the south by the Snowbird Tectonic Zone (STZ).

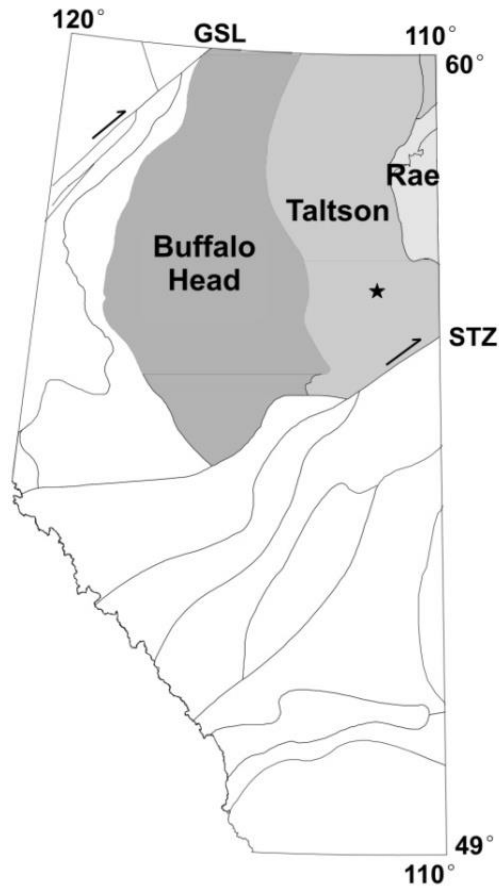


Figure 3-2. Tectonic domains and shear zones for the subsurface basement of Alberta mentioned in this thesis. The Hunt well is marked by a star in the Taltson magmatic domain. GSL and STZ stand for Great Slave Lake and Snowbird tectonic shear zones respectively (GIS polygons compiled by the Alberta Geological Survey in report by Ross *et al.*, 2008)*.

* Ross, G. M., J. Broome, and W. Miles (2008), Tectonic Domains for the Basement of WCSB (GIS data, polygon features), Digital Data DIG 2008-0007, Retrieved on March 19, 2013 from http://www.ags.gov.ab.ca/publications/DIG/ZIP/DIG_2008_0007.zip.

It has been suggested that dextral transcurrent shearing was observed in the deformed granites within the Great Slave Lake shear zone that is prominent in the Taltson arc until at least 1.9 Ga (as cited in Boerner *et al.*, 2000). In the exposed section of TMZ in northeastern Alberta, the TMZ comprises of granitoids, metasedimentary gneisses, granitic basement gneisses, and amphibolites (Chacko *et al.*, 2000). Specifically, the available basement rock samples at the Hunt well are recently characterized as a hercynite biotite garnet gneiss (samples from 1656.5 to 1657.5 m depth) and orthopyroxene granite at 2350 to 2364 m depth (Walsh, 2013).

3.2. Depositional Setting and Stratigraphy

The Canadian Shield is exposed in the northeastern part of Alberta where the geology of the crystalline basement can be traced unambiguously into the subsurface (Figure 3-3) (Ross, 2000). The basement rocks of the Canadian Shield rocks dip gently toward the southwest at 4 to 5 metres per kilometre and are overlain by the Western Canada Sedimentary Basin (WCSB). Basement topography reveals that differential erosion has occurred prior to the deposition of the overlying sedimentary successions (Burwash et al, 1994). The Precambrian crystalline basement is commonly hypothesized to have been reactivated during the Phanerozoic eon (541 Ma to present), which may explain the long, linear or anomalous trends of the sedimentary deposits. Such deposits include abrupt facies changes, orientation of reef trends and clastic strandlines, development of fracture porosity, the localization of hydrothermal fluids and the accumulation of hydrocarbons (Ross and Eaton, 1999). As a result of the Precambrian orogenic activity from more than 1.8 Ga, faults and shear zones formed at the time were interpreted in the shallow seismic profiles that offset the Phanerozoic section (Ross and Eaton, 1999).

The Western Canada Sedimentary Basin is a wedge of Phanerozoic strata that thickens westward from a zero-edge along the Canadian Shield of northeastern Alberta to the disturbed foreland thrust fold belt of the Rocky Mountains and the Foothills. In northern Alberta, the undeformed wedge deposited during the Lower

and Middle Devonian period in which the seas transgressed from the northwest to southeast over the topographic depression of the craton, is enclosed by the craton arches (Bachu *et al.*, 1991). Figure 3-4 shows the generalized stratigraphic chart of northeastern Alberta. The Devonian succession includes variably argillaceous limestones and dolomites that crop out extensively in the valleys of the major rivers and their tributaries in northeastern Alberta. It comprises of strata from the Elk Point, Beaverhill Lake, and Woodbend groups consist of carbonate, evaporite, and clastic rocks. It is also bounded unconformably above and below by the regional sub-Cretaceous units and the Precambrian basement respectively (Cotterill and Hamilton, 1995).

The Elk Point group includes the successions with the lowermost Devonian formation known as the La Loche Formation (granite wash) – a coarse to pebbly, arkosic sandstone unit. The next unit deposited is the Contact Rapid Formation made up of dolomite, dolomitic siltstone and variably sandy shales, with minor anhydrite and gypsum (Cotterill and Hamilton, 1995). The Middle Devonian formations contain the deposition of clean, often porous Winnipegosis-Keg River dolomites with variable thickness (Cotterill and Hamilton, 1995). The last two units of the Elk Point Group is marked by an eastward thinning wedge of salt and anhydrite with thin interbeds of carbonate and shale (Prairie Evaporites formation), and then overlain disconformably by a blanket of distinctive, dolomitic shales of the Watt Mountain Formation.

The beginning of the Upper Devonian period is marked by the Beaverhill Lake Group which is primarily an inter-platform basin as a result of two depositional transgressive and regressive phases of shallow marine carbonate platforms (Bachu *et al.*, 1991). In ascending order, this group consists of Fort Vermilion, Slave Point, and Waterways formations. Fort Vermilion consists of anhydrite with interbeds of limestone or dolostone. Reefal carbonate complexes known as the Slave Point Formation lie conformably above the Fort Vermilion succession in the form of mudstones with interbedded shale laminae. The Waterways formation is the final group of Devonian strata identifiable in northeastern Alberta and is an

alternating succession of calcareous shales and carbonates (Bachu *et al.*, 1991). This formation is further subdivided into the Firebag, Calumet, Christina, Moberly and Mildred members which are all mappable across the region (Crickmay, 1957; Cotterill and Hamilton, 1995).

Pre-Cretaceous erosion has partially removed some of the older eastward tapering wedge of Devonian successions prior to the overlain of Cretaceous siliciclastics as the foreland-basin strata (Bachu, 1993; Cotterill and Hamilton, 1995). Basin-wide sedimentation of the Mannville Group strata occurs with a marine transgression during the Lower Cretaceous period on top of the pre-Cretaceous unconformity (Carrigy, 1966). The Mannville Group includes the McMurray, Wabiskaw, Clearwater and Grand Rapids formations as a combination of interbedded sands, shales and oil sands (Bachu *et al.*, 1991). Further toward the northeastern part of Alberta, both the Mesozoic and Paleozoic strata subcrop with increasing age toward the exposed Canadian Shield. The top of the foreland-basin strata is covered by a thin veneer of Pleistocene deposits consisted of the unconsolidated sands and gravels with variable thicknesses (Bachu *et al.*, 1991, 1993).

Significant topographic relief can be explained by a combination of partial erosion of carbonate units, orogenic uplift, syndepositional solution-collapse of the Devonian evaporites, and post-Cretaceous erosional events (Cotterill and Hamilton, 1995; Machel *et al.*, 2000; Langenberg *et al.*, 2002; Paulen *et al.*, 2004). As a result of depositional and erosional events during the Cretaceous and early Tertiary phase, present-day topography ranges in elevation from 1200 m in the southwest edge of the basin to slightly less than 200 m in the northeastern corner of the basin near the Precambrian Shield (Figure 3-5) (Bachu, 1999). Unconsolidated sediments overlying the bedrock include sediments of both Tertiary and Quaternary age. Drift thickness ranges from 0 m to 300 m in Alberta (Fenton *et al.*, 1994; Pawlowicz and Fenton, 1995; Fenton and Pawlowicz, 2000). All of northern Alberta is covered by a number of glacial tills. In the study area of this project, drift thickness has been reported to be less than 15 m thick (Pawlowicz and Fenton, 1995).



Figure 3-3. Surficial geology of Alberta compiled by Energy Resources Conservation Board and Alberta Geological Survey. This map illustrates the geology at or near the modern land surface. The general relationship between bedrock topography and the origin and distribution of surficial deposits show that large parts of the modern Alberta landscape relate to the topography of the underlying bedrock (Fenton *et al.*, 2013) ^{*}.

^{*} Reprinted from Surficial Geology of Alberta, AER/AGS Map 601, Fenton, M. M., E. J. Waters, S. M. Pawley, N. Atkinson, D. J. Utting, and K. McKay, Copyright Alberta Energy Regulator (2013), reprinted with permission from AER.

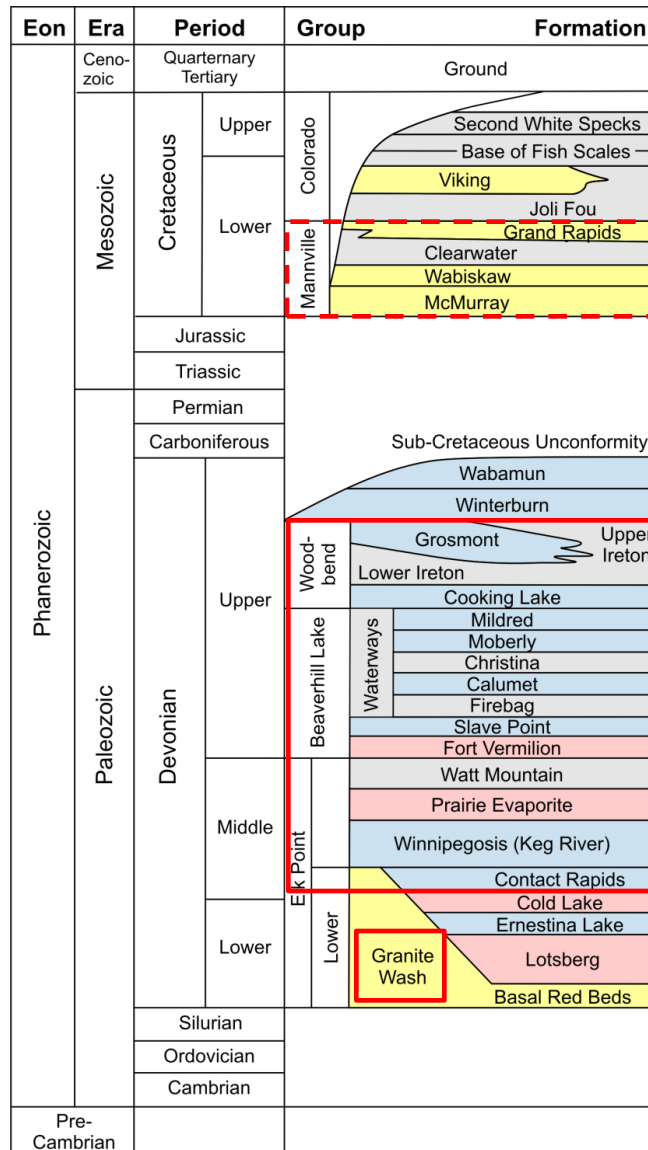


Figure 3-4. Generalized stratigraphic column of northeastern Alberta. The lithological colour codes are: grey – shales, blue – carbonates (limestone, dolomite), pink – evaporites (anhydrite, halite), yellow – clastics (sandstones, siltstones, and conglomerates). Red rectangles outline formations interpreted in the Hunt well by Schneider *et al.*, (2012). Dashed red rectangles highlight formations that are also present in the region with no existing log information available to verify their depths in the Hunt well. Figure generated with reference from Bachu *et al.* (1991) and ERCB (2009)*.

* Bachu, S., J. R. Underschlutz, D. McPhee, and D. K. Cotterill (1991), Regional geology and hydrostratigraphy in northeast Alberta (Prepared for Conservation and Protection, Environment Canada), 162 pp, Alberta Geological Survey, Edmonton, Alberta, Canada.

* Energy Resources Conservation Board (ERCB) (2009), Table of Formations, Alberta, ERCB Information Services, Calgary, Alberta, Canada.

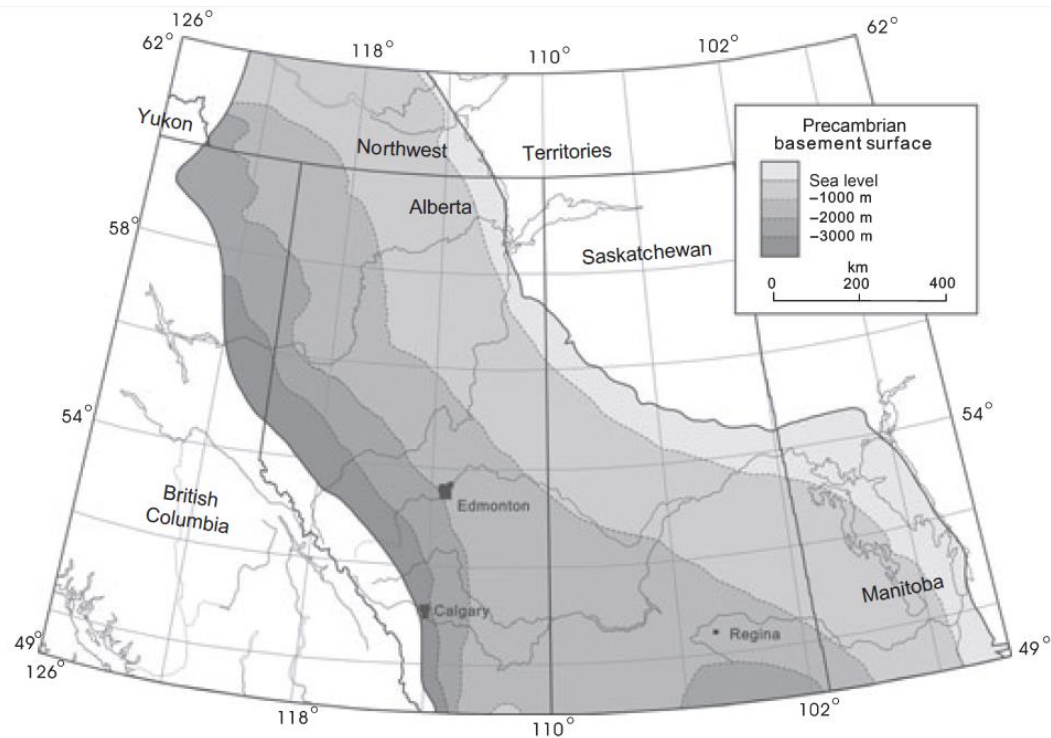


Figure 3-5. Precambrian basement surface of the Western Canada Sedimentary Basin (Bell and Grasby, 2012) *.

3.3. Summary

The tectonic setting of the basement domains, depositional setting and stratigraphic of the Canadian Shield have been reviewed in this chapter. With the thin sedimentary cover in the Fort McMurray area, geothermal development requires drilling deep into the Precambrian basement rocks to reach the sufficient temperature for oil sands processing. Existing crustal seismic studies revealed structural complexities of the subsurface rocks in the basement domains. Therefore, knowledge of the geological framework of the study area is important in the interpretation of seismic and borehole data for a thorough integrated study for geothermal reservoir development.

* Reprinted from *Geofluids*, 12, Bell, J. S. and S. E. Grasby, The stress regime of the Western Canadian Sedimentary Basin, 150-165, Copyright John Wiley and Sons (2012), with permission from John Wiley and Sons.

Chapter 4

Geophysical Well Logging

A standard operation in any drilling activity is to acquire a series of geophysical well logs to study the *in-situ* physical properties of the rocks and to provide information regarding the depths to different geological features. Normally various tools are lowered to the bottom of the borehole and ‘logging’ of the physical properties occurs as the tool is pulled upward. The continuous record of the signals from the sonde is referred to as a log and it records the physical parameters of the rocks as a function of depth. In Alberta, borehole logging has mainly focused on the Western Canadian Sedimentary Basin for hydrocarbon production. Consequently, log measurements of the Precambrian basement rocks are rarely recorded and analyzed. The Hunt well is a 2.36 km well drilled into the crystalline basement rocks located west of Fort McMurray (latitude 56°45’N, longitude 111°33’W). It is by far the deepest well drilled into the basement below the sedimentary successions in Alberta and provides us an unparalleled opportunity to assess these deep rocks.

The current objectives of geophysical log analysis for the Hunt well are:

- (1) to understand the petrophysical rock properties in the Precambrian basement that is not commonly studied in Alberta,
- (2) to assess the geological formations and fractures intersected by the well in the basement rocks that could act as indicators of enhanced fluid potential or flow pathways,
- (3) to analyze the acoustic responses of rock properties (density, compressional wave velocity and acoustic impedance) to assist in the interpretation of seismic surveys, and
- (4) to understand the nature of seismic reflectors observed in the upper crust (Chapter 5).

This chapter presents the compilations of log responses encountered primarily in the basement section of the Hunt well, and discusses how the physical properties can contribute to the understanding of the subsurface, and in turn to the potential engineered geothermal system development in Alberta. The interpretation section will be divided into the characterization of the rocks, heat generation, fracture detection, acoustic properties and thermal logging of the crystalline rock formation in the borehole.

4.1. Borehole Logging

Due to the limited cores available at the Hunt well, wireline geophysical logs become the most effective tool available for subsurface characterization at this location. The common applications of logs toward geothermal investigations include assessing the geological formations and fractures intersected by the well, studying the relationship between petrophysics of the formation rocks and its permeability, and understanding the relationship between natural fracture distribution, fluid flow and the ambient tectonic stresses in the subsurface (Rose *et al.*, 2005; Sausse *et al.*, 2006; Steingrímsson, 2011). The following sub-sections include the general physics principles of the individual logging measurements recorded in the Hunt well, and their relevant applications in meeting the objectives of this study. The depth of the measurements in this thesis are reported with respect to the Kelly bushing (KB) of the well which is at an elevation of 409.3 m above sea level (masl).

4.1.1. Natural Gamma Ray (GR)

The Earth's natural gamma ray (GR) radiation originates from the spontaneous decay of three radioactive isotopes which includes potassium (^{40}K) and the decay series of uranium (^{238}U and ^{235}U) and thorium (^{232}Th). Scintillation counters are generally used in the modern era to measure the total intensity or the energy spectrum of gamma radiation (Schlumberger, 1991). The recording of a gamma ray is a passive measurement of the total natural gamma radiation of the formations. A detector is lowered into the well to record the natural radiation from

the surrounding rocks. With the variation in size and efficiency of the counters used in the logging tools, GR recordings are primarily calibrated to a reference well at the University of Houston and logs are presented in API (American Petroleum Institute) units. This unit is defined from an artificial radioactive formation to simulate approximately twice the radioactivity of marine shale to ~200 API units (Ellis and Singer, 2007). The reported API units in sedimentary formations generally range from a few API units in anhydrite or halite to 200 API or more in shales (Schlumberger, 1991). GR responses range widely from 40 to 550 API in several deep boreholes drilled into the metamorphic rocks. The average GR values for plutonic and gneisses are approximately 250 to 350 API and below 210 API respectively (Figure 2-10; Pechnig *et al.*, 2005).

A GR log is commonly used for discrimination between different lithologies, determination of shale content (in sedimentary rocks), and correlation between wells. This log is almost always used as part of every logging combination run since it is useful for depth correlation across different data sets. It is also the most common nuclear log used for stratigraphic correlations in a geologic cross-section since it can be recorded in cased boreholes. For the purpose of geothermal exploration, GR log is further used to determine the amount of heat generation in the Earth's crust from the concentration of detected radioactive elements. Using a linear relationship of the total radioactivity measurements and heat generation (Rybach, 1986; Bückner and Rybach, 1996), radiogenic heat generation (A) can be predicted as followed:

$$A = 0.0158 (GR - 0.8) \quad , \quad (4-1)$$

where A is the heat generation value in $\mu\text{W}/\text{m}^3$ and GR is the gamma intensity in API units. This equation was derived (Rybach, 1986) and refined (Bückner and Rybach, 1996) based on a number of research boreholes measured from the natural gamma spectrometry tool at the time. The mean total GR intensity for the Hunt well in the Precambrian basement (1005 to 1873 m) is calculated to be 194.55 API which predicts a heat generation value of $3.06 \mu\text{W}/\text{m}^3$. Compared to the boreholes discussed by Pechnig *et al.* (2005), the GR value at the Hunt well is

in the rock category with gneissic composition since it is below 210 API (Pechnig et al., 2005).

4.1.2. Spectral Gamma Ray (SGR)

A spectral gamma ray log (SGR) measures radiation emitted from the three separate radiogenic isotopes (^{40}K , ^{238}U , and ^{232}Th) as they decay into their respective stable forms. The decay of ^{40}K delivers a monoenergetic gamma radiation of 1.46 MeV into the stable argon. ^{232}Th and ^{238}U decay in a series of steps that result in more complex energy spectra before ending at the stable lead isotopes, with gamma ray activities at 2.62 MeV and 1.76 MeV, respectively (Figure 4-1).

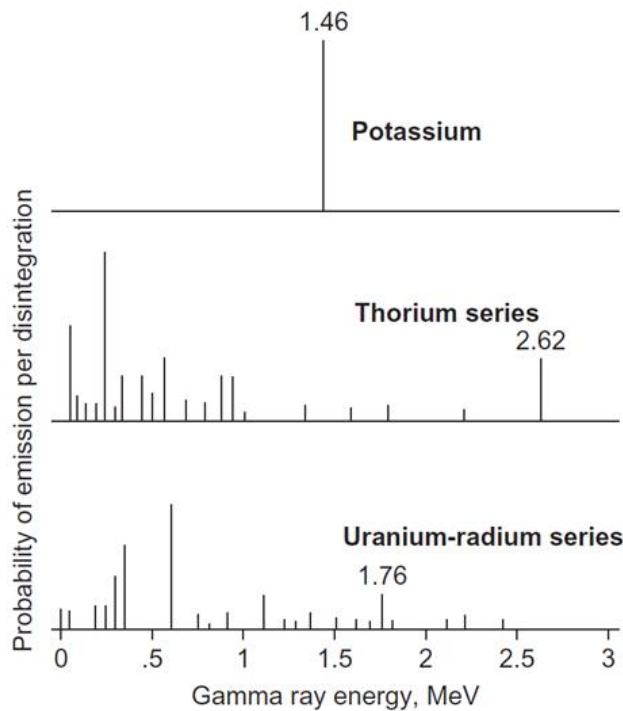


Figure 4-1. Distribution of gamma ray energies from the three radiogenic elements in the Earth's crust as measured by the spectral gamma ray tool (Ellis and Singer, 2007)*.

* Reprinted from Well Logging for Earth Scientists, 2007, Pg. 269, 11. Gamma Ray Devices, Ellis, D. V. and J. M. Singer, Fig. 11.2, Copyright Springer Science and+Business Media B.V., with kind permission from Springer Science+Business Media B.V.

In the two deep boreholes of the Los Alamos Scientific Laboratory's Hot Dry Rock geothermal project, SGR logs were demonstrated to be useful in determining rock types, in detecting fracture zones, and in examining the mobility of the heat-producing elements K, Th, and U in the crystalline basement rocks (West and Laughlin, 1976). These three elements are a result of the original contents of igneous or sedimentary materials that may have been changed by metamorphic processes, which then get adsorbed and redistributed according to the degree of metamorphic transformation (Rybach and Cermak, 1982). Higher concentrations of these elements are associated with elevated heat flow and can be considered as heat sources for geothermal exploration (Majorowicz *et al.*, 2012).

By plotting each radioactive element separately, SGR logs can be used as a quantitative clay indicator in sedimentary rocks. Clay types can be identified in terms of the relative contributions of the specific radioactive components. Potassium can be found in previously potassium-enriched phyllosilicates minerals such as illite $((K,H_3O)(Al,Mg,Fe)_2(Si,Al)_4O_{10}[(OH)_2,(H_2O)])$, and biotite $(K(Mg,Fe)_3(AlSi_3)O_{10}(OH)_2)$ (Sausse *et al.*, 2006). Uranium is water soluble and is highly mobile in an oxidizing environment. It can be easily leached and removed from the rock matrix, then precipitated along fractures with enhanced permeability causing local peaks in the uranium SGR log. Thorium can be found in clay minerals by means of ionic exchange or adsorption. Unlike uranium, thorium is effectively insoluble in natural waters (Langmuir and Herman, 1980). It can contribute to the radioactivity of a rock in the form of a heavy mineral component, or adsorbed onto the surfaces of clay minerals (Hesselbo, 1996).

The average concentrations of uranium, thorium and potassium in the Earth's crust are about 3 ppm, 12 ppm, and 2.6 % respectively (Schlumberger, 1991). For a more specific study on the concentrations of these elements in the continental crust, Rudnick and Gao (2003) published separate values for the upper crust, middle crust, lower crust, and the bulk continental crust.

Using the equation by Bückner and Rybach (1996), heat generation can be calculated using the reported radiogenic concentration values from the SGR logs by:

$$A = 10^{-5} \rho (9.52 U + 2.56 Th + 3.48 K) \quad , \quad (4-2)$$

where ρ is the density of the rocks (kg/m^3), concentrations for U and Th are in parts per million (ppm) and K as a percentage value. This equation was derived when the natural gamma spectrometry tool became more widely used in boreholes with improved records on the U, Th, and K contents, and also rock density values from the litho-density tool (LDT) measurements (Section 4.1.6). The reported mean values in the Hunt well from the latest data for U, Th, and K are 1.65 ± 1.05 ppm, 35.24 ± 19.60 ppm, and 3.22 ± 1.37 % respectively between depths 1005 m to 1873 m with a mean heat generation of $3.05 \mu\text{W/m}^3$. Only open hole measurements were used in the calculation of radiogenic heat concentration as SGR data needs to be corrected for borehole effects, mainly the effect of the GR-absorbing metal casing.

4.1.3. Caliper (CALI, C)

The caliper log is a tool for measuring the borehole diameter with 2, 4 or more extendable arms. The latest caliper logging run at the Hunt well was recorded using a 4-arm (dual caliper) dipmeter tool from the ICDP-OSG. This tool is commonly run in the hydrocarbon industry to analyze the strike and dip of the bedding, and also to estimate the volume of cement required for the borehole casing (Reinecker *et al.*, 2003). When the borehole has the same diameter as the drill bit size, it is referred to as *on* or *in gauge*. Otherwise, if a fractured zone is encountered during drilling, rock edges are often chipped away causing the borehole to enlarge (borehole breakout) and/or elongate in the plane of the fracture system. A widening in the borehole can sometimes be related to open fractures. In general, caliper log response should not be solely used as fracture detection since other factors such as directional drilling and a deviated borehole can also contribute to the ellipticity.

The development of an engineered geothermal system (EGS) requires preferential pathways for fluid flows between the injection and production wells. At the Soultz-sous-Forêts EGS test site in France, the granitic basement has been strongly altered by fluid flows in the fractured graben as a result of tectonic extension of the Rhine Graben (Sausse *et al.*, 2006). The possible altered path and flow path at the interface between standard granite and mica-enriched granite was interpreted from the borehole casing section in the caliper logs (Cocherie *et al.*, 2004; Hooijkaas *et al.*, 2006). In our work here at the Hunt well, caliper logs are expected to be useful in identifying potential fractured or caved zones and borehole breakouts that could act as fluid pathways between wells. Furthermore, they could be used as quality assessment of other geophysical log responses that could be affected by the condition of the borehole walls.

4.1.4. Self Potential (SP)

The self potential (also known as the spontaneous potential, SP) log measures the potential difference of an electrode in the borehole and a fixed surface electrode. The spontaneous current flow arises primarily from the salinity contrast between the formation water and the mud filtrate against permeable beds as ions move between the borehole fluid and its surrounding rocks and formation fluids. The electrochemical potential arises from the electrical interactions between various chemical constituents of the rocks and fluids, whereas the electrokinetic potential arises from the movement of electrically-charged ions in the fluid relative to the formation rocks. Since conductive fluids are required to create a SP response, SP recording is limited to water- or mud-filled open hole environments.

The SP log has no absolute scale as it is interpreted based on the relative changes in the measurements. That said, nearby relative changes can be interpreted in terms of the salinity variations (actual chemical activity) between the borehole and the connate *in-situ* fluids. In a log display, the SP response is shown in millivolts (mV), with negative deflections to the left and positive deflections to the right. The main uses of this log in the sedimentary layers are to identify bed boundaries and thicknesses, detect permeable beds, determine the formation water

resistivity, and correlate between wells. Frequent forms of water storage in crystalline rocks include zones of dense fracturing and weathering. Bram *et al.* (1995) reported abnormal SP deflections occurring across mineralized fault systems and zones of water influx in the deep crystalline rocks of the KTB borehole in Germany. In a landslide study, SP was used to identify fluid flow variations within major faults and fractures at the edge of a landslide (Bruno and Marillier, 2000; Jongmans and Garambois, 2007). In the crystalline terrain, Medeiros and Lima (2005) reported appreciable negative SP deflections and resistivity minima that correspond to fractures intersecting the borehole. Therefore, in basement studies where crystalline rocks are known for their low porosity and permeability, the SP log serves to identify any permeable zones in the subsurface that could have a possible correlation to fracture zones.

4.1.5. Resistivity (R)

The resistivity log measures a formation's apparent resistivity (R_a), *i.e.* the ability of the formation rock to conduct electrical current. The tool setup involves sending an electric current flow from the current electrode to the potential electrodes that are variably-spaced. The spacing between the electrodes determines the depth of investigation and the resistivity reading of the invaded zone (R_{xo}) or of the true formation (R_t). Generally an increase in spacing between the electrodes results in an improved depth of investigation and a closer reading to R_t but with the cost of reduced resolution. The primary constraint for resistivity tools is the mud fluid type. A conductive (water-based) mud is required during logging to allow current flow in the formation. Resistivity logs are presented in logarithmic scale in ohm-m due to their wide range of values. Two types of focused electrode configurations for resistivity measurements were used in the Hunt well: Dual laterolog (DLL) acquired by Schlumberger and ICDP-OSG and micro-spherically focused log (MSFL) acquired also by Schlumberger.

The measured current of a laterolog constitutes a series current through the drilling mud, mud cake, flushed zone, invaded zone and the undisturbed formation rocks. DLL is a form of deep-reading electrode log that measures R_t of

the formation. By focusing the electrode current to flow laterally into the formation, this form of deep-reading resistivity device was designed so that its response is determined by the virgin formation beyond the invaded zone. It has a response range of 0.2 to 40,000 ohm-m which is a much wider range than the traditional laterolog devices (Schlumberger, 1991). The depth of investigation of this log is approximately 60 to 90 cm with a vertical resolution of 80 cm. A simultaneous measurement of the deep (LLD) and shallow (LLS) laterolog resistivities can be recorded by rapidly changing the roles of the various electrodes on the tool (Ellis and Singer, 2007). The vertical resolution of LLS is the same as that of LLD, but the focusing current is less strongly focused as the current is returned to the nearby electrodes. This causes the current to diverge more quickly as it entered the formations with a much shallower depth of investigation.

The electrode spacing for the micro-spherically focused log (MSFL) is smaller than that for the dual laterolog (DLL). The source electrode emits a highly-focused beam which results in a shallower depth of investigation, to about 10 cm, for penetrating the mud cake. It was designed to improve the accuracy of the invaded zone (R_{xo}) measurements, and provide a better estimate of the mudcake resistivity (R_{mc}) and thickness (H_{mc}) (Eisenmann, 1994). MSFL is ideal for identifying thin beds and for detecting permeable zones in the borehole. The buildup of a mud cake is a qualitative indicator for permeable layers since it only forms on invaded formations.

Low porosity crystalline rocks are generally known to be highly resistive except for cases where they contain substantial graphite or base metal sulphides and oxides. The presence of interstitial fluids, alteration minerals, total amounts of dissolved solids, surface conduction, connective or effective porosity, and temperature are factors that can affect the conductivity of crystalline rocks. The first two phenomena are sometimes associated with geothermal activity (Jackson *et al.*, 1992; Manzella, 2000; Boness and Zoback, 2004). Fractures in such resistive rocks may act as major conduits for the flow of electric current in the

presence of formation fluids (Jackson *et al.*, 1992). Deep resistivity reading tools can detect open fracture zones in the case that mud filtrate penetrate the fracture space due to the resistivity contrast between mud filtrate and the formation rocks. They present a more accurate representation of the undamaged formation properties. The vertical resolution of resistivity logs allow us to identify the clear boundaries of lithological variations, particularly conductive zones that could be related to fractured zones in the crystalline rocks. Low resistivity anomalies were identified previously in other geothermal studies in which they represent the boundaries of the geothermal reservoir where altered conductive minerals have been formed (Steingrímsson, 2011).

4.1.6. Litho-Density

The litho-density tool (LDT) is designed to direct gamma rays into the formation. Gamma ray flux resulting from the scattering and absorption effect of the formation will then be measured by the detectors. The Cesium-137 radiation source on the LDT emits gamma rays at an energy level of 0.662 MeV, which undergo Compton scattering as they travel and lose energy to the rock mass (Ellis and Singer, 2007).

Separate gamma ray windows which have both high (hard gamma rays: 0.25 to 0.662 MeV) and low (soft gamma rays: 0.00 to 0.04 MeV) energy spectrum will be measured. The number of scattered gamma rays returning to the tool detectors in the Compton scattering region is inversely related to the electron density of the formation. The greater the formation mass density, the lower the gamma ray counts at the detectors. Measurements include the effect of both the rock matrix and the contained fluids (McEwen *et al.*, 1985). Since the Compton scattering effect is directly proportional to the rock density, the bulk density (ρ_b) can be accurately estimated as a response to the electron density (ρ_e) of the formations as defined by Ellis *et al.* (1985):

$$\rho_e = \rho_b \left(\frac{2Z}{A} \right) , \quad (4-3)$$

where Z/A is the average value of the ratio between the atomic number (number of protons per atom) to the atomic weight of the scattering formation. Note that $2Z/A$ is often close to unity because the number of protons and neutrons (A) in most of the elements in rock forming minerals is twice the number of protons (Z) alone. Density values are typically reported in kg/m^3 or g/cm^3 (g/cc).

As gamma rays are progressively scattered they lose energy, and once they are reduced (below 0.2 MeV), they are absorbed by the atoms in the rocks through photoelectric absorption. In this spectral region, the gamma ray counts become inversely related to both the electron density and the photoelectric absorption factor (PEF, P_e). P_e (in barns/electron unit) can be approximated by the empirical relationship (Ellis *et al.*, 1985):

$$P_e = \left(\frac{Z}{10}\right)^{3.6}, \quad (4-4)$$

which is dependent on the lithology of the formation rocks. PEF is a good lithology indicator if there is no barite in the drilling mud (Farag *et al.*, 2010). Table 4-1 lists the density and PEF values of minerals commonly found in metamorphic rocks.

RHOB and PEF from LDT have a depth of investigation of 50 to 60 cm which varies by the spacing between the radiation source and detectors. Together, they are useful for narrowing down the possible mineralogy in the rock mass in the absence of cores. The density of rocks is affected by porosity, water content and chemical composition. Most of the density variations within igneous and metamorphic rocks are due to the variations in proportions of mafic and felsic minerals. Rocks with higher percentages of mafic minerals have higher densities than those with higher proportions of felsic minerals (Mwenifumbo and Mwenifumbo, 2012).

A density log is primarily acquired in an open hole environment and is an essential parameter for defining the porosity (ϕ) of reservoir rocks using the following empirical relationship:

$$\phi = \frac{(\rho_{gr} - \rho_b)}{(\rho_{gr} - \rho_w)} , \quad (4-5)$$

where ρ_{gr} is the mean grain density, and ρ_w is the density of the pore fluid that is usually assumed to be water. In the low porosity metamorphic rocks, the porosity is expected to be small (< 1%).

Table 4-1. Density and photoelectric factor values for common minerals found in metamorphic rocks compiled from Schlumberger (2009) and Schön (2011).

Minerals	Log Density (g/cm ³)	Measured Density (g/cm ³)	Photoelectric Factor, PEF (barns/electron)
Biotite	2.99	2.90	6.3
Calcite	2.71	2.71	5.1
Chlorite	2.76	2.80	6.3
Hematite	5.18	5.73	21
Hornblende	3.20	3.08	6
Magnetite	5.08	5.20	22
Muscovite	2.82	2.83	2.4
Orthoclase	2.52	2.57	2.9
Pyrite	4.99	5.01	17
Quartz	2.64	2.65	1.8
Zircon	4.50	4.67	69

4.1.7. Neutron Porosity (NPOR, NPHI)

Neutron logging undergoes three processes of interest: neutron emission, neutron scattering and neutron absorption. Neutrons are neutrally-charged particles and have great penetration depth. Each neutron has a mass almost identical to the mass of a hydrogen atom. The compensated neutron log (CNL) tool contains a high-energy radioactive source and two detectors. The neutron sources used in logging are a mixture of two elements – an alpha emitter and a neutron-producing

target element such as beryllium (Be). One common source used is Americium-Beryllium (AmBe) (Ellis *et al.*, 2003).

Neutron scattering involves both inelastic and elastic collisions between the neutron and the nucleus. A compound nucleus is formed in an excited state after inelastic scattering. It decays rapidly to the original nucleus while emitting a neutron which then emits a gamma ray to become an atom of the target nuclide in its ground state. The GR produced from the collisions are characteristic of the energy levels of the target nucleus (Hearst *et al.*, 2000). The more common interaction is elastic scattering, which refers to the process in which neutrons interact with the nuclei of atoms within the formation. A good analogy to this is the elastic interaction between billiard balls. During the elastic scattering process, energy transfer occurs in which the energy and momentum of the neutron and nucleus are conserved. Energy loss depends on the mass of the collided isotope and the angle of scattering between the scattered neutron and nuclei (Figure 4-2).

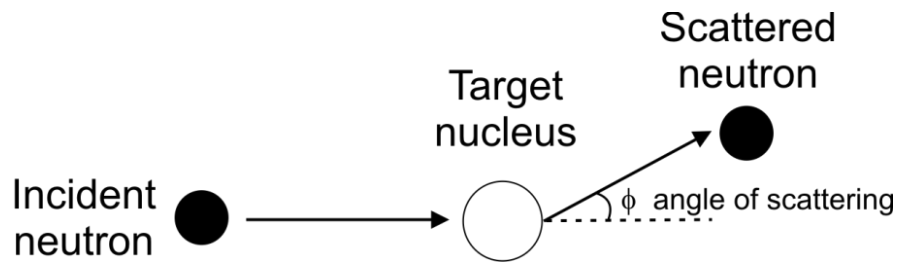


Figure 4-2. Schematic diagram of elastic scattering between neutron and nuclei of atoms in the formation.

Successive elastic collisions reduce the energy level of the neutrons to their thermal state (energies of around 0.025 eV). These slow moving neutrons are absorbed by the nuclei of the formation atoms. The greatest energy loss occurs when the high energy neutrons collide with hydrogen nuclei (equal mass). More collisions lead to fewer neutrons arriving at the detectors which indicate the presence of more hydrogen atoms (*e.g.* water content bound in minerals like phyllosilicates or amphiboles) in the formation.

Thermal neutrons recorded from the CNL tool is typically presented in limestone porosity units toward the delineation of porous formations and their porosity. This means that the porosity reading in a limestone (*i.e.* pure calcite) formation will be exact, but the readings in other formations will need to be corrected using a correction chart (*i.e.* Chart Por-11, Schlumberger, 2009). This type of log is primarily carried out in an open hole section, but can still be carry out in a cased section subjected to signal attenuation (Steingrímsson, 2011). Since pore space in the crystalline basement rocks is mostly very low, the measured neutron porosity (NPOR or NPHI) is more sensitive to the enhanced porosity in the formation rocks. Enhanced porosity is generally restricted to zones of faulting and fracturing in crystalline rocks where hydrogen nuclei can be found in fluid-filled pore spaces or fluids in open fractures (Pechinig *et al.*, 1997).

4.1.8. Sonic (DT)

The sonic log (or acoustic log) measures the acoustic travel time (known as delta-t, Δt , interval transit time, or slowness) over a unit distance of an elastic wave travelling through the formation to infer porosity. The transmitter of the tool emits pulses of acoustic energy that travel through the formation rocks, undergo dispersion and attenuation, and arrive at the end receiver. The speed of sound depends on the elastic properties of the rock. Measured slowness varies based on the lithology, distribution of pore fluid and the porosity of the formation rocks. Porous formation decreases the velocity of acoustic waves through the rock mass which consequently increases the interval transit time recorded.

Errors in sonic measurements can be introduced due to hole-size changes and tool alignment in the borehole. These errors can be minimized by measuring the difference in the travel times between the source to two receivers located at different distances. The borehole compensated sonic tool has two transmitters and four receivers that measure the averaged Δt . As the tool only measures the first detectable signal, only the compressional interval transit time (DTCO or DT) is recorded. Using the reading of the sonic log (t_{log}) in $\mu\text{s}/\text{ft}$ or $\mu\text{s}/\text{m}$, porosity can be calculated using the Wyllie time-average equation below (Wyllie *et al.*, 1958) :

$$\Delta t = \frac{1}{V_p} = \left(\frac{\phi}{V_f} \right) + \frac{(1 - \phi)}{V_m} \quad , \quad (4-6)$$

$$\phi = \frac{(\Delta t - \Delta t_m)}{(\Delta t_f - \Delta t_m)} \quad , \quad (4-7)$$

where V_p is the formation velocity, $V_f = 1/\Delta t_f$ is the velocity in the fluid which fills the pore spaces, $V_m = 1/\Delta t_m$ is the velocity in the rock matrix, t_m is the transit time of the rock matrix, and t_f is the transit time in the pore fluid. It must be noted that Wyllie's formula has only a weak theoretical underpinning, and while it may provide good results for some sandstones it should be used with caution as it overestimates porosity in unconsolidated formations. The key purpose of sonic logs is for calibrating seismic responses as a record of seismic velocity and travel time. Its use toward the generation of synthetic seismograms will be further discussed in Chapter 5.

4.1.9. Full Waveform Sonic (FWS)

Conventional sonic logs (DT) measure only the travel time of the compressional wave. However, knowledge of the amplitudes and travel times of subsequent arrivals can also convey important borehole information such as permeability and fracture zone identification. A full waveform sonic (FWS) log records the entire waveform from a series of receivers that includes compressional (P-), shear (S-) and Stoneley waves. Multiple receivers allow signals to be detected from each transmitter pulse to ensure constant source characteristics. The tool is designed to have a greater transmitter-to-receiver offset compared to the traditional sonic logging for a greater depth of penetration into the formation. Thus it is less likely to be affected by formation alteration, relaxation damage from drilling process, and enlarged borehole (Schlumberger, 1991). The tool employed for measuring full waveform logs at the Hunt well by the GFZ-UofA collaboration had one transmitter and two receivers. A monopole transmitter is used to excite compressional- and shear-wave propagation at high frequency, and also the Stoneley wave using a lower frequency pulse.

Typical waveforms are shown in Figure 4-3 for multiple receivers which reveal the compressional, shear, and Stoneley waveforms. The arrival time of the various waveforms increases with the transmitter-receiver spacing. With the known transmitter-receiver spacing and arrival time (measured in μs), the slope (move-out) of the line drawn through the arrival time of the same component represents the slowness of the wave component over the interval measured by the receiver array. However, not all arrivals are always recognizable with such clarity, as shown. An alternative waveform-processing technique known as slowness time coherence processing (STC) can be utilized to analyze the propagating waves automatically using a semblance algorithm. This technique detects the coherence of the signals in the receiver arrays and estimates their interval transit time along all moveouts. It does not make any assumptions regarding the nature or velocity of the arrivals (Hornby and Murphy, 1987). Coherence values vary between 0 to 1 with 1 as the peak of coherence. As mentioned in the previous section, fracture porosity can be derived from the measured interval transit time. The additional Stoneley wave sonic logs are commonly used to identify permeable zones and effective fractures for fracture classification derived from other techniques (Farg *et al.*, 2010).

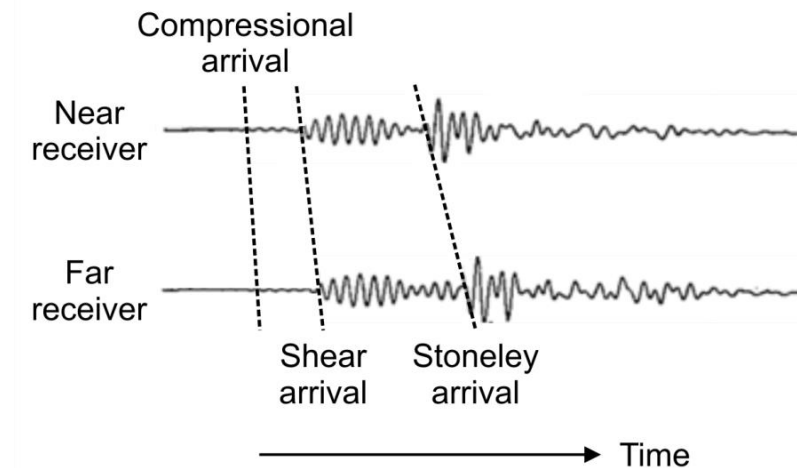


Figure 4-3. Sample waveforms from a sonic array tool showing the compressional, shear, and Stoneley arrivals. The horizontal and vertical axes are time and distance travelled, respectively.

4.1.10. Dipole Shear Sonic Imager (DSITM)

Monopole sonic tools generate a pulse of energy that strikes the formation. The compressional wave pattern travels at the compressional slowness of the fluid until it reaches the borehole wall. Some of the energy is reflected and some travel along the borehole as a compressional head wave (Alford *et al.*, 2012). In the case of a fast (or hard) formation where the shear slowness in the formation is less than the compressional slowness in the borehole fluid, the compressional (P-) wave from a monopole source is critically refracted into the formation and some compressional energy becomes converted to shear (S-) waves that refract into the formation (Alford *et al.*, 2012). The later arrival of S-waves can be detected by the receivers and the shear velocity can then be determined. For a slow (or soft) formation where shear slowness in the formation is greater than the compressional slowness in the borehole fluid, critical refraction does not occur for P-waves and thus no shear head wave is generated for the determination of the shear wave velocity. The monopole source method is heavily dependent on the presence of borehole fluid and the formation properties and is generally used for obtaining the compressional slowness of the formation.

The dipole shear sonic imager (DSITM) tool employs a monopole and two dipole acoustic transmitters to excite sonic wave propagations in the formation. The dipole transmitters excite flexural waves at low frequency around the borehole, which are dispersive. Flexural waves travel at the velocity of shear waves at low frequencies which allow shear slowness to also be measured in slow formation (Alford *et al.*, 2012). An array of eight receiver groups is set up to record the sonic waveforms, each consisting of four orthogonal elements that are aligned with the dipole transmitters. The output signals of the monopole and dipole waveforms produce monopole-equivalent (compressional and Stoneley) or in-line and cross-line dipole signals (Shipboard Scientific Party, 1998). In addition to slowness measurements, the additional transit time measurements in multi-receivers sonic array tool (*e.g.* FWS, DSITM) can provide information on the mode

amplitudes, shear-wave polarization, and Poisson's ratio to infer lithology, porosity, and anisotropy (Shipboard Scientific Party, 1998).

4.1.11. Formation MicroImager (FMITM)

The fullbore Formation MicroImager (FMITM) tool obtains a fine scale (~ cm) electrical resistivity image of the borehole wall using 192 microresistivity measurement electrodes in water-based mud. Sensors are placed on eight pads mounted on four orthogonally-placed caliper arms. An alternating current with a focusing electrode device is used to ensure that the currents are focused into the formation as they travel from the lower to upper electrodes (Schlumberger, 2002). The spacing and positioning of the pads provides 80 percent coverage of the borehole wall in an 8-inch diameter hole, with a vertical resolution of 5 mm that allows features greater than 5 mm to be easily identified in their true scale. The degree of borehole coverage decreases as the borehole size increases. Data output from the FMITM logging tool includes 192 microresistivity curves, variable voltage, cable tension, hole size calipers, borehole azimuth, borehole deviation, relative bearing, and pad 1 azimuth. Prior to interpretation, a data processing workflow is implemented which includes speed correction, button equalization to correct for tool and borehole effects, button correction to ensure there is no defective trace, and correction for variations in current flow (Bassim *et al.*, 2009). The microresistivity curves are then normalized and color-scaled to produce unwrapped resistivity images of the borehole wall in static and dynamic color displays. Static display is when normalization by a single mapping is applied to the entire section of image data and dynamic display is when normalization is applied in a sliding window.

The FMITM log display is an unwrapped image of the borehole oriented in the geographic north direction. If we cut along the northerly direction of a borehole, any planar dipping surfaces would be represented as a sinusoidal curve whereas horizontal surfaces or bedding planes will appear as straight lines (Bonner *et al.*, 1996) (Figure 4-4). Presence of fractures can strongly attenuate the shear wave energy resulting in smaller amplitudes and an increase in the travel time of shear

waves. Since the diameter of the borehole is also measured, the dip direction of the planar feature is given by:

$$\theta = \tan^{-1} \left(\frac{h}{d} \right) , \quad (4-8)$$

where θ is the angle of dip, h is the height of the sinusoidal curve, and d is the diameter of the borehole. The lowest point on the sinusoid trough defines the azimuth of the dip. Resistivity contrasts on FMITM logs allows us to identify the characteristics of bed boundaries, stratigraphic surfaces, faults and fractures (Schlumberger, 2002). If borehole breakouts and drilling-induced fractures are identified, they can be used toward geomechanical analysis of the borehole and assist in the positioning of boreholes in engineered geothermal system development (Tingay *et al.*, 2008).

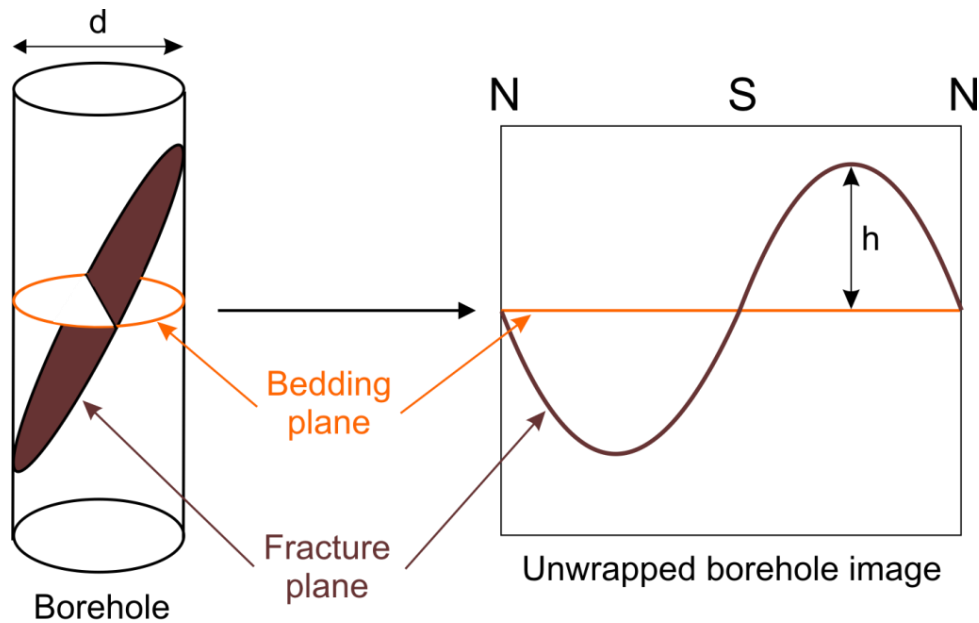


Figure 4-4. Image display of the Formation MicroImagerTM log revealing the image of the borehole in the presence of the bedding and fracture planes.

4.1.12. Magnetic Susceptibility (MSUS)

Magnetic susceptibility (MSUS) is the degree of magnetization of a formation in response to an induced magnetic field. It is represented by the ratio of the

intensity of magnetization of a material to the intensity of an applied magnetic field (Chopra *et al.*, 2002). The logging probe consists of a system of coils in a non-magnetic, non-conductive case. An alternating magnetic field is generated from the transmitter coil at a frequency of approximately 1000 Hz (Krammer, 1990). As the probe passes through the volume of rock, the inductance of the coil changes and the electrical bridge circuit in the sonde needs to re-balance by adjusting the energizing frequency. The change in frequency is dependent on the magnetic susceptibility of the surrounding formation and is converted into the SI susceptibility unit which is dimensionless when measured (Mwenifumbo and Mwenifumbo, 2012).

The main source of local magnetic anomalies originates from ferromagnetic mineral content, mainly magnetite and pyrrhotite hosted within the rock (Telford *et al.*, 1990). Magnetic susceptibility measurements can be used to infer lithological changes, degree of homogeneity and the presence of alteration zones in the rock mass based on the change in magnetic minerals in their altered (or oxidized) forms (Mwenifumbo and Mwenifumbo, 2012). It was also suggested that borehole magnetic susceptibility measurements can possibly help to identify the origin of radiogenic heat in geothermal studies (Ali and Potter, 2012).

4.1.13. Temperature (T)

One of the most fundamental parameters for geothermal investigation is subsurface temperature. Temperature logging provides a continuous temperature profile of a borehole with temperature generally increasing with depth (Gosnold *et al.*, 2011). Thermal anomalies reveal any temperature contrasts between the temperature of the borehole fluids and the formation fluid (or formation). Equilibrium temperature logs have been recorded at the Hunt well under the supervision of Dr. Jacek Majorowicz (senior geothermal research scientist) in 2008 and 2010 with a platinum thermometer probe by SondexTM. To enhance the interpretation, the temperature gradient can be calculated from the measurements and any changes observed may be an indication of active flow in fracture zones. More information about the thermal data recorded at the Hunt well can be found

in the paper published by Majorowicz *et al.* (2012). Evidence for the presence of open fractures was reported by Majorowicz *et al.* (2012) from the rapid drop in water levels in the Hunt well.

4.2. Data Analysis

The latest logging program in July 2011 expanded the existing geophysical log collection in the Hunt well with a particular focus from the bottom of the casing collar (1006 m) to 1880 m depth in the open hole section. To ensure that all logs are referenced to the same datum prior to interpretation, depth matching using GR logs was performed on all newer logs followed by depth correcting them relative to the Kelly bushing (KB) of the older logs at 409.3 m. Interpretation of the well logs was performed using two commercial log interpretation software tools: Interactive Petrophysics™ 4.0 (Senergy Software Limited) and WellCAD™ 4.4 (Advanced Logic Technology). Analysis of the geophysical logs available at the Hunt well will focus on any log responses that might be indicative of fracture zones important for engineered geothermal system (EGS) development. Some of the more common indicators to look for include borehole enlargement, decrease in bulk density, delay in acoustic travel times, and decrease in resistivity (Keys, 1979; Sausse *et al.*, 2006; Tingay *et al.*, 2008).

4.2.1. Precambrian Unconformity

A structural contour map for the top of the Precambrian basement has been compiled by Burwash *et al.* (1993) using the available geological and geophysical data in Alberta at the time. At the Hunt well the only conventional logs acquired continuously throughout the well that crossed the Phanerozoic sediment-Precambrian basement interface are gamma ray (GR), neutron porosity (NPOR) and sonic (DT) logs. All three curves display deflections at the interface at 541.3 m, and this interface could also be verified based on the resistivity contrast of the Formation MicroImager (FMI™) image log (Figures 4-5 to 4-7).

4.2.2. Rock Characterization

With the limited cores available for the Hunt well, measurement from the spectral gamma ray (SGR) log in the crystalline basement rocks is the next useful tool in determining rock types (Figure 4-9). The Precambrian basement rocks in Alberta generally have complex rock assemblages with the most abundant rock types being quartzo-feldspathic gneiss and granitoid (granitic rock) (Burwash *et al.*, 1994). Walsh (2013) characterized rock samples from the Hunt well as hercynite biotite garnet gneiss at 1656.7 m to 1657.5 m and orthopyroxene granite at 2350 to 2364 m depths (Table 2-1). Three sets of SGR logs were acquired by different operators in the past years with varying quality. The latest logging run by ICDP-OSG was used in this study as the results are more consistent with an earlier data set collected by Schlumberger in 2003. The observed mean values from the most recent data for U, Th, and K are 1.65 ± 1.05 ppm, 35.24 ± 19.60 ppm, and 3.22 ± 1.37 %, respectively, between 1005 m to 1873 m depth interval. These values follow the suite of rock type broadly categorized as granitic rock (Schlumberger, 1982).

From 1760 to 1797 m depth a strong anomaly associated with a significant increase in density (RHOB), photoelectric factor (PEF) and magnetic susceptibility (MSUS) were detected (Figure 4-8). Rocks with higher content of mafic minerals tend to have higher RHOB and PEF than those with felsic minerals (Mwenifumbo and Mwenifumbo, 2012). The increase in MSUS can be attributed to the abundance of ferromagnetic minerals such as magnetite and pyrrhotite. Such magnetic behaviors can be influenced by alteration processes such as the alteration of mafic minerals into chlorite and magnetite that lead to an increase in both the MSUS and the degree of alteration (Platou, 1968; Henkel and Guzman, 1977). Any local variations in the abundance of magnetic minerals may be used as an indicator of a lithologic contact which helps to constrain its depth (McNeill *et al.*, 1996). These observations suggest the potential of an intrusive mafic dyke with an approximate thickness of 37 m in the older Precambrian rocks.

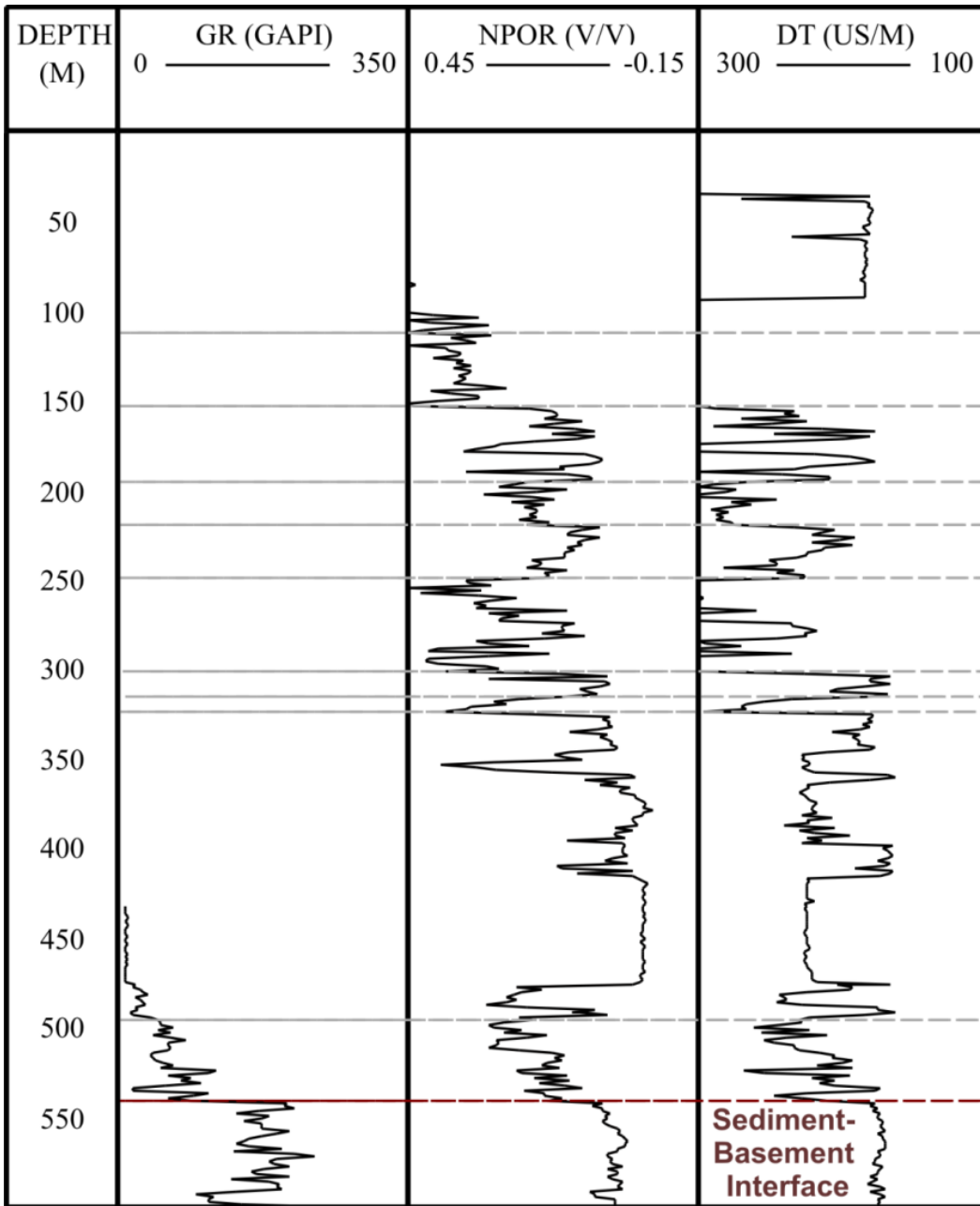


Figure 4-5. Plot of gamma ray, neutron porosity, and sonic logs which reveal sharp deflections at the sediment-basement interface at 541.3 m. Grey lines mark the boundaries between sedimentary formations.

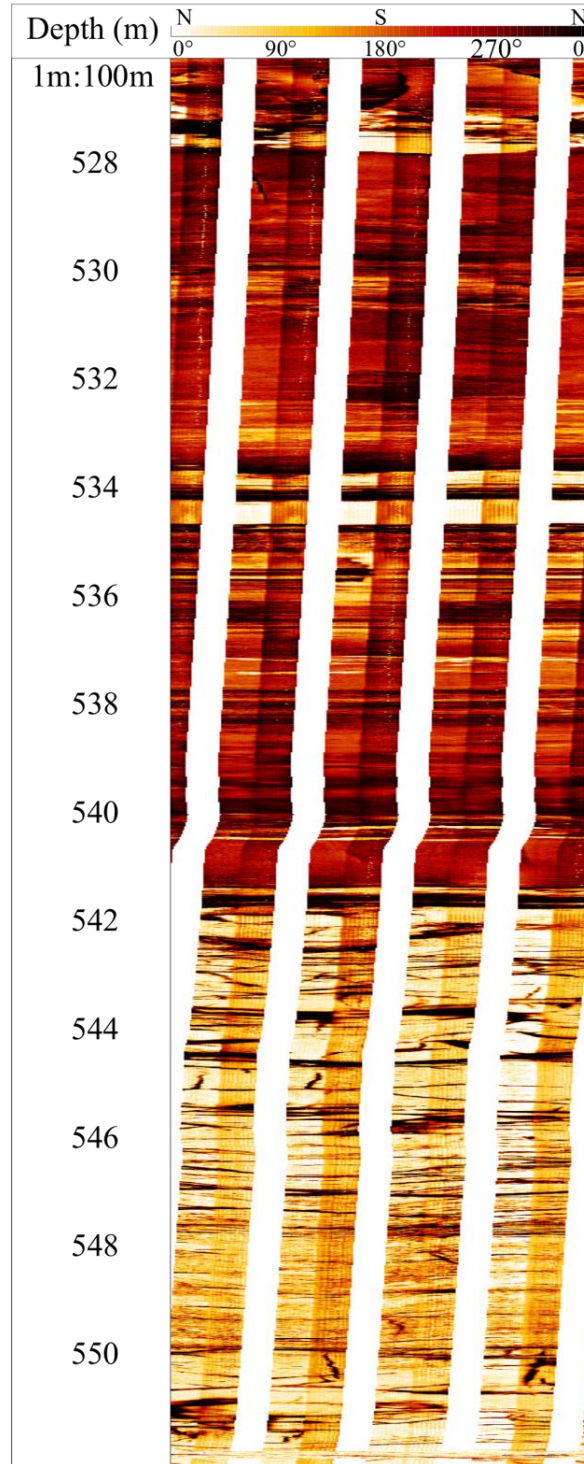


Figure 4-6. Formation MicroImager (FMITM) static log display near the sediment-basement boundary. Resistivity contrast observed at 541.3 m verifies the boundary identified in Figure 4-5. Image logs are displayed using bright colors for resistive units and lower resistivity units are displayed using dark colors.

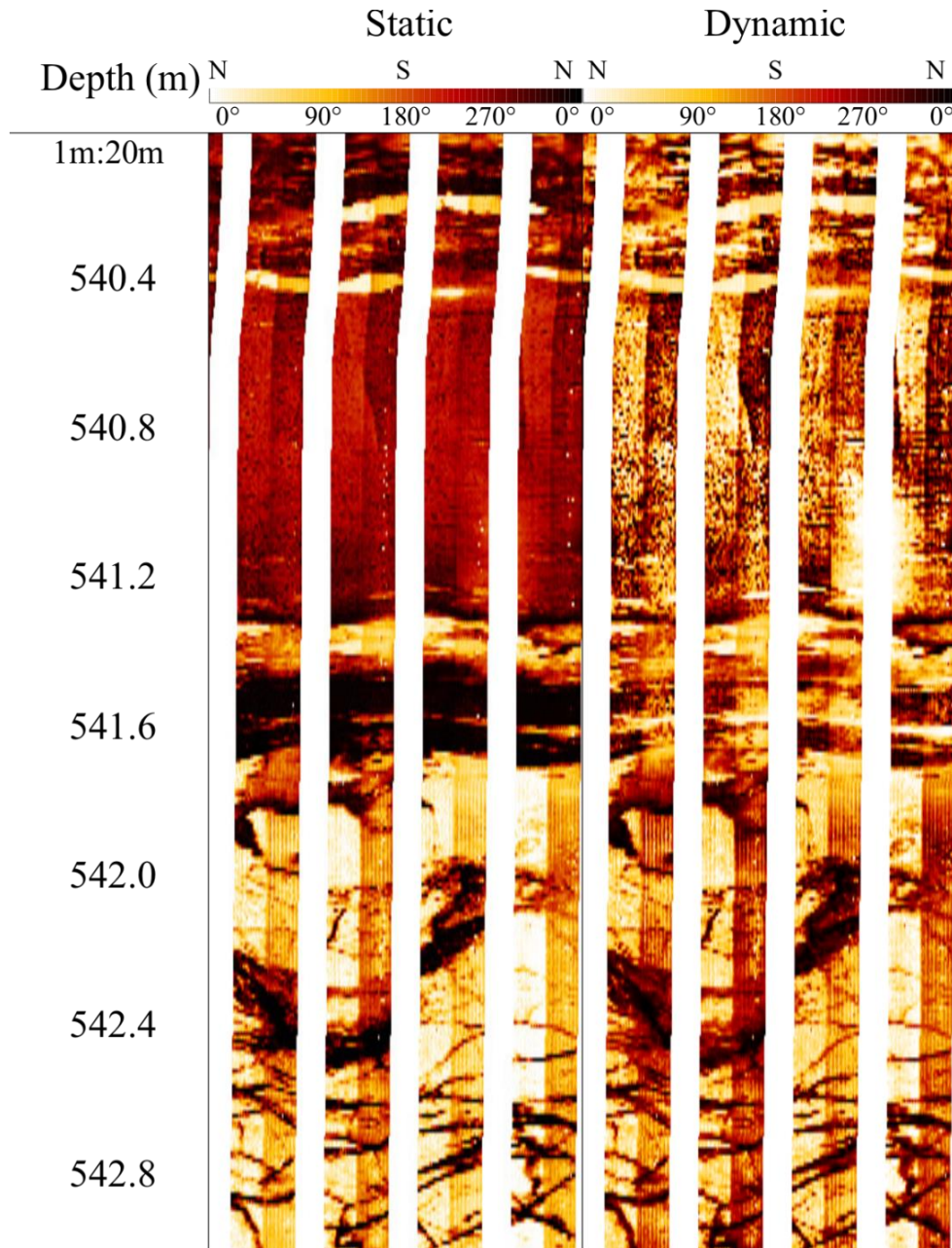


Figure 4-7. Enlarged FMITM image of the sediment-basement interface at 541.3 m. In comparison, the dynamic display does not reveal the proper resistivity contrast when color normalization is applied in a dynamic range. Image logs are displayed using bright colors for resistive units and lower resistivity units are displayed using dark colors.

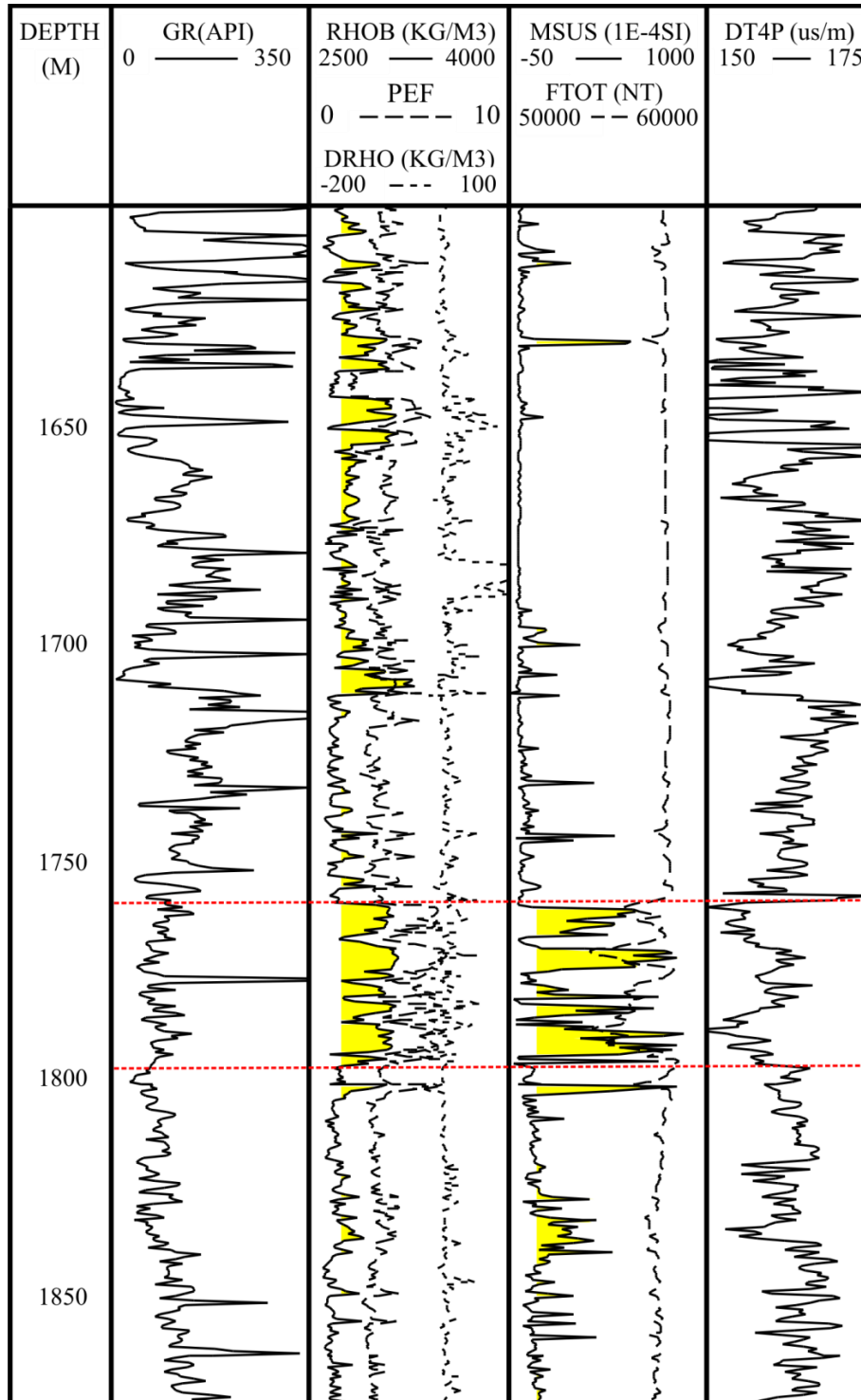


Figure 4-8. Log display of gamma ray, density, photoelectric factor, density correction, magnetic susceptibility, total magnetic field and interval transit time. Note the anomalously high values of RHOB, MSUS, and PEF between 1760 to 1797 m which suggest the possible presence of a mafic dyke.

4.2.3. Heat Generation

Heat generation is driven by the concentration of radiogenic elements in the basement rocks which is valuable for the feasibility study for geothermal application. The previous value reported by Jones and Majorowicz (1987) for radiogenic heat generation of basement samples in the Western Canadian basin revealed a mean value of $2.06 \mu\text{W}/\text{m}^3$. This value was considered to be higher than the values reported for the Superior and Churchill cratons (Majorowicz *et al.*, 2012). A value of $3.06 \mu\text{W}/\text{m}^3$ (from Equation 4-1) and $3.05 \mu\text{W}/\text{m}^3$ (from Equation 4-2) offers a good agreement between different GR measurements. The first reported value was calculated using the total GR measurements whereas the second value was calculated using the density and spectral gamma ray measurements. This suggests that reasonable radiogenic heat generation can still be obtained if only a normal total GR reading is available. Walsh (2013) reported significantly lower radiogenic heat production values ($0.71 \pm 0.38 \mu\text{W}/\text{m}^3$) of 12 Hunt well core samples from ~ 1600 and 2300 m depth. The discrepancy between core sample analysis and SGR logs suggests that the core samples analyzed may not be representative of the well as a whole (Majorowicz *et al.*, 2012).

Burwash and Burwash (1989) reported the radiometric heat production value for 132 Alberta samples of Precambrian rocks. Selected samples in the northeastern Alberta are listed in Table 4-2. A mean value of $2.57 \mu\text{W}/\text{m}^3$ is reported from the 6 selected samples. Based on the log calculations, the values for the basement rocks of the Hunt well are higher than the range of values previously reported in northeastern Alberta (Table 4-2). As such, this offers a promising result for radiogenic heat source to be found in the basement of the Canadian Shield rocks (Jones and Majorowicz, 1987).

4.2.4. Fracture Detection Using Indirect Methods

Borehole image logs are expensive to run and intact cores are not always readily available at all depths. Hence one would need to rely on the conventional wireline logs to deduce the potential fracture zones in the subsurface. Typically, fractures

can be indirectly detected using caliper, resistivity, neutron density, and full waveform sonic logs if the fractures are wide enough to be resolved by the tools (Keys, 1990; Luthi, 2005). However, no information on the orientation or the width of fractures is directly available from these methods. In the SGR logs, higher local concentrations for both Th and U are observed between 1140 and 1405 m depth (Figure 4-9). Concentration of K is also higher at a similar depth interval. This can be explained by the possible precipitation of alteration minerals along fractures (Keys, 1979). U peaks are commonly correlated to fracture zones as U is highly mobile and easily leached by fluids (Sausse *et al.*, 2006). K and Th peaks are likely due to trace minerals that are very rich in elements such as monazite and bastnasite (T. Chacko, personal communication, 2013). K is also found in potassium feldspar and biotite in which these minerals were previously identified by Walsh (2013) in core samples at greater depths. These minerals are considered to be easily altered into potassium-enriched clay minerals (Sausse *et al.*, 2006). Despite a widening of the borehole observed from 1140 to 1405 m depth, large washout zones generally only cause slight decreases in GR counts as a result of attenuation. Full waveform sonic (FWS) logs reveal localized waveform attenuation at 1156 m and 1191 m which also corresponds to the Th and U peaks (Figures 4-10 and 4-11). PEF at these depths are between 2.6 to 7.1 with K concentrations of 3.4 to 5.2 %. One can interpret this zone to contain localized natural fractures with possible mineral filling.

Table 4-2. Results of heat generation measurement in the Precambrian rocks near the study area from Burwash and Burwash (1989).

#	Location	Depth (m)	Density (g/cm ³)	Magnetic susceptibility (emu)	Heat generation ($\mu\text{W}/\text{m}^3$)
1	10-23-87-22W4	197.8	2.67	6.1	2.26
2	7-8-83-3W4	575.3	2.65	3.7	5.12
3	2-32-89-12W4	711.5	2.58	6.3	3.30
4	13-31-96-6W4	869.0	2.76	22.9	1.31
5	5-34-78-6W4	873.3	2.63	5.7	0.80
6	10-10-66-6W4	1356.5	2.91	29.8	2.61
			Mean		2.57

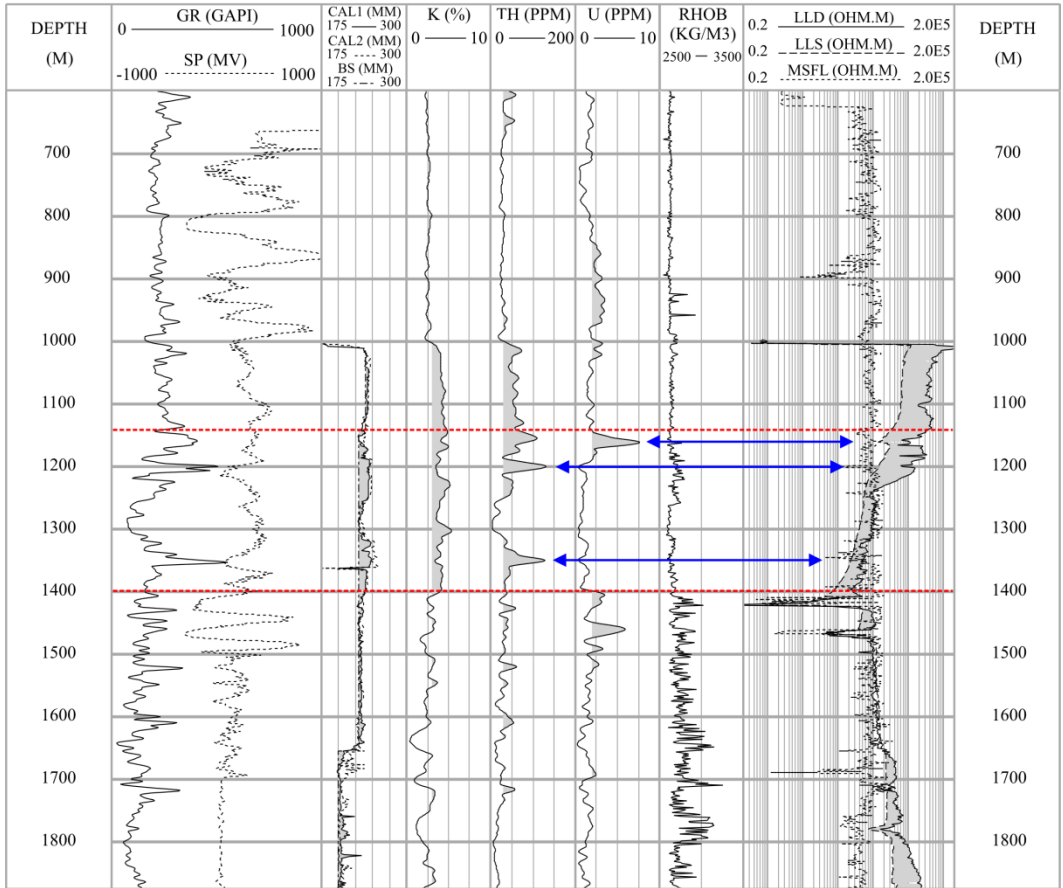


Figure 4-9. Major geophysical logs for the 600 to 1880 m depth interval. The widened caliper zone is bounded by the red lines between 1140 to 1405 m depth. Blue arrows identify zones with localized thorium and uranium peaks corresponding to a decrease in resistivity and increase in sonic travel time (Refer to Figures 4-10 and 4-11).

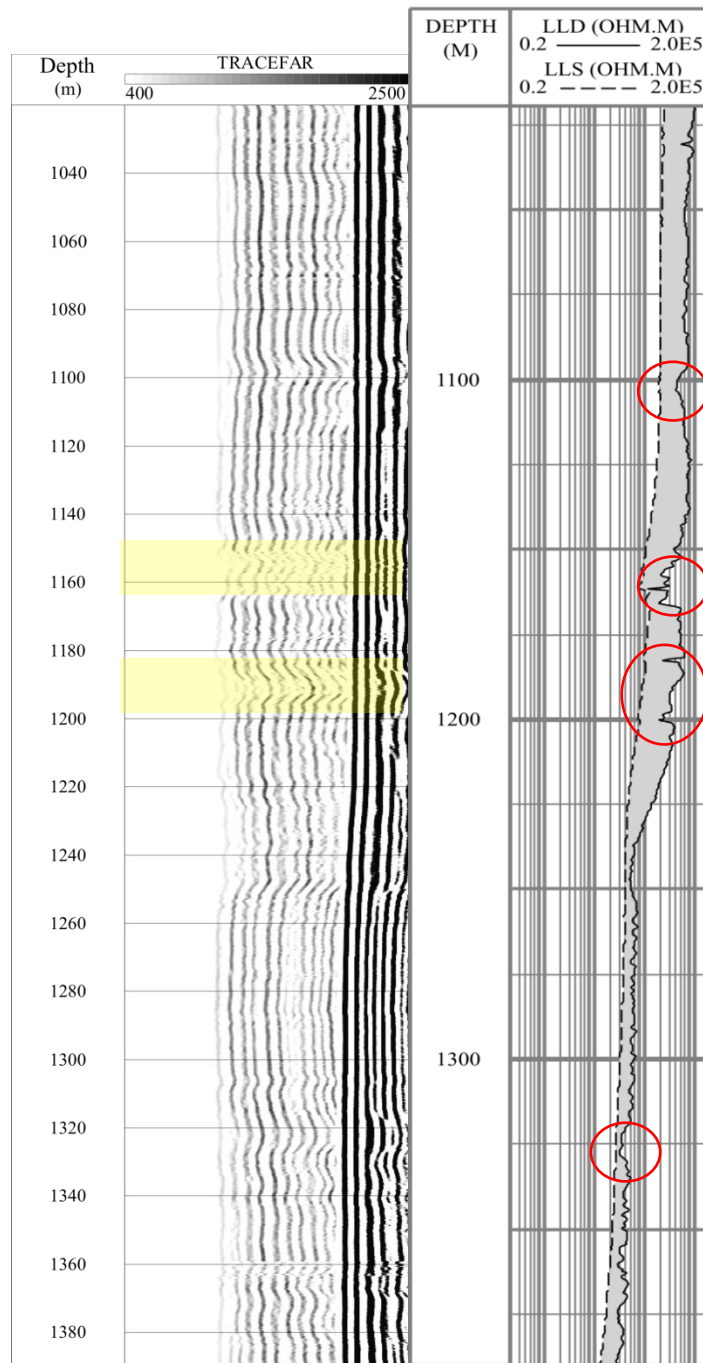


Figure 4-10. Display of full waveform sonic data for the far-receiver in variable density format (**left**) and resistivity laterologs (**right**) between the 1020 to 1390 m depth intervals. Yellow boxes highlight some of the zones with attenuated waveforms corresponding to the thorium and uranium peaks at 1156 m and 1191 m. Red circles outline selective zones detected by both deep resistivity laterologs and full waveform sonic log.

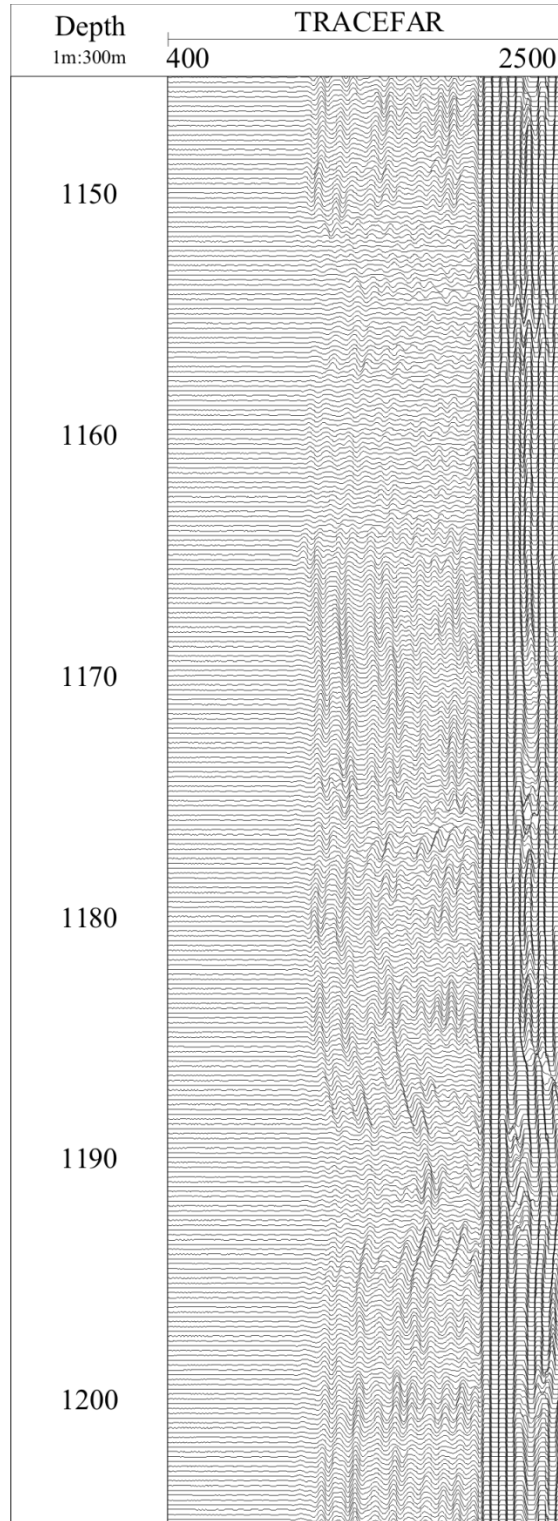


Figure 4-11. Display of waveform attenuation of full waveform sonic data in wiggle format between 1140 to 1220 m depth (zones indicated by blue arrows). These zones are also highlighted in Figure 4-10.

A significant decrease in resistivity was detected at 1406 to 1481 m, with a corresponding increase in the uranium concentrations, density, and acoustic velocities, and also appreciable self potential deflections (Figures 4-9 and 4-19). These changes can be explained by the structural and textural variations in the rocks since log responses are particularly sensitive toward fractures and porosity. The shallow and deep resistivity laterologs generally follow similar trends throughout the borehole in the resistive basement rocks. The separation between the deep and shallow curves is likely due to electrical shorting of the shallow log measurements by the highly conductive fluids in the borehole. Separation between the curves is also possibly related to the tool geometry that emphasizes the different oriented features. LLS emphasizes the horizontally-oriented features, whereas LLD emphasizes any deeper and vertically-oriented features (*e.g.* Pezard, 1990; Goldberg and Burgdoff, 2005). The presence of fractures containing conductive minerals might also contribute to the lowered resistivity. The higher relative uranium concentration can be a result of minerals previously leached by fluids and deposited into this fractured zone. SP deflections indicate a probable permeable zone related to open fractures and the inflection points were used to define the zone boundary. The newer set of DLL also serves to verify the validity of similar features seen in the older MSFL, as peaks in the MSFL could result from the effect of the flushed zone in the borehole (Figure 4-9). Fluid resistivity is currently planned to be measured in the borehole in the upcoming logging program to verify the presence of conductive fluids in the identified zones above. Localized natural fractures can also be detected by the decrease in resistivity by LLD throughout the borehole. These localized peaks are further verified by the attenuation of waveforms in the FWS. Such logging responses cannot provide the information on whether the natural fractures were opened or closed, but should be taken into consideration as they could not always be detected in the flushed zone (Figure 4-10).

Zones of alteration and fractures are generally related to one another indicating past or present migration of fluids (Keys, 1979). The 1760 to 1797 m depth range interpreted in Section 4.2.2 can be defined as a fractured and altered zone filled

with magnetic minerals as indicated by the magnetic susceptibility log measurement (Figure 4-8).

4.2.5. Fracture Detection Using Direct Methods

Unlike conventional geophysical logs, oriented image logs provide better resolution and direct observations of the borehole wall, and thus provide geological, petrophysical, and geomechanical information of the studied interval. A Formation MicroImagerTM log was acquired in this borehole in three separate logging runs: 433 to 602 m, 600 to 1651 m, and 1559 to 2357 m. Acquisition artifacts possibly related to the very high resistivity of the rock and the low resistivity of the brine filling in the wellbore caused a significant issue in the data quality, particularly in the deepest run. This could be due to a lack of understanding in logging in the resistive borehole environment and also the presence of high fluid conductivities during logging (Figure 4-12).

Natural discontinuities such as fractures and cracks form potential fluid pathways in crystalline rocks for the circulation of water in engineered geothermal system (EGS) development. The main use of the resistivity image logs is to identify any stress-induced wellbore failures such as borehole breakouts and drilling-induced tensile fractures. The orientation of fractures from image logs can provide insight into the interconnectivity of fractures around the borehole and their relationship to the stress regime that can influence the productivity of EGS (Farak *et al.*, 2010).

Planar features (*e.g.* bedding, fractures) were interpreted using a manual interactive dip-picking tool which involves sinusoidal curve fitting of these features that intersect the borehole. Using Equation 4-8, the lower point on the sinusoid indicates the dip azimuth while the amplitude of the sinusoid defines the dip magnitude. The average dip angles of the natural fractures range from 25° between 542 to 600 m to 44° between 600 to 1651 m. Fracture orientations are displayed using both the rosette and pole diagrams and strike generally to the north-south direction (Figures 4-13 and 4-14). Natural fractures were clearly visible between 541 to 600 m (Figures 4-6, 4-7, and 4-12). Unfortunately, due to

the poor quality of the FMITM logs below 600 m, not all fracture zones identified using the conventional logging methods could be confidently verified. Despite the poor quality, natural fractures at 1410 to 1423 m and 1461 to 1468 m were still visible (Figure 4-15). Natural fractures are typically related to the tectonic history and are obviously older than the drilling-related fractures, although the disturbance of the drilling may activate reopening.

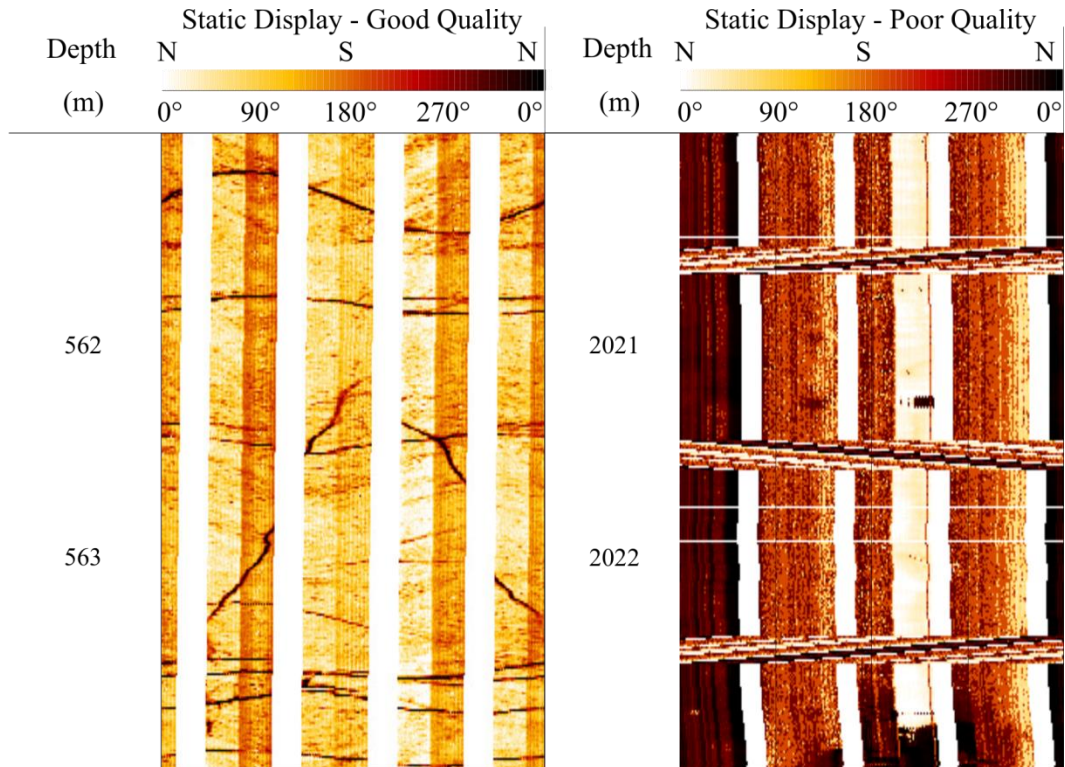


Figure 4-12. Quality comparison of processed Formation MicroImager (FMITM) logs of the Hunt well. FMITM logs in the upper section of the Precambrian basement reveal distinctive fractures (**left**). The lower sections of the FMI logs are affected by poor quality and structural features are hardly distinguishable from the processed results (**right**).

Drilling-induced tensile fractures (DITF) are developed as narrow, sharply-defined features with minimal borehole enlargement in the fracture direction (Tingay *et al.*, 2008). When the borehole stress concentration exceeds that required to cause tensile failure of the borehole wall, DITF are formed in response to the borehole stress and commonly lie close to the orientation of the maximum

horizontal principal stress resolved on the borehole wall (Aadnoy and Bell, 1998; Barton and Zoback, 2002; Barton *et al.*, 2009; Barton and Moos, 2010). Such features were interpreted between 1638 to 1643 m and oriented to approximately 078/258°N (Figures 4-13 and 4-14). Figure 4-16 is a dipmeter log containing the diameter of the borehole in two orthogonal directions; azimuth of pad 1 of the caliper arm and borehole deviation. Between 1652 to 1740 m depth, one caliper arm is locked in the enlargement direction at an average azimuth of 336° and the tool ceased to rotate in this zone. This suggests a zone of stress-induced borehole breakouts.

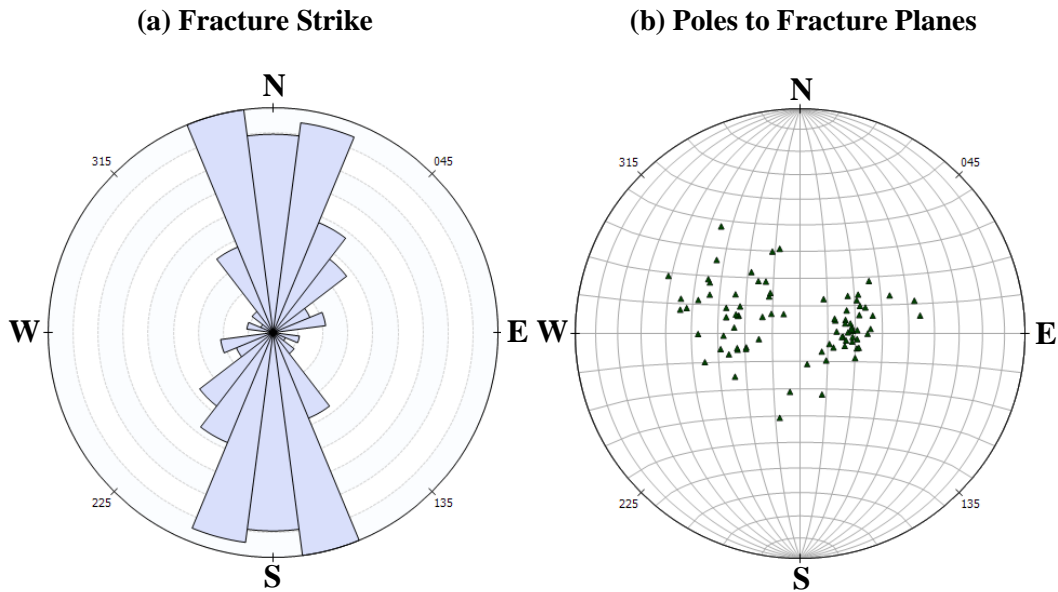


Figure 4-13. Interpreted fractures in the Hunt well between 541 to 600 m depth displayed in the form of: **(a)** Rosette diagram representing a histogram of the strike of natural fractures. Pie slices represent the orientation and circular grid lines scaled at 10°. **(b)** Lower hemispheric equal-area projection showing the poles to fracture planes. Small triangles represent fracture dips. Latitude and longitude lines are displayed every 10° and they specify the north-south and east-west positioning of points respectively. A total number of 83 fractures were interpreted in this section, limited to the good quality intervals available for interpretation.

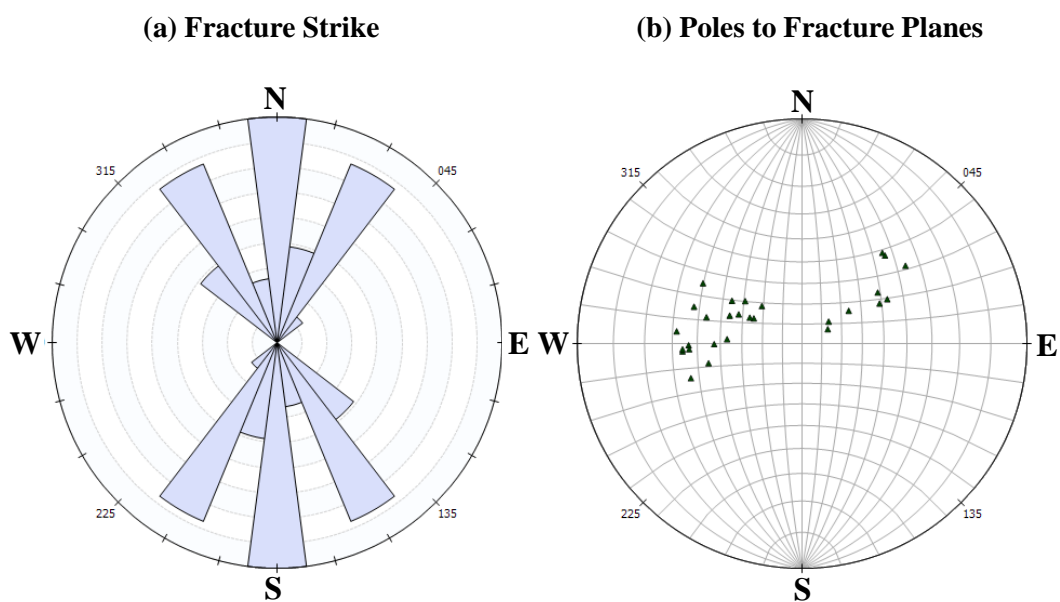


Figure 4-14. Interpreted fractures in the Hunt well between 1400 to 1500 m depth displayed in the form of: **(a)** Rosette diagram representing a histogram of the strike of natural fractures. Pie slices represent the orientation and circular grid lines scaled at 10° . **(b)** Lower hemispheric equal-area projection showing the poles to fracture planes. Small triangles represent fracture dips. Latitude and longitude lines are displayed every 10° and they specify the north-south and east-west positioning of points respectively. A total number of 28 fractures were interpreted in this section, limited to the good quality sections available for interpretation.

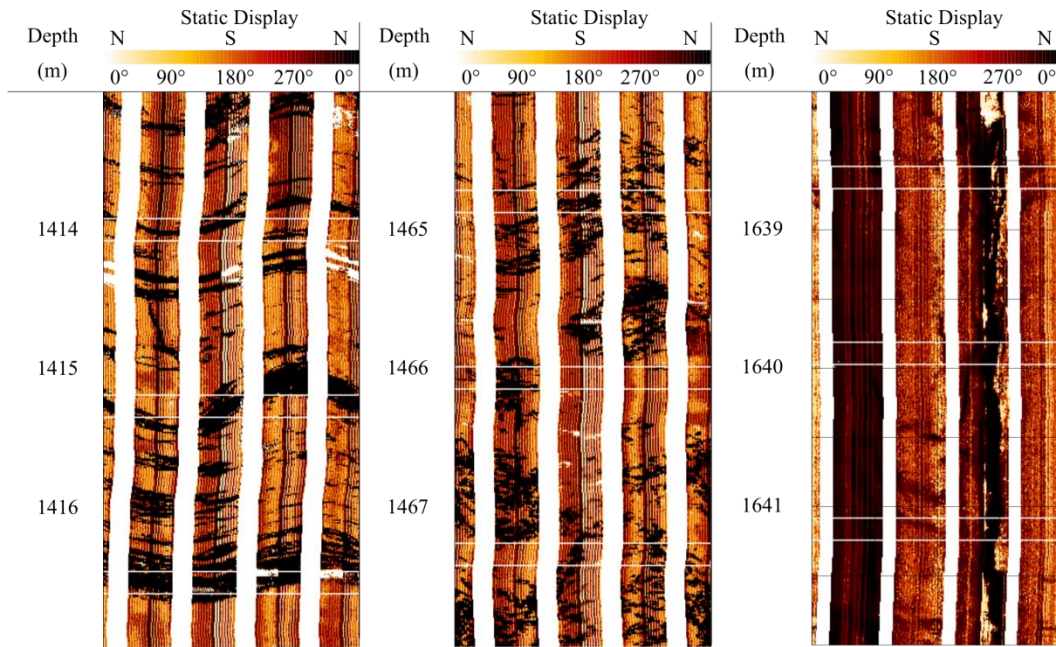


Figure 4-15. Examples of natural fractures of Formation MicroImager (FMITM) logs between depth intervals of 1410 to 1423 m (**left**) and 1461 to 1468 m (**center**), and of drilling induced tensile fractures at 1638 to 1643 m (**right**) in the Precambrian basement.

Interpretation of fractures along the entire borehole wall was performed but not all fractures were interpretable due to the poor quality of the data. Natural fractures appear to orient in the same direction for those that were more confidently interpreted. Zones with minor fracturing were interpreted using logs presented in Figures 4-9 to 4-11. If the image logs were properly acquired, fully processed and interpreted, we could expect a more complete survey of the fracture details including fracture geometry, aperture or thickness, and presence or texture of fracture-filling materials. It is also important to note that fractures are not always perfectly planar as assumed for dip calculations. Errors arise in the interpretation process when the sinusoidal curve is fitted across a zone with complex fractures. This could explain some of the scattered strike and dip of fractures plotted on the rosette and pole diagrams in Figures 4-13 and 4-14.

Natural fractures interpreted in the upper crystalline rocks (541 to 600 m) have a mean strike azimuth of 162° which is roughly perpendicular to the strike of the

drilling-induced tensile fractures that indicate the direction of maximum horizontal stress (S_{Hmax}) (Figure 4-17). The strike azimuth of the natural fractures is roughly parallel to the direction of minimum horizontal stress (S_{Hmin}). The orientation of S_{Hmin} could generally be associated with that for borehole breakouts when they are identified in borehole logs. This suggests that the natural fractures in the upper crystalline rocks could be formed under the present-day stress field. Natural fractures were also interpreted between 1400 to 1500 m depth in zones correlated with lower relative resistivity peaks (Figure 4-9). These sets of fractures are not oriented along the same direction as those in the upper section (541 to 600 m) of the crystalline rocks which suggests possible association with other geological events at the time or changes in stress direction. A summary of all fractures interpreted from the FMITM logs is listed in Table 4-3.

Table 4-3. Geometry of fractures interpreted from FMITM and dipmeter logs.

Top depth (m)	Bottom depth (m)	No. of Data points	Mean strike azimuth	Min-Max strike azimuth	Mean dip angle	Min-Max dip angle	Type of fractures
541	600	83	162°	11 – 348°	25°	9 – 54°	Natural
1400	1500	28	110°	73 – 242°	34°	15 – 60°	Natural
1638	1643	-	078/258°	-	-	-	DITF
1652	1740	-	336°	-	-	-	BB

Legend:

DITF – drilling-induced tensile fracture; BB – Borehole breakout

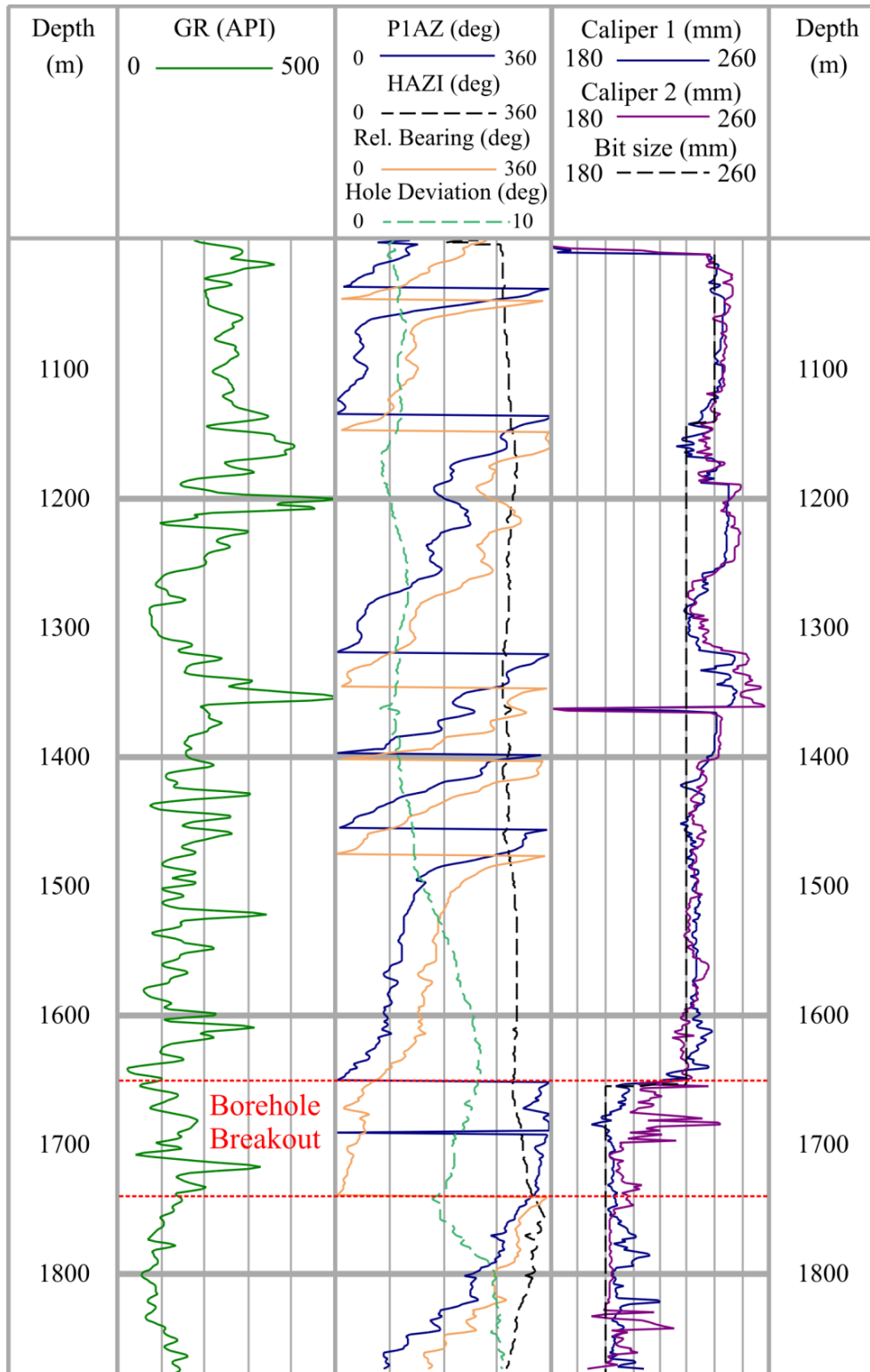


Figure 4-16. Dipmeter log display shows the borehole breakouts between 1652 to 1740 m depth. One caliper arm locks into breakout zone with P1AZ at an average azimuth of 336°.

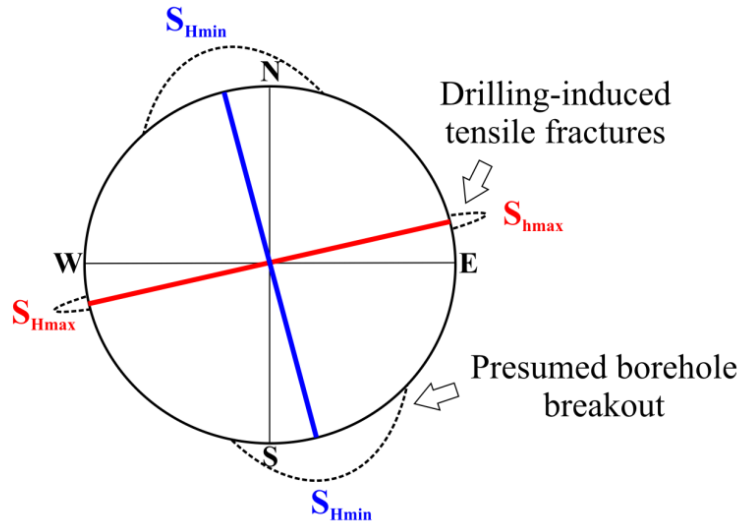


Figure 4-17. Orientations of drilling-induced tensile fractures and natural fractures of the Hunt well in a borehole cross-section. A pair of drilling-induced tensile fractures are oriented approximately $078^{\circ}/258^{\circ}\text{N}$ as indicated by S_{Hmax} . Natural fractures have a mean azimuth of 162° between 495 to 600 m depth as indicated by S_{Hmin} which is closely perpendicular to S_{Hmax} . The orientation of borehole breakout is at approximately 336° from the dipmeter log.

4.2.6. Acoustic Properties

Raw traces for the near- and far-offset receivers of the FWS log are displayed in variable-density format in Figure 4-18. An Ormsby bandpass filter (corner frequencies at 2-6-12-17 kHz) was applied to enhance the signal-to-noise ratio of the data for first-arrival picking. Using the process semblance tool in WellCADTM a cross-correlation analysis of traces between the receivers was performed and provided an array of semblance values at each depth position. The semblance plot shows slowness (unit: $\mu\text{s}/\text{m}$) with the signal amplitude corresponding to the semblance value. A darker band in the plot indicates a higher correlation of the signal amplitudes at certain slowness values. The first and second high correlation bands are generated by the compressional (P-) and shear (S-) wave amplitudes. Slowness values were picked from the output of the semblance analysis manually for quality assurance and picks were adjusted to the nearest maximum semblance

values. The final picks were then inverted and converted to the appropriate units for sonic velocities.

The average P- and S-wave velocities are 5868 m/s and 3428 m/s respectively in the depth interval between 1012 m to 1865 m. As expected, P- and S- wave velocities generally increase with depth due to the increased pressure from the overburden. At 1651 m depth velocities begin to experience a slight decrease as it approaches the interpreted mafic dyke discussed in Section 4.2.2. The end depth of this decreased velocity zone is beyond the available depth data of the FWS log. However, velocity data was also available using the old dipole shear imager (DSI™) data acquired at the bottom of the borehole from 1660 m to 2335 m. This data was provided to us in its processed form with both P- and S-wave velocities interpreted and, as such, we are unable to assess the quality to the same degree as the data we collected. Based on the assumption that this data set was processed and interpreted properly it extends the decreased velocity zone from 1651 m down to 1970 m possibly due to the increased fracturing in this zone (Figure 4-19). A slight velocity increase can be observed in the interpreted mafic dyke between 1760 m to 1797 m depth.

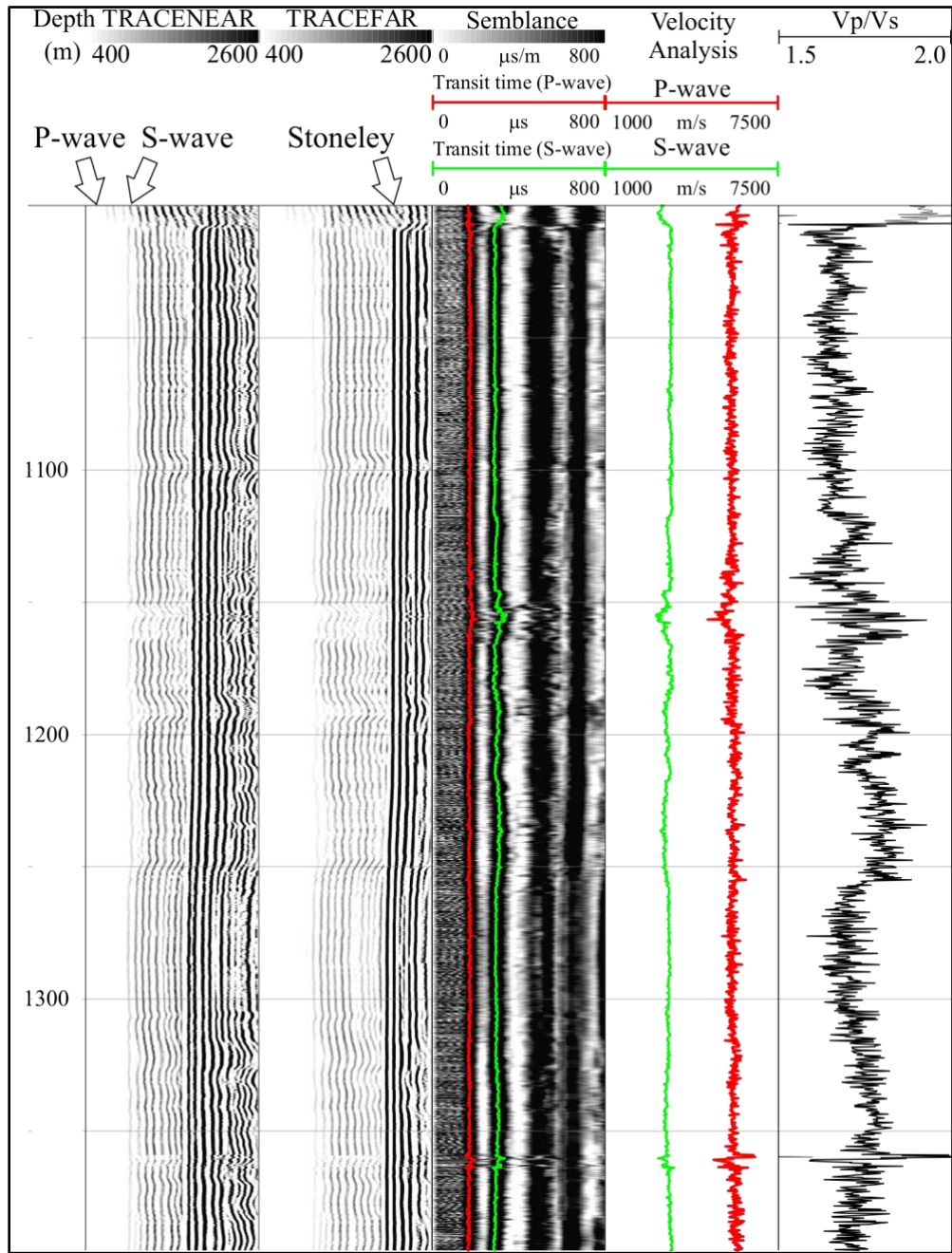


Figure 4-18. Processing and interpretation of FWS data. Track 1: depth; Tracks 2 and 3: data acquired by near- and far-offset receivers respectively; Track 4: semblance analysis and transit-time picking; Track 5: velocity analysis; Track 6: Vp/Vs ratio.

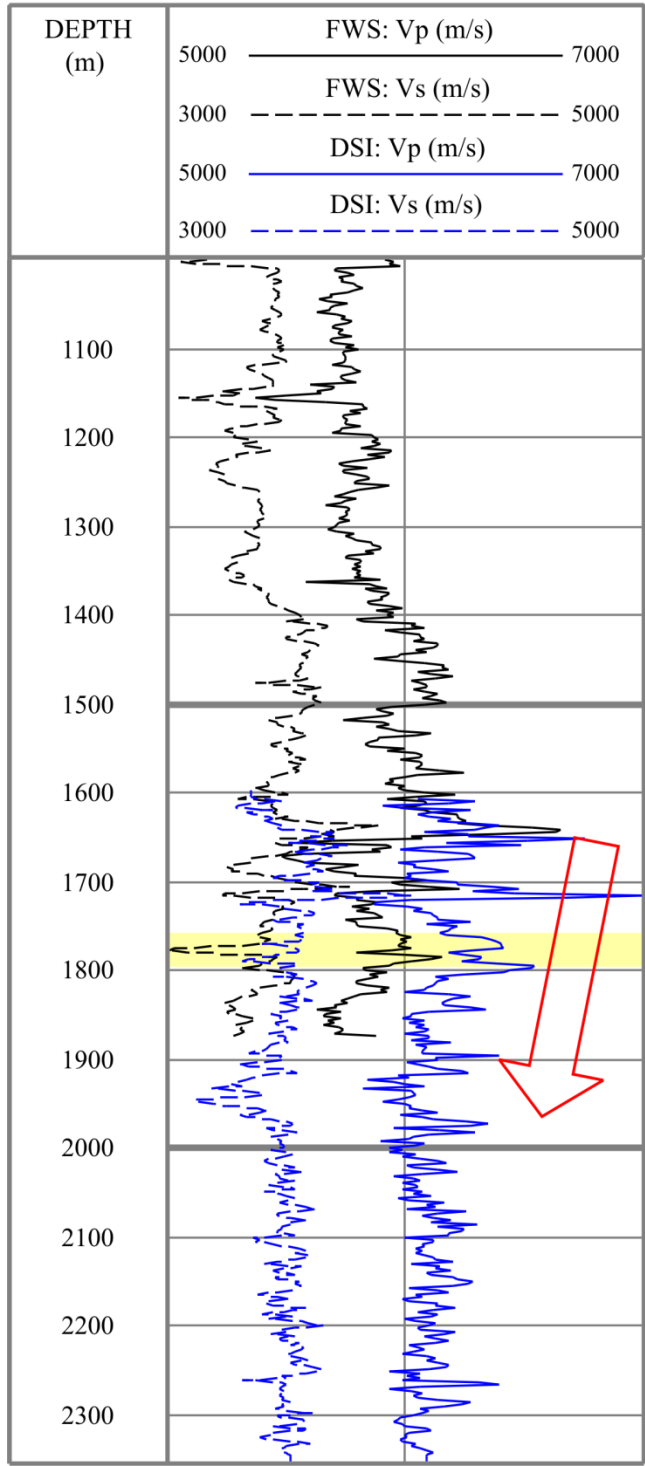


Figure 4-19. Results of the compressional (P-) and shear (S-) wave velocities from full waveform sonic and dipole-shear sonicTM imager logs. The red arrow indicates the decreased velocity zone between depth intervals 1651 m to 1970 m. Yellow box highlights the mafic dyke at 1760 m to 1797 m.

The ratio of P- and S-wave velocities (V_p/V_s) can be used as an indicator of the presence of fluids and fractures. It is controlled mainly by rock type and pore fluid. Higher values of V_p/V_s indicate higher fluid content, porosity and fracture counts (Sibbit, 1995; Boness and Zoback, 2004; Issacs *et al.*, 2008). At the 1012 m to 1865 m interval the V_p/V_s ratio has an average value of 1.71. Typical V_p/V_s values range from 1.5 to 2.5 for sandstone, shale, and siltstone, and 1.2 to 3.5 in an anisotropic case (Castagna *et al.*, 1985). In a crystalline rock environment, V_p/V_s values generally range from 1.6 to 2.0 (Bourbie *et al.*, 1987).

4.2.7. Thermal Logging

At the top of the Precambrian basement, the temperature was measured to be 11 °C. The optimal temperature needed for geothermal heat exchange with the aid of heat pumps in engineered geothermal system (EGS) development is 80°C. Using a thermal gradient of 21.2 °C/km, one would expect to reach an optimal temperature at the Hunt well at a depth of about 4 km (Majorowicz *et al.*, 2012). A thermal gradient was calculated using a 2 m moving window (Figure 4-20). In the sedimentary layers, the temperature gradient changes according to the change in physical properties of the rock matrix. In the crystalline basement rocks, fluid flow in rock is likely due to the presence of fractures which shift the temperature profile (Goldberg *et al.*, 1991). During the temperature logging campaign, it was observed that the water level in the well began to drop once the hole was filled, which may indicate the presence of open fractures in the borehole. Such observations, in addition to the temperature logging measurements, are relevant indicators offering optimistic indication for EGS development at greater depth in the Precambrian basement.

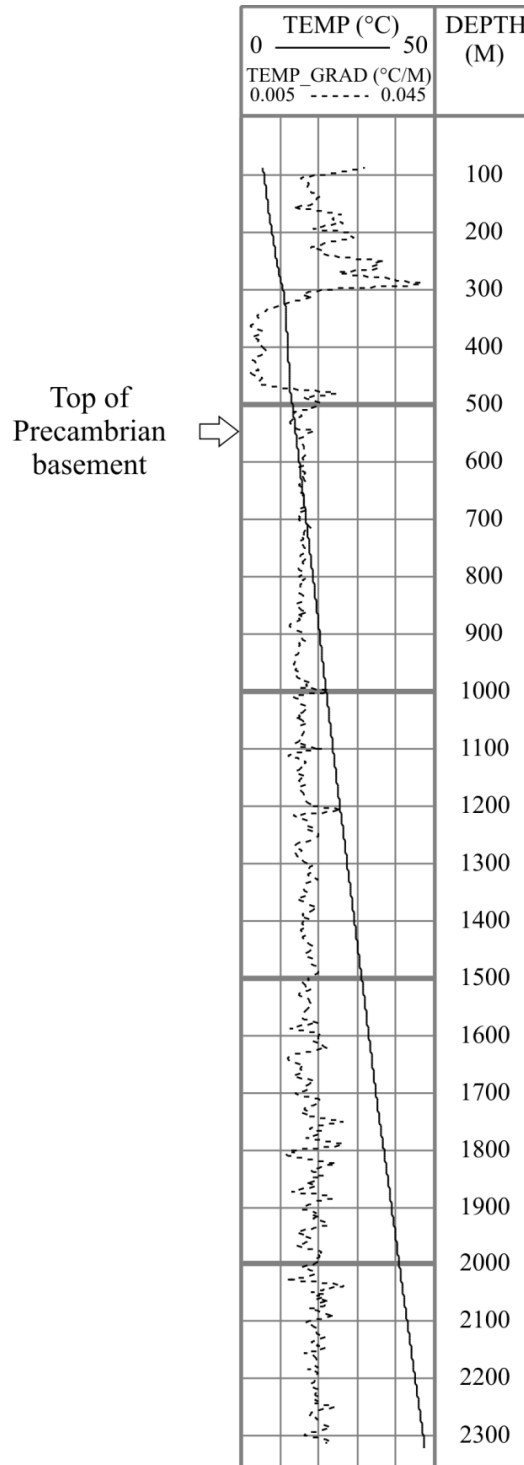


Figure 4-20. Temperature profile at the Hunt well. The top of the Precambrian basement has a recorded temperature of 11°C. Temperature at the bottom of the borehole was measured to be at 47.5°C. Dash and dotted lines represent the temperature and temperature gradient profile respectively.

4.3. Summary

A comprehensive suite of geophysical logs have been acquired at the Hunt well. The latest logging program focused on the Precambrian crystalline basement between 1005 m to 1880 m depth. With the limited cores available knowledge on the *in-situ* physical properties of the subsurface rocks is primarily understood using the available geophysical logs. Crystalline rocks are generally considered to be intrinsically tight (*i.e.* low permeability) with low porosity, and also with complex mineralogy. Hence, fluid transport in the basement rocks for engineered geothermal system (EGS) development would need to rely on macrofractures that are often surrounded by a zone of microfractures (Bremer *et al.*, 1992). Log responses reveal that the crystalline basement contains a concentration of radiogenic spectral elements that broadly resembles that of the granitic rock type with the top of the basement can be reached at 541.3 m.

Fracture zones were identified based on the different log responses from the conventional geophysical logging with possible altered mineral filling. Electrical imaging using Formation MicroImager (FMITM) reveals the presence of natural fractures in the upper section of the crystalline basement rocks (541 m to 600 m), and also in the mid-borehole sections that corresponds to lower resistivity (1406 m to 1481 m). A zone of borehole breakout was also interpreted from the dipmeter logs at 1652 m to 1740 m depth. Waveform attenuation in FWS logs corresponds to lower resistivity and can be a possible indication of minor fractured zones at 1156 m and 1191 m depth.

The orientation of drilling-induced tensile fractures reveals the maximum stress direction to be along 078/258°N. Natural fractures are oriented with a mean strike azimuth of 162° in the upper crystalline basement rocks (541 m to 600 m). A mean strike azimuth of 110° was identified between 1400 m to 1500 m depth. Its orientation difference from the upper 541 m and 600 m indicate that this section could be attributed to separate geological events or changes in stress directions.

There is no absolute role for individual logs toward a thorough understanding of the heterogeneous nature of the granitic basement rocks. However, one could try to maximize their understanding of the subsurface using an integrative approach on the accessible data. This chapter provided the insight that electrical images like the Formation MicroImager™ logs can provide clear images of fractures and verify fractures interpreted from the conventional geophysical logs. Knowledge of fracture zones along the well should be taken into account prior to the next stage of EGS development since fractures could affect the hydraulic circulations of fluids in the subsurface. The identified fracture zones also serve to support the presence of fracture zones in the Hunt well that was previously reported by Majorowicz *et al.* (2012). Acoustic log responses provide direct measurements of seismic properties that could be used toward generating a proper velocity model for seismic processing (Chapter 5). The next stage of geophysical logging in the Hunt well should include hydraulic tests to verify the zone(s) of potential fluid loss in the borehole, *i.e.* fracture zones that have been identified. Not all logs were discussed in this chapter as they do not all provide relevant information related to EGS development, or are affected by the quality and the limited depth coverage.

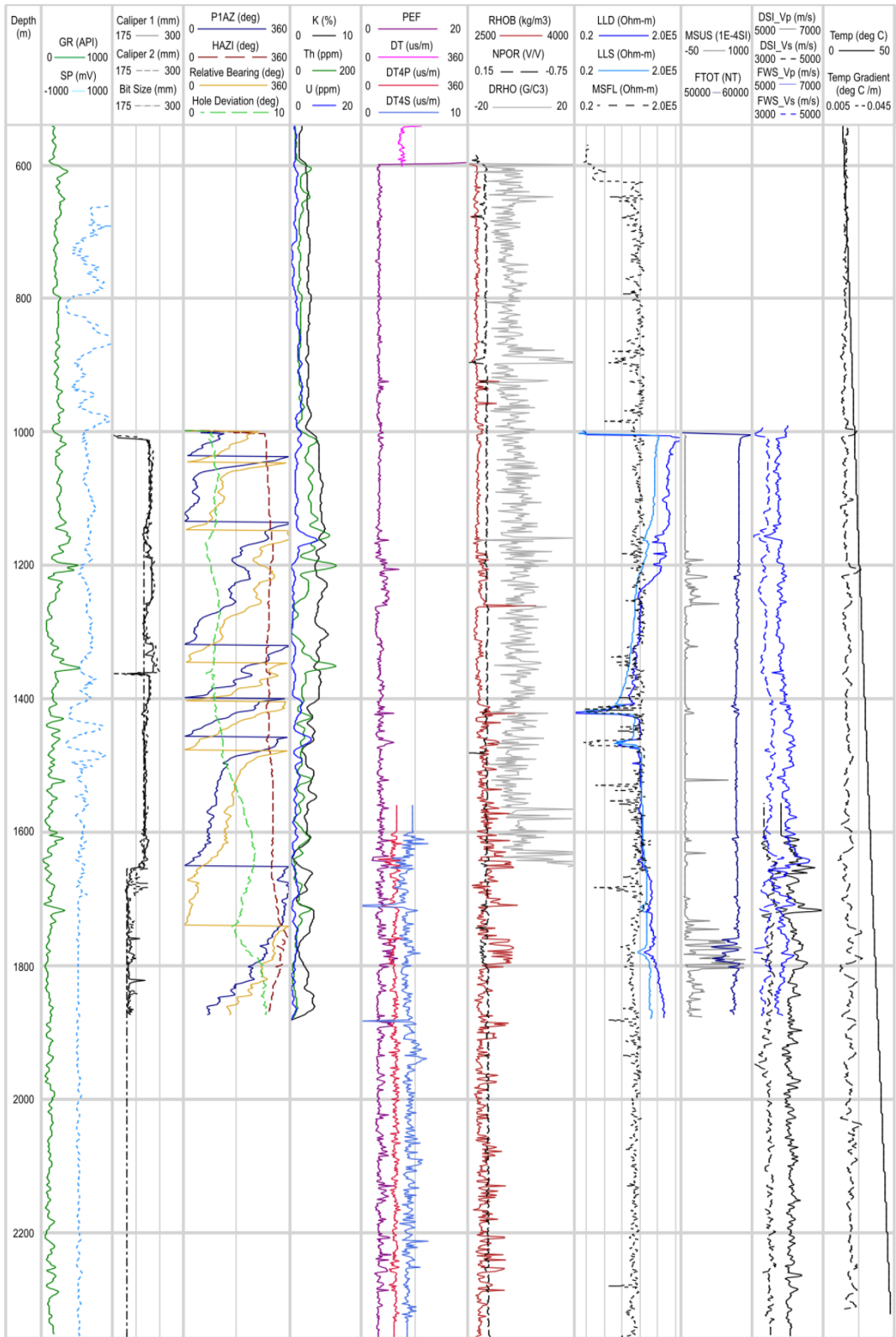


Figure 4-21. A composite of all logs acquired at the Hunt well in the Precambrian basement.

Chapter 5

Seismic Reflection Profiles

The first type of seismic data used in this project is seismic reflection profiles. The workflow is divided into three main stages: acquisition, processing and interpretation. Such profiles are useful in delineating subsurface structures in a cross-sectional view after they have been properly processed and interpreted. This chapter encompasses two of the 2D seismic reflection profiles (Lines: Thickwood and Tower Road) available near the Hunt well. An overview of seismic reflection and the basic geophysical theory behind this method are provided at the beginning of the chapter. Subsequent sections provide information on the acquisition parameters and processing workflow. This chapter concludes with the final processed seismic sections and interpretation. The principal goal of interpreting the seismic reflection profiles is to allow proper imaging of the upper crust and to identify any geological features that may provide zones of enhanced fracture permeability for the development of an engineered geothermal system in the Precambrian basement.

5.1. Seismic Overview

The principle of seismic reflection utilizes the propagation of elastic (seismic) waves from an energy source through the Earth and reflects back to the surface from the interfaces between different rock types. This process depends on the elastic properties of the rocks and the reflected waves are categorized into body and surface waves. Body waves consist of waves that propagate through the body of a medium. The first type of body wave is a P-wave (V_p), also known as a primary, compressional, or longitudinal wave. The particle motion of a P-wave travels back and forth along the direction of wave propagation. A P-wave is the first-arriving seismic wave detected by geophones, which propagates in both solids and fluids. The velocity of a P-wave is influenced by the elastic modulus (λ), the shear modulus (μ), and the density (ρ) of the medium:

$$V_p = \sqrt{\frac{\lambda + 2\mu}{\rho}} \quad (5-1)$$

The second type of body wave is the S-wave (V_s), also referred to as a secondary, shear or transverse wave. Its particle motion is transverse to the direction of wave propagation and is resolved into vertical and horizontal components. It is generated by the incidence of P-waves on interfaces other than normal incidence (Sheriff, 2002). S-waves travel slower than P-waves and cannot propagate through fluids since they cannot support a shear stress. The velocity of a S-wave is dependent on the shear modulus and density of the medium:

$$V_s = \sqrt{\frac{\mu}{\rho}} \quad (5-2)$$

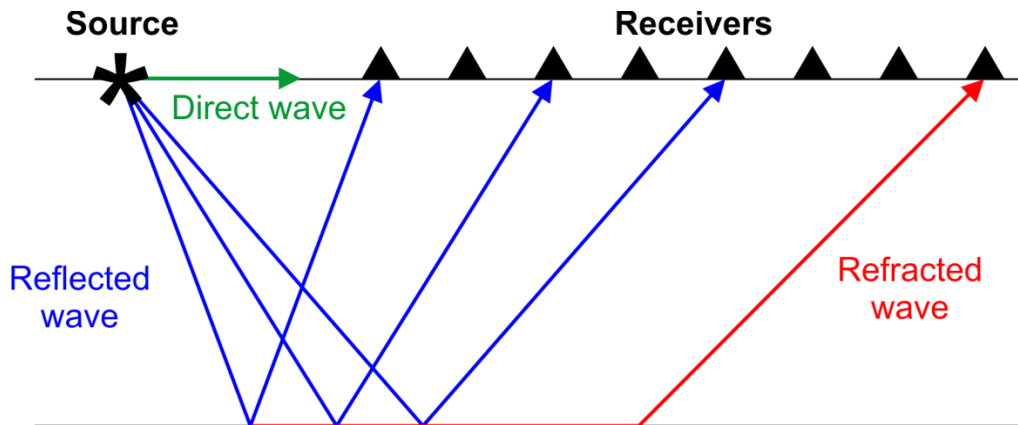


Figure 5-1. Diagram illustrating the principle of reflection and refraction at an interface.

Surface waves consist of waves that travel along the ground surface or at the boundary between two media. The first type is a Rayleigh wave. Its particle motion is a combination of longitudinal and transverse motion, and is confined to the vertical plane containing the direction of wave propagation. Its direction of travel is opposite to the direction of propagation at the top of its elliptical path (retrograde) (Sheriff, 2002). Ground roll is a modified Rayleigh wave with low

velocity, low frequency, and high amplitude. Its high amplitude frequently obscures the desired reflection signals in a seismic record. Rayleigh waves travel slightly slower than S-waves and they are dependent upon the elastic constants near the surface.

The second type of surface wave is the Love wave. It is characterized by the horizontal motion perpendicular to the direction of wave propagation with no vertical motion (Sheriff, 2002). The Love wave travels slower than Rayleigh waves and is generally not a problem on exploration seismic records unless special energy sources are used to generate the horizontal motion.

Seismic wave propagation is described by the concepts of ray paths and wavefronts. As seismic waves propagate in the subsurface from a point source, successive positions of wavefronts can be drawn that vary according to the velocity structure of the Earth (Figure 5-2). Huygens Principle states that each point on the wavefront can be regarded as the source of a subsequent wave. Ray paths are traces through the subsurface between sources and receivers, and they are drawn at right angles to their associated wavefronts in an isotropic media. The principle in which the travel time is a minimum between two points (*i.e.* first-order variation of travel time with respect to the neighboring paths is zero) is known as Fermat's principle.

As waves propagate through the subsurface and encounter changes in the elastic properties of the rocks they are reflected and refracted at the interface. The geometry of a ray path is predicted by Snell's Law when a wave changes direction after crossing a boundary between two strata or layers (Figure 5-2). Snell's law states that the angles of incidence and refraction of the ray paths of a reflector are related by:

$$\frac{\sin \theta_1}{v_1} = \frac{\sin \theta_2}{v_2} = p \quad , \quad (5-3)$$

where θ_1 and θ_2 are the angles of incidence and refraction, respectively, v_1 and v_2 are velocities for their respective layer, and p is the ray parameter. When a ray

travels through a number of parallel beds, Snell's law requires the ray parameter to remain constant everywhere for all reflected and refracted rays originating from a single ray. Ray theory is conveniently used to determine the travel times and depths of interfaces in the subsurface, but it does not provide information on the amplitudes of the waves.

An expression for the amplitude of a normal-incidence reflection using the contrast in acoustic impedance (Z) across an interface follows (Aki and Richards, 1980):

$$R_{12} = \frac{Z_2 - Z_1}{Z_2 + Z_1} = \frac{\rho_2 v_2 - \rho_1 v_1}{\rho_2 v_2 + \rho_1 v_1} , \quad (5-4)$$

where R_{12} is the reflection coefficient at the interface separating two layers, ρ_1 and ρ_2 are the bulk densities, and v_1 and v_2 are the P-wave velocities of layers 1 and 2. The acoustic impedance is the physical property defined by the product of density and P-wave velocity (ρv) at normal incidence. The reflection coefficient (R) is primarily determined by the contrast in velocities across an interface. If R is negative, the reflected wavelet has opposite polarity with respect to the incident wavelet.

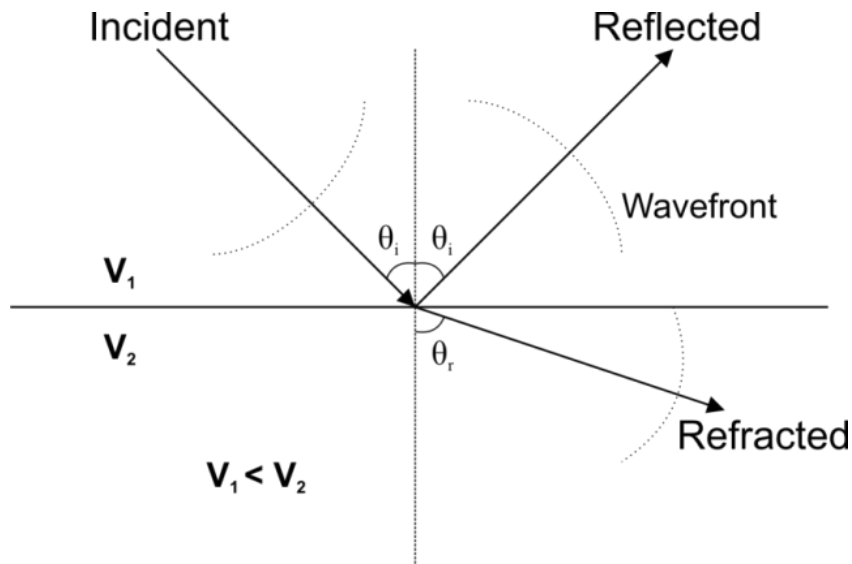


Figure 5-2. Illustration of ray paths and wavefronts at a velocity interface.

In the sedimentary basins, variations in acoustic impedance are controlled mostly by velocity changes between formation layers. Conversely, crystalline crust is generally characterized by uniformly high velocities and also changes in density that could be significant in controlling the seismic reflectivity in the crystalline rocks. For example, Milkereit and Eaton (1998) interpreted dense and massive iron-oxide or sulphide bodies in the mining district of the Canadian Shield as the source of strong seismic reflectors in the crystalline rocks. An understanding in the type of geological features present in the crystalline crust is important in the accurate imaging of the subsurface basement rocks. Such information helps to identify any structural features, such as faults and/or fracture zones, and their target depths relevant for geothermal development and exploration. Proper seismic processing is important to minimize any artifacts introduced in the workflow for accurate structural imaging. In the case where borehole logs are available, seismic imaging serves to correlate the localized borehole interpretation to the greater seismic coverage area.

5.2. Data Acquisition

One of the earliest 2D seismic reflection surveys acquired along Tower Road was done in 1978 using a rammer as the seismic source. This older data set was re-processed but was deemed too poor quality to be further interpreted. New seismic reflection surveys have been conducted along Tower Road in the southeast-northwest orientation with easy access for truck-mounted seismic source vibrators (Figure 2-4b). A summary of the acquisition parameters is listed in Table 5-1. The older profile, Thickwood (TW) survey, was acquired in 1993 as requested by Mr. Hunt with a crooked profile length of 24 km. This profile was designed to have a far receiver offset of 6.3 km to allow subsurface imaging deep into the crystalline basement rocks (approximately 35 km depth). The TW seismic survey was acquired using a Failing Y2700 vibrator with a correlated record length of 12 seconds and frequency range between 6 Hz and 60 Hz. A split-spread setup was employed with 361 channels at the two ends of the survey and a symmetric split-spread setup was employed in mid-section of the survey. A symmetric split-

spread setup occurs when geophones are spread symmetrically on either side of the shot point. This type of setup ensures a continuous coverage of subsurface reflectors. Using a shot interval of 105 m, seismic traces were acquired using 14 Hz geophones organized in groups of 9 wired together in series and distributed over a 35 m interval.

To improve the vertical and lateral resolution of the subsurface and to establish a better geological framework in the upper Precambrian basement, a higher resolution 2D seismic survey (TR survey) was acquired in July 2011 focusing along the straight section of Tower Road closest to the deep borehole. The nearest geophone is located approximately 165 m southwest of the borehole. A split-spread cable setup was employed with geophones in groups of 12 spaced at 4 m apart. A 240-channel seismograph recorded seismic data from a total of 2 km of spread length using a high-frequency MinivibTM unit (Industrial Vehicles International of Tulsa, Oklahoma) as the source. It generated 2 sweeps in the 10 Hz to 160 Hz frequency range at 4 m to 8 m intervals and the correlated record length is 3.4 s with a far-offset distance close to 1.2 km.

The seismic survey with longer offset distance (*i.e.* TW survey) is expected to be more effective in imaging deeper reflective events in the Precambrian basement. However, the decrease in shot spacing of the TR survey allows for a higher spatial resolution of the sedimentary layers and the upper part of the basement. With the small impedance contrasts between different crystalline lithologies, the basement section consists of weaker reflectivity in comparison with the sedimentary basins. Consequently, low-fold seismic reflection surveys are generally not recommended for basement imaging (Milkereit and Eaton, 1998). The TR survey was also conducted with a broader and higher frequency range than the TW survey. Existing shallow crystalline crustal studies reveal seismic data with higher frequencies enabled the mapping of shallow fracture systems in the Canadian Shield (Green and Mair, 1983), and an improvement in the signal-to-noise ratio is achieved with seismic frequencies greater than 100 Hz (Dahle *et al.*, 1985).

Table 5-1. Acquisition parameters for 2D seismic reflection surveys along Tower Road by the Hunt well.

Parameter	Thickwood (TW)	Tower Road (TR)
Year of acquisition	1993	2011
Line direction	SE-NW	SE-NW
Type of survey	2D crooked line	2D straight line
Source information		
Energy source	Failing Y2700 Vibrator	6000-lb IVI Minivib™
Shot interval	105 m	4 m to 8 m
Sweep frequencies	6 Hz to 60 Hz linear	10 Hz to 160 Hz linear
Sweeps per vibrator point	12	2
Number of shots	222	636
Receiver information		
Receiver type	Geospace 14 Hz	OYO 14 Hz
Station configuration	9 geophones/group	1 geophone/group
Geophone spacing	4.4 m	4 m
Spread type	Split-spread and symmetric split-spread	Split-spread
Far offset distance	6300 m	1200 m
Nominal fold	60	60
Acquisition system		
Recording system	ARAM	Geometrics Geode™
Number of channels	361	240
Correlated record length	12 s	3.4 s
Length of survey	24 km	3 km
Sample rate	2 ms	1 ms

5.3. Pre-Stack Processing

Data processing is multi-stage and requires processors to implement a workflow to generate an interpretable subsurface image from the raw seismic traces. Many of the digital signal processing steps applied to seismic data involve the use of a Fourier transform. The Fourier transform allows the conversion of a time function (waveform, seismic record trace, etc.) into its frequency-domain representation, and vice versa, without losing any information in the transformation process (Telford *et al.*, 1990; Sheriff, 2002). Seismic data in this project were processed using the VISTA™ Seismic Data Processing software package provided by GEDCO. The processing sequence for both TW and TR surveys are listed in Tables 5-2 and 5-3. The standard processing procedure includes application of amplitude balancing, static corrections, deconvolution, estimation of stacking velocities, common midpoint stacking, and post-stack filtering. The processing parameters were examined at each stage of the sequence in order to produce an optimal seismic image prior to stacking the raw gathers. Each processing sequence applied will be discussed in the following sections.

Table 5-2. Processing sequence and parameters for Thickwood (TW) 2D seismic line.

Processing step	Parameters	Justification
Geometry set-up		
First arrivals picking		Characterize near surface layer thicknesses and velocities
Trace editing		Remove dead and poor quality traces
Gain correction	Exponential gain: 1.6 Surface-consistent scaling AGC window length: 400 ms	Compensate for energy losses
Refraction statics	Datum: 450 m Replacement velocity: 1900 m/s Weathering velocity: 650m/s	Compensate for variable near-surface conditions
Ormsby band-pass filtering	6/11-55/60 Hz	Remove random noise outside of acquisition bandwidth
F-K filtering		Attenuate ground rolls
Predictive deconvolution	1 st pass: Operator length: 200 ms Pre-whitening: 1 % Prediction lag: 0 ms Operator taper: 20 ms 2 nd pass: Prediction lag: 24 ms	Attenuate multiples
Time-variant Ormsby filter	0-700 ms: 10/15-45/50 Hz 700-1800 ms: 10/15-55/60 Hz 1800-6000 ms: 6/11-45/50 Hz	Emphasize deep reflections
CMP Sort	In-line bin size: 6 m Cross-line bin size: 1000 m	
Velocity analysis	3 iterations	Semblance, common velocity stack
NMO corrections	35% stretch mute	Correct for normal moveouts
Residual statics		Compensate for random trace-to-trace time delays
CMP Stacking		
F-X 2D Prediction	Type of filter: Wiener Levinson Filter length: 3 traces	Eliminate random noise
Velocity model smoothing		
Finite different migration		Place dipping reflectors in correct positions

Table 5-3. Processing sequence and parameters for Tower Road (TR) 2D seismic line.

Processing step	Parameters	Justification
Geometry set-up		
Vibroseis Correlation	Sweep channel #: 1 Sweep length: 13 s	Correlate vibroseis trace with the sweep wavetrain
First arrivals picking		Characterize near surface layer thicknesses and velocities
Trace editing		Remove dead and poor-quality traces
Gain correction	Exponential time power: 1.0 AGC window length: 250 ms	Compensate for energy losses
Ormsby band-pass filtering	10/20-100/120 Hz	Minimize surface waves
Elevation/Refraction statics	Datum: 450 m Replacement velocity: 1900 m/s Weathering velocity: 650m/s	Compensate for variable near-surface conditions
F-K filtering		Attenuate near-surface refracted waves
Radial trace transform	25/30-150/200 Hz	Attenuate coherent noise
Predictive deconvolution	Operator length: 140 ms Pre-whitening: 1 % Prediction lag: 0 ms Operator taper: 20 m	Attenuate multiples
CMP Sort	In-line bin size: 2 m Cross-line bin size: 20 m	
Velocity analysis	3 iterations	Semblance, common velocity stack
NMO corrections	20% stretch mute	Correct for normal moveouts
Residual statics		Compensate for random trace-to-trace time delays
CMP Stacking		
Time-variant Ormsby filter	-200 to 400 ms: 30/40-90/100 Hz 400 to 800 ms: 30/40-150/180 Hz 800 to 2500 ms: 30/40-90/100 Hz	Emphasize deep reflections
F-X 2D Prediction	Filter length: 3 traces	Eliminate random noise
Velocity model smoothing		
Finite different migration (optional)		

5.3.1. Geometry Setup

To ensure that each seismic trace is properly identified in the processing workflow, each trace is accompanied with its own header information including shot point and geophone locations, channel numbers and elevation values. Frequently, such information is stored in a separate geometry file as geodetic information is acquired separately from seismic data. Each seismic survey should also include notes recorded by the surveyors and observers. These records allow processors to understand the acquisition geometry, cause of erroneous shot gathers and traces, and surface condition of the site, etc. Data with errors in geometry assignment will not be stacked properly and can result in the misinterpretation of structural feature locations important for exploration programs. Field geometry must also be applied preceding any gain correction that is offset-dependent. Each field record represents a wavefield that is generated by a single shot and each shot is considered as a point source that generates a spherical wavefield.

5.3.2. Vibroseis Correlation

A raw vibroseis shot record is not interpretable as it consists of the superposition of many long reflected wavetrains that overlap. Vibroseis correlation involves the correlation of the vibroseis trace with the sweep wavetrain to produce an interpretable record (Figure 5-3). The sweep is a frequency-modulated vibroseis source signal with known sweep type, sweep length, beginning and end frequencies, and taper length. The raw seismic record for the TW survey was already correlated when data was provided, making vibroseis correlation unnecessary. When the TR survey was acquired by the University of Alberta crew, correlated records were displayed on the field computer during acquisition for quality assurance. The vibroseis sweep was stored in the first channel of each shot record. By storing the uncorrelated records in the field, subsequent reassessment of the vibroseis sweep can be later executed to have better data quality control of each vibroseis sweep and allow the processor to have more control on the shot gathers used for seismic processing.

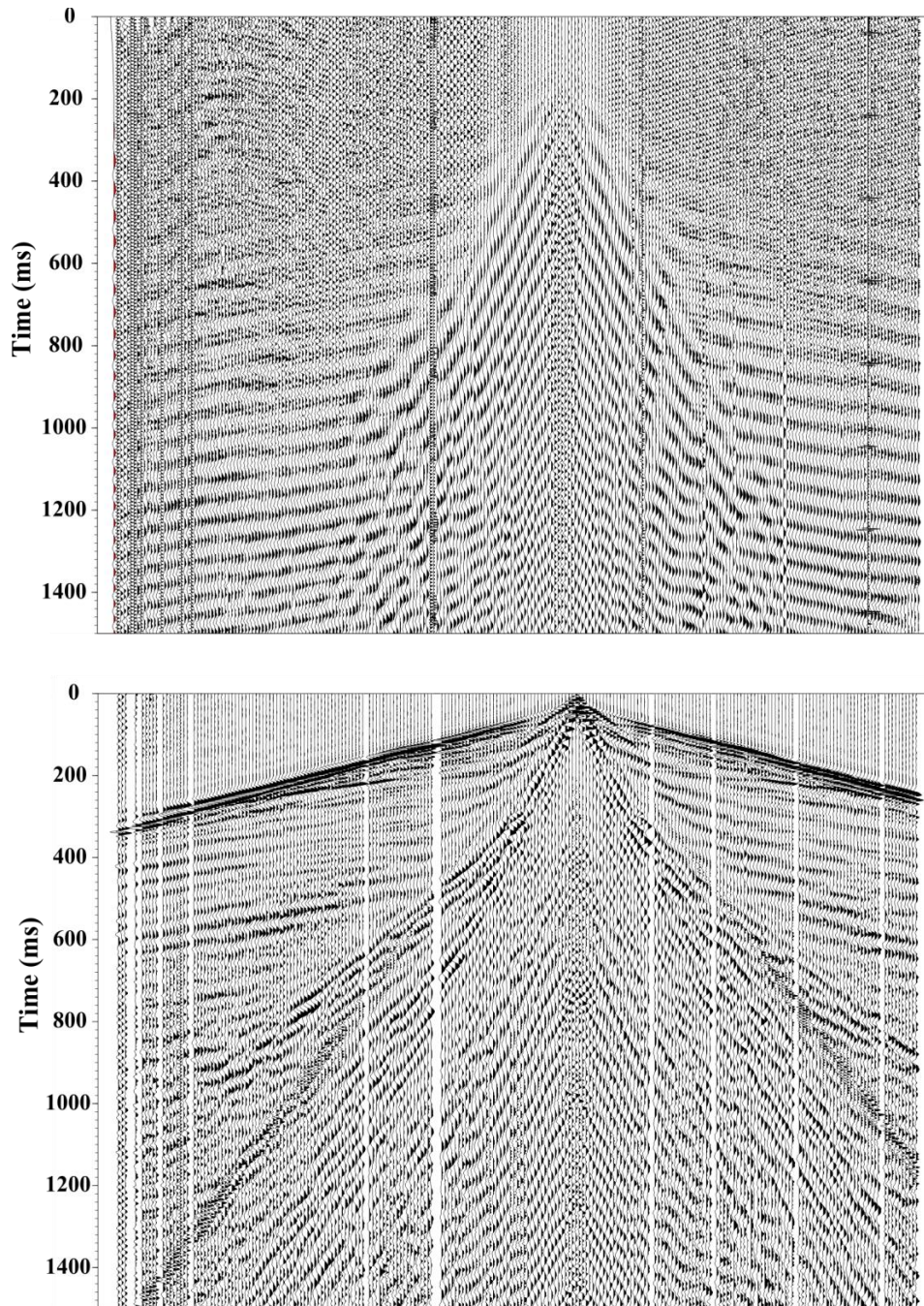


Figure 5-3. Example of uncorrelated (**top**) and correlated (**bottom**) shot gathers of Tower Road (TR) survey. Anomalous traces have already been removed from the correlated shot gather and automatic gain control was applied for display purpose. The first (far left) trace in the uncorrelated shot gather is the vibrator sweep trace. A 13 s sweep and 16 s recorded data yield a 3.4 s correlated record in this survey.

5.3.3. Trace Editing

Noisy traces are inevitable when seismic data is acquired along the road. Raw data needs to be reviewed carefully for noisy traces based on visual inspection of the shot gathers, statistical display of traces to identify those with anomalous amplitude and frequency content, and observations noted in the field report (*e.g.* traffic noise, poor geophone location). The signal-to-noise ratio of the data is improved when noisy traces were muted from the raw data. All reflected seismic energy identified in the data is considered signals whereas noise includes all other undesired components of the record. Noise are categorized into two general types: random and coherent. Random noise includes those naturally-occurring such as wind, rain, vehicular or foot traffic and noisy instruments. Common coherent noise includes source-generated such as ground roll, air blast, multiples and power line signal (60 Hz). Random noise can be muted (or killed) to enhance the reflection signal manually. However, removal of coherent noise primarily relies on seismic processing sequences to attenuate their effects in the seismic records, which will be discussed in the later sections. Figures 5-4 and 5-5 show the different types of events in a sample shot gather of the surveys. Besides the noise events, the characteristic hyperbolic form represents a primary reflection. Refracted arrivals are also distinguishable based on their linear characters and they need to be discriminated from regular reflection events during seismic processing.

5.3.4. First Arrivals Picking

Even though the refracted arrivals are discarded when a stacked seismic section is generated, information about such arrivals is still valuable to seismic processors to characterize the near surface layer thicknesses and velocities. The refracted arrivals are associated with the base of the weathering layer and constitute the first arrivals on a shot gather (Figure 5-5). Quality of the first breaks varies from shot to shot depending on near-surface conditions. Any deviations observed in the linear trends of the first arrivals can be attributed to elevation differences or near-surface irregularity along the shot profile (Yilmaz, 2001). Therefore, manual first

arrival picking was performed over the automated procedures in the seismic processing software to ensure accuracy of the picks for determining statics corrections.

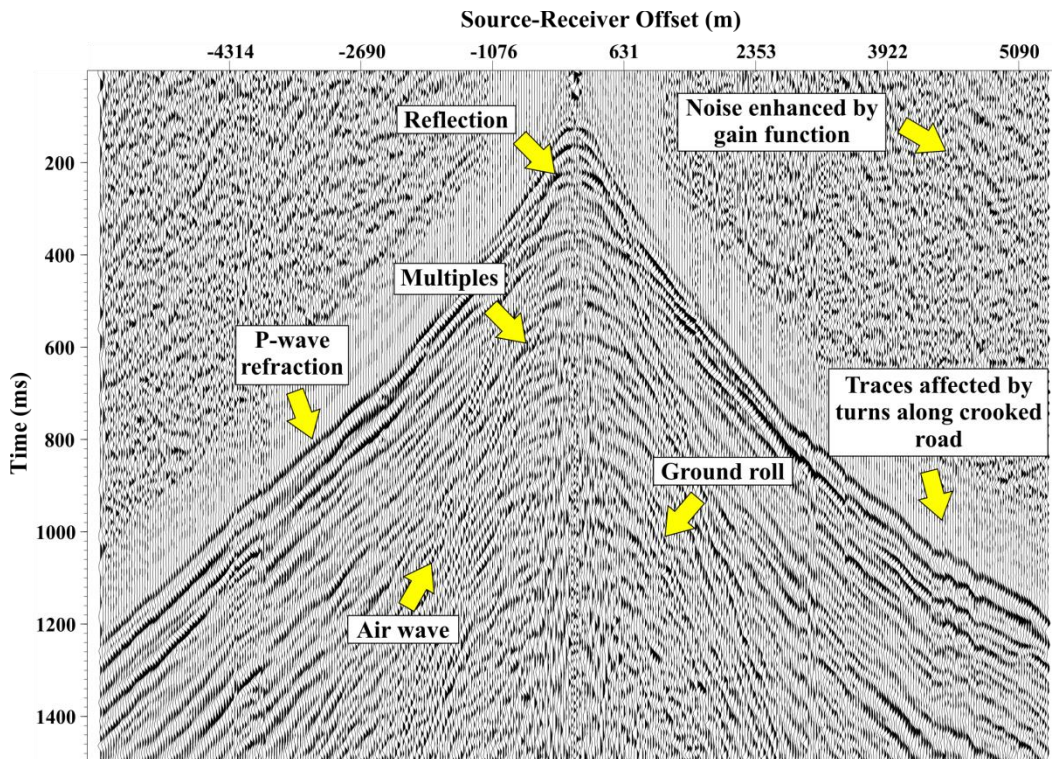


Figure 5-4. Types of events on a shot gather in the Thickwood (TW) 2D seismic survey. Shot gather is displayed with source-receiver offset along the x-axis and two-way travel time along the y-axis.

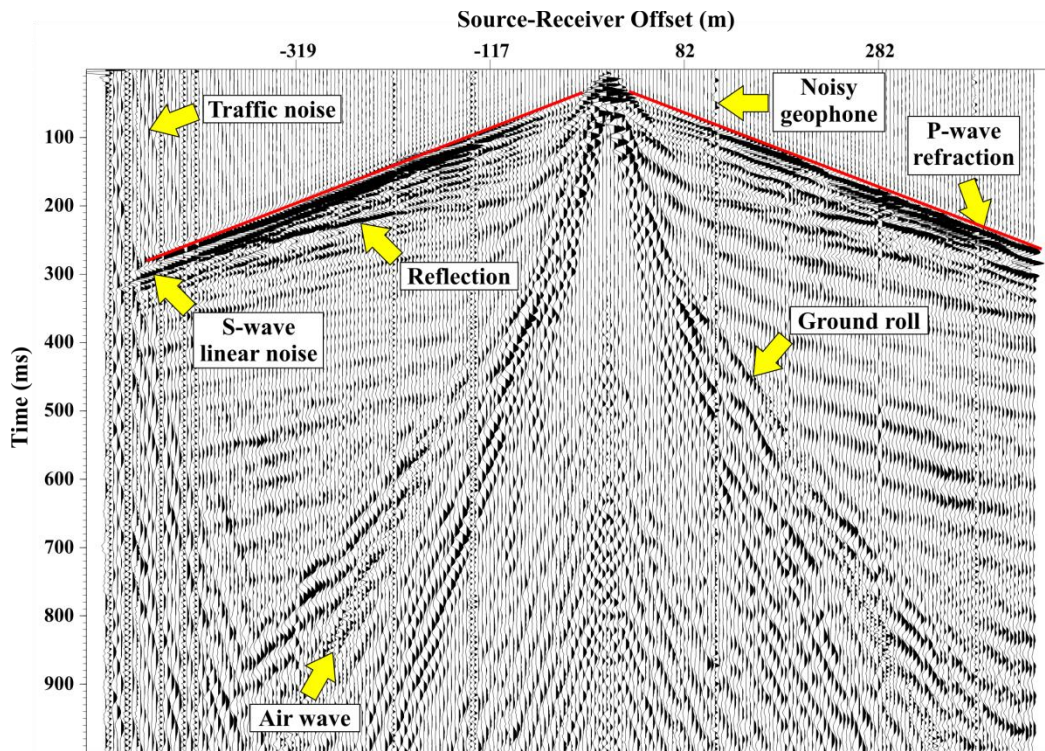


Figure 5-5. Types of events on a shot gather in the Tower Road (TR) 2D seismic survey. Shot gather is displayed with source-receiver offset along the x-axis and two-way travel time along the y-axis. First break linear trends are outlined by the red lines.

5.3.5. Gain Application

As energy propagates from source to receivers amplitude decays occur due to wavefront divergence, scattering, and frequency-dependent absorption from the intrinsic attenuation of the rocks. This creates a problem for the display since only the high amplitude early arrivals and ground rolls are observed in the raw shot gather (Figure 5-6). To enhance the decaying signal, a scaling function is applied to the shot gathers to compensate for the energy losses.

The simplest gain function is the automatic gain control (AGC) and it is often applied to seismic data for quick display. The amount of gain from the AGC is determined automatically from the mean trace amplitude of the input signal computed within a specified moving time gate. After the AGC has been applied,

the seismic trace has constant average amplitude throughout its length. It is important to note that the AGC boosts both signal and noise; hence time gates should be selected carefully. The input, $A_i(t)$, and output traces, $A_o(t)$ of an AGC function are related by:

$$A_o(t) = A_i(t)g(t) \quad , \quad (5-5)$$

where t is time and $g(t)$ is the gain function applied to each input trace.

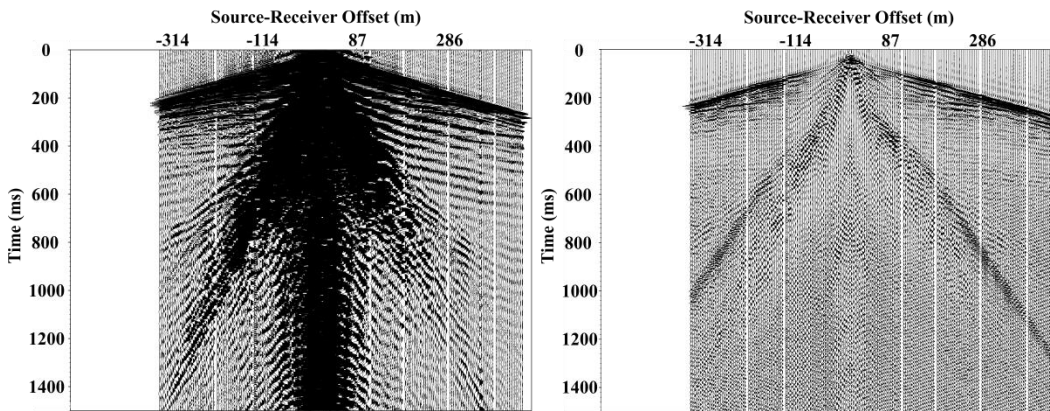


Figure 5-6. (Left) An example of the raw shot gather of the Tower Road (TR) seismic survey without any gain application. Reflection events cannot be clearly identified as they are masked by surface waves and reverberation. **(Right)** A processed shot gather with noisy traces removed, followed by applying an exponential time power gain and frequency filtering. Blank traces on the far left of the shown gathers are traces that have been removed due to traffic noise contaminations as seen in Figure 5-5.

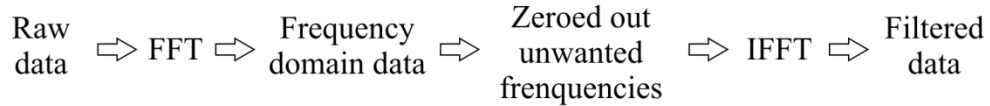
In reality, energy attenuation is a form of exponential decay. In a homogeneous medium energy attenuation is proportional to $1/r^2$, and amplitude attenuation is proportional to $1/r$, where r is the radius of the spherical wavefront originating from the point source (Yilmaz, 2001). Thus, a more preferred method to scale the seismic data is to account for the geometrical spreading and absorption of seismic energy by exponential scaling. The gain function that increases exponentially with time (t) is given by:

$$A_o(t) = A_i(t)e^{ct} \quad , \quad (5-6)$$

where c is an exponential time constant. This relation approximates the effect of absorption with some transmission losses.

5.3.6. Frequency Analysis

Amplitude spectral analysis is used for assessing the bandwidth of the seismic traces (Figure 5-7). If the amplitude spectra of the signal and noise differ, they can be separated on the basis of frequency using a fast Fourier transform (FFT) in the following operation:



Bandwidth is the frequency range present in a wavelet. Seismic traces are measured in the time series with a selected sampling interval (Δt , sample rate) that determines the restorable frequency bandwidth of the digitized data. The highest frequency that can be restored is called Nyquist frequency (f_N) and is given by:

$$f_N = \frac{1}{2\Delta t} \quad . \quad (5-7)$$

A temporal aliased signal is generated when a signal is sampled at sampling frequency (f_s) greater than f_N . Using Equation 5-7, the Nyquist frequencies for TW ($\Delta t = 2$ ms) and TR ($\Delta t = 1$ ms) surveys are 250 Hz and 500 Hz, respectively. Therefore, both seismic surveys have maximum bandwidths below f_N and are not affected by temporal aliasing.

To relate desired frequency components to the actual signal or noise, frequency panels are generated by applying different narrow bandpass filters to the data set. This helps to identify the dominant frequency range for the reflected signal and allows processors to safely remove ground roll, guided waves, and scattered energy using a bandpass filter without compromising the useful signals.

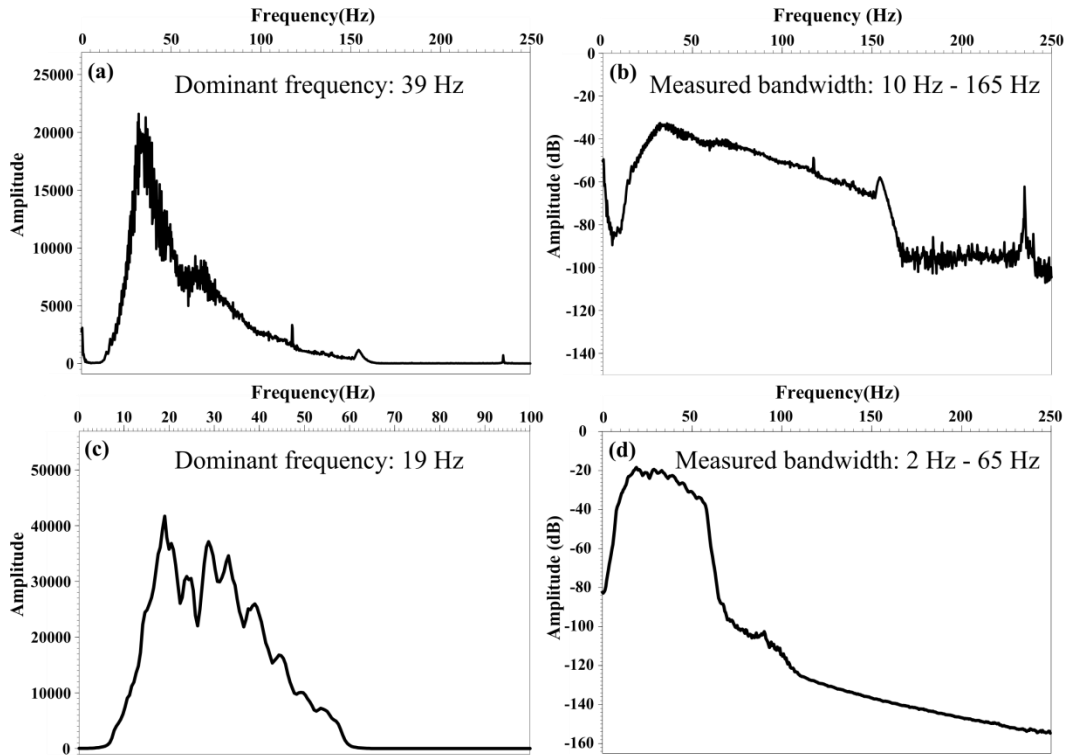


Figure 5-7. Frequency spectral analysis of Tower Road (a, b) and Thickwood (c, d) 2D seismic surveys in linear (a, c) and decibel (b, d) formats.

5.3.7. Elevation and Refraction Statics

Seismic acquisition on land needs to account for the variable near-surface conditions. Seismic ray paths are affected by the elevation differences between source and receiver locations, the thickness of the near-surface (weathered rock) layer and the topographic variation along the seismic line. These cause static shifts in the seismic arrival times between adjacent traces and hence degrade the continuity of seismic reflections. The weathered layer is characterized by its low velocity and rapid absorption of high-frequency energy (Ashcroft, 2011). In the Fort McMurray area, the near-surface weathering layer typically has a drift thickness of less than 15 m and is of glacial origin (Fenton and Pawlowicz, 2000).

Statics corrections allow processors to correct for the effects of elevation and weathering layers. Time shifts are added or subtracted from each seismic trace to account for the effects and to reduce data to a common datum. A common datum

elevation allows multiple seismic data sets to be aligned properly in depth for interpretation. In a crystalline rock environment, refraction static corrections have been reported as an important step in seismic processing to compensate for the high-velocity basement rocks (> 6000 m/s) relative to the overburden that result in large static shifts (Milkereit *et al.*, 1992; Wu *et al.*, 1992; Juhlin, 1995; Adam *et al.*, 1998; Schijns *et al.*, 2012). Choosing an appropriate datum and replacement velocity is necessary for the proper calculation of static shifts. Large bulk static shifts should be avoided as they will degrade the processes of normal moveout correction and migration.

Refraction static corrections are applied to remove the effect of the weathering layer and elevation by adjusting differences in travel times of first arrivals. The slope of the first breaks represents the base of a weathering layer and provides a good approximation on the replacement velocity. Using a datum elevation of 450 m and a replacement velocity of 1900 m/s, a near-surface velocity model was deduced and static shifts were applied to each trace. Subsequently, each trace has a new “time zero” which represents data collected from an imaginary flat surface at the defined elevation datum known as “seismic datum”. Elevation differences between shot and receivers and between the receivers are also eliminated.

5.3.8. Noise Attenuation

The quality of seismic data is frequently affected by the coherent and incoherent noise as mentioned in Section 5.3.3. Poor quality data results in a low signal-to-noise ratio (S/N). When the noise has appreciable energy outside the principal frequency range of the signal, frequency filtering can be applied without affecting the reflected signal responses. Bandpass filtering is useful in reducing the effect of surface waves as seen in the spectral analysis of the Tower Road survey (Figure 5-7a). However, the noise energy spectrum often overlaps with the signal spectrum in which simple frequency filtering is no longer useful in noise attenuation. As mentioned earlier, frequency panel tests were performed to determine the frequency ranges of signal and noise prior to applying any bandpass filtering to avoid the risk of filtering useful signals.

Source-generated noise such as surface waves, air waves and ground roll are linear noises that propagate with constant velocities in the time-offset domain. Noise suppression has been successful in attenuating linear noise according to the velocity properties of seismic waves (*e.g.* Juhlin, 1995; Schmelzbach *et al.*, 2007; Hedin *et al.*, 2012). The next few sub-sections review the velocity filtering methods used in the seismic processing routines for the Thickwood and Tower Road seismic surveys to address different coherent linear events. The final goal is to improve the overall quality of the final stack sections after noise suppression methods have been implemented in the seismic processing routine.

5.3.8.1. Frequency-Wavenumber (F-K) Filtering

Coherent linear events in the time-offset (*t-x*) domain can be separated in the frequency-wavenumber (*f-k*) domain by their dips or apparent velocity differences (Yilmaz, 2001). The velocity (*v*) of the incidence in the *t-x* domain corresponds to the slope of the spectrum in the *f-k* domain according to:

$$v = \frac{2\pi f}{k} \quad , \quad (5-8)$$

where *f* represents frequency and *k* is the wavenumber (reciprocal of the wavelength). For non-dispersive (fixed velocity) wave modes, the wave would appear as a linear slope in the *f-k* domain (Figure 5-8a). The design of *f-k* reject bands is defined by the processor. Narrow reject bands would produce less signal distortion but one should also be aware of Gibb's phenomenon for the ringing artifacts in the frequency spectra. Each reject band is defined to remove one event in the case of multiple coherent noise in a shot gather.

A 2-D Fourier transform is first applied to shot gathers to convert data from the *t-x* to *f-k* domain which separates signal and noise. Reject filters are designed in the *f-k* domain by setting the amplitude spectrum of the filter to zero within the selected zone and to one in the pass zone. This *f-k* filter is applied by multiplying the amplitude spectrum with the original data. Finally, an inverse Fourier transform is applied for the output of noise-filtered output. This procedure has been applied to both the TW and TR seismic surveys but they serve different

purposes (Figure 5-8b, c). F-k filters were applied to TW and TR surveys to attenuate ground roll and near-surface refracted waves, respectively. Despite the successful attenuation of linear noise in the shot gathers, f-k filters can result in signal distortion and smoothing, and also possible introduction of filtering effects (March and Bailey, 1983). This is due to the overlapping of signal and noise in the f-k domain (Duncan and Beresford, 1994).

Wide frequency-wavenumber (f-k) rejection bands were found to cause too much signal distortion, so only a narrow f-k rejection band was selected for attenuating refracted waves. However, some of the near-surface refracted waves could not be completely attenuated after f-k filtering. Another coherent noise attenuation method implemented was a radial-trace (R-T) transform. This method was chosen over a second pass of f-k filter wherever possible to avoid further signal distortion and filtering effects from the f-k filters and will be discussed in the next section.

5.3.8.2. Radial-Trace (R-T) Transform Filtering

A R-T transform is a simple point-to-point mapping by extracting wavefield amplitudes and interpolating them onto the velocity and travel time plane (Henley, 2001, 2003; Ogunsuyi and Schmitt, 2011). Amplitudes are transferred into the new domain in the form of radial traces. These transformed radial traces consist of amplitude values gathered along the linear trajectory of constant apparent velocity (Henley, 2003). Linear events are transformed into small groups of low-frequency traces in the R-T domain. In addition to the remaining un-filtered refracted events by f-k filter attenuation, high-amplitude, low-frequency, and low velocity ground rolls were also observed that overwhelm the reflection signals in the shot gathers of Tower Road survey (Figure 5-5). Low-frequency refracted waves and ground rolls are suppressed by applying a 25 Hz low-cut filter to the radial traces. This frequency filter was chosen by inspecting the frequency filter panels to ensure that the selected frequency does not remove signal responses. The filtered radial traces are then transformed back to the x-t domain and reflections at farther offset distances become more apparent.

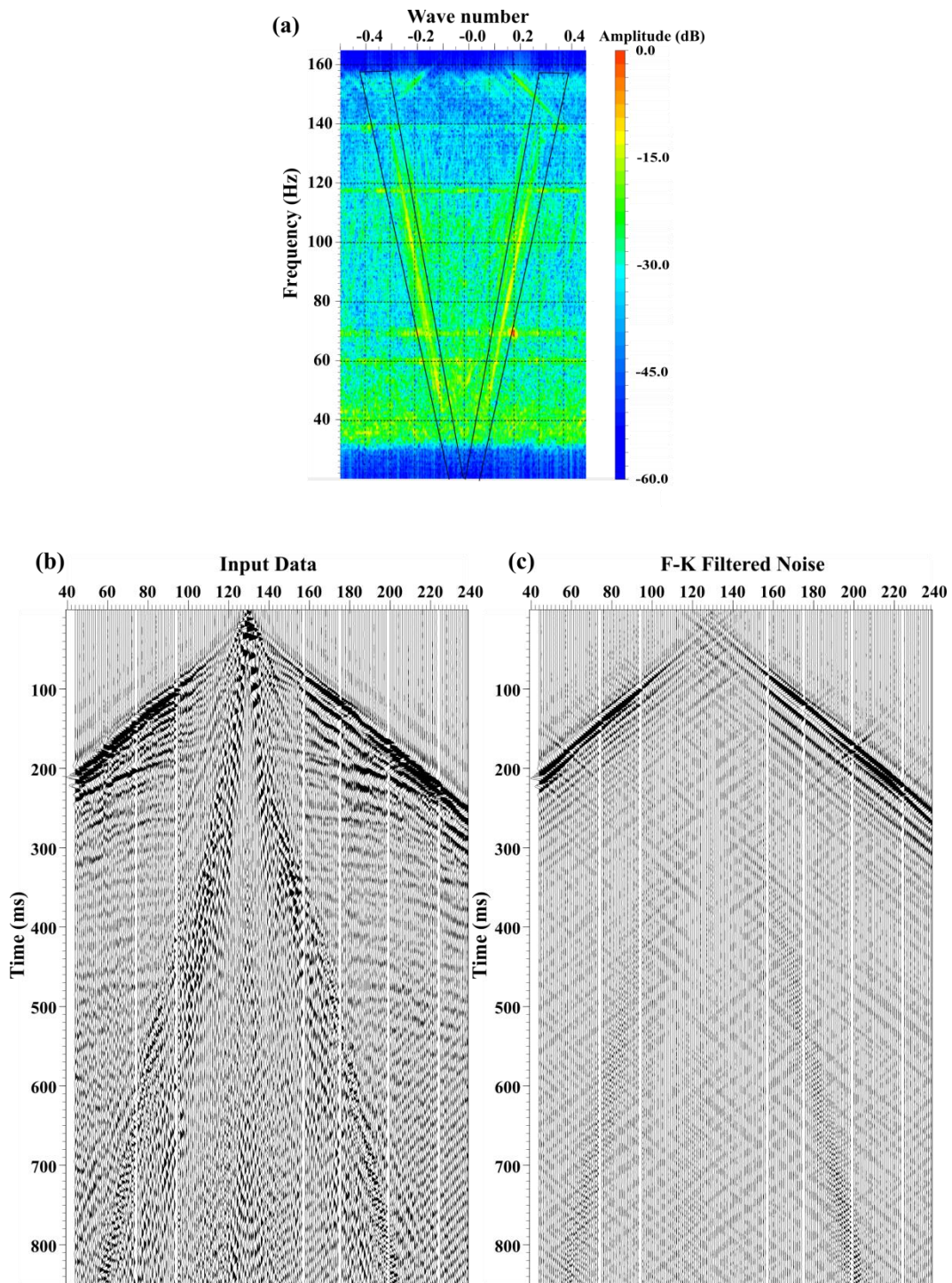


Figure 5-8. Frequency-wavenumber (f-k) filtering to attenuate linear noise. (a) Design of reject filters in the f-k domain. Reject filters of linear noise are outlined by the black fan-shaped polygons. (b) Shot gather before f-k filtering. (c) F-k filtered linear noise. Horizontal axis contains the trace number of the shot gather.

5.3.9. Predictive Deconvolution

One of the biggest concerns in the stacked seismic sections is the presence of multiple reflections generated by repeated reflections within the sedimentary sequence (Ashcroft, 2011). The problem of multiple reflections arriving at the same time as seismic arrivals from the Precambrian basement was deemed to be the biggest concern in the existing processed data of the TW survey. These sedimentary multiples masked the true but weaker reflections that might be of importance. As such, re-processing of the TW data set was carried out in an attempt to further suppress these multiples.

Multiple reflections and reverberations are attenuated using techniques based on their periodicity or differences in moveout velocity between multiples and primaries (Yilmaz, 2001). One multiple attenuation method that exploits periodicity is predictive deconvolution. Predictive deconvolution aims to improve the temporal resolution by sharpening the seismic signals and attenuate multiples from the seismic section. A recorded seismogram $x(t)$ is modeled as a convolution of the Earth's reflectivity, $r(t)$, with the seismic wavelet, $w(t)$, and random ambient noise, $n(t)$, as:

$$x(t) = w(t) * r(t) + n(t) \quad , \quad (5-9)$$

in which $w(t)$ includes components of the energy source, recording filter, surface reflections, and receiver-array response, and $r(t)$ is comprised of primary reflections and all possible multiples (Yilmaz, 2001).

Deconvolution yields a representation of the subsurface reflectivity by estimating $r(t)$ from $x(t)$. This is commonly performed using predictive deconvolution which uses information from the earlier part of a seismic trace to predict and deconvolve the later part of the trace (Sheriff, 2002). This method predicts some types of systematic noise, such as multiples and reverberations. It relies on the assumptions that (1) the seismogram obeys the convolution model in Equation 5-9, (2) $r(t)$ and $n(t)$ are random, and (3) $w(t)$ is a minimum phase. A minimum phase wavelet has most of the energy concentrated nearest the time onset of the

wavelet and is the one with the least change in phase along the frequency axis (Nickerson, 2007).

In practice, predictive deconvolution requires several parameters to be specified: pre-whitening, operator length, prediction lag, design window, and design window taper. The specific values used for the TW and TR seismic surveys are listed in Tables 5-2 and 5-3. An important note regarding the operator length of the deconvolution operator is that long operators may introduce artefacts. Several different operator lengths were tested for each seismic survey before reaching the final result. Moreover, the design window was chosen such that deconvolution focuses on the design time gate containing the higher signal-to-noise ratio. A second pass of the predictive deconvolution approach was chosen for the TW survey to further attenuate multiples and reverberations. Spiking deconvolution was not used in the processing routines as it exaggerated the high-frequency noise in the records. A comparison of a shot gather before and after deconvolution is shown in Figure 5-9.

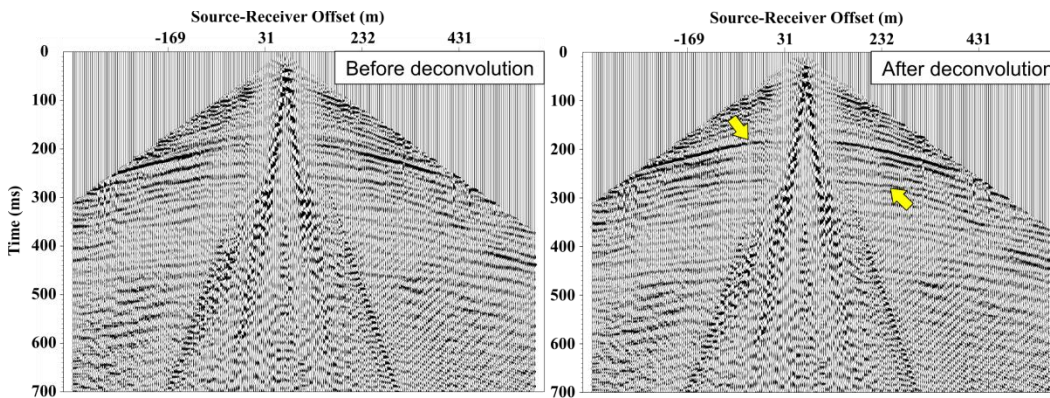


Figure 5-9. Comparison of shot gathers before and after predictive deconvolution. Yellow arrows indicate reflectors that became more distinct and continuous after deconvolution was applied. Refracted waves were muted using the R-T transform filtering prior to applying predictive deconvolution.

5.3.10. Time-Variant Bandpass Filtering

Deeper seismic reflections tend to have a higher percentage of low-frequency energy than shallow reflections due to the attenuation effect of high-frequency energy through absorption and attenuation of the rocks (Telford *et al.*, 1990). Therefore, a time-variant bandpass filter is utilized to adjust the frequency bandwidth toward lower frequencies as record time increases to improve the resolution of the data. This step helps to emphasize deeper reflections while also to reduce source-generated noise at earlier travel times (Dehghannejad *et al.*, 2010). Another usage of time-variant filtering is to limit the boosting effects of higher frequencies from previous deconvolution processes. Frequency noise tends to be boosted by the deconvolution process in the seismic section which leads to the broadening of the amplitude spectra (Bruno *et al.*, 2002). After deconvolution, time-variant bandpass filtering was applied to filter the data back to the signal bandwidth. This processing sequence can also be applied in the post-stack processing sequence (Section 5.4) to further attenuate any random noise that was boosted after common midpoint stacking.

5.3.11. Common Midpoint (CMP) Sort

Before this step seismic data has been sorted in common shot gathers. To attenuate random effects and events whose dependence on offset is different from that of primary reflections, a sorting of traces by common midpoint (CMP) in seismic processing improves any discrimination against noise when traces are sorted by coincident midpoints between sources and receivers (Sheriff, 2002). CMP sorting is designed to improve the signal-to-noise ratio (S/N) acquired along a straight seismic profile (*e.g.*, Tower Road survey, Figure 5-10) in which reflection points are assumed to lie below the midpoint between the source and the receiver (Kashubin and Juhlin, 2010). Traces from different shot point and receiver locations are stacked when their CMP fall in the same bin. In-line and cross-line bins are designed into square boxes that equal to the half-distance between shots and receivers. The more traces in the CMP bin, the greater the S/N after traces are stacked.

Unfortunately, seismic reflection data is not always acquired in a straight line. Crooked line profiles are rather common for cost and access reasons (Wu, 1996). As a result, CMP gathers along crooked profiles are characterized by a variable fold and uneven offset distribution (*e.g.* Thickwood survey, Figure 5-11). CMP are scattered from a straight line and sorted into rectangular bins. After experimenting with complete straight-line binning, slalom-line binning, and a series of straight-line segment binning geometries, the latter method was chosen for the better sampling of the data and is less likely to have uneven fold coverage (Dehghannejad *et al.*, 2010). The in-line bin size retains the half-distance CMP position between shots and receivers, but the cross-line bin size was chosen to sample a larger subsurface area to capture most of the CMP scatters with minimal intersection between adjacent bins. This avoids any sudden drops in fold coverage and maintains a sufficient offset distribution (Wu, 1996; Nedimović and West, 2003; Kashubin and Juhlin, 2010).

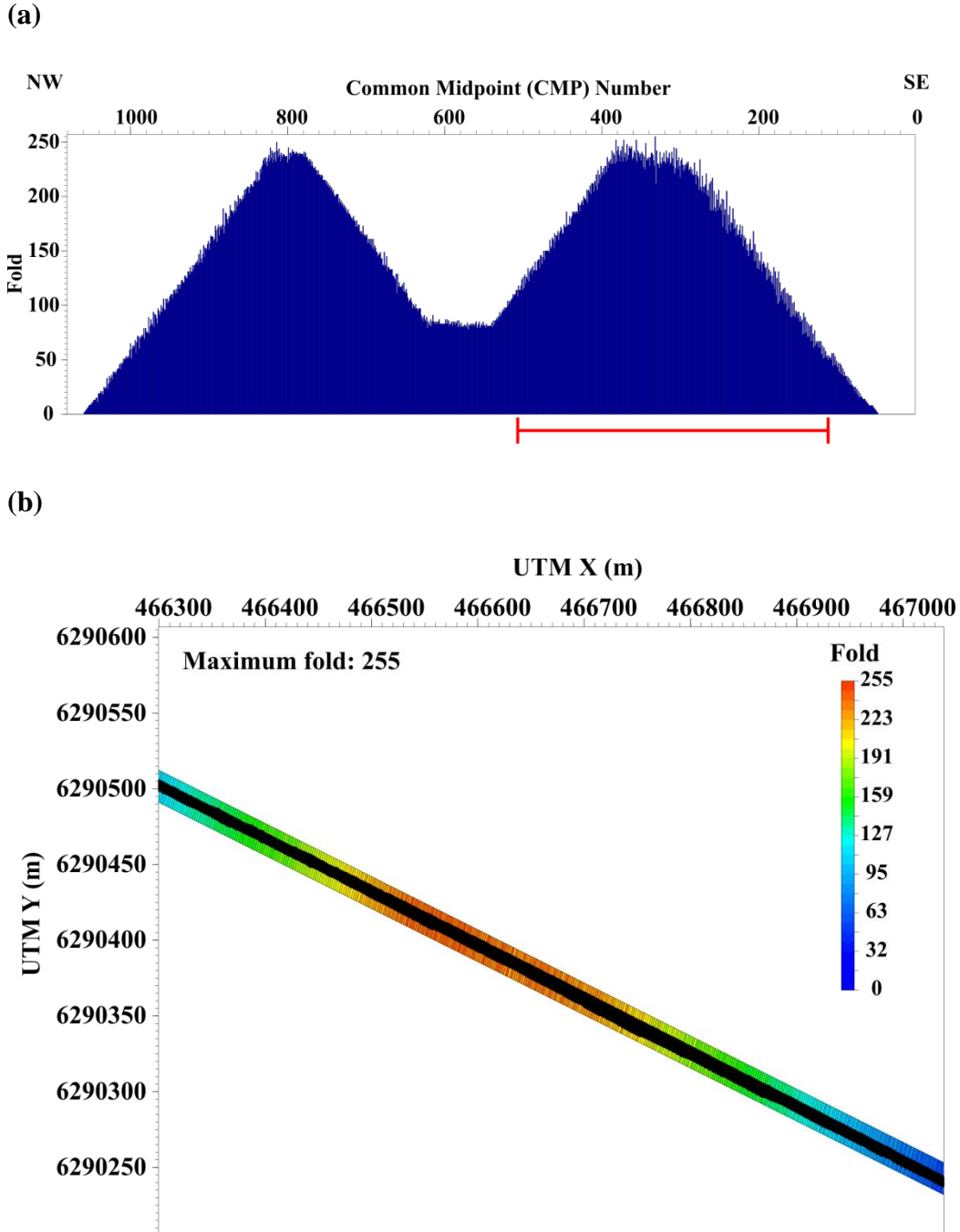


Figure 5-10. Common midpoint sort for Tower Road 2D seismic profile. This profile was shot in two separate spreads (west and east) thus shows a decrease in fold in mid-section of the profile. (a) Distribution of fold along the profile. (b) CMP binning for a selected section of the profile as indicated by red arrow in (a). Black dot clusters in bins are common midpoint locations. An in-line bin size of 2 m was used for CMP binning. Maximum fold coverage for this 2D profile is 255.

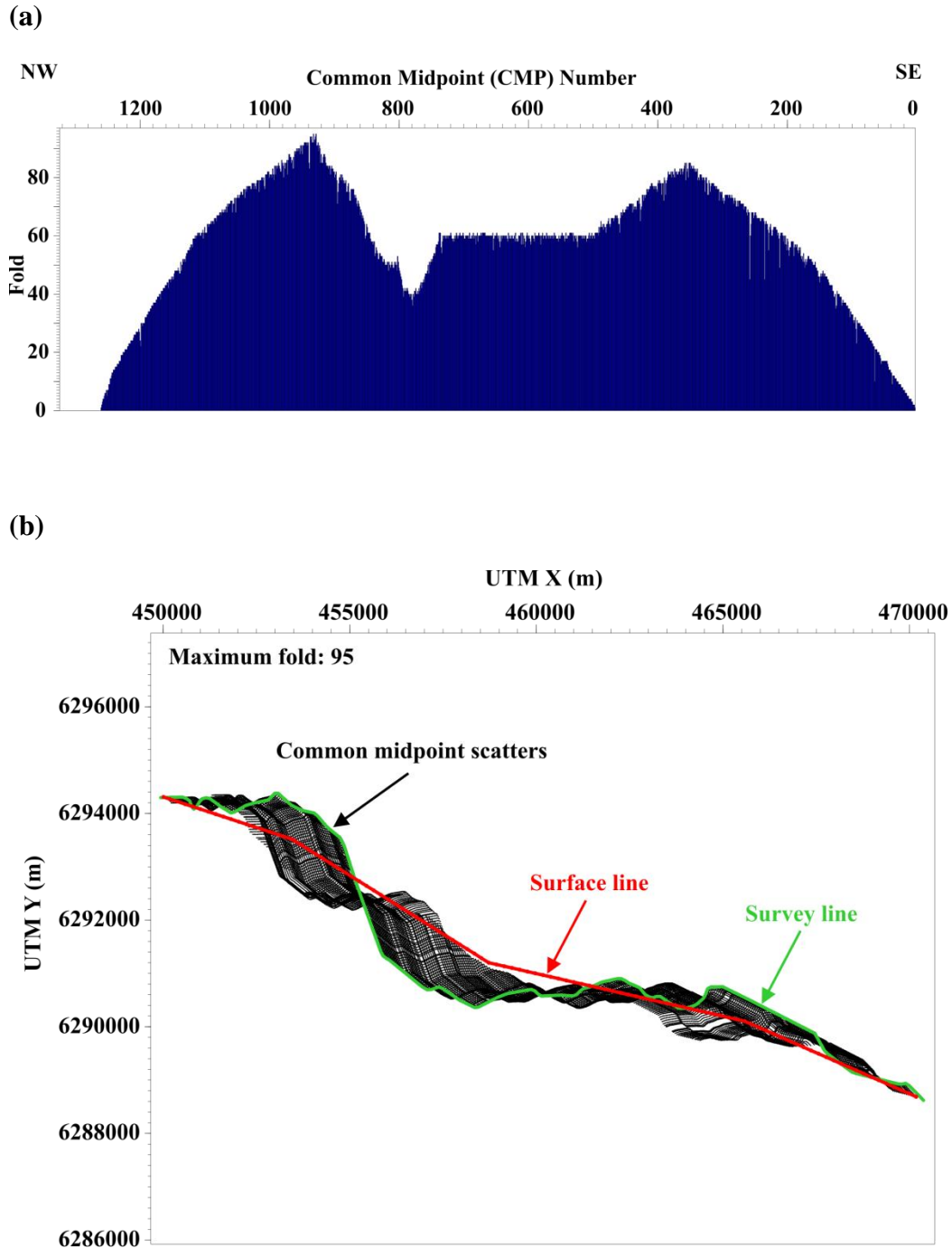


Figure 5-11. Common midpoint sort for Thickwood 2D seismic profile. (a) Distribution of fold along profile. Uneven fold is due to the crooked line geometry. (b) Common midpoint scatters along the crooked profile. Using a slalom surface line, an in-line bin size of 16.7 m and cross-line bin size of 1000 m was used to capture a sufficient number of CMPs in the bins. Maximum fold coverage for this 2D profile is 95.

5.3.12. Velocity Analysis

The purpose of a velocity analysis is to determine the stacking velocity required to correct for the difference in seismic arrival times at receivers as a result of increasing offset (normal moveout). Since velocity generally varies laterally along a line, velocity analysis is performed at CMP intervals and time-velocity pairs are generated to create a velocity model. This can be done interactively using a semblance plot and/or the constant velocity stack (CVS) (Figure 5-12). A common midpoint gather can be displayed in the same window to verify the accuracy of velocity and time pair picks before and after normal moveout correction.

A semblance plot is a velocity spectrum display of selected velocity ranges and the sampling interval (Figure 5-12a). The colours in the spectrum represent the signal coherence along the hyperbolic trajectories dependent on velocity, offset, and travel times (Yilmaz, 2001). The hyperbolic trajectories are the theoretical normal moveout required to correct for the arrival time difference at the geophone locations using the relation:

$$t^2 = t_0^2 + \frac{x^2}{v^2} , \quad (5-10)$$

where x is the offset distance between source and receiver, v is the stacking velocity, and t_0 is the travel time at zero-offset. A high coherence measure of seismic energy (*i.e.* presence of a reflector at that depth and velocity) indicates the best stacking velocity along the selected trajectory. An alternative and complementary method of velocity analysis is the constant velocity stack (CVS) (Figure 5-12b). The CVS involves generating trial stacks of selected velocity ranges that are constant in time and space to determine the best velocity function (Sheriff, 2002). Using a combination of the semblance plot and CVS for velocity analysis, the resultant velocity pick is referred to as the “stacking velocity”. The velocity function is described as a best-fit hyperbola to the travel time curve of the seismic data. It is important to note that the stacking velocities are not the true

material velocity but are more closely related to the root mean squared average velocities for horizontal layers and small offsets.

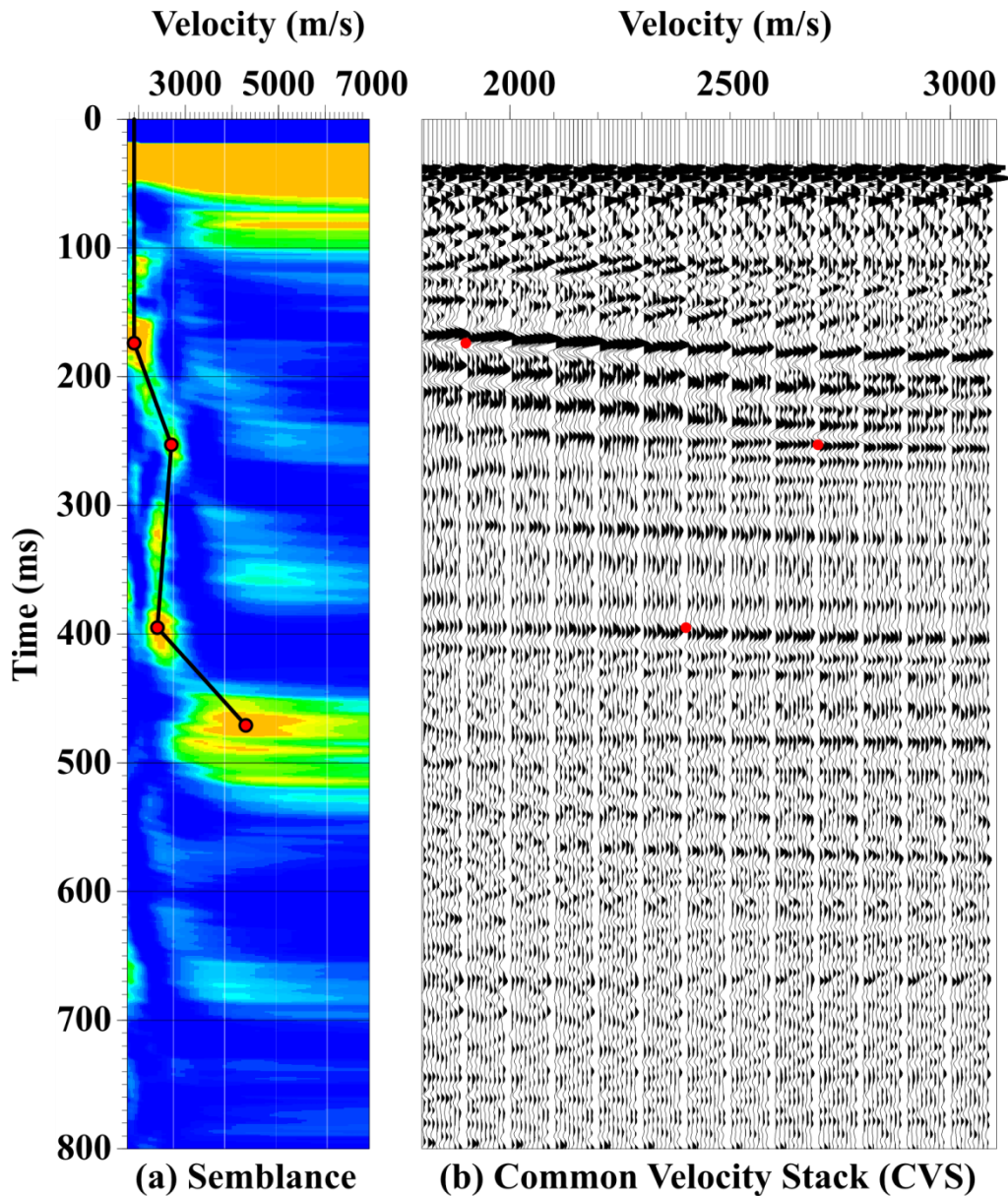


Figure 5-12. Interactive velocity analysis using (a) semblance plot and (b) common velocity stack (CVS). Sample velocity and time pairs are interpreted by red dots on both methods. The red color display on the semblance plot indicates the best stacking velocity with greatest coherence measure of the seismic energy. Only a partial suite of common velocity stacks are displayed here.

Unlike sedimentary basins, the crystalline basement typically lacks pronounced continuity of seismic reflectors and is often characterized by uniformly high velocities (Milkereit and Eaton, 1998). As such, velocity analyses using semblance and CVS do not offer sufficient accuracy in velocity picking for normal moveout corrections. For the near-surface layers, another mean to guide the velocity analysis is to use the velocity measured from the slopes of the direct waves and refracted waves. Deeper layers will have to rely on other available data such as geophysical logs acquired in nearby boreholes. Velocities measured using sonic logs (Section 4.2.6) and the zero-offset vertical seismic profile at the Hunt well (Section 6.4.1) reveal a velocity range of 5500 m/s to 6500 m/s for the crystalline basement. This velocity range was used as a guideline to generate the velocity model in the crystalline basement where reflectors could not be identified. The final velocity model was obtained after three iterations of the velocity analysis and residual static corrections (Section 5.3.14) to improve its overall quality (Figure 5-13).

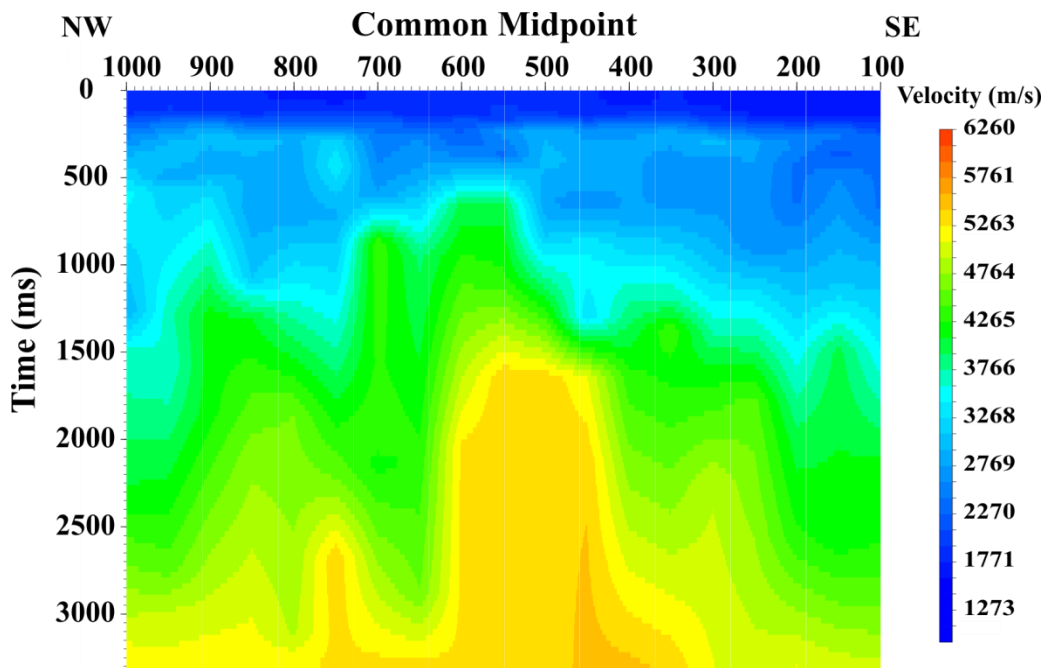


Figure 5-13. Result of velocity analysis for Tower Road Survey. Velocity and time pairs were more confidently identified in the upper 470 ms in the semblance plot and common velocity stacks.

5.3.13. Normal Moveout Correction

With the velocity function derived in the previous section, a normal moveout correction is then applied to remove the offset effect from travel times by:

$$\Delta t = t - t_0 = \sqrt{t_0^2 + \frac{x^2}{v^2}} - t_0 \quad , \quad (5-11)$$

where Δt is the time difference needed for the normal moveout (NMO) correction. Fundamentally, t_0 and x are known for each trace in the CMP gather where Δt is calculated when v is known from the velocity analysis. Each trace is then shifted in time from the recorded time (t) to the zero-offset time (t_0). This procedure involves stretching longer offset traces, resulting in seismic wavelet distortions on the outer traces known as “NMO stretch” (Nickerson, 2007). Consequently, such trace distortion degrades the resolution of the seismic stacked section. To reduce the effects of direct and refracted arrivals in the near surface, a stretch-mute function was utilized, a top mute function superimposed on the NMO-corrected gather (Schmelzbach *et al.*, 2005). A proper stretch mute must be selected carefully, dependent on the amount of distortion and offsets, without significantly reducing the fold and introducing excessive frequency distortion (Miller, 1992). One advantage of the stretch mute function is that it can preserve shallow reflectors without changing the bandwidth of the data (Adam *et al.*, 1998).

5.3.14. Residual Statics

In Section 5.3.7, travel time distortions due to irregular topography and a near-surface weathering layer were corrected by elevation and refraction statics. However, they do not account for the random trace-to-trace time delays beneath the shots and receivers. Residual statics errors lead to ineffective velocity analysis and stacking from trace to trace degrades the continuity of reflectors in a seismic section. The objective of the residual statics correction is to remove any deviations in reflection times that are not associated with subsurface structure and

stratigraphy. These deviations are typically due to the anomalous conditions in the shallow subsurface and velocity errors (Gadallah and Fisher, 2005).

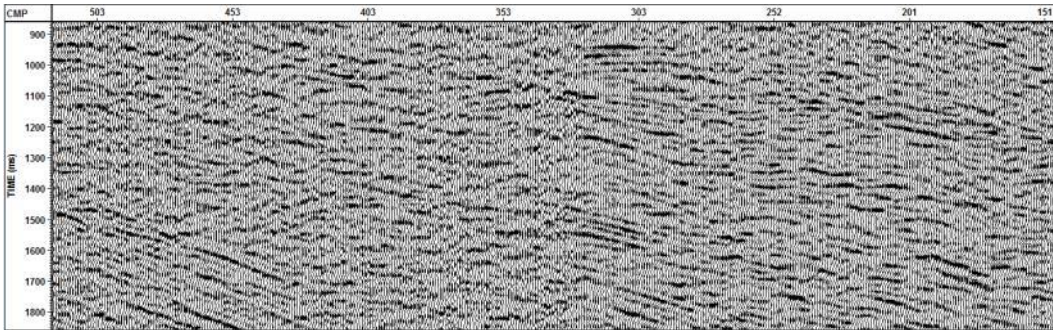
After the normal moveout correction, the observed time shift between adjacent traces can be estimated. Using a stack power optimization, surface consistent statics are calculated by separating the residual statics into source and receiver components (Ronen and Claerbout, 1985). This technique is based on minimizing the difference between modeled and actual travel time deviations in the NMO-corrected CMP gathers of reflectors (Yilmaz, 2001). The CMP gathers and model stack are the input data sets required for the automated algorithm in calculating the needed time shifts. It is an iterative procedure in which each trace in the CMP gather is cross-correlated with the trace from the model stack with the same CMP (Nickerson, 2007). The only other parameters that need to be supplied to this flow are the maximum allowable shift and correlation window. Maximum allowable shift should be sufficiently long to account for any static shifts between adjacent traces. It should not be too long such that noise in the data will affect the cross-correlation between traces, such as “cycle skip” (Nickerson, 2007). The selection of a correlation window should include a strong reflector that would correlate well between the NMO-corrected gathers and modeled traces. Three iterations of the velocity analysis and residual statics were performed on the NMO-corrected gather to reduce velocity errors and enhance the continuity of reflectors.

5.3.15. CMP Stacking

After pre-stack processing of random and coherent noise attenuation, statics and normal moveout corrections, seismic traces are combined (stacked) to generate a common-midpoint section that approximates the traces that would be recorded by a coincident source and receiver at each location (Sheriff, 2002). This process can act as a powerful mechanism to suppress multiples, increase the coherent signal content and reduce incoherent noise (Galbraith, 2002). A comparison of stacked seismic sections of the TW survey using various offset distance data is shown in Figure 5-14. The two compared sections reveal that a longer offset distance improves the imaging of deeper reflectors and they appear more continuous

laterally. This was also demonstrated by Nakagome *et al.* (1998) and Heinonen *et al.* (2013). This form of partial-stacking of the NMO-corrected CMP bin gathers can increase the signal-to-noise ratio at greater depths. In principle, this is effective in regularizing the data density but does not preserve amplitude balance of the data (Nedimović and West, 2003).

(a) Offset distance: 70 to 1000 m



(b) Offset distance: 70 to 3000 m

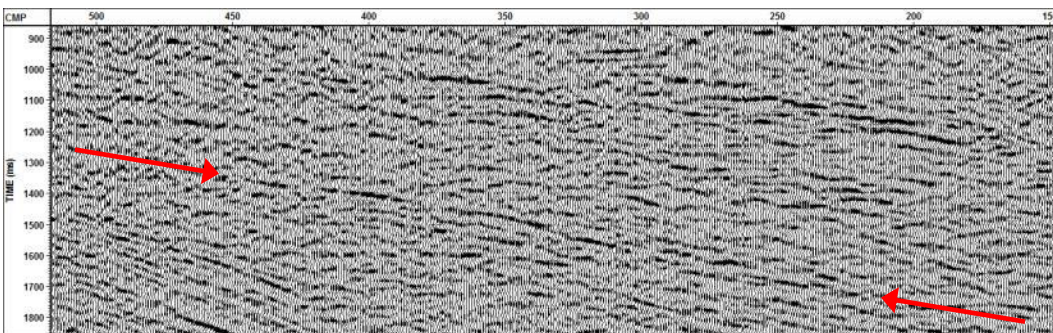


Figure 5-14. Comparison of stacked seismic sections of the TW survey using different offset distances **(a)** 70 to 1000 m and **(b)** 70 to 3000 m. A seismic section using greater offset distances shows clearer deep reflections between 1250 ms to 1850 ms as indicated by the red arrows.

5.4. Post-Stack Processing

Post-stack operations involve additional processing after seismic traces are stacked to further enhance the signal-to-noise ratio of the data. Some typical sequence includes deconvolution, time-variant spectral whitening, time-variant

bandpass filtering (Section 5.3.10), random noise attenuation, migration, and display gain (Yilmaz, 2001). A F-X 2D prediction was applied to both the TW and TR 2D seismic surveys, followed by finite difference migration.

5.4.1. F-X 2D Prediction

F-X 2D prediction is a spatial prediction filter based on trace to trace predictability and frequency using the concept that spatially random noise is uncorrelated from trace to trace independent of temporal frequency (Canales, 1984; Gulunay, 1986). The algorithm first calculates the Fourier transform of each input seismic trace. Each sample in the transformed data has both real and imaginary components. Events with similar dip angles appear as a sinusoidally complex signal along a frequency slice (Bruno *et al.*, 2002). A two-sided complex Wiener prediction filter is calculated for each frequency series and then applied to the input data (Robinson and Treitel, 1964; Treitel, 1974). Linear events are predicted from adjacent traces for interpolation between missing data (*e.g.* missing traces due to variable-offset binning) and random noise attenuation in the frequency-space domain. The filter is then applied and the inverse Fourier transform is calculated to output the noise-attenuated data. In practice, the size of the Wiener prediction filter is designed using a group of stacked traces with a moving window. The end result is a reduced data volume with regularized data density and a preserved dominant dipping energy (Bruno *et al.*, 2002; Nedimović and West, 2003).

5.4.2. Finite Difference Migration

In a stacked seismic section, a seismic wavelet is positioned directly beneath their respective common midpoint locations. However, the positioning of the reflector is only accurate when the reflector is flat. Lateral placement error occurs when there is a dipping reflector and this is particularly problematic in complex structural areas. Migration is the lateral repositioning of dipping reflections to their true subsurface positions and collapses diffractions (Yilmaz, 2001). The

diffraction hyperbolas are caused by sharp discontinuities at both ends of the reflector (*e.g.* faults).

There are a number of different migration algorithms that can accommodate the different velocity fields and dips. Finite-difference (FD) migration was implemented for the TW seismic survey (Figure 5-16). This form of migration uses steep-dip algorithms and provides a theoretical dip accuracy of up to 45 degrees performed in the time-space domain (Yilmaz, 2001). Additionally, there is an option to increase the dip accuracy to 65 degrees in the frequency-space domain with longer run times. The velocity model applied was a smoothed stacking velocity model to minimize the risk of generating any artefacts in the image due to abrupt changes in the lateral velocity. Note that there is considerable migration noise from those portions of the profile where the data is poor quality (*i.e.* below 1500 ms in the TW survey). In the TR survey, reflectors are imaged properly since, in this shallower survey, they are relatively flat. Thus, a migration algorithm was deemed unnecessary in the TR survey.

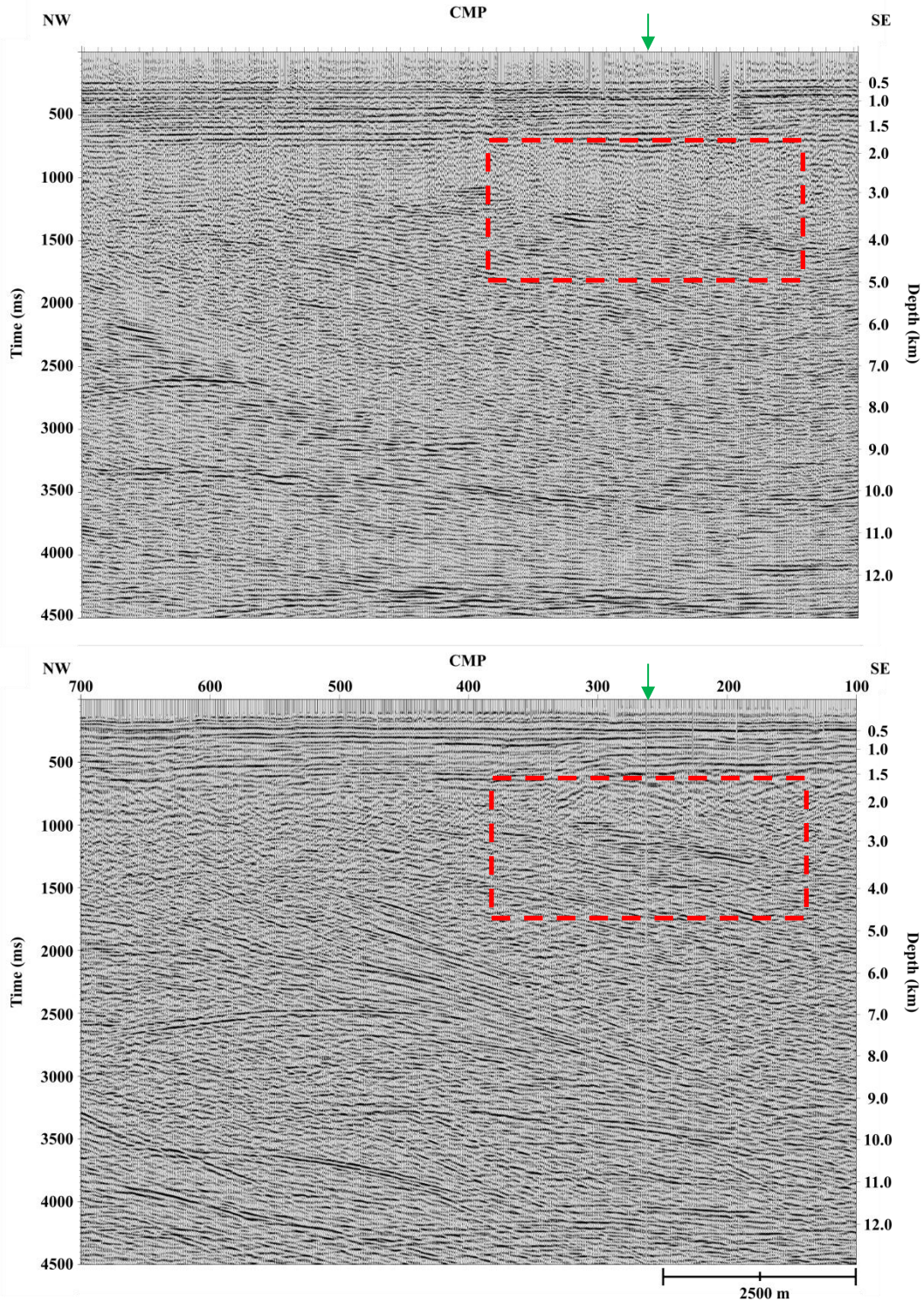


Figure 5-15. (Top) Original stacked section of TW seismic survey processed in June 1993. **(Bottom)** Re-processed stacked section of the same section in January 2013. Near-surface formations and dipping reflectors in the upper Precambrian basement (inside red rectangle) can be more distinctively interpreted in the re-processed section. Dipping reflectors might intersect the deep borehole discussed in Chapter 4 of this thesis. Green arrow indicates the position of the Hunt well projected onto the seismic section. Both sections have a vertical exaggeration of 1.2.

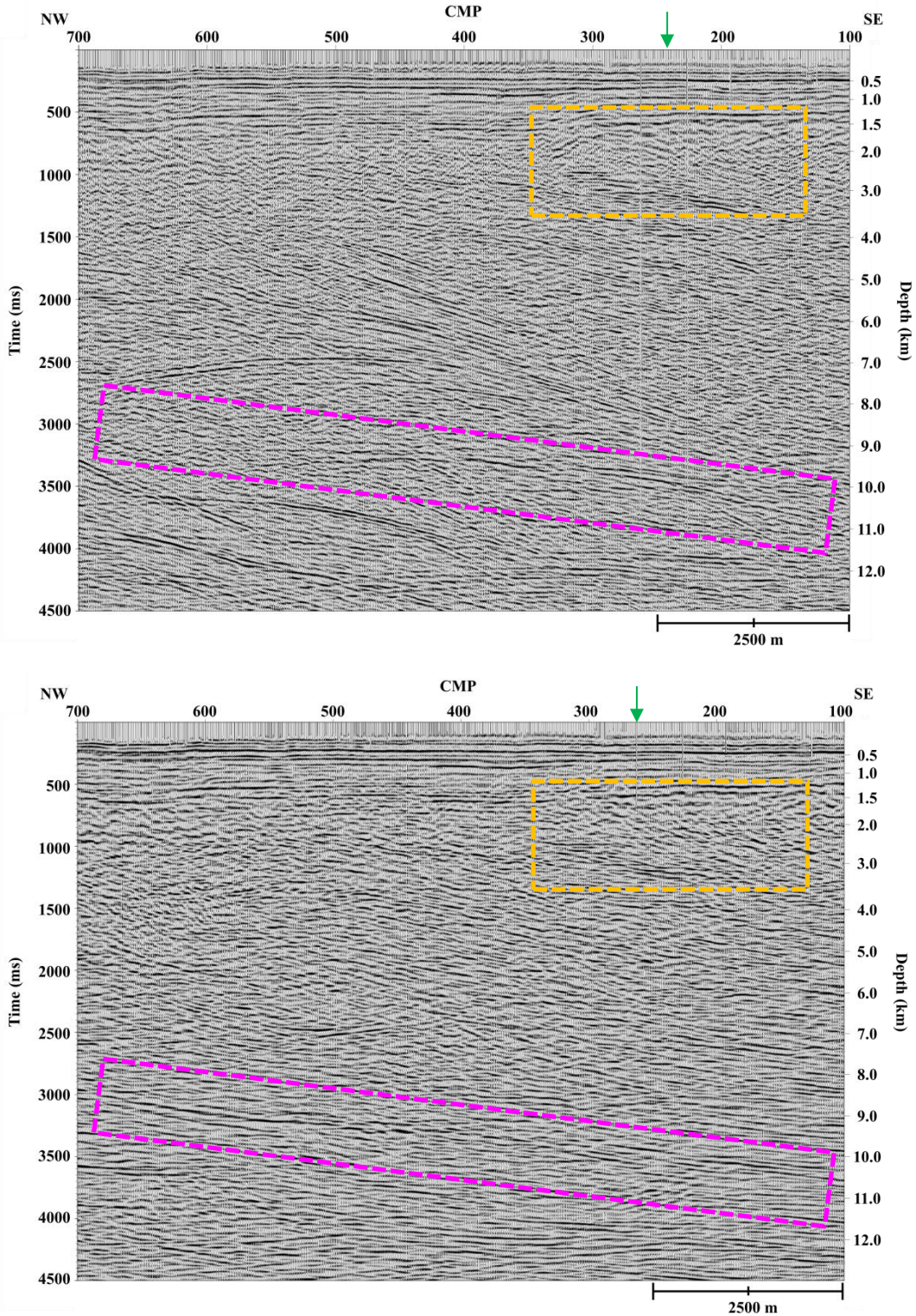


Figure 5-16. Comparison of TW seismic section before (**top**) and after (**bottom**) finite-difference migration. Green arrow indicates the position of the Hunt well projected onto the seismic section. This section has a vertical exaggeration of 1.2. Evident diffraction hyperbolae in the stacked section as convex events have been eliminated in the migrated section. Pink rectangular boxes indicate a potential eastward-dipping fault location.

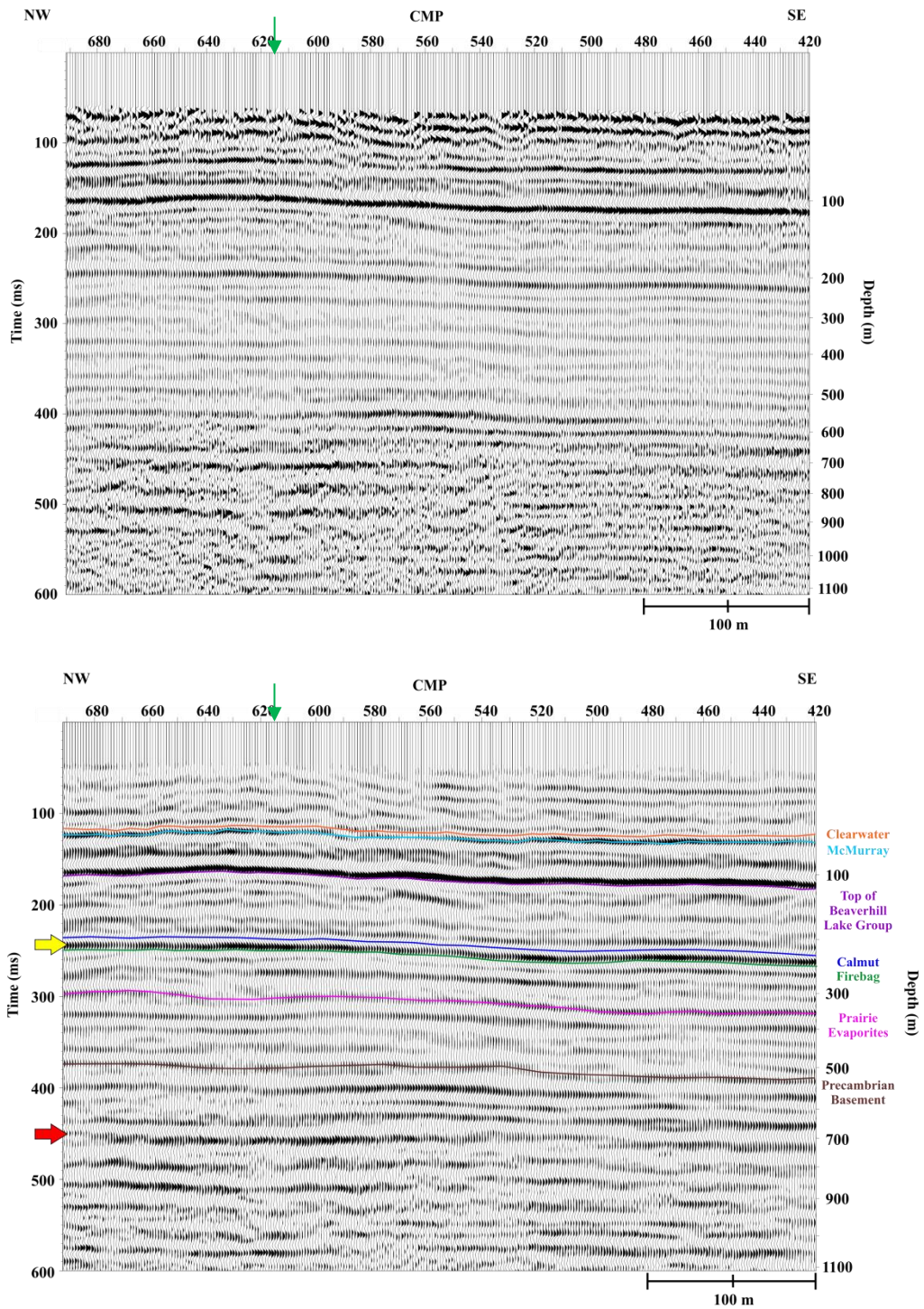


Figure 5-17. Stacked section of the TR seismic survey with a time-variant Ormsby filter applied (**top**) followed by F-X predictive deconvolution with interpreted horizons (**bottom**). Horizons in the sedimentary layers are interpreted with the aid of a synthetic seismogram from the Hunt well. The green arrow indicates the position of the Hunt well projected onto the seismic section. The yellow arrow indicates a horizon that has improved continuity and the red arrow indicates multiples that were enhanced. Both sections have a vertical exaggeration of 2.6.

5.5. Data Analysis

2D seismic reflection surveys are commonly shot for reconnaissance purposes and the necessity of 3D data is typically based on interpretations of the available 2D data. Processing sequences applied to both the TW and TR surveys focus on noise suppression in the near surface and multiple reverberations to better image geological features that could be of importance to geothermal development. This section focuses on linking the final seismic images to the geological formations and identifying any structural features visible in the subsurface. Partial seismic images with the discussed features will be displayed in the next few sub-sections. Full seismic sections are available at the end of the chapter in Figures 5-19 to 5-24.

5.5.1. Synthetic Seismograms

Seismic-to-well ties allow interpreters to compare well data (measured in depth) to seismic data (measured in time) through the use of synthetic seismograms. Density and sonic logs are used to calculate a set of reflection coefficients (RC) which are then frequency-filtered to match the bandwidth of the seismic data. Thus, the RC are dependent on contrasts in acoustic impedances (AI), which is the product of density (RHOB) and compressional-wave velocity. The synthetic seismogram involves the convolution of RC in time with a seismic wavelet. A seismic wavelet is the response of the seismic system and is defined by estimating the pulse from the real seismic data, or using a standard pulse with a defined polarity, peak frequency and phase. The synthetic seismograms were generated using the estimated pulse from each seismic survey and formations are identified by using the known well tops and their respective depths (Figure 5-18). The well logs used are calibrated using a vertical seismic profile (to be discussed in Chapter 6) to minimize any correlation errors in time between the sonic log and seismic data.

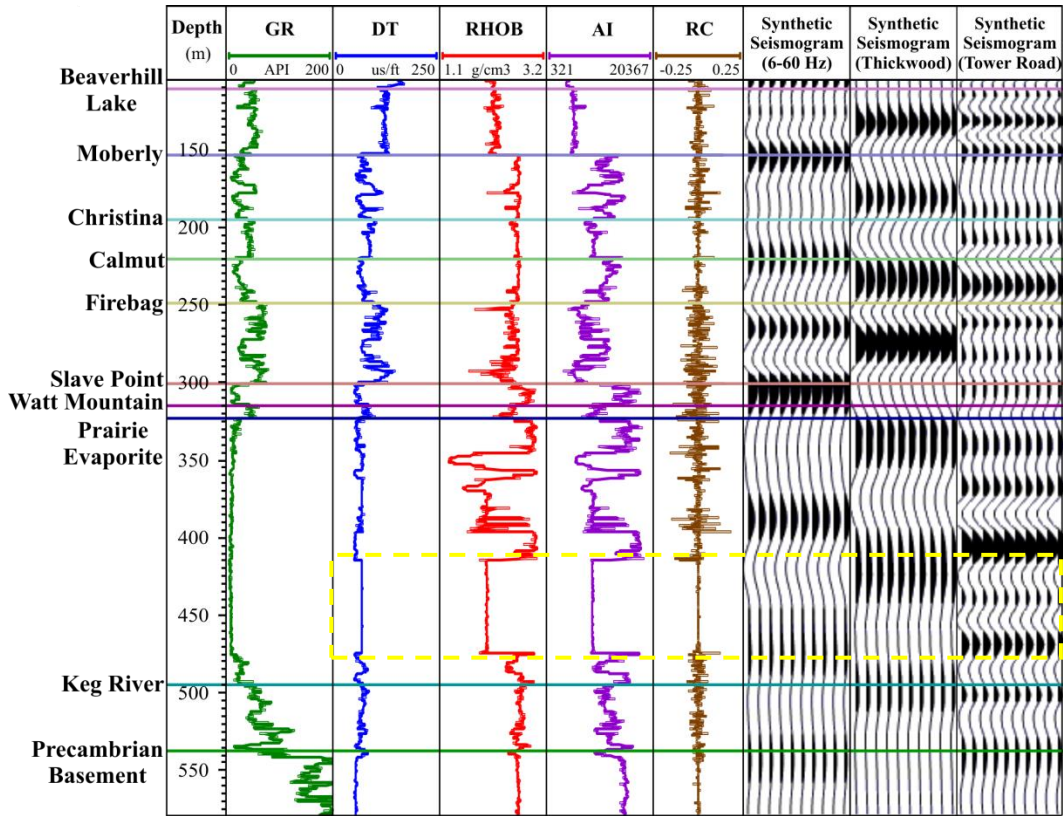


Figure 5-18. Synthetic seismograms generated using wavelet extraction from Thickwood and Tower Road seismic surveys. The associated acoustic impedance (AI) and reflection coefficient (RC) responses used to generate the synthetic seismograms are displayed on the left. Missing DT and RHOB data at 450 m depth also led to an erroneous reflector in the synthetic seismogram (yellow rectangle).

5.5.2. Horizon Interpretations

Horizons are surfaces separating two different rock layers based on reflection events in seismic sections (Sheriff, 2002). Using a synthetic seismogram generated from the nearby borehole (*i.e.* Hunt well), prominent horizons in the sedimentary layers were easily interpreted in the TR seismic section when the borehole is projected onto the seismic section (Figure 5-17). For the TW section, interpretation gaps occur toward the western part of the survey due to poor reflector continuity. Other nearby boreholes only have well logs of the Cretaceous strata for the generation of synthetic seismograms. Thus no other useful seismic-

to-well ties were available in the deeper formation layers. Horizons were mostly interpreted by copying a window of data on the east side of the survey near the borehole and superimposing it onto the west side to compare reflection patterns. Further complications arise in areas where faults are present that could affect the continuity of the seismic reflectors. The contact between the sedimentary basin and high-velocity Precambrian basement cannot be clearly identified in both seismic sections. This is due to the remnant effect of multiples that mask the true reflectors beneath the sedimentary successions. Horizon layers in the sedimentary successions and in the crystalline basement also appear to be more disturbed in the close vicinity of the borehole (Figures 5-15, 5-16, and 5-20).

5.5.3. Dipping Reflectors

The deeper seismic reflection profile (*i.e.* Thickwood survey) reveals a series of gentle to steeply dipping reflectors in the Precambrian basement (Figures 5-15 and 5-16). Existing basement studies using reflection seismic data have suggested the relation of dipping reflectors to the presence of fracture zones or mafic bodies within the crystalline rocks (Mandler and Clowes, 1997; Ross and Eaton, 1997; Mandler and Clowes, 1998; Ross and Eaton, 1999; Welford, 2004; Schmelzbach *et al.*, 2007). Some of the observed reflections on the profile are also likely representing out-of-plane reflections (side-swipes) since the 2D survey was not acquired along the geological dip orientation. In this case, normal incidence data may not represent a vertical plane and may contain geological information from out-of-plane sections.

Under the assumptions that the reflectors are in the normal incidence plane, eastward-dipping reflectors are observed at 525 ms, 700 ms and 1100 ms, which corresponds to approximately 960 m, 1450 m, and 2750 m respectively. Time-to-depth conversion was performed using the calibrated sonic time-depth curve from the zero-offset vertical seismic profile. Despite improvement in the temporal resolution of the TW data after seismic processing, the time of the intersecting reflectors are still difficult to identify precisely which leads to an approximate 100

m error. It is also interesting to note that 1450 m was also the depth in which the presence of natural fractures were verified according to the logs interpreted in Chapter 4.

5.6. Summary

Engineered geothermal system requires the development of a fractured system in the subsurface to improve the rate of fluid flow between boreholes. Drilling into the deep basement rocks is uncommon in Alberta since they are not deemed to be prospective for petroleum exploration. However, seismic reflection data offers an alternative solution to imaging the subsurface at a reduced cost and greater areal coverage compared to borehole drilling. An existing 2D seismic survey (*i.e.* Thickwood survey) reveals numerous dipping reflectors in the Precambrian basement. For logistical reasons, the older survey was acquired along the crooked Tower Road which focused on imaging the crystalline basement. Due to the crookedness of the TW profile, energy from out-of-plane can degrade the overall stacked image, and reflections in the shot gathers may also not be properly imaged. To improve the interpretation of the sedimentary successions and upper crystalline crust, a higher-frequency seismic data (*i.e.* Tower Road survey) was acquired along the same road with increased lateral resolution for the interpretation of the upper 1200 m of the subsurface.

One of the biggest concerns of the old processed data was the presence of multiple attenuation that masks the true reflectors in the upper crystalline crust. As such, seismic (re-) processing focused on both multiple and near-surface noise attenuation to improve the temporal resolution of the stacked seismic sections, including the implementation of frequency-wavenumber filtering, radial trace transform, predictive deconvolution, and time-variant filtering. The final stacked and migrated TW seismic surveys reveal eastward-dipping reflectors in the crystalline basement, with possible borehole intersection at 960, 1450, and 2750 m depth. Such dipping reflectors could play significant roles in improved permeability toward the development of engineered geothermal systems in the Precambrian basement rocks.

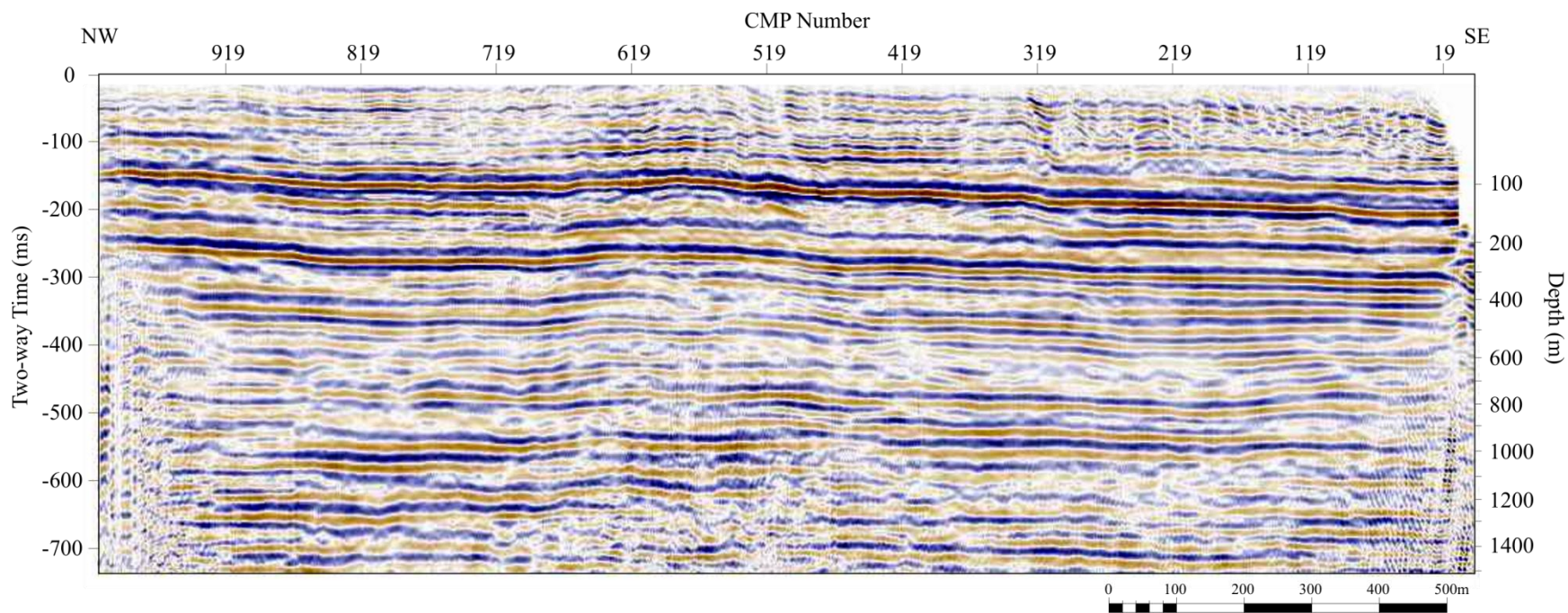


Figure 5-19. The stacked profile of the Tower Road 2D seismic survey with F-X prediction applied.

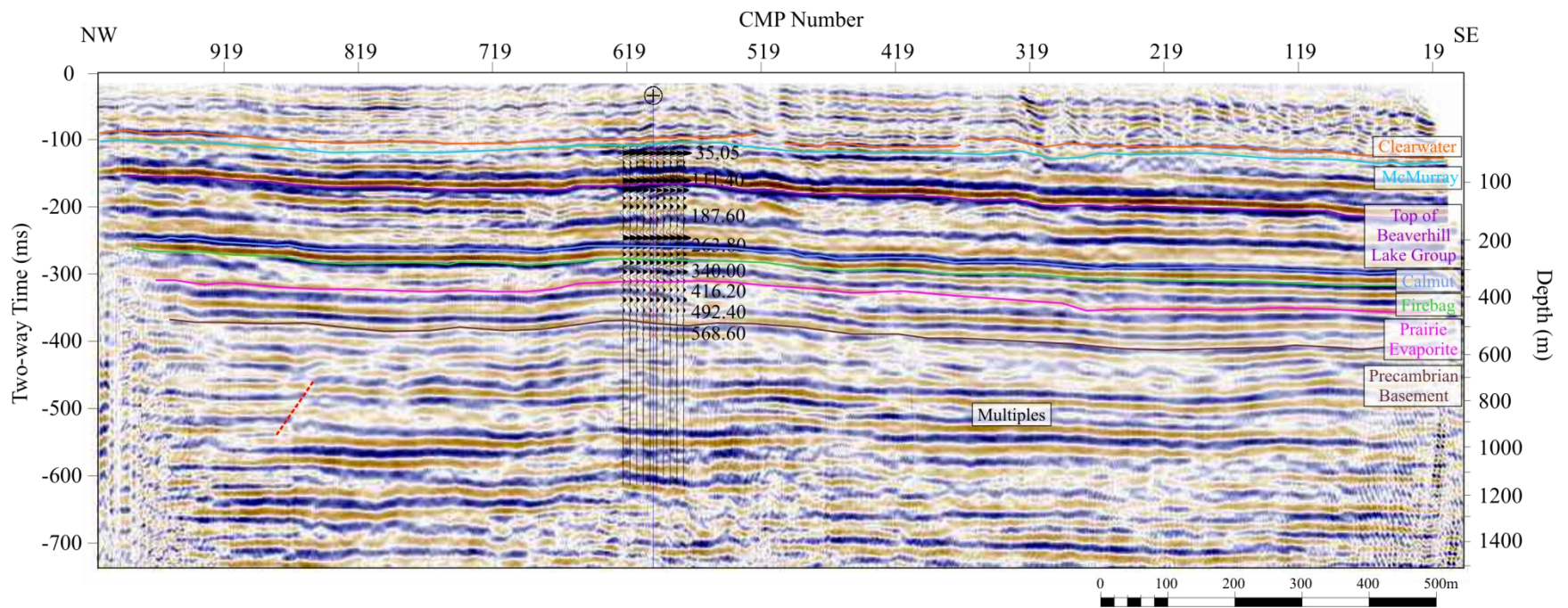


Figure 5-20. The interpreted stacked profile of the Tower Road 2D seismic survey with F-X prediction applied. The Hunt well is projected onto the profile from an offset of ~165 m.

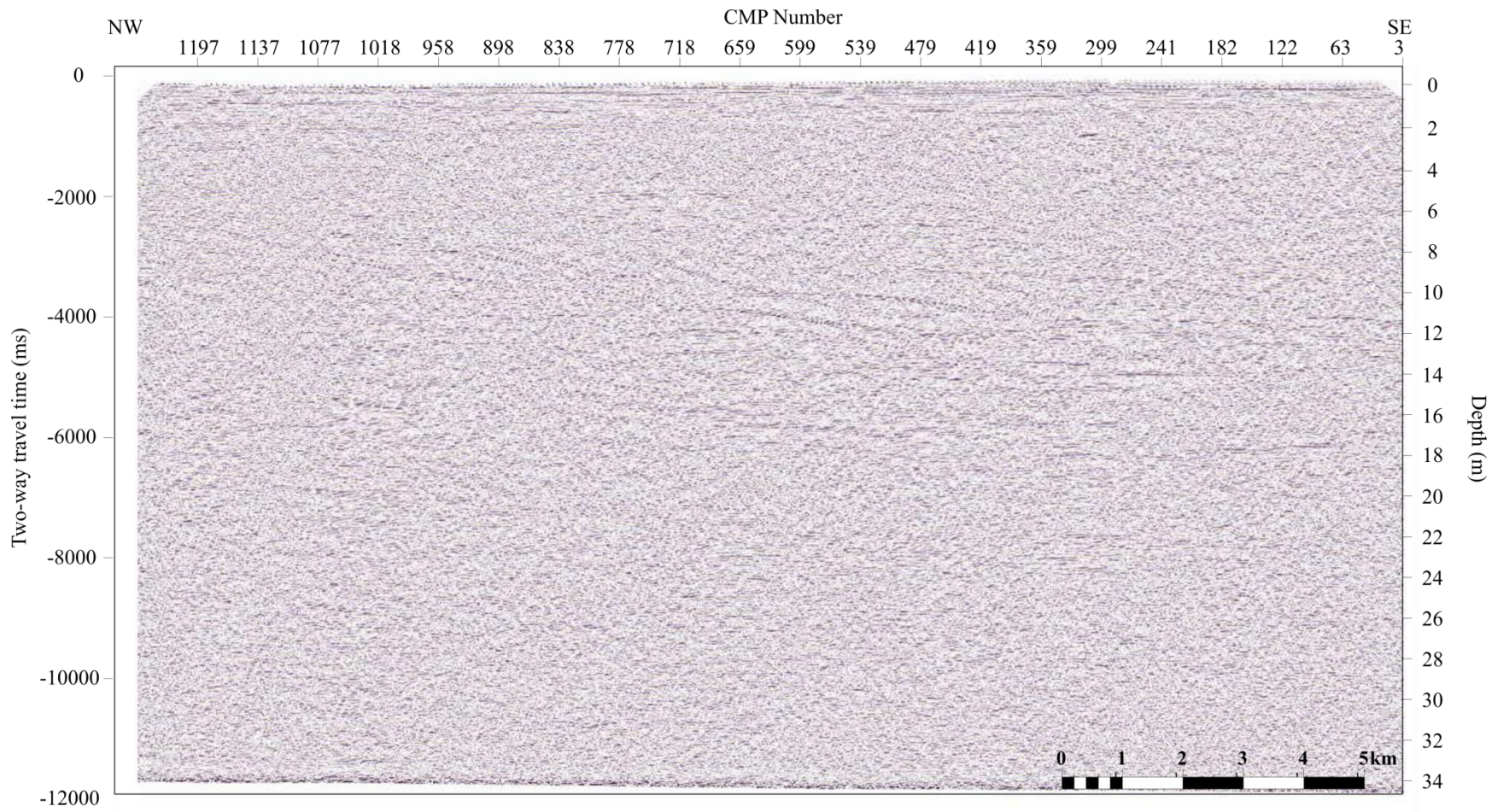


Figure 5-21. The stacked profile of the Thickwood 2D seismic survey generated using offset distances between 70 to 1000 m.

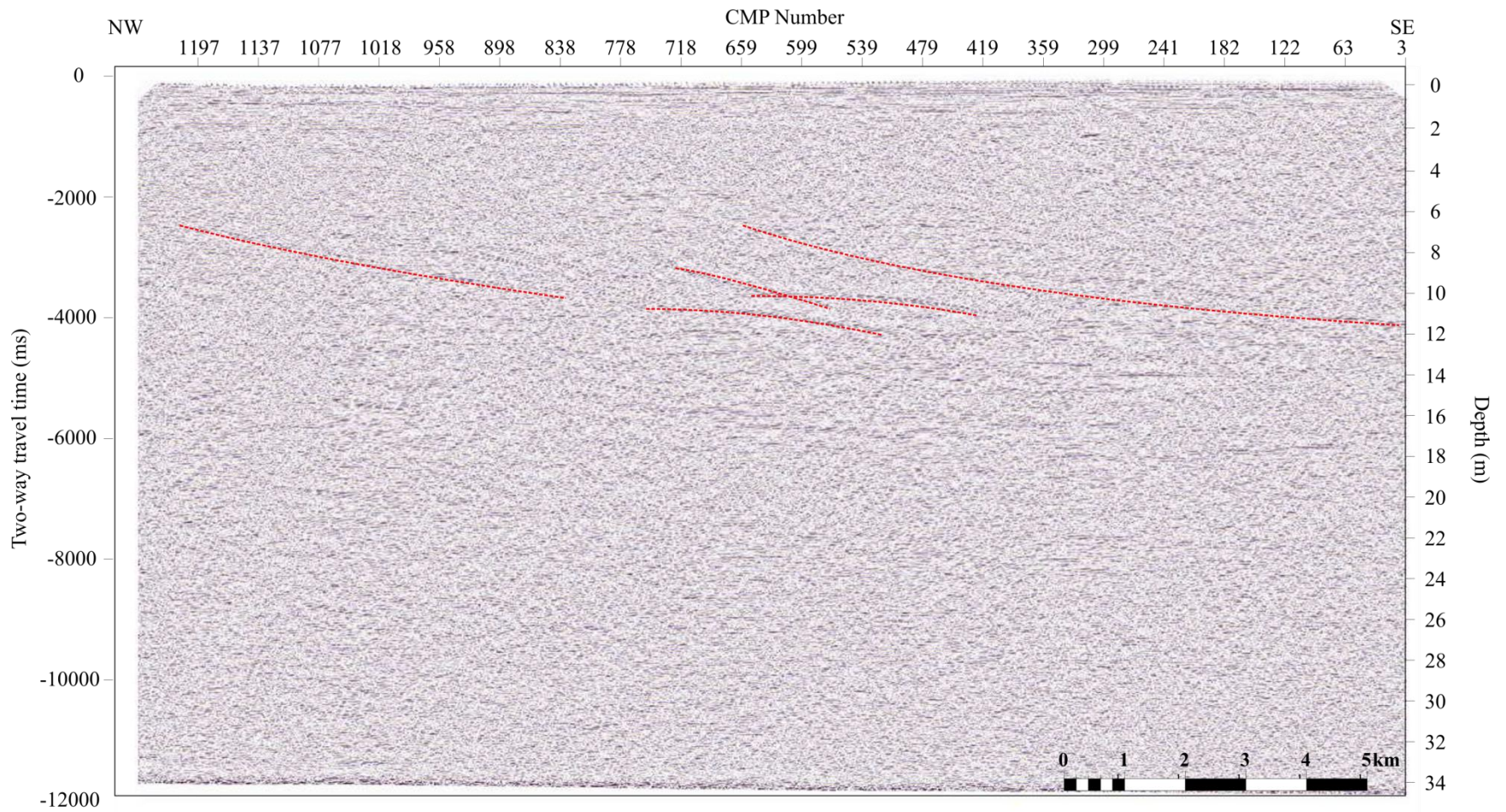


Figure 5-22. The stacked profile of the Thickwood 2D seismic survey generated using offset distances between 70 to 1000 m with interpretations.

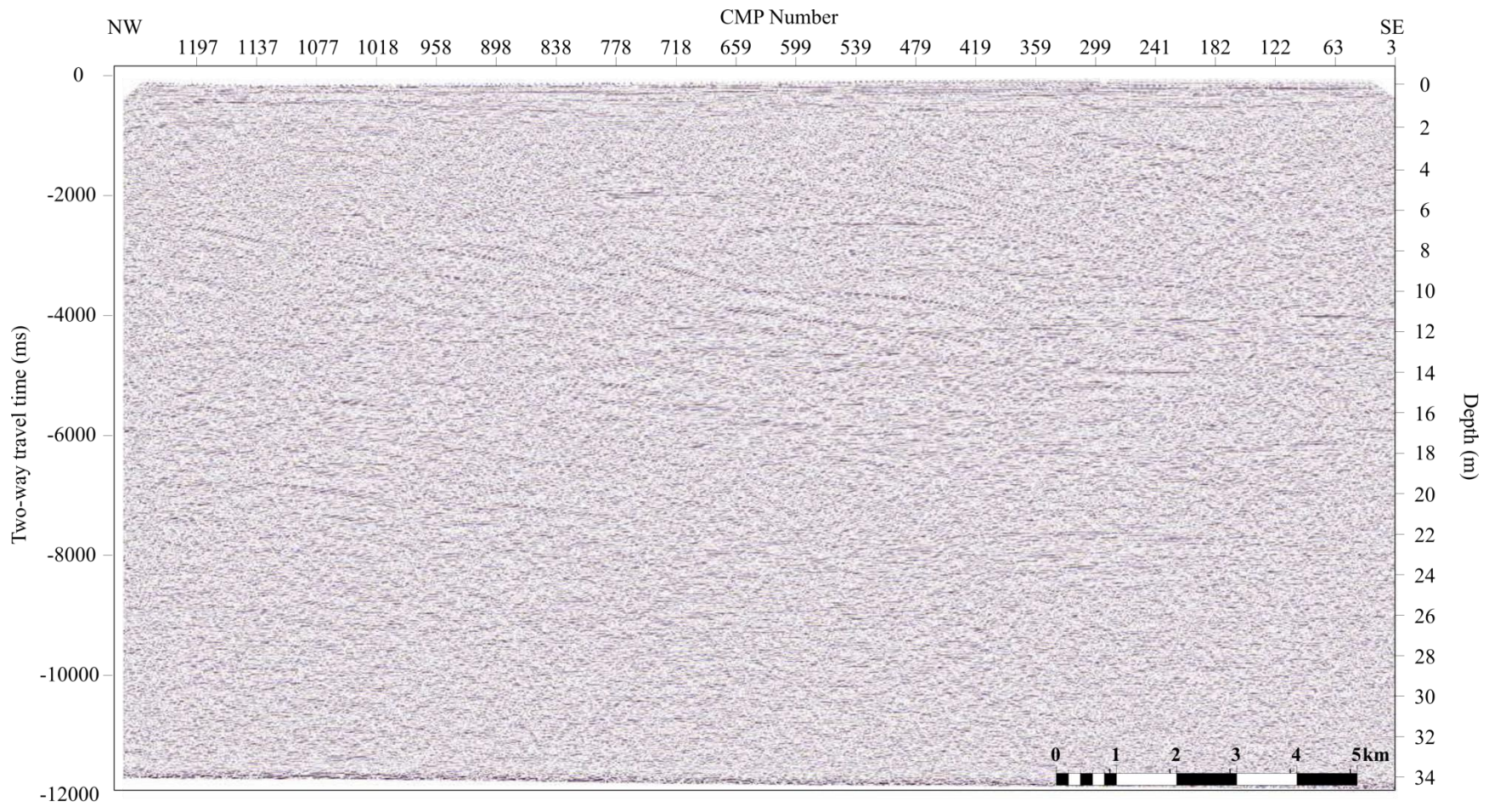


Figure 5-23. The stacked profile of the Thickwood 2D seismic survey generated using offset distances between 100 to 3000 m.

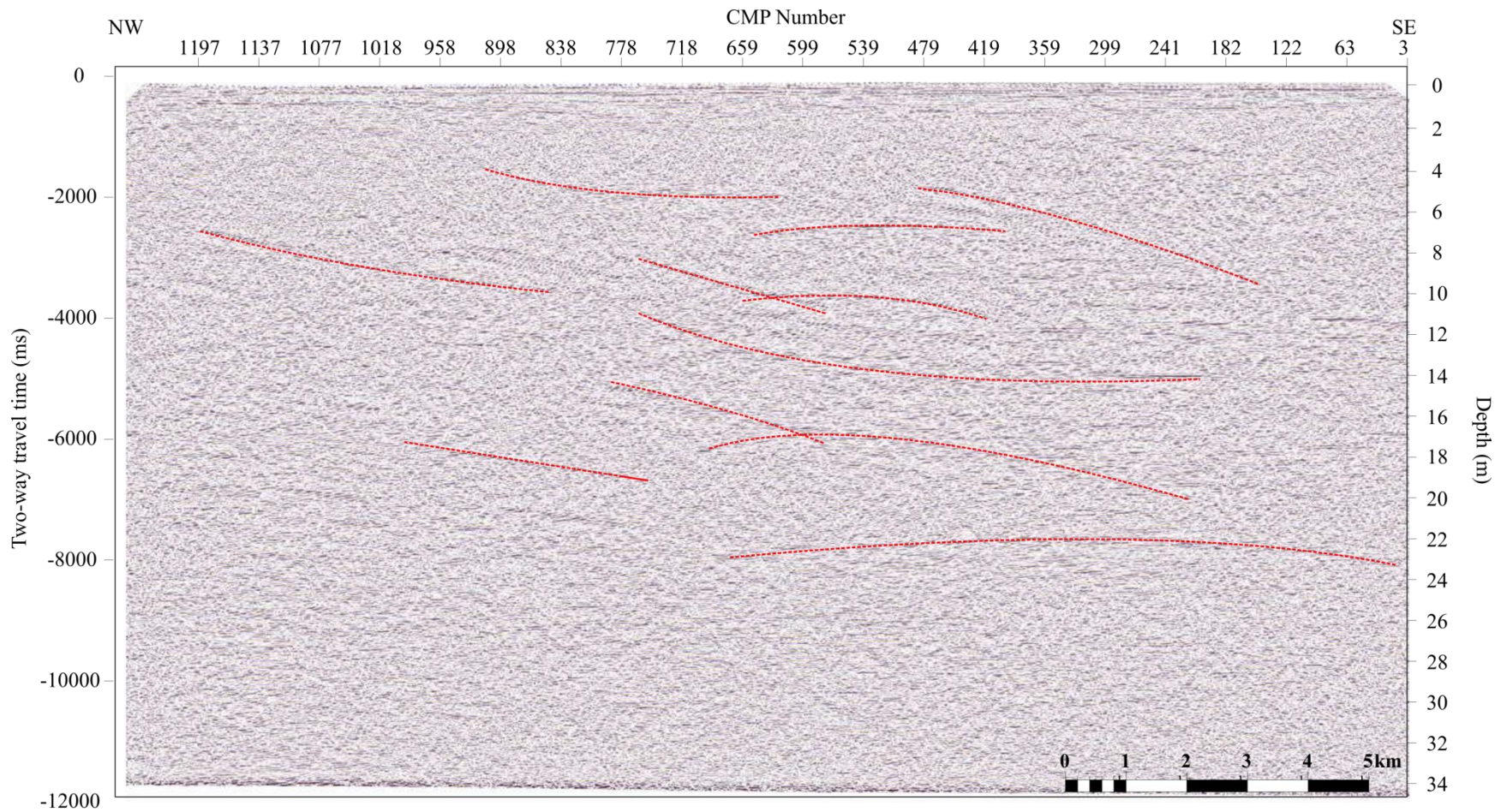


Figure 5-24. The stacked profile of the Thickwood 2D seismic survey generated using offset distances between 100 to 3000 m with interpretations. Deeper reflectors are more visible in this section using longer offsets for CMP stacking.

Chapter 6

Zero-Offset Vertical Seismic Profile

The second type of seismic methods used in this project is the vertical seismic profile (VSP). VSP responds to both upgoing and downgoing seismic events as geophones are placed directly in the borehole beneath the surface. Processing of VSP involves separating the wavefields and identifying primary upgoing events. This chapter focuses on the first VSP recording in the borehole – Zero-offset VSP. The first section of this chapter begins with an overview of this seismic method and its acquisition procedure. Subsequent sections of this chapter review the processing sequence used to generate the final VSP section and corridor stacks for interpretation. The goals of this zero-offset VSP consist of three parts: (1) to obtain a time-depth relationship for depth conversion in seismic reflection profiles, (2) to distinguish between real seismic reflectors and multiples in the seismic section using the corridor stack output, and (3) to identify fracture zones from the upgoing tube waves in the processed VSP section.

6.1. Overview

A vertical seismic profile (VSP) is a measurement in which the seismic source is generated at the surface and seismic signal is recorded by geophones secured at various depths to the borehole wall (Hardage, 2000) (Figure 6-1). This form of borehole geophysics provides *in-situ* measurements of rock properties including velocity, acoustic impedance, attenuation, and anisotropy (Stewart, 2001). Since geophones are placed directly in the borehole, VSP has a better seismic resolution compared to surface seismic profiles since the data quality is less likely to be compromised by the effect of surface layers. Frequency content of the VSP encounters less attenuation effects in the one-way travel path versus the two-way travel path in seismic reflection profiles. The one-way travel path from source to receivers leads to an enhanced image of the reflectors in the subsurface after a proper processing routine has been applied. Furthermore, the *in-situ* material

velocities are obtained and used toward relating travel time to depth in the subsurface. However, this is more restricted to the area between the seismic source and borehole location (Schmitt *et al.*, 2007). The two types of vertical seismic profiles investigated in this project are zero-offset VSP (current chapter) and walk-away VSP (Chapter 7). Seismic energy sources positioned within tens of meters of the borehole are considered to be a zero-offset VSP (Stewart, 2001).

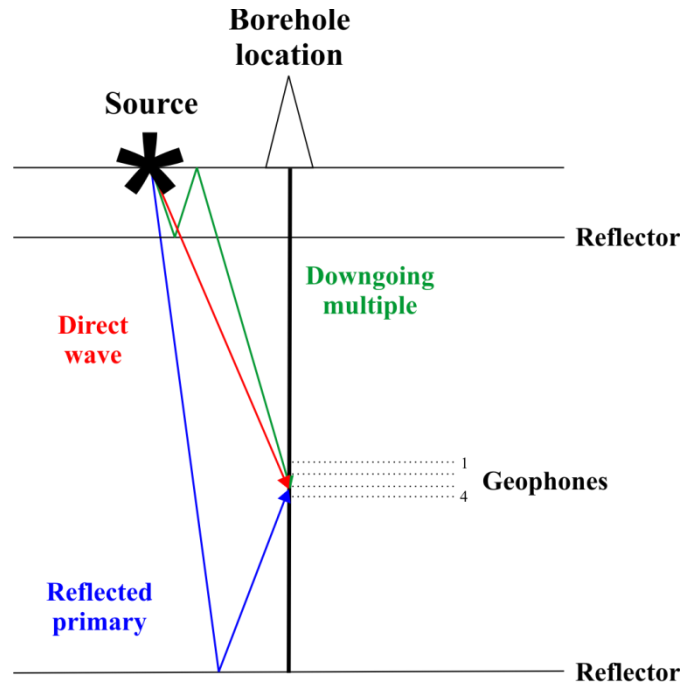


Figure 6-1. The basic components of a vertical seismic profile consist of a borehole, seismic energy source, downhole geophones lowered into the borehole, data recording system, and wireline to connect the geophones to the recorder.

6.2. Data Acquisition

A zero-offset vertical seismic profile (VSP) was conducted at the Hunt well on July 14th to 15th, 2011 and its acquisition parameters are listed in Table 6-1. Using a high-frequency MinivibTM unit (Industrial Vehicles International of Tulsa, Oklahoma) as the seismic energy source, data were logged upward from 1880 m to 5 m depth with 4 levels of receivers spaced 10 m apart recorded at 2.5 m intervals. Conventional VSPs are typically acquired at relatively large intervals of 10 m or more, an increased depth sampling of 2.5 m was taken to obtain greater

spatial resolution on the *in-situ* seismic velocities (Schmitt *et al.*, 2007). The source employed 13 s linear taper sweeps with frequencies at 10 to 160 Hz and was positioned at an approximate 27 m offset from the borehole. Each shot was repeated for the summation of shots at common depths to increase the signal-to-noise ratio of the traces.

The three-component receivers used were part of the Sercel’s SlimWave™ borehole geophone chain owned by the operational support group of International Continental Scientific Drilling Program (ICDP-OSG). Waveforms were recorded as functions of time and plotted against depth to produce the vertical profile. One important note is that this zero-offset VSP data set was acquired with a 200 ms time lag. This must be corrected prior to correlating the final corridor stack with other seismic data.

Table 6-1. Acquisition parameters of the zero-offset vertical seismic profile.

Parameter	Zero-Offset VSP
Year of acquisition	2011
Source type	6000-lb IVI Minivib™
Source elevation	404.3 m
Sweep frequencies	10-160 Hz linear
Offset distance	27 m
Receiver type	Sercel’s SlimWave™ borehole geophone chain
Geophone spacing	10 m
Number of 3C geophones sondes	4
Top measured depth (relative to KB)	5 m
Bottom measured depth (relative to KB)	1880 m
Number of measured levels	186
Sampling depth interval	2.5 m
Correlated record length	5 s
Sample rate	0.5 ms

6.3. Data Processing

The positioning of receivers in the borehole allow them to record both downgoing and upgoing wavefields directly. Downgoing wavefields are dominant in the

unprocessed VSP such that it becomes difficult to interpret the upgoing primary reflections. Furthermore, random and coherent noise in the raw data also needs to be attenuated to improve the signal-to-noise ratio of the data prior to interpretation. Similar to the seismic reflection data, vibroseis correlation is required to produce an interpretable VSP record from the raw traces (Section 5.3.2). Traces are then stacked at constant recording depth to improve the signal-to-noise ratio prior to application of the VSP processing routine. A typical VSP processing routine comprises of geometry assignment, trace editing, noise attenuation, first arrivals picking, velocity analysis, wavefield separation and corridor stack generation (Table 6-2). Since the first few steps are similar to the seismic reflection data processing sequence, they will not be discussed in this chapter. Only the vertical component of the zero-offset VSP was used in processing and analysis. Data processing was done using the VISTA™ Seismic Data Processing software package provided by GEDCO.

6.3.1. Data Quality

An inspection of the raw VSP traces reveals both downgoing and upgoing wave modes which overlay one another. Similar to seismic reflection data, VSP data are also subjected to amplitude decay effects including spherical divergence, transmission losses, scattering and absorption that would need to be corrected by a gain function. The amplitude spectrum of the VSP data reveals broad frequency range due to the decrease in seismic wave attenuation in the one-way travel paths (Figure 6-2).

Strong amplitude events are referred to as downgoing waves which travel directly from the source to the receivers (Figure 6-3). Such events are so strong that the primary upgoing reflections particularly in the sedimentary layers are, hardly visible in the VSP section. The first arrival downgoing events are used to develop a detailed velocity profile for the borehole with data points at every 2.5 m. Upgoing events traveling from the source to receivers via major impedance boundaries were recorded by the receivers located at those boundaries.

VSP can be conducted in both open and cased hole environments. However, cased holes are often preferred due to the mechanical clamping mechanism to maintain tool stability and geophones are protected from sloughing and differential pressure sticking problems (Stewart, 2001; Gadallah and Fisher, 2005). This allows proper seismic coupling between the geophones and the steel casing or the borehole wall.

The seismic traces are more noisy below 1006 m in the open hole environment. Borehole rugosity, as indicated by the caliper log at 1140 m to 1405 m depth, affects the clamping of the geophone to the formation which resulted in weaker recorded signals (Figures 4-11 and 6-3). Another problem was the arms of the tool were too short and could not properly lock the tool in place in the wide open hole section. Tube waves can be created by compressional body waves when they encounter strong impedance contrasts within a borehole, such as casing point or change in borehole diameter. The strongest upgoing waves displayed in Figure 6-3 originated at 1006 m and 1654 m and can be attributed to the change in borehole diameter as indicated in Figure 2-6.

Table 6-2. Processing sequence for the zero-offset vertical seismic profile.

Processing step	Justification
Geometry set-up and trace editing	Prepare data for processing and eliminate bad traces
Vibroseis correlation	Correlate vibroseis trace with the sweep wavetrain
Stacking at constant recording depth	Increase signal-to-noise ratio with repeated recording at common depth
Component separation	Separate X, Y, Z component
First arrival picking	Calculate interval velocity and generate time-depth relationship
Gain correction	Compensate for energy losses
FK filtering	Minimize the effect of tube waves
Median filtering	Separate downgoing and upgoing wavefields
Deconvolution	Remove multiples from upgoing wavefield
Corridor stack	Apply vertical summation to yield a single stacking trace emphasizing upgoing events

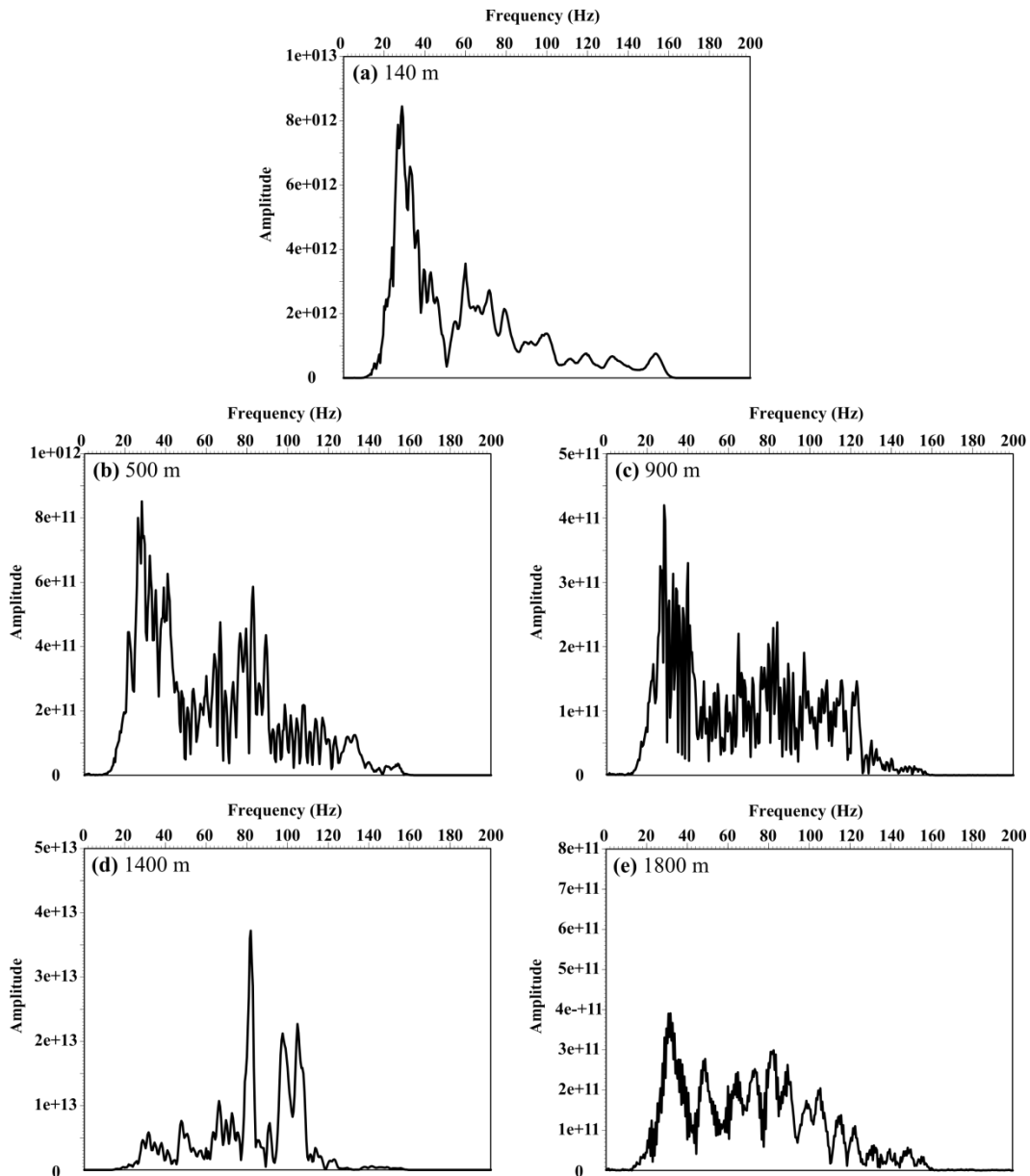


Figure 6-2. Frequency spectrum of the zero-offset vertical seismic profile at various depths. Receiver depths (a) and (b) are located in the sedimentary successions, where frequencies are dominant between 10 Hz to 50 Hz. Receiver depths (c) to (e) are located in the metamorphic crystalline basement and the frequency spectrum shows greater amplitude variations, especially at depth (d) where the data is affected by noise contamination.

6.3.2. Wavefield Separation

To separate the upgoing and downgoing events from the seismic data, various numerical procedures can be applied to attenuate the downgoing modes without seriously affecting the upgoing events (Hardage, 2000). Existing methods employed in wavefield separation include frequency-wavenumber filtering (*e.g.* Yilmaz, 2001), median filtering (*e.g.* Hinds *et al.*, 1996; Hardage, 2000), radial trace filtering (*e.g.* Henley, 2000) and tau-p filtering (*e.g.* Moon *et al.*, 1986). The two methods tested on the zero-offset VSP data are: frequency-wavenumber filtering and median filtering. The latter method was selected to be the more optimal wavefield separation method for this data.

The basic theory of frequency-wavenumber (f-k) filtering has already been discussed in Section 5.3.8.1. When downgoing energy is arbitrarily defined as having a positive propagation velocity, downgoing waves are expressed by the positive wavenumbers in the f-k domain after a Fourier transformation. Conversely, upgoing events are transformed into the negative quadrant of the f-k domain (Figure 6-4). The segregation of VSP events into two different planes of the f-k space allows the design of a velocity filter to suppress the downgoing events (Hardage, 2000). However, a narrow velocity pass band filter can create severe spatial mixing of upgoing events. This becomes problematic as the depths of VSP events are more difficult to determine.

An alternative wavefield separation method is median filtering (Figure 6-5). Median filtering is considered as a data smoothing filter by selecting the middle value of an ascending-ordered sequence of numbers from a moving window of input data (Stewart, 1985; Hardage, 2000). Data is first shifted to vertically align downgoing events in the VSP data using the first break arrivals. The first arrivals (downgoing waves) are then enhanced vertically as a function of depth at a fixed recording time using a selected median filter along the depth axis. A root mean square (RMS) scaling was also applied such that the RMS energy is the same for all traces. After shifting the data back to its original position, the smoothed and scaled downgoing wavefield is then subtracted from the original VSP data which

results in its removal and only the upgoing wavefield remains. This arithmetic subtraction method is considered to be extremely effective as the median filter honors any discontinuity of the data (Stewart, 1985). Anomalous noise spikes are removed without interfering with the overall quality of the VSP data. Two major advantages of using the median filter are its ability to reject noise spikes and to pass step functions (*i.e.* discontinuities in the data) without smearing the edges. One important note in the wavefield subtraction process is that first break times must be interpreted carefully to minimize any static time shift error in the wavefield separation (Stewart, 1985; Hardage, 2000). A 19-point median filter was applied to the zero-offset VSP data to enhance the downgoing waves. A separate 5-point median filter was applied to display the two-way travel time of the upgoing wave (Figure 6-6).

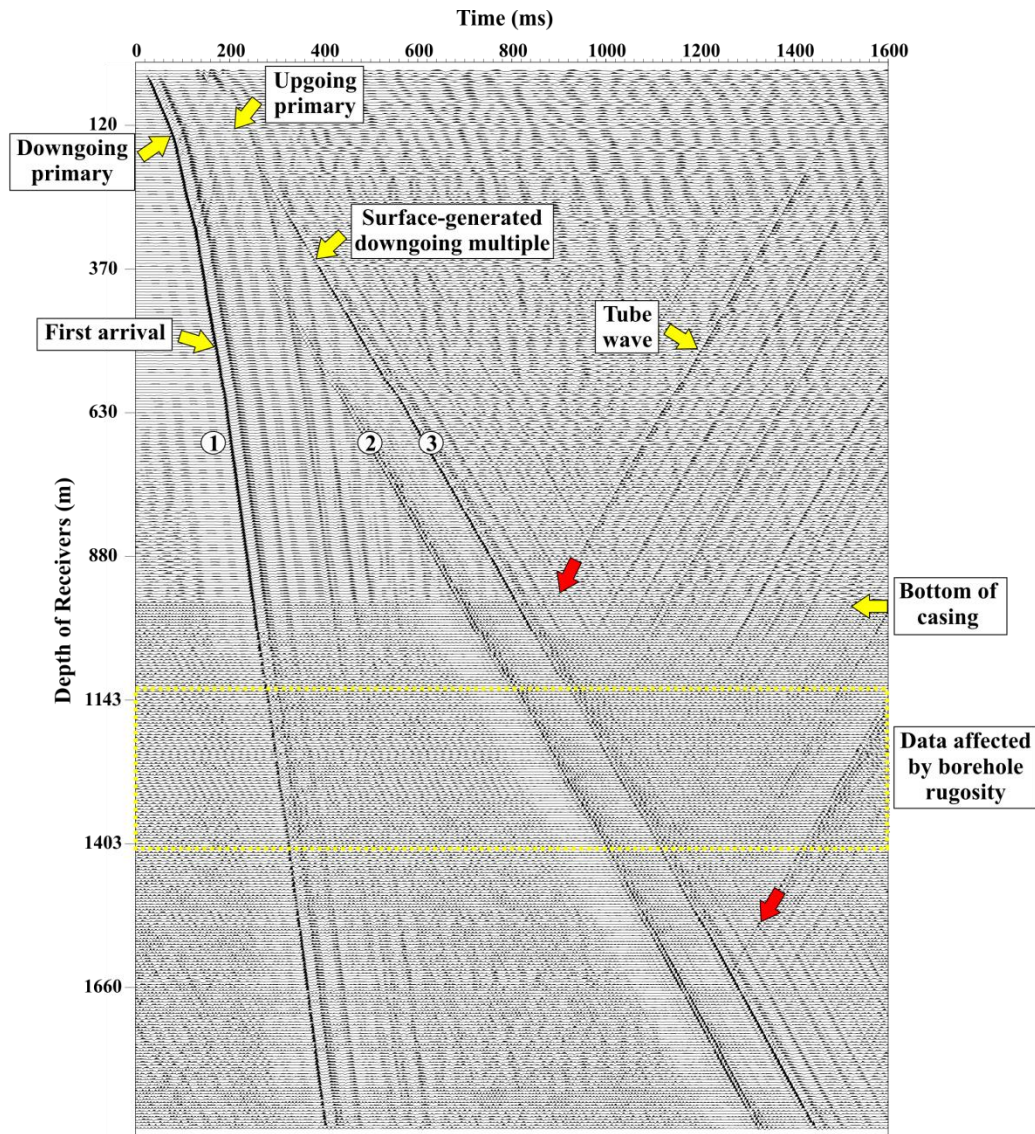


Figure 6-3. Display of zero-offset vertical seismic profile after stacking traces at the common depth and applying an automatic gain function. Examples of upgoing tube waves are marked by red arrows and will be further discussed in Figure 6-12.

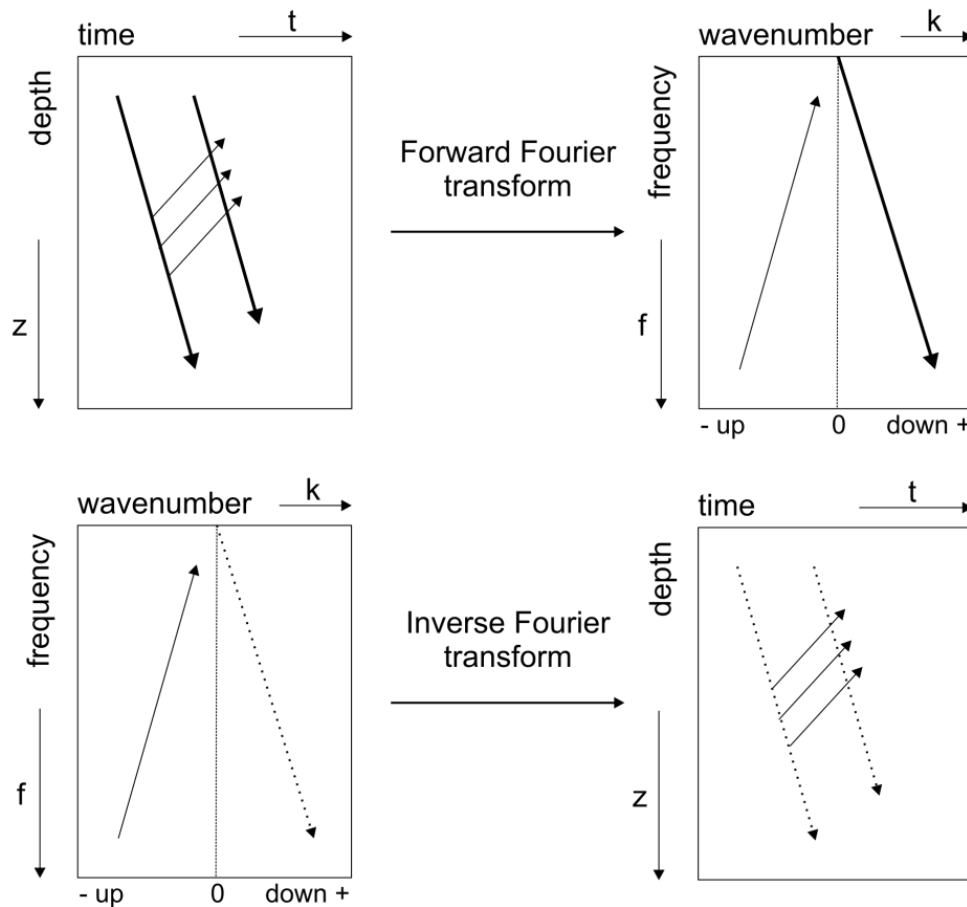


Figure 6-4. The concept of frequency-wavenumber (f-k) filtering. The original VSP data is displayed in depth and time with downgoing events shown as thick arrows. Upgoing events are displayed by the thin arrows. After the application of a Forward Fourier transform, upgoing events are displayed in the negative half plane and downgoing events in the positive half plane. The positive half plane is multiplied by a small number to attenuate the downgoing events followed by an inverse Fourier transform. Upgoing events are now more apparent than the downgoing events in the depth-time display (Hardage, 2000)*.

* Reprinted from Vertical Seismic Profiling: Principles, Hardage, B. A., pg. 217, Copyright Elsevier, with permission from Elsevier.

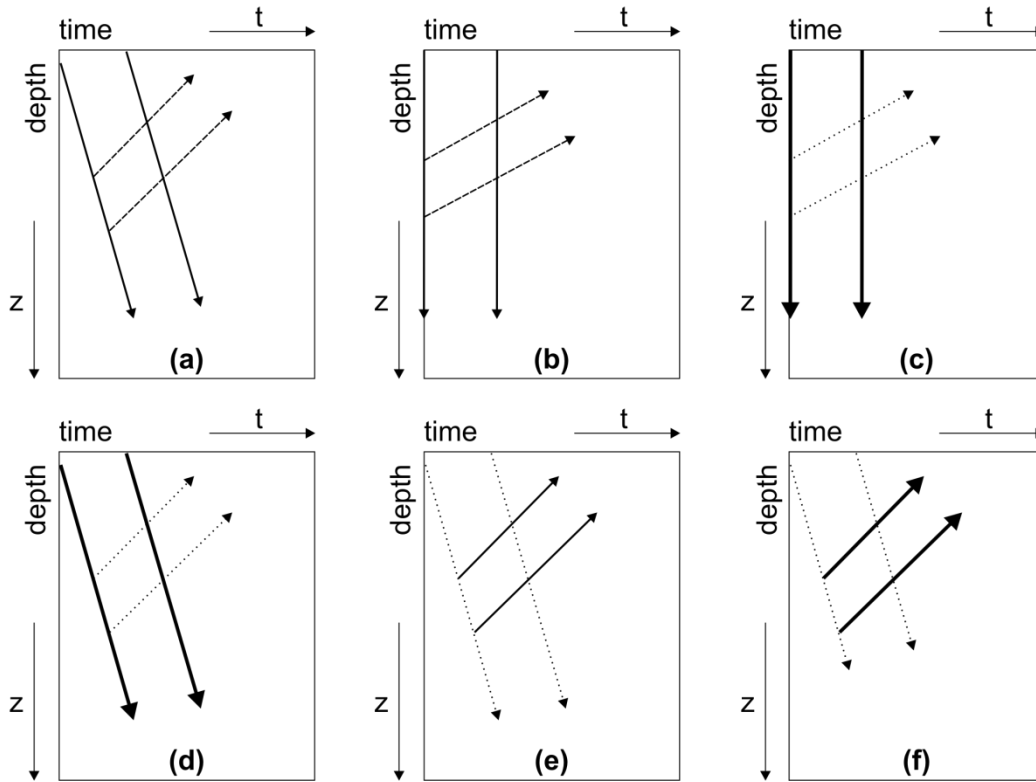


Figure 6-5. Separation of downgoing and upgoing waves in VSP data using median filtering method and arithmetic subtraction. **(a)** Original VSP data is displayed in depth-time format. **(b)** Data undergoes static correction such that downgoing events are aligned vertically. **(c)** Smoothing and enhancement of downgoing events using a median filter along the depth axis. **(d)** Data is shifted back to the original alignment after processed with a median filter. **(e)** Downgoing events are attenuated and upgoing events are enhanced by subtracting processed data in (d) from (a). **(f)** Upgoing events are emphasized by applying another median filter along the step out direction (Hardage, 2000)*.

* Reprinted from Vertical Seismic Profiling: Principles, Hardage, B. A., pg. 231, Copyright Elsevier, with permission from Elsevier.

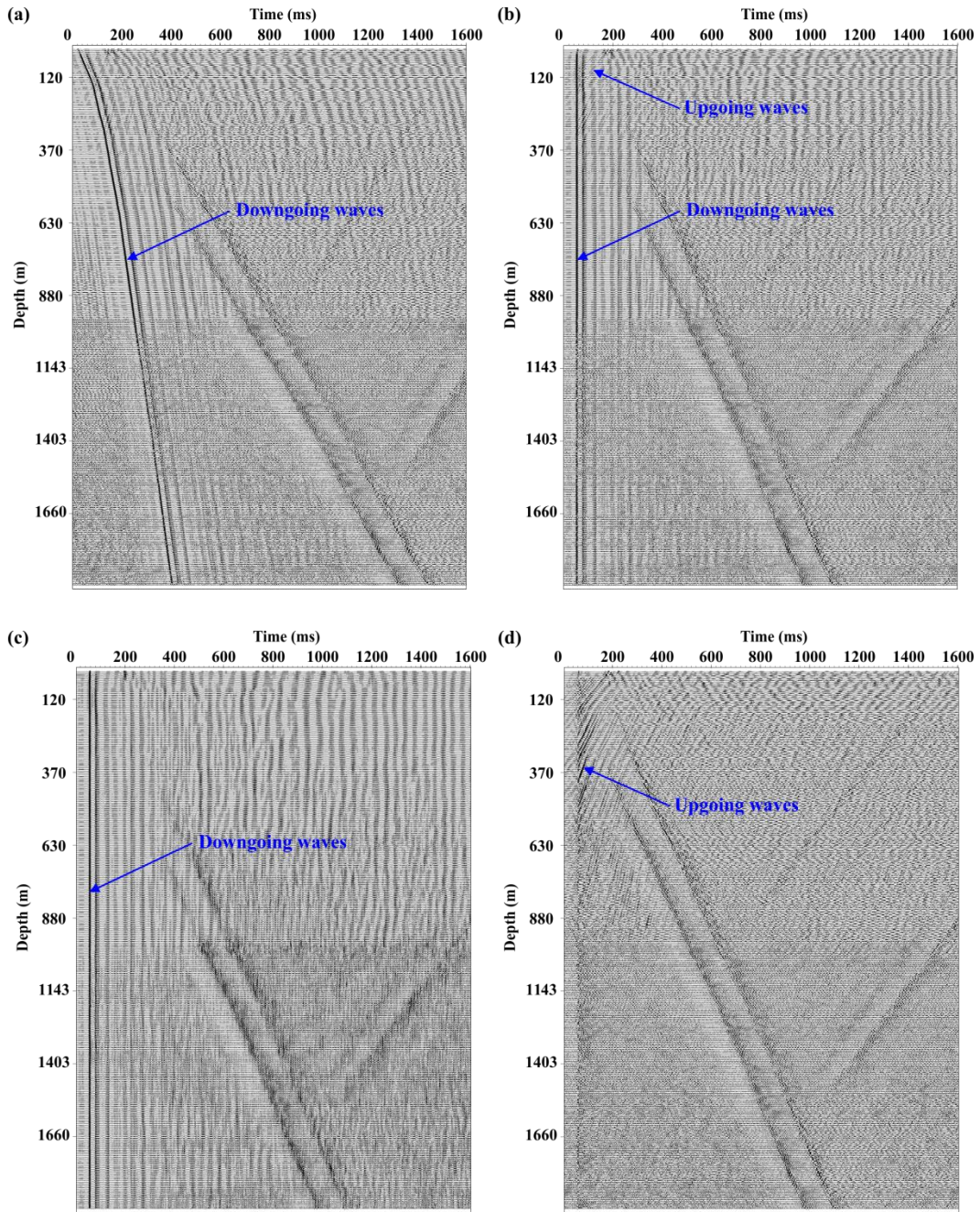


Figure 6-6 (a) to (d). Figure caption on next page.

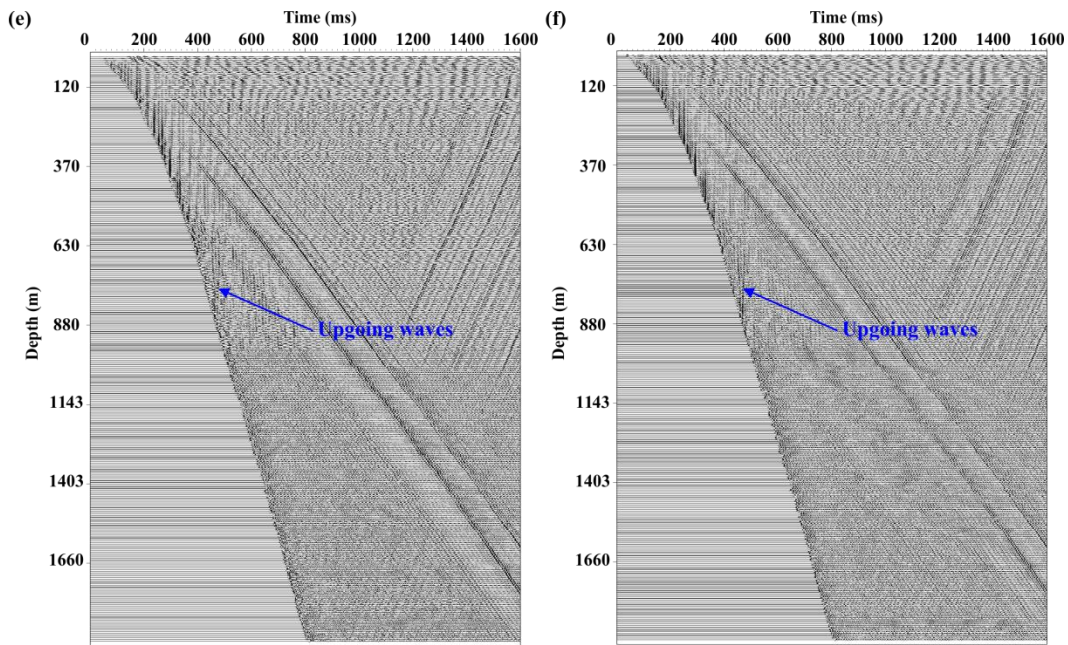


Figure 6-6. Wavefield separation of zero-offset VSP data collected at the Hunt well using the vertical component. **(a)** Data after noise attenuation and amplitude compensation. **(b)** Downgoing waves are flattened after statics correction followed by a 19-point median filter to separate events into **(c)** downgoing and **(d)** upgoing waves. **(e)** Upgoing waves are flattened and displayed in two-way travel time. **(f)** A VSP deconvolution is performed to enhance the upgoing events observed in (e).

6.3.3. Deconvolution

Since geophones are placed in the subsurface in a VSP survey, they record both the downgoing wavefield which includes the source signature, such as multiples and attenuation, as well as the upgoing wavefield. After wavefield separation has been performed, the downgoing wavefield is used to design deconvolution operators for removing multiples from the upgoing wavefield since it has stronger signal strength than the upgoing wavefield (Hardage, 2000). The deconvolution operator is designed by choosing a start and end window. A 200 ms operator length was chosen for the zero-offset VSP data using the downgoing wavefield. This small design window helps to minimize any noise contamination in the design filter. The VSP deconvolution command in the VISTA™ software works

by using the data immediately behind the first breaks. The auto-correlations of these data are then summed and a minimum phase (spiking) operator is derived for the “average” autocorrelation (GEDCO, 2010). The derived operator is then convolved with the upgoing wavefield to suppress multiples (Figures 6-7 and 6-8). After deconvolution, a static time shift according to first break arrivals is applied to convert the one-way travel time of the VSP into a two-way travel time to facilitate comparison between borehole seismic and seismic reflection profiles. This also allows workers to accurately identify the depth of reflectors.

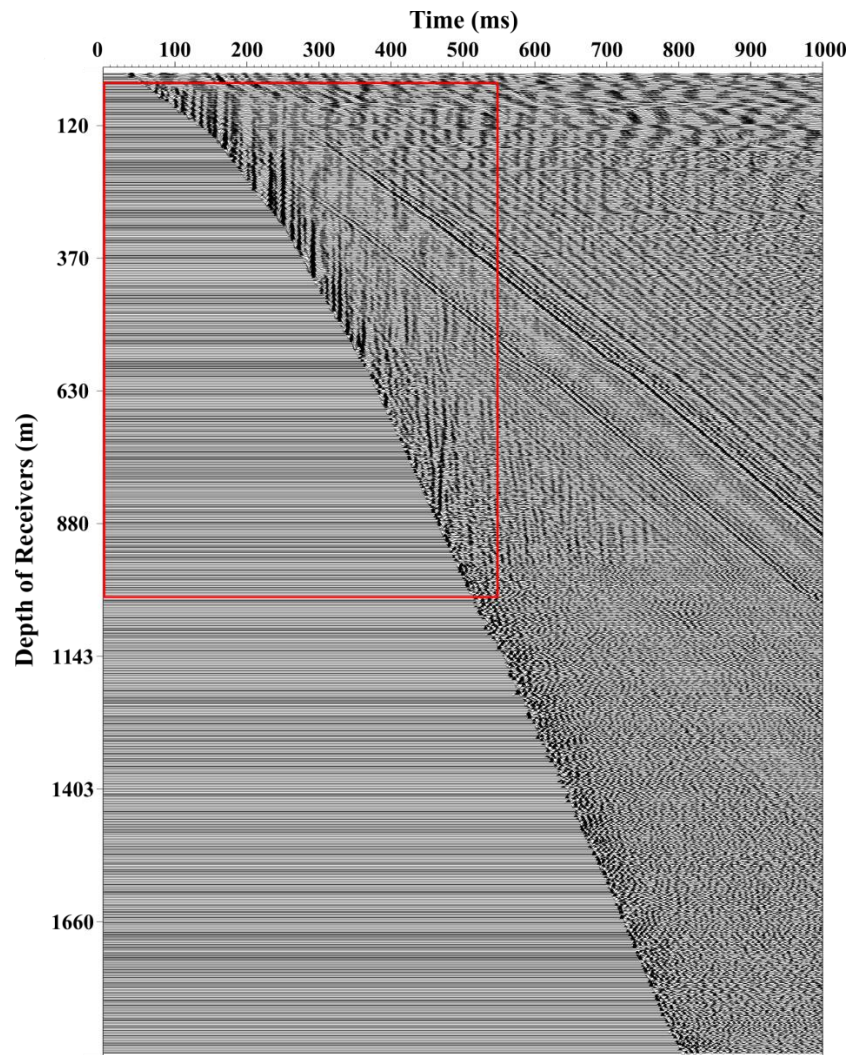


Figure 6-7. Upgoing wavefield after deconvolution in two-way travel time. Reflectors in the sedimentary layers become more apparent compared to the raw VSP shown in Figure 6-3. The section within the red box is enlarged in Figure 6-8.

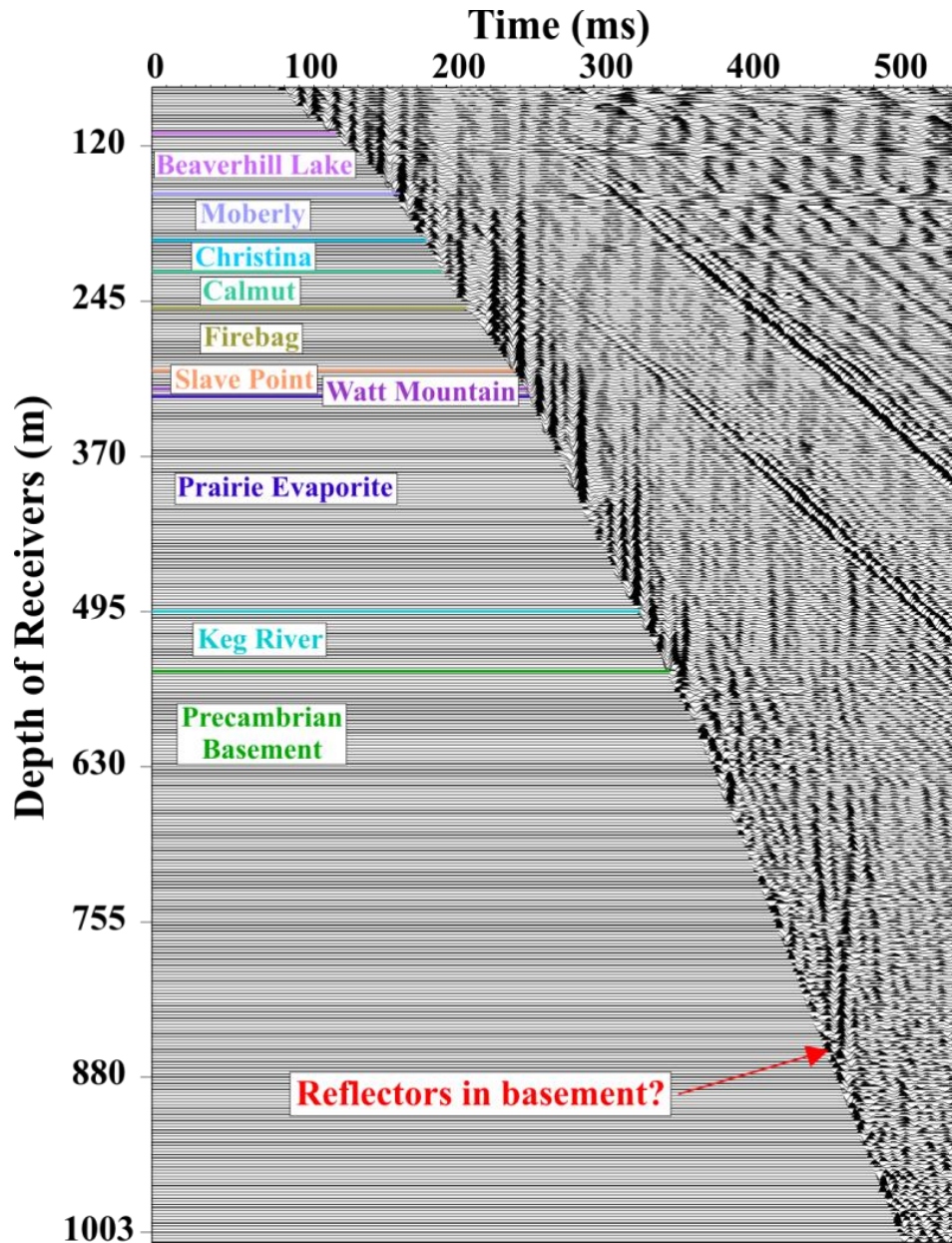


Figure 6-8. Upgoing wavefield after deconvolution in two-way travel time in the cased hole section. Reflectors in the sedimentary layers become more apparent compared to the raw VSP shown in Figure 6-3 and are labelled according to their formation layers.

6.3.4. Corridor Stack

A corridor stack is a vertical summation procedure that sums the set of time-shifted traces to yield a single trace containing all upgoing events (Hardage, 2000; Sheriff, 2002). For display purposes, each trace is plotted repeatedly in the same track (Figure 6-9). Vertical summation is performed on the outside corridor data window (Hardage, 1985). This outside corridor window contains data beginning from a slight delay of first-break time and processors select the end time with equal time lines at each trace. It is expected to contain only primary reflections and any interbed multiples with periods less than or equal to the length of the time window (Burton and Lines, 1996) (Figure 6-10). It is also based on the assumption that the reflectors are flat and horizontal.

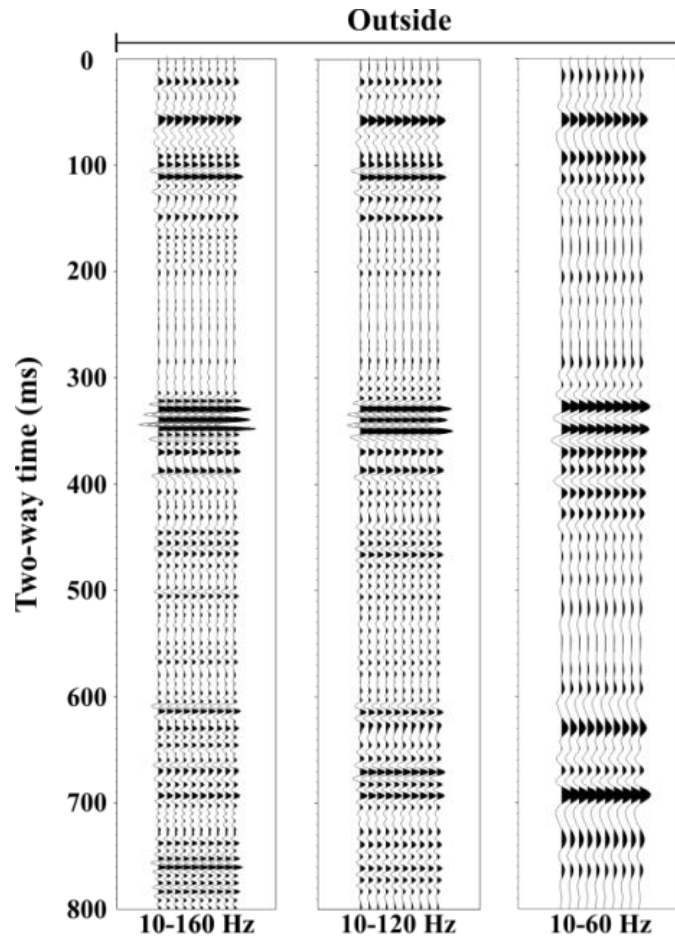


Figure 6-9. Outside corridor stacks of a zero-offset VSP containing mostly primary reflections.

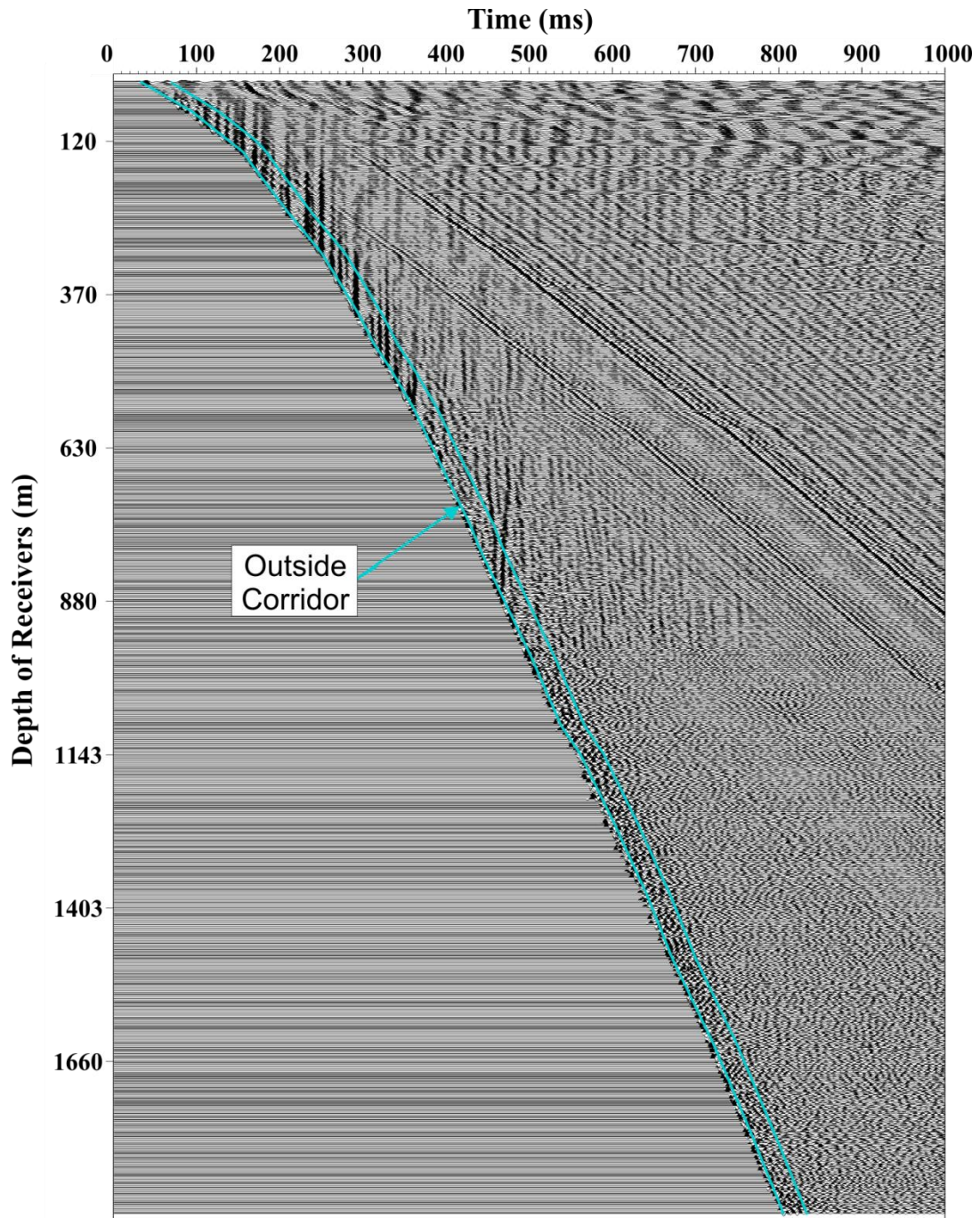


Figure 6-10. The 25 ms outside corridor zone selected for corridor stacking of the zero-offset VSP.

6.4. Data Analysis

A processing workflow was applied to the zero-offset vertical seismic profile to assist in the interpretation of seismic reflection data and borehole logs. Data analysis is performed to extract information focusing on the velocity profile and understanding the origin of tube waves. The quality of traces in the Precambrian basement was degraded due to the rugosity of the borehole leading to poor coupling between geophones and the borehole wall. Corridor stacks generated in the final steps of data processing (Section 6.3.4) remain noisy in the basement section. Thus using them for the differentiation between primary reflections and multiples is questionable. However, they are still valuable for the interpretation of horizons in the sedimentary successions in the upper 300 ms where the borehole contains the steel casing thus provides better geophone coupling.

6.4.1. Velocity Profile

First break times were selected on the vertical component traces manually since automated time picking becomes more complicated when noise is present in the traces. The zero-crossing point from trough to peak was used as the selection criterion for the first breaks. The presence of amplitude noise can result in a smeared first arrival and affects the accuracy in the travel time determination. *In-situ* interval velocities were determined from the travel times and plotted in Figure 6-11 for comparison with other sonic log measurements, including full-waveform sonic and dipole shear sonic imagerTM logs from Chapter 4. Sonic logging provides measurements of interval velocities at higher frequencies (approximately 20 kHz) and penetration depth of a few centimeters. Initial comparison of sonic log velocities to VSP velocities is difficult due to the frequency dispersion resulting from both scale and rock property dependent effects (Sams *et al.*, 1997; Schmitt *et al.*, 2007) . There is a significant amount of variation in VSP interval velocity as minor fluctuations in the first arrival pick could easily cause variation in the velocities at the measured interval of 2.5 m. This error is reduced using larger intervals in the velocity calculation at the cost of reduced resolution. This

step is facilitated by smoothing the interval velocities using a variety of averaging methods including a simple arithmetic mean (V_A):

$$V_A(z) = \frac{\sum V_p(z_i)}{N} ; \quad (6-1)$$

a long-wavelength approximation, assuming a constant velocity medium, known as Backus average (V_B) (Backus, 1962; Rio *et al.*, 1996):

$$V_B(z) = \left[\frac{\sum V_p^{-2}(z_i)}{N} \right]^{-1/2} ; \quad (6-2)$$

a high-frequency, ray theory time or harmonic average (V_W) (Schmitt *et al.*, 2007):

$$V_W(z) = \frac{N}{\sum V_p^{-1}(z_i)} ; \quad (6-3)$$

where N is the number of sonic velocity samples over the range of depths centered on a specific depth (z). Using a least-squares fit, an estimation of the local tangent slope of the travel time curve was also calculated. A 100 m depth range was selected for the above averaging techniques. V_B and V_W represent the expected low and high frequency limits of the interval velocities (Schmitt *et al.*, 2007).

The difference of the VSP travel time to the sonic log transit time is called drift in the common vernacular of applied seismology. A positive drift occurs when VSP travel times are greater than the integrated sonic times. This implies a lack of environment effects on the sonic log which usually increases the sonic slowness over time. A negative drift (sonic interval time greater than VSP) is more commonly found in volcanic or crystalline rocks as a result of spatial changes in rock composition and orientation of rock foliation.

In summary, time drifts between the measurements can be explained by a number of factors including (Stewart *et al.*, 1984; Li and Richwalski, 1996; Christie *et al.*, 2006):

- Presence of dipping reflectors
- Effect of seismic anisotropy
- Dispersion effect between seismic and sonic frequencies
- Spatial changes in rock composition
- Orientation of rock foliation
- Effect of drilling damage in the surrounding borehole walls
- Difference in geometry and source frequencies hence different volume of rocks are investigated
- Variation in instrumental errors and analysis inaccuracy
- Difference in wave propagation characteristics.

Figure 6-11 reveals an increase in velocity with depth expected as a result of the overburden. The interval velocity varies from 4700 m/s to 7000 m/s in the crystalline basement rocks. Localized velocity peaks in the interval velocity profile are observed at two different depths indicated in the figure corresponding to the density peaks, especially based on the velocity curve generated using the local tangent slope. These two zones can also be identified in the higher-frequency velocity profiles extracted from the borehole sonic logs. A possible explanation for this observation is the change in rock composition and texture in the basement (*e.g.* Vernik *et al.*, 1994). However, with the limited cores available in this deep borehole, it is difficult to understand the causes of the localized increases in velocity and density in the basement. The increase near 1760 m depth can be correlated to the mafic dyke that was previously identified in Chapter 4.

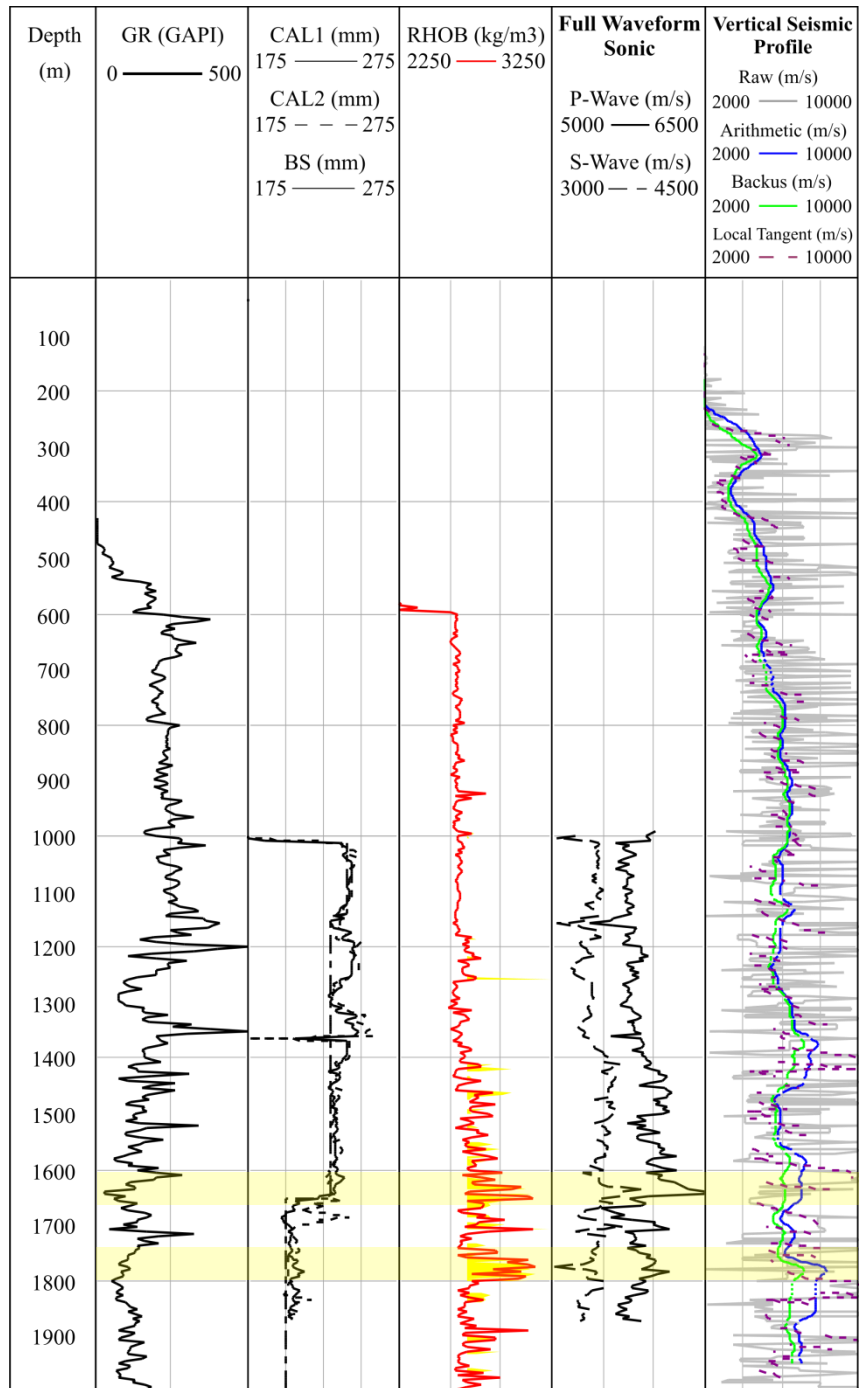


Figure 6-11. Display of velocity profiles generated from zero-offset vertical profile using different averaging methods. Gamma ray, caliper, and P- and S-wave velocities from full-waveform sonic logs are also plotted for comparison and interpretation. Zones of increased velocity and density are highlighted in yellow.

6.4.2. Tube Waves

Tube waves are Stoneley waves that occur at the low frequencies of seismic data and are generated when the fluid in the well is displaced by a seismic source, such as ground roll. They are considered as one of the most damaging types of noise in a vertical seismic profile because they represent the coherent noise mode that repeats itself in every seismic shot (Hardage, 2000). In a cased borehole environment, a tube wave is an interface wave when the Rayleigh wave propagates down the borehole along the interface between the fluid in the borehole and the borehole wall. In an open borehole environment, the tube wave is confined to the fluid column and is subjected to the cross-section area about the axis of the borehole. Thus, tube waves are greatly affected by changes in the borehole diameter (*e.g.* variations in tubings, borehole caving), casing conditions, cement bonding, or contrasts in acoustic impedance (Hardage, 2000).

Tube waves were found to dominate the upgoing events in the basement section of the zero-offset vertical seismic profile. A total of three sets of tube waves are interpreted from the processed section at 1010 m, 1402 m and 1635 m with an expected error of ± 20 m from the uncertainties of noisy traces which mask the depth origin of the waves (Figure 6-12). Multiple-scattered tube waves are observed at the same depth from the multiple downgoing events in the profile. These downgoing tube waves are traced upward to determine their points of origin. They are labelled from 1 to 3 in Figure 6-12. The amplitude for the first downgoing tube waves fade near the surface, but the linear slope of this wave mode can still be traced upward toward the first casing shoe depth at approximately 94 m. The second and third downgoing waves are traced to the surface at an offset distance from the well head. The exact origins of these downgoing waves are unknown. One likely explanation is ground roll impinging on the well head and propagating downward to the subsurface (*e.g.* Li and Richwalski, 1996). An alternative explanation is the presence of an air wave that provides a pressure pulse into the open borehole.

The relatively stronger sets (higher amplitudes) of upgoing tube waves are identified at approximately 1010 m and 1635 m depth. These are close to the depths at which there is a change in borehole diameters at 1006 m and 1654 m, suggesting that small-scale fluctuations in borehole diameter (22 mm to 60 mm) are sufficient to generate tube waves in the borehole (Figure 6-12). The casing shoe at 1005.7 m also corresponds to a change in borehole impedance which creates a tube wave as a propagating body wave that interacts with a strong impedance change.

One of the useful applications of tube waves are fracture zone analysis (*e.g.* Li *et al.*, 1994). The high-frequency tube waves have greater resolution than body waves and thus allow thin layers to be detected, including fracture zones (Mjelde, 1992). At 1402 m depth, this set of tube waves are not related to the borehole diameter change and can be explained by the presence of the fracture zones. This zone was also close to the low-resistivity fracture zone that was previously identified in the geophysical well logs in Chapter 4 and the dipping reflector that may intersect the borehole mentioned in Chapter 5. Tube wave energy can be attenuated by fluid interaction between the borehole and the formation rock due to the presence of permeable fractures. This could explain the lower amplitudes of this set of upgoing tube waves compared to the aforementioned sets.

6.5. Summary

A zero-offset seismic vertical profile was acquired at the Hunt well with the main intention of differentiating between primary reflections and multiples. Despite multiple recordings of seismic shots at each depth for common depth stacking, the signal-to-noise ratio of the traces remain low and the quality of corridor stacks was greatly affected in the Precambrian basement. The quality is also likely due to the poor coupling between geophones and the rugosity of the borehole wall observed in the caliper logs discussed in Chapter 4. However, the corridor stacks are still useful for seismogram comparison with seismic reflection data in the sedimentary successions to facilitate horizon interpretation. The velocity profile generated from first arrival picks is used to generate a model of *in-situ* interval

seismic velocity and is useful for velocity analysis of the normal-moveout correction for processing the seismic reflection data. Localized increases in velocity correlate with density peaks and could be assumed to be related to changes in rock composition and textures. Analysis of the upgoing tube waves reveals the effect of borehole diameter changes and the fracture zone that was also interpreted in the available geophysical logs.

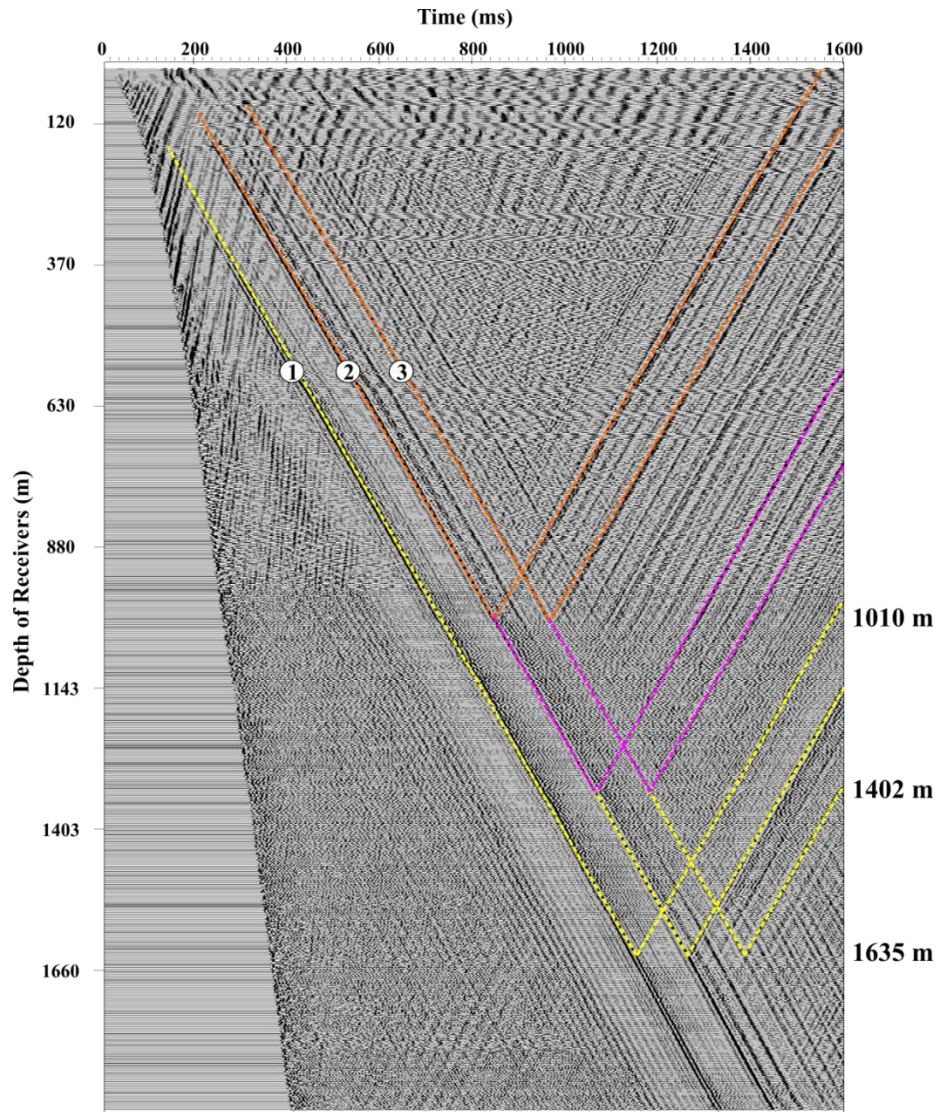


Figure 6-12. Outlines of downgoing and upgoing primary and multiple tube waves in the zero-offset vertical seismic profile. The depth origins of upgoing tube waves are marked on the right. Due to the rugosity of the borehole wall and noisy traces, the approximate depth error is ± 20 m.

Chapter 7

Walk-Away Vertical Seismic Profile

Fractures and textures in the basement rocks can cause strong seismic velocity anisotropy and create problems in a stacking velocity analysis during seismic data processing. The anisotropic effects of rocks need to be considered in the processing of seismic data in order to remove the anomalies caused by the directional variations of seismic velocities. A walk-away vertical seismic profile was acquired at the Hunt well at two different receiver depths to determine the degree of seismic velocity anisotropy. The workflow starting from field acquisition to the derivation of the seismic velocity anisotropy will be discussed in this chapter.

7.1. Overview

The processing of surface seismic reflection data (Chapter 5) reveals a number of dipping seismic reflectors. With the lack of cores available at the nearby Hunt well, it is currently unclear whether the strong reflectors could be resulting from foliated metamorphosed rock, fault-zone anisotropy, impedance contrasts, fractures, or poor seismic processing workflow. The preferential alignment of minerals can result in a strong intrinsic anisotropy. The aligned cracks in the present-day stress field also have an influence on the anisotropy of the overall formations (Schijns *et al.*, 2012). Regional tectonic stress system can control the closure and opening of microfractures (Crampin, 1990). Such uncertainties motivated the acquisition of a walk-away vertical seismic profile (VSP) to understand the degree of seismic velocity anisotropy present in the Precambrian basement rocks. Seismic velocity anisotropy is referred to as the study of the directional dependence of seismic velocities (Rabbel and Mooney, 1986).

Existing studies have used VSP methods to measure seismic velocity anisotropy in sedimentary and metamorphic formations (*e.g.* Rabbel, 1994; Kebaili and Schmitt, 1996; Rabbel *et al.*, 2004; Zhou *et al.*, 2004; Tsvankin *et al.*, 2010;

Schijns *et al.*, 2012). By placing the geophones directly in the borehole and using a series of source points on the surface, the ray geometry for each receiver is equivalent to that of the downgoing ray in a common-depth point reflection profile (Kebaili and Schmitt, 1996). The wavefront geometry created by a seismic energy source and detected by the borehole geophones approximates an ellipse (Figure 7-1). The subsurface wavefront arrival time is recorded at a sequence of geophone depths for various source offset distances. The seismic velocity is then determined from the known recording depth, source offset distance, and arrival time. The anisotropy can be quantitatively described by the coefficient of anisotropy (A) as denoted by (Birch, 1960, 1961):

$$A = \frac{V_{max} - V_{min}}{V_{max}} , \quad (7-1)$$

where V_{max} and V_{min} are the maximum and minimum velocity values. The reader should note that this is just one definition of ‘anisotropy’, and one needs to take note of how a given author has defined it.

Metamorphic rocks are more heterogeneous in that foliations and lineations can result in strong intrinsic anisotropy due to preferential alignment of minerals (Crampin, 1981; Cholach and Schmitt, 2006; Schijns *et al.*, 2012). Rocks are still considered “weakly anisotropic” for $A \ll 1$ despite the fact that many of the constituent minerals in the rocks are highly anisotropic (Thomsen, 1986).

A common form of anisotropy observed in the Earth is hexagonal, or more commonly in geophysics, transverse isotropy (TI), in which elastic properties are the same in any direction perpendicular to a symmetry axis but different parallel to the axis (*i.e.* single axis of rotational symmetry) (Tsvankin, 2001; Sheriff, 2002). The seismic signature in this form of anisotropic symmetry system has hexagonal symmetry and this form of symmetry is similar to a crystal. Note that the elastic properties follow a TI character with a single rotational axis of symmetry in the hexagonal system. To avoid confusion it must be pointed out that this differs from the six-fold optical symmetry seen in minerals. TI requires five

independent elastic constants which are dependent on the angle between the propagation direction and the symmetry axis. The detailed equations of calculating for elastic stiffnesses using directional velocity and density values of TI are included in Appendix E.

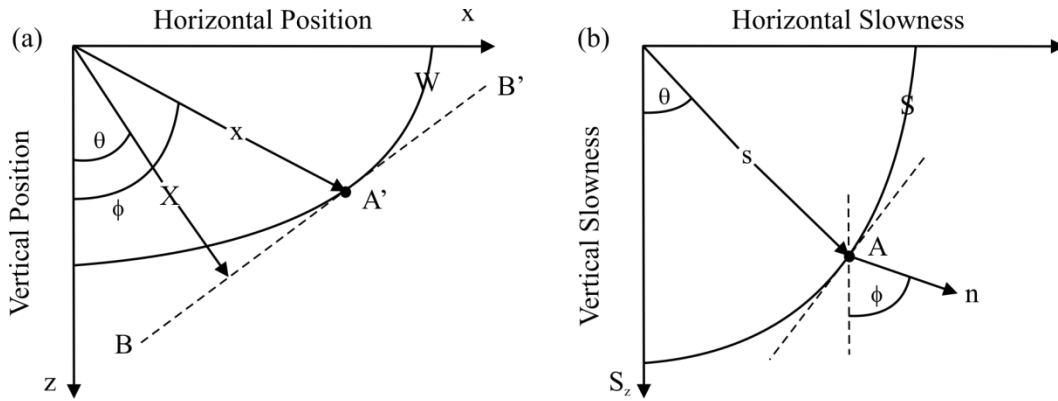


Figure 7-1. (a) Hypothetical wave surface (W) in x - z space at time t ; A' at the endpoint of spatial vector x at ray angle ϕ . (b) Hypothetical phase slowness surface S corresponding to W in a plane of an anisotropic material with respect to the vertical and horizontal directions (Kebaili and Schmitt, 1997)*.

The velocity of energy transport radially outward from a point source is referred to as the group (ray) velocity. This is determined from the travel time between the source-receiver pair at a known separation distance (Kebaili and Schmitt, 1997). In an anisotropic media, the magnitude of the group velocity (energy flux direction) depends on the direction of propagation and does not coincide with the phase velocity (wave surface normal or slowness direction) (Figure 7-1). Group velocities can be directly calculated from the time picks assuming a homogeneous layer. However, phase velocities are more preferable for analysis since they can also be used directly to calculate for the material's elastic stiffnesses with a known density value. The phase velocity can be estimated from VSP data by the

* Reprinted with permission from American Institute of Physics. Copyright 1997, Acoustic Society of America.

difference in travel times of a constant phase between two receivers in the well (de Parscau, 1991). In summary, group (ray) velocity is the velocity of energy propagation along a ray path, whereas phase velocity is the velocity of the plane wave. These two velocities are equivalent for an isotropic material, but will need to be considered separately for an anisotropic material in order to properly relate the velocities to elastic constants.

7.2. Data Acquisition

A multi-azimuth walk-away vertical seismic profile (VSP) was acquired using the GFZ Sercel SlimWaveTM receiver array of 4 three-component geophones in the Hunt well to analyze the overall anisotropy of the basement rocks near the well (Figure 7-2). The receivers were spaced 10 m apart and the top geophone in the chain was placed at 797 m and 1777 m depth. The 1797 m depth was selected since it was in the zone containing a possible mafic dyke as discussed in Chapter 4. Using the University of Alberta's high-frequency MinivibTM unit (Industrial Vehicles International of Tulsa, Oklahoma) as the seismic energy source, shots were fired at 4 m to 8 m interval along Tower Road (Figure 7-3). Negative and positive offset distances represent source locations to the left and right of the borehole respectively. The source employed 13 s linear taper sweeps with frequencies at 10 Hz to 160 Hz and was positioned at an approximate source-receiver offset distance between 156 m to 948 m. The final correlated record length is 5 s with a sampling rate of 0.5 ms. This walk-away VSP data set was acquired with a 200 ms time lag and this must be accounted for during processing.

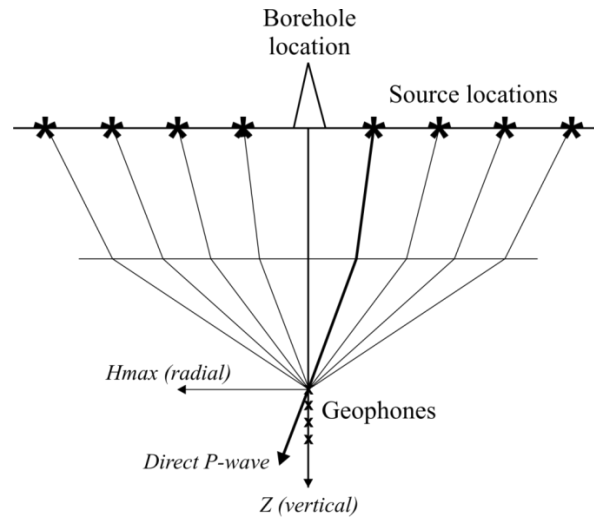


Figure 7-2. Field geometry for the walk-away VSP at the Hunt well. Three-component geophone chains were placed at two different depths with the top geophones located at 797 m and 1797 m depth. Source locations were placed along Tower Road.

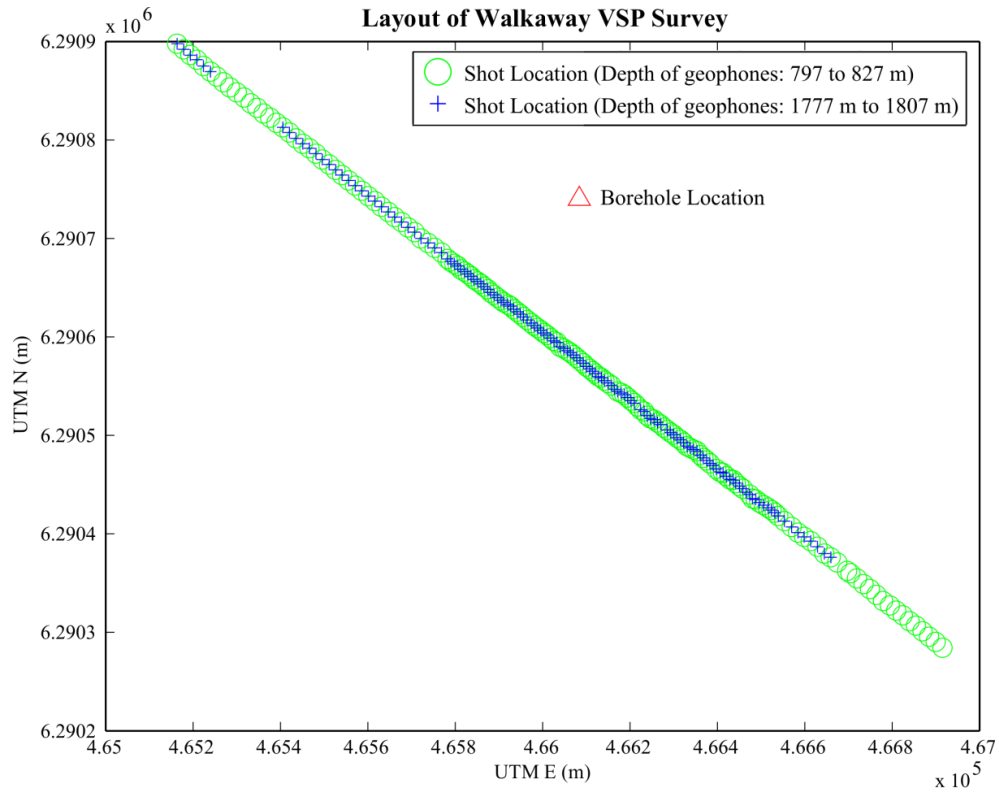


Figure 7-3. Acquisition of the walk-away VSP data along the straight segment of Tower Road.

7.3. Data Processing

Similar to other types of seismic data, the raw traces of the walk-away vertical seismic profile (VSP) were loaded into VISTA™ Seismic Data Processing software package provided by GEDCO for processing. The first steps involve setting up the VSP geometry and inspecting the data for quality assurance. Poor coupling between the downhole receivers and borehole walls caused the signal-to-noise ratio of the seismic records to be lower than desired, especially in the crystalline basement rocks. This problem arose because the borehole diameter was too large for the locking arms on the Sercel unit. The data was then further processed, including component separation, first breaks picking (Figure 7-4), hodogram rotation, downgoing and upgoing event separation, and tau-p inversion of seismic travel times for the calculations of velocity anisotropy.

7.3.1. Component Separation and Orientation

Three-component (3-C) VSP data offers the opportunity for a more complete description of the seismic wavefront than just the vertical component of motion (Hardage, 2000). The recorded VSP data is encoded in a single SEG-Y file format regardless of its directional components. Various processing flow requires each directional component (X, Y, Z) to be stored in individual components. The vertical Z axis follows along the longitudinal axis of the downhole VSP tool. The separation of components is easily performed in the VISTA™ software by outputting each component according to the trace header (Figure 7-5). First arrivals are clearly identified in all three components and are selected according to the first strongest arrival peak. The three components record both upgoing and downgoing wave modes. The X and Y horizontal components reveal noise at approximately 800 ms that result from the cable vibrating in the borehole.

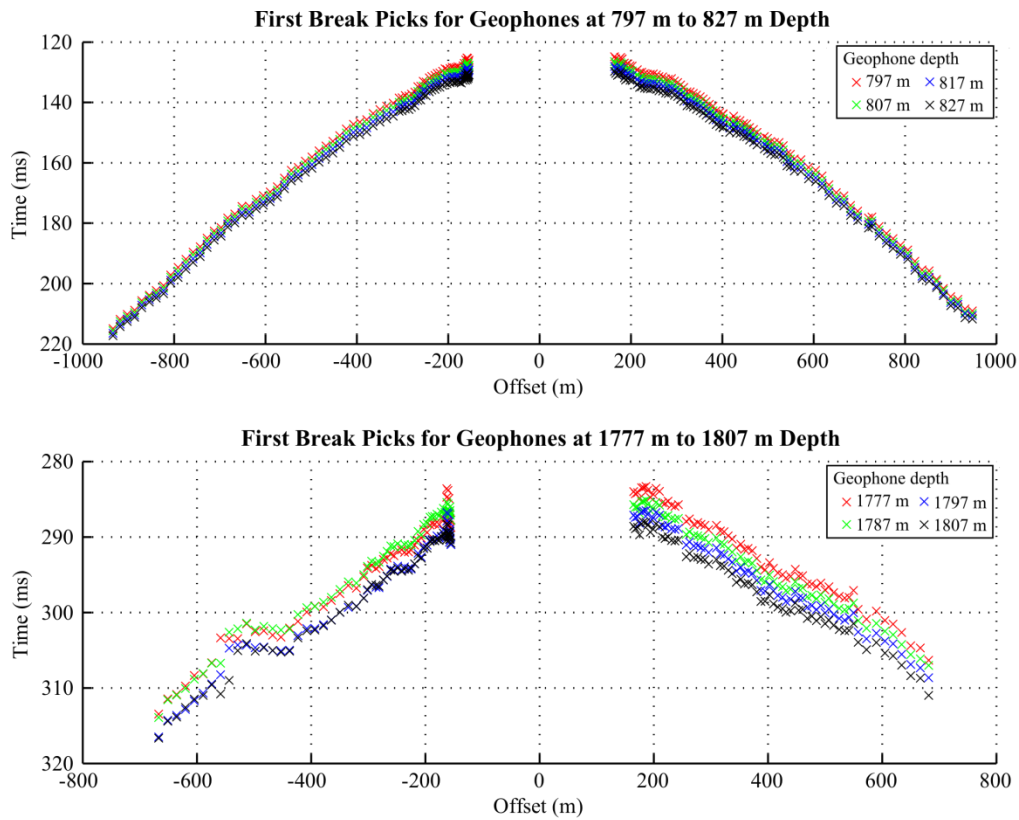


Figure 7-4. First arrival picks of the walk-away VSP data. Data quality of the deeper VSP recordings is affected by the poor geophone coupling in the borehole and near-surface statics issues. Different marker colors represent geophones at different depths in the geophone chains.

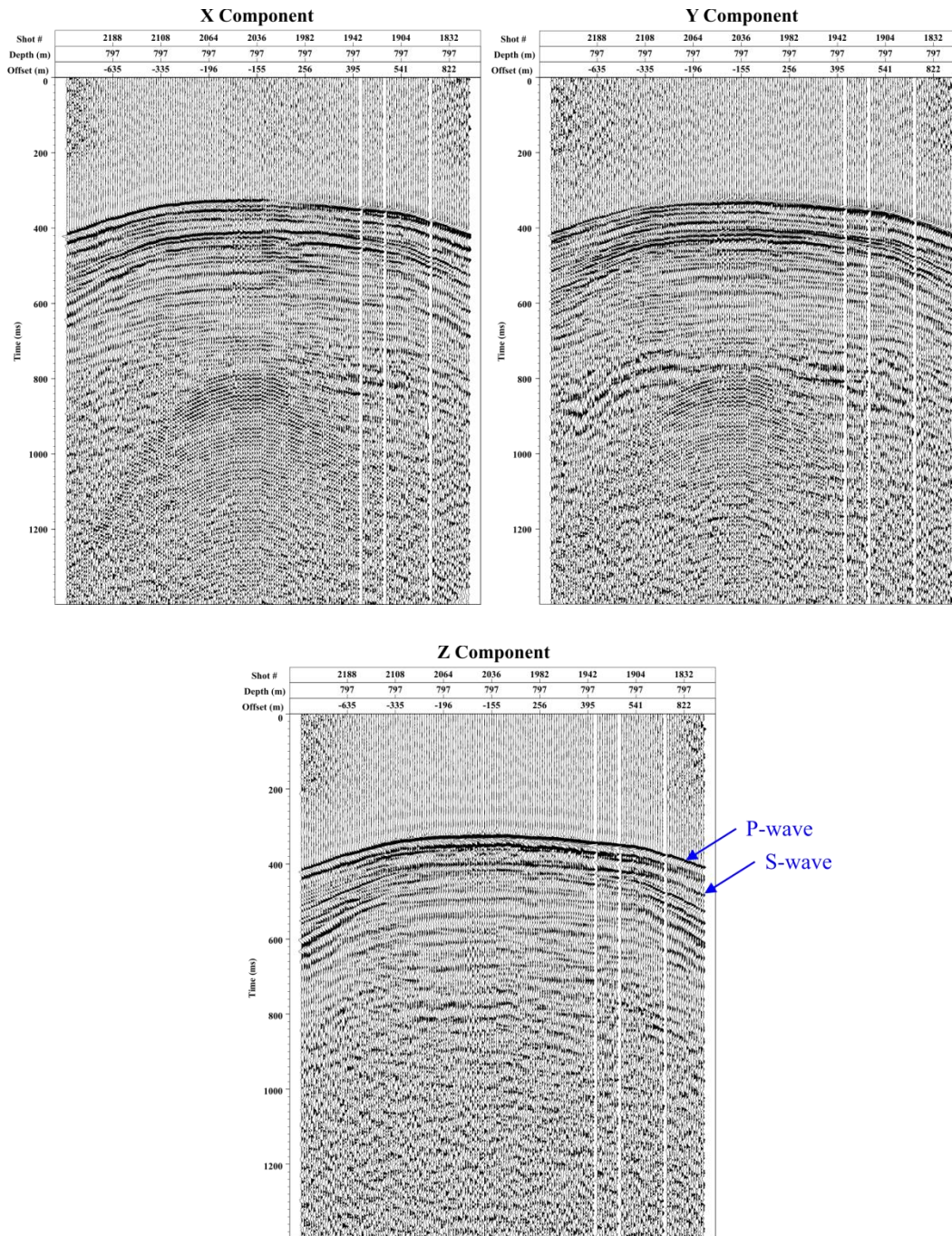


Figure 7-5. The three components of the walk-away vertical seismic profile at 797 m depth after geometry setup, trace editing and component separation. Each component contains 652 traces and is displayed in common receiver gather. Automatic gain control was applied to the data for display purposes. The data has a 200 ms time delay.

To optimize the far offset processing, two hodogram rotations are performed to orient the components toward the source. Using a plot of the motion of a point as a function of time (*i.e.* display of a particle path) of the multi-component receivers, hodogram analysis is used to determine the direction of the wave's approach to the detectors (Sheriff, 2002). The first hodogram rotation involves rotation in the horizontal plane to orient one component inline with the source-receiver direction (often referred to as the horizontal radial component, Hmax) and the orthogonal component (horizontal transverse component, Hmin) (Kuzmiski *et al.*, 2009). Hmin captures the horizontally-polarized shear (SH) wavefield and out-of-plane reflections, and they are visible at both measured depths (*e.g.* Figure 7-6).

Mode conversion may occur due to the source offsets and the 3-C recording facilitates the separation of compressional P-waves and SV-waves (vertically polarized shear) using the second hodogram rotation. This rotation is in the source-receiver plane using the oriented Hmax and vertical component to separate the P and SV waves (Figure 7-7) (Kuzmiski *et al.*, 2009). These results show the existence of clear P and S waves. Future work should consider the use of an eigenvalue polarization filter in order to highlight the energy within the 3-component signal (*e.g.* Flinn, 1965; Montalbe and Kanasewi, 1970; Vidale, 1986; Jurkevics, 1988; Du *et al.*, 2000; Schijns *et al.*, 2012).

7.3.2. Plane-Wave Decomposition

To obtain the phase velocity from the processed walk-away VSP data, plane-wave decomposition was performed using tau-p (τ -p) transform (also known as slant stack and Radon transform) (*e.g.* Stoffa *et al.*, 1981; Kebaili and Schmitt, 1996; Schijns *et al.*, 2012). The transform is defined by:

$$F(\tau, p) = \int_{-\infty}^{\infty} F(x, \tau + px) dx \quad , \quad (7-2)$$

where x is horizontal offset between the source and the borehole, and τ is the intercept time or zero-offset arrival time. The horizontal phase slowness (p) is given by:

$$p = \frac{dt}{dx} = \frac{\sin \theta}{v} \quad , \quad (7-3)$$

where θ is the angle of incidence, and v is the magnitude of the phase velocity. τ is given by:

$$\tau = t - px \quad , \quad (7-4)$$

where t is the travel time (Figure 7-8). Using the above equations, the τ - p transform is then defined by:

$$F(\tau_i, p_j) = \sum_{k=1}^n f(x_k, \tau_i + p_j x_k) \Delta x \quad . \quad (7-5)$$

There is no “mixing” between adjacent receiver depths since the transform is performed separately at each depth. The last parameter needed for the calculation of phase velocities and propagation angle is vertical slowness (q). In an anisotropic medium, vertical slowness is dependent on the horizontal slowness (p) and the phase propagation angle (θ) (Mah, 1999; Schijns *et al.*, 2012). Under the assumption of a homogeneous medium over a defined interval, vertical slowness (q) is calculated using (Kebaili and Schmitt, 1996; Schijns *et al.*, 2012):

$$q(p) = \frac{\tau_2(p) - \tau_1(p)}{z_2 - z_1} \quad , \quad (7-6)$$

where τ is the intercept time at a constant horizontal slowness (p) and z is the receiver depth in the borehole.

After applying τ - p transformation on the walk-away VSP data, the intercept time and horizontal slowness value are picked manually to calculate the resulting phase velocity and angle of incidence (Figures 7-9 and 7-10) (Schijns *et al.*, 2012):

$$v(\theta) = \frac{1}{\sqrt{q^2(\theta) + p^2(\theta)}} \quad , \quad (7-7)$$

$$\theta = \arctan\left(\frac{p}{q}\right) \quad . \quad (7-8)$$

The accuracy of the phase velocity is mostly dependent on the signal-to-noise ratio and frequency content of the walk-away VSP data. A frequency-wavenumber (f-k) filter and an Ormsby filter were applied to the data prior to the manual picking of τ and p to improve the overall signal-to-noise ratio of first break picking. The final radial and transverse components reveal strong energy at approximately 500 ms at the near-offset traces but they are not visible in the vertical component (Figure 7-6). The origin of the noise is likely due to the vibration of the wireline cable.

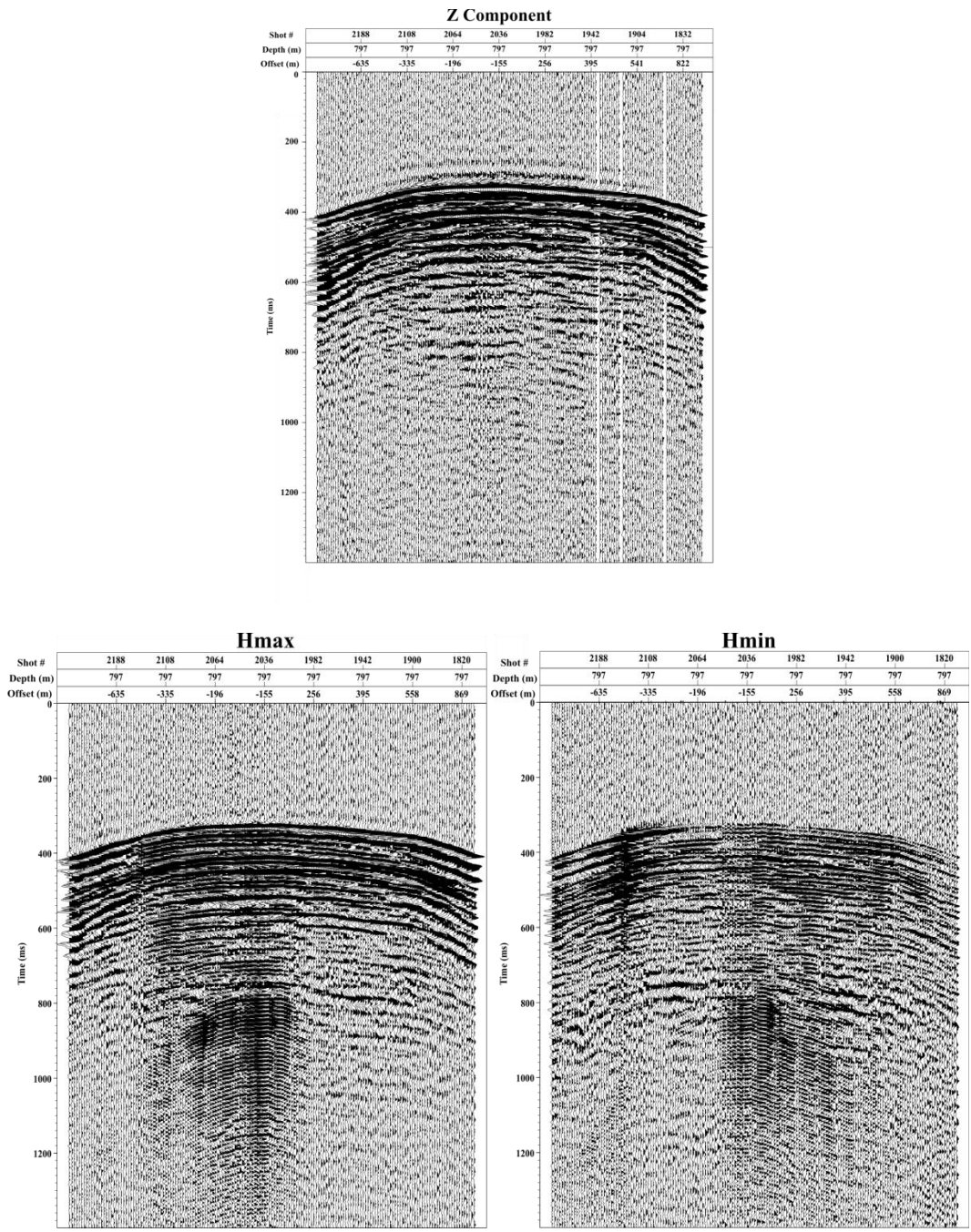


Figure 7-6. First rotation of the X and Y components at 1777 m depth for the outputs of Hmax and Hmin. The data has a 200 ms time delay.

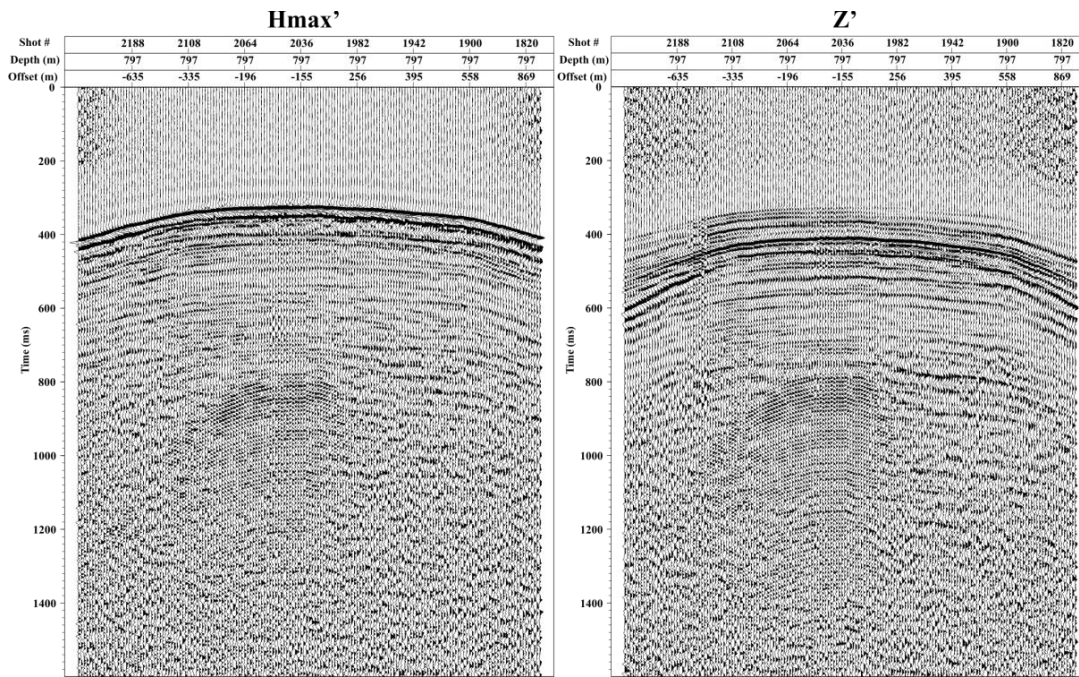


Figure 7-7. Second rotation of the Hmax (horizontal radial) and Z (vertical) components for the outputs of Hmin, oriented (Hmax') and transverse (Z') components. The data has a 200 ms time delay.

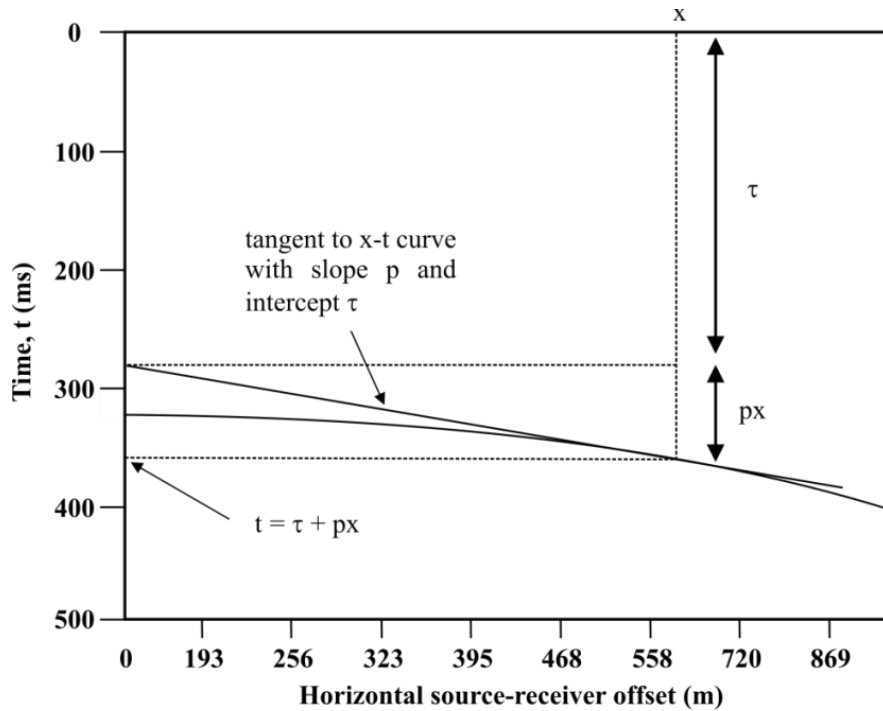


Figure 7-8. Relationship between the τ - p and x - t spaces. This illustration is based on the walk-away VSP data at 797 m depth. Figure adapted from Kebaili and Schmitt (1997)*.

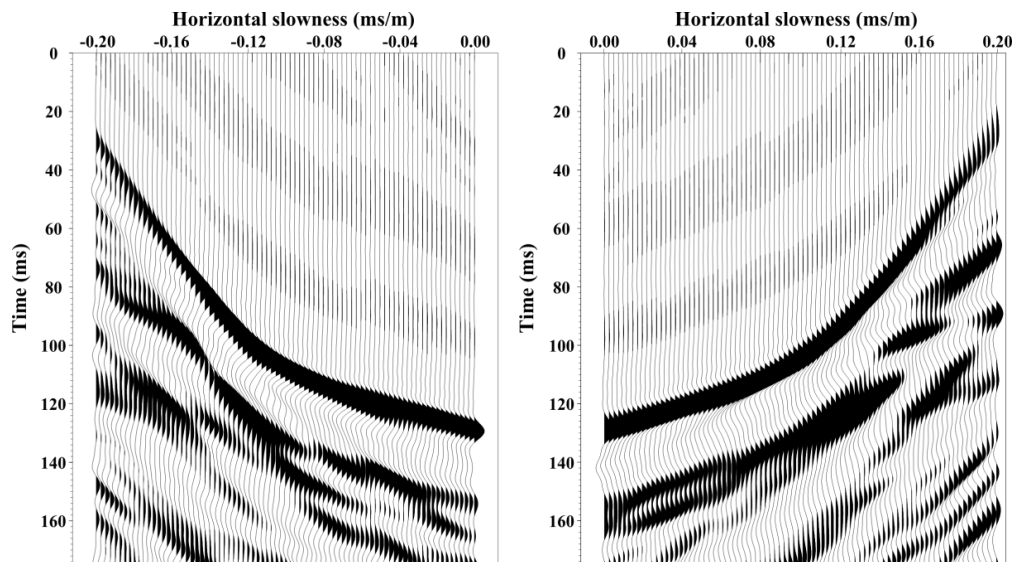


Figure 7-9. Display of intercept time and horizontal slowness for the walk-away VSP data at 797 m depth.

* Reprinted with permission from American Institute of Physics. Copyright 1997, Acoustic Society of America.

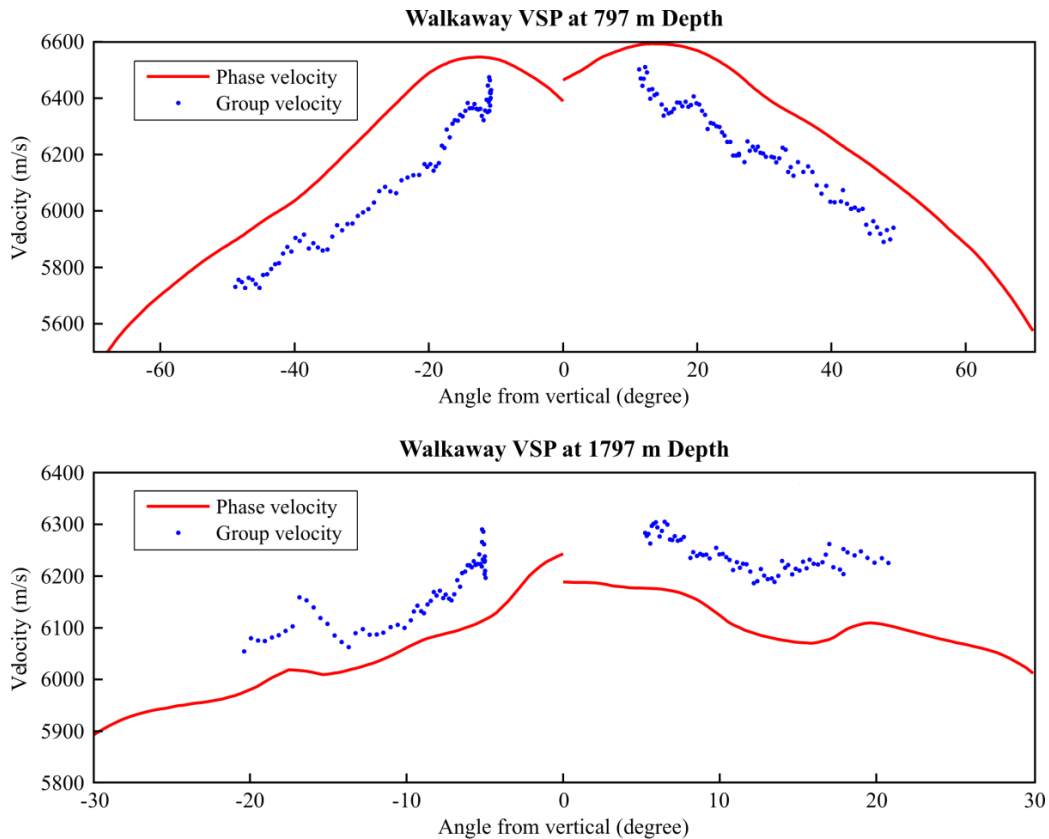


Figure 7-10. P-wave phase and group velocities measured and calculated from the two levels of the walk-away VSP at the Hunt well versus the phase and group angles, respectively. Note that the group and phase angles normally do not match for a given pair of group and phase velocities, as shown in Figure 7-1.

7.4. Data Analysis

The propagating wavefront for each seismic shot along the surface could be measured as a function of horizontal offset, vertical depth, and travel time. Under the assumption that the wellbore has no vertical deviation, ray paths for the calculation of the seismic velocity anisotropy are created using various offset distances between varying source locations along Tower Road and receivers lowered into the borehole. The seismic velocity anisotropy was calculated to be in the range of 12 % to 15 % from surface to the upper recording depth (797 m to 827 m depth) and 16 % to 18 % between the upper (797 m to 827 m depth) and

lower (1777 m to 1807 m depth) recording depths. This reveals an increase in bulk velocity anisotropy as depth increases in the subsurface.

As noted in the earlier sections, the observed seismic anisotropy depends on both the intrinsic elasticity of the rock, due to its mineralogical texture, larger structural effects such as layering, and the existence of fractures. Laboratory measurements of compressional- and shear-wave phase velocities were carried out on a metamorphic rock using the ultrasonic pulse transmission technique up to a confining pressure of 60 MPa. This rock sample originated from the 2350 m depth of the Hunt well with an identifiable foliation plane. The intention was to determine the acoustic and elastic behaviour of the rock. Under the assumption of transverse isotropy, velocities were measured parallel, perpendicular, and at 45° to the foliation plane under confining pressure. As the confining pressure increased, the effect of microcracks on the anisotropy was expected to lessen, and the remaining anisotropy more likely to result from layering and preferred orientation of minerals, *i.e.* intrinsic anisotropy. Details on the laboratory measurements and results are reported in the term paper submitted for the GEOPH 620 course Rock Physics and Mechanics taught by Dr. Douglas R. Schmitt in Fall 2011 and is attached in Appendix E of this thesis. The final value for the P-wave velocity anisotropy measured in the laboratory in the presence of a foliation plane was averaged to be 12 % at 2350 m depth. This foliation plane was found to be not fully parallel to the faces of the sample after the sample was prepared, thus the reported anisotropy could be slightly lower than the actual value. Schijns *et al.* (2012) also suggested that the *in-situ* bulk anisotropy of the rocks could be subjected to the aligned microcracks or fractures in the subsurface, which in turn causes disagreement between the laboratory measurements and the walk-away VSP observations.

Seismic anisotropy in the crust is often explained by structural or compositional layering, fractures oriented by regional stress field, intrinsic material properties such as foliations, and anisotropic minerals or cracks oriented in a preferred direction (Rabbel and Mooney, 1986; Rabbel, 1994; Okaya *et al.*, 2004; Rabbel *et*

al., 2004; Schijns *et al.*, 2012). The anisotropy in sedimentary rocks is often presumed to be governed by the horizontal layering of formation rocks or by vertically-aligned fractures (Schijns *et al.*, 2012). Metamorphic rocks are known to be more heterogeneous in nature. According to the geophysical logs, the Hunt well intersects the top of the Precambrian metamorphic basement rocks at 541.3 m. Geophysical logs of the Hunt well reveal the presence of fractures at numerous depths of the borehole and a potential mafic dyke at 1760 to 1797 m depth (Chapter 4) which could explain the increase in seismic anisotropy in the deeper basement rocks.

7.5. Summary

A multi-azimuth walk-away vertical seismic profile was conducted along Tower Road to examine the degree of seismic velocity anisotropy with varying angle of incidence at the Hunt well. A τ - p transform of seismic travel times recorded at two separate receiver depths was implemented to determine the degree of velocity anisotropy. An anisotropic velocity function derived from the walk-away VSP represents an average over several hundred meters of depth. Significant anisotropy was observed with reported values of 12 to 15 % between surface to 797 m depth and 16 to 18 % between 797 to 1777 m depth. Higher anisotropy values at greater depth can be attributed to the presence of fractures and the mineral composition of a potential mafic dyke in the metamorphic basement rocks. Since only two receiver depths were recorded, the degree of bulk velocity anisotropy could be underestimated from the averaging of data. Factors including lateral inhomogeneity and statics were also not accounted for in the processing steps of the data sets. Laboratory measurements of a core sample from 2350 m depth reported an *in-situ* intrinsic anisotropy of 12 % in the presence of a foliation plane. The difference in the degree of velocity anisotropy between laboratory measurements and walk-away VSP observations can be attributed to the presence of aligned microcracks or fractures in the subsurface. Future work could include applying the τ - p transform to the shear wave components towards an understanding of the S-wave velocities. Additional investigations could also be

performed by implementing forward modeling of the phase velocities and incorporating fracture compliance in the modeling for comparison with the field measurements.

Chapter 8

Conclusions

The availability of a deep borehole (Hunt well) offers an unprecedented opportunity to correlate surface seismic data to borehole measurements in the metamorphic rocks of northeastern Alberta. As part of the feasibility study for the development of engineered geothermal systems (EGS) in Alberta under the Helmholtz-Alberta Initiative, this thesis provides a detailed subsurface characterization of the basement rocks by integrating the existing deep surface seismic profile with the borehole seismic and log measurements that were primarily acquired in July 2011. The purpose of geothermal energy research in Alberta is to implement alternative energy resources for water heating in oil sands processing, which would decrease greenhouse gas emissions in the province. Existing thermal gradient studies suggested that deep drilling into the crystalline basement rocks is needed to reach the desired temperature for the development of geothermal energy in northeastern Alberta. Crystalline basement rocks have low porosity, but the presence of highly-fractured rocks still provides an ideal environment for the development of any geothermal system. As such, physical discontinuities including cracks, voids and joint systems, and major faults and fractures are features to target for geothermal exploration. The focus of this thesis is to identify any geological features, including zones of fractures in the basement rocks that could act as indicators of enhanced fluid potential – a necessary component for any viable geothermal system.

The Hunt well is a vertical borehole located west of Fort McMurray, Alberta, Canada that is completed to a depth of 2363.3 m. Three 2D seismic reflection surveys have been acquired along Tower Road located next to the borehole site, and they have been (re-) processed and interpreted for the purpose of this study. One of the earliest data available for this project was the 2D crooked seismic profile with an imaging depth of approximately 35 km. This profile reveals a series of gentle to steeply eastward-dipping reflections in the basement rocks.

Such dipping reflectors suggest possible geological structures intersecting the borehole and are considered early observations of potential zones of interests for geothermal development. As such, it motivated further data acquisition in the borehole which includes a comprehensive suite of borehole logs and seismic data for a better understanding of the seismic reflectors identified.

8.1. Contributions of This Thesis

With the limited cores available at the Hunt well, this project focused on all the data available and extracted all relevant information pertaining to the future development of engineered geothermal systems. The comprehensive geophysical logs acquired in July 2011 focused on logging of the Precambrian basement below the casing. Geophysical well logs serve to understand the *in-situ* rock properties in the basement, to assess the geological formations and fractures that could act as fluid pathways, and to analyze the acoustic responses of rock properties for supporting the processing and interpretation of seismic surveys.

Key observations from the geophysical logs are:

- The top of the Precambrian basement is at 541.3 m with respect to the KB level and the basement is considered to be granitic in composition.
- The observed mean values from the spectral gamma ray logs are 1.65 ± 1.05 ppm for uranium, 35.24 ± 19.60 ppm for thorium, and $3.22 \pm 1.37\%$ for potassium.
- A 37 m thick mafic dyke is observed between 1760 m to 1797 m depth with increased magnetic mineral compositions as indicated by the magnetic susceptibility log measurement.
- A radiogenic heat generation value of $3.0 \mu\text{W}/\text{m}^3$ is calculated from the natural and spectral gamma ray logs.
- A number of localized natural fractures with possible mineral fillings are interpreted between 1104 to 1405 m depth.
- A significant decrease in resistivity is detected between 1406 to 1481 m with a possible correlation to the structural and textural variations in the

rocks. This is also a probable permeable zone related to open fractures according to the obvious SP deflections.

- The full waveform sonic data reveals waveform attenuations that correspond to localized fracture zones.
- The average P- and S-wave velocities are 5868 m/s and 3428 m/s respectively, in the depth interval between 1012 to 1865 m, measured from the full waveform sonic logs.
- A V_p/V_s ratio of 1.71 is obtained from the velocity profiles which agree with the typical value in a crystalline rock environment.

Key observations from Formation MicroImager (FMITM) logs include:

- The natural fractures are visible between 541 m to 600 m, 1410 m to 1423 m, and 1461 m to 1468 m depth intervals.
- The average dip angle of natural fractures is 25° between 542 m to 600 m depth with a mean strike azimuth of 162°.
- The average dip angle of natural fractures is 44° between 600 m to 1651 m depth with a mean strike azimuth of 110°.
- Drilling-induced tensile fractures are visible at 1638 m to 1643 m oriented to approximately 078/258°N.
- A potential borehole breakout zone is interpreted from the dipmeter logs between 1652 to 1740 m depth with a mean strike azimuth of 336°.

Based on the anomalous changes in density, photoelectric factor, magnetic susceptibility and interval transit time, an intrusive mafic dyke was observed. Using both the conventional geophysical logs and image logs, a number of fracture zones were also interpreted throughout the borehole. These zones were interpreted indirectly via observations inferred from the conventional geophysical logs, and directly via interpretations made from image logs. Image log data was unavailable for the entire borehole due to the poor quality. However, various types of fractures were still interpretable using the available sections including natural fractures, drilling-induced tensile fractures and borehole breakouts. The

latter two types of fractures are considered as reliable stress indicators in understanding the stress geometry of the borehole as geothermal exploration requires drilling wells in the direction with the optimal fluid pathways. Changes in the orientation of natural fractures at different depths were indicators of separate geological events or changes in stress directions.

The interpreted acoustic properties from both full-waveform sonic and dipole shear sonic imagerTM logs generated a velocity profile useful for seismic processing. As expected, the velocity increased with depth as a result of the increased pressure from the overburden. A slight decrease in velocity in the zone containing the mafic dyke suggested possible fracturing at that depth. Decreased velocities at greater depths may also be caused by the preferred orientation of the anisotropic minerals presence in the basement rocks. Lastly, the ratio of compressional and shear wave velocities also provided a reasonable value typical for the crystalline rock environment.

Other relevant indicators observed from the borehole logging include the thermal gradient inferred from temperature logging and the radiogenic heat generation value inferred from gamma ray log responses. Temperature logging of the Hunt well was performed under the supervision of Dr. Jacek Majorowicz. Using the calculated thermal gradient and measured temperatures in the well, it was possible to estimate the expected depth needed for the optimal temperature toward geothermal exploration in the Athabasca Oil Sands area. The radiogenic heat generation offered an optimistic value in the borehole when determining the amount of heat generation of rocks in the absence of cores.

Besides the deep seismic reflection profile discussed earlier, two other surveys were available along Tower Road. Surface seismic data allowed us to investigate a greater area near the borehole with restricted resolution in comparison with the geophysical logs. The first and earliest 2D seismic survey in 1978 acquired in the area was re-processed, but was deemed of poor quality to be further interpreted for the purpose of this project. The third and newest 2D seismic survey was acquired in 2011. This profile has an improved vertical and lateral resolution of

the subsurface and was used to establish a better geological framework in the sedimentary successions and upper Precambrian basement. One of the biggest challenges in processing the seismic profiles was minimizing the presence of multiple reverberations that masked the seismic section at times below the top of the Precambrian unconformity. It also masked the contact between the sedimentary basin and the high-velocity basement rocks. The contact was interpreted from the deflections observed in the gamma ray, neutron porosity and sonic logs, and also the resistivity contrasts identified from the Formation MicroImager (FMITM) logs. Using the velocity information from the sonic logs and vertical seismic profiles, the depths to the dipping reflectors revealed in the deepest seismic profiles in the project were derived. The depth of one of the dipping reflectors suggested a possible correlation with the natural fractures interpreted in the borehole logs.

Two types of vertical seismic profiles (VSP) were available for interpretation. The first type is the zero-offset vertical seismic profile. The goals of this profile was to generate a proper time-depth relation for depth conversion of the seismic reflection profiles, to distinguish between the real seismic reflectors and multiples in the seismic data, and to identify fracture zones from the upgoing tube waves in the processed VSP section. The generated velocity profile suggested two zones of interest with increased velocity with and density. This could be explained by the change in rock composition and texture in the basement rocks, but could not be verified due to the limited cores available at the Hunt well. Three major sets of tube waves were interpreted. Two sets were found to be related to the change in the borehole diameter suggesting small-scale diameter fluctuations in borehole diameter are sufficient to generate tube waves in the borehole. The last set of tube waves corresponded to the depth of the fracture zone and dipping reflector interpreted from the borehole logs and 2D seismic survey.

The second set of VSP was the walk-away VSP. Receivers were lowered at two different depths which allowed us to calculate the degree of seismic velocity anisotropy between two different depth intervals. An increase in bulk velocity

anisotropy was found as depth increased, and the reported values were found to differ from the previous laboratory measurements made on a core sample of the borehole. This could be attributed to the presence of aligned microcracks or fractures in the subsurface. Geophysical logs of the borehole revealed the presence of fractures at numerous depths and a potential mafic dyke located between the two depths (797 m to 1777 m) of the VSP measurements. These could explain the increase in seismic anisotropy in the deeper basement rocks of this borehole.

With the number of logs and seismic data sets available for this borehole, detailed interpretations of each method were discussed at the end of their respective chapters. Log interpretations revealed greater details on the numerous fracture zones and a potential mafic dyke that could not be interpreted using surface seismic data only. Understanding the crystalline basement rocks using an integration of borehole data and surface seismic data is uncommon in Alberta since exploration interests focus on the sedimentary successions of the Western Canada Sedimentary Basin. Surface seismic data serves as a good preliminary imaging of the basement rocks since it offers coverage over a broader area of interest when deep boreholes are not commonly available in Alberta. Borehole seismic data was integrated into the data sets by providing an improved seismic velocity model for the processing of seismic reflection data, and verifying the zone of fractures interpreted from the borehole logs.

8.2. Unresolved Issues and Direction for Future Work

Future work for this project should consist of further improving the imaging of the crystalline basement rocks using seismic reflection data. A conventional seismic processing routine was used for the processing of all 2D seismic profiles in this project. However, more advanced seismic routines need to be considered for the processing of the crooked profiles and the suppression of multiples in the crystalline basement rocks for an improved image of the basement. The newly-acquired seismic profile had an improved resolution compared to the older seismic profiles for imaging the sedimentary successions and the upper

Precambrian basement rocks. However, longer offsets are needed to extend the imaging to the target depth of the geothermal reservoir deeper in the basement rocks. It is also good to note that this newer survey is useful for a more precise determination of the near surface ‘static’ time shift corrections following the methodology of Schijns *et al.* (2012).

For the walk-away VSP, additional processing steps such as migration could be added to potentially image other dipping seismic events generated by structures that were not imaged by the surface seismic profiles. Since the analysis was only performed on the compressional (P-) waves, future work could include applying similar tau-p procedure to the shear (S-) waves toward an understanding of the S-wave velocities. Additional investigations could also be performed by implementing forward modeling of phase velocities and incorporating fracture compliance in the modeling for comparison with the field measurements (*e.g.* Schijns *et al.*, 2012).

The presence of fractures can impact the permeability and porosity of a reservoir, which affects the overall reservoir performance. To date, fracture analysis in this borehole had been mainly inferred from the conventional geophysical logs since the resolution of the image logs was limited. Knowledge of fracture properties, such as fracture aperture, was restricted to the limited availability of the image logs. To fill the data gaps regarding the properties of these fractures, acquisition of an ultrasonic borehole televiewer is currently part of the future logging plan to provide a detailed image of the entire borehole and to gain a better understanding of the *in-situ* stress state. An advantage of using an ultrasonic borehole televiewer over the FMITM is that it provides a full image of the entire borehole while the FMITM only offers 80 percent of borehole coverage dependent on the size of the borehole. Additionally, hydraulic tests are also planned in the next logging programme to verify the zone(s) of potential fluid loss in the borehole.

8.3. Implications for Geothermal Exploitation

This thesis encompasses the detailed investigation of all currently available data for the Hunt well that is relevant for the investigation of EGS development in the basement rocks of northeastern Alberta. Integration of all data sets allow one to narrow the zones of interest from the approximate depths derived in the surface seismic data to the actual depths in the borehole as identified in the wireline logs. The temperature at the bottom of the borehole suggested that drilling deeper into the crystalline basement rocks is required to reach the optimal temperature of 80°C for EGS development in the Athabasca oil sands area. The log and seismic interpretations also suggested that *in-situ* fractures are indeed present in the crystalline basement rocks which could provide fluid pathways between the injection and production wells for EGS development.

Bibliography

- Aadnoy, B. S., and J. S. Bell (1998), Classification of drilling induced fractures and their relationship *in-situ* stress directions, *The Log Analysis*, 27-42.
- Adam, E., B. Milkereit, and M. Mareschal (1998), Seismic reflection and borehole geophysical investigations in the Matagami mining camp, *Canadian Journal of Earth Sciences*, 35(6), 686-695, doi:10.1139/cjes-35-6-686.
- Aki, K., and P. G. Richards (1980), *Quantitative Seismology, Theory and Methods*, 557 pp., W. H. Freeman and Company, San Francisco, California.
- Al-Ali, Z. A., M. H. Al-Buali, S. AlRuwaili, S. M. Ma, and A. F. Marsala (2009), Looking deep into the reservoir, *Oilfield Review*, 21(2), 38-47.
- Alford, J., M. Blyth, E. Tollefsen, J. Crowe, J. Loreto, S. Mohammed, V. Pistre, and A. Rodriguez-Herrera (2012), Sonic logging while drilling — Shear answers, *Oilfield Review*, 24, 4-15.
- Ali, A., and D. K. Potter (2012), Temperature dependence of the magnetic properties of reservoir rocks and minerals and implications for *in-situ* borehole predictions of petrophysical parameters, *Geophysics*, 77(3), Wa211-Wa221, doi:10.1190/Geo2011-0282.1.
- Ameen, M. S. (2003), Fracture and *in-situ* stress characterization of hydrocarbon reservoirs, 216 pp., Geological Society Special Publications, London, doi:10.1144/GSL.SP.2003.209.01.18.
- Archie, G. E. (1950), Introduction to petrophysics of reservoir rocks, *AAPG Bulletin*, 34(5), 943-961.
- Ashcroft, W. (2011), *A Petroleum Geologist's Guide to Seismic Reflection*, 1st ed., 157 pp., Wiley-Blackwell, West Sussex, UK.
- Babcock, E. A. (1978), Measurement of subsurface fractures from dipmeter logs, *American Association of Petroleum Geologists Bulletin*, 62(7), 1111-1126.
- Bachu, S. (1993), Basement heat-flow in the Western Canada Sedimentary Basin, *Tectonophysics*, 222(1), 119-133, doi:10.1016/0040-1951(93)90194-O.
- Bachu, S. (1999), Regional-scale geothermal and hydrodynamic regimes in the Alberta Basin: A synthesis, in *Geothermics in Basin Analysis*, edited by A. Förster and D. F. Merriam, pp. 81-98, Kluwer Academic/Plenum Publisher, Dordrecht, the Netherlands.
- Bachu, S., J. R. Underschlutz, D. McPhee, and D. K. Cotterill (1991), Regional geology and hydrostratigraphy in northeast Alberta (Prepared for Conservation and Protection, Environment Canada), 162 pp, Alberta Geological Survey, Edmonton, Alberta, Canada.
- Bachu, S., J. R. Underschlutz, B. Hitchon, and D. K. Cotterill (1993), Regional-scale subsurface hydrogeology in Northeast Alberta, *Alberta Research Council Bulletin*, 61, 44 pp.
- Backus, G. E. (1962), Long-wave elastic anisotropy produced by horizontal layering, *Journal of Geophysical Research*, 67(11), 4427-4440, doi:10.1029/Jz067i011p04427.
- Bartetzko, A., H. Delius, and R. Pechnig (2005), Effect of compositional and structural variations on log responses of igneous and metamorphic rocks. I: mafic rocks, in *Petrophysical Properties of Crystalline Rocks*, edited, pp. 255-278, Geological Society, London.

- Barton, C, and M. D. Zoback (2002), Discrimination of natural fractures from drilling-induced wellbore failures in wellbore image data-implications for reservoir permeability, *SPE Reserv Eval Eng*, 5(3), 249-254.
- Barton, C., and D. Moos (2010), Geomechanical wellbore imaging: Key to managing the asset life cycle, in *Dipmeter and Borehole Image Log Technology: AAPG Memoir*, edited by M. Poppelreiter, C. Garcia-Carballido and M. A. Kraaijveld, pp. 81-112, American Association of Petroleum Geologists, Tulsa, Oklahoma.
- Barton, C, M. D. Zoback, and D. Moos (1995), Fluid-flow along potentially active faults in crystalline rock, *Geology*, 23(8), 683-686, doi:10.1130/0091-7613(1995)023<0683:FFAPAF>2.3.Co;2.
- Barton, C., D. Moos, and K. Tezuka (2009), Geomechanical wellbore imaging: Implications for reservoir fracture permeability, *AAPG Bulletin*, 93(11), 1551-1569, doi:10.1306/06180909030.
- Bassim, E. A. E. A., K. Yamaguchi, and D. Juandi (2009), Integrated fracture study using formation micro imager, stoneley waves and formation evaluation results in carbonate reservoir at Gulf of Suez, Egypt, in *SPE Middle East Oil and Gas Show and Conference*, edited, pp. 1-10, Kingdom of Bahrain.
- Bell, J. S. (1990), Investigation stress regimes in sedimentary basins using information from oil industry wireline logs and drilling records, in *Geological Applications of Wireline Logs*, edited by A. Hurst, M. Lovell and A. Morton, pp. 305-325, *Geol. Soc. Lond. Spec. Publ.*, London, UK.
- Bell, J. S. (1996a), *In-situ* stresses in sedimentary rocks (Part 1): Measurement techniques, *Geoscience Canada*, 23, 85-99.
- Bell, J. S. (1996b), *In-situ* stresses in sedimentary rocks (Part 2): Applications of stress measurements, *Geoscience Canada*, 23, 135-153.
- Bell, J. S., and D. I. Gough (1979), Northeast-southwest compressive stress in Alberta - Evidence from oil-wells, *Earth and Planetary Science Letters*, 45(2), 475-482, doi:10.1016/0012-821x(79)90146-8.
- Bell, J. S., and S. E. Grasby (2012), The stress regime of the Western Canadian Sedimentary Basin, *Geofluids*, 12, 150-165, doi:10.1111/j.1468-8123.2011.00349.x.
- Bell, J. S., and R. E. McCallum (1990), *In-situ* stresses in the Peace River Arch area, Western Canada, *Bulletin of Canadian Petroleum Geology*, 38A, 270-281.
- Bell, J. S., and P. R. Price (1989), *In-situ* stresses in Western Canada - Implications for the oil industry (Poster), in *Geological Survey of Canada Oil and Gas Forum*, Calgary, Alberta.
- Bell, J. S., P. R. Price, and P. J. McLellan (1994), *In-situ* stress in the Western Canada Sedimentary Basin, in *Geological Atlas of the Western Canada Sedimentary Basin*, edited by G. D. Mossop and I. Shetsen, pp. 439-446, Canadian Society of Petroleum Geologists and Alberta Research Council, Calgary, Alberta.
- Birch, F. (1960), The velocity of compressional waves in rocks to 10 kilobars (Part I), *J. Geophys. Res.*, 65, 1083-1102.
- Birch, F. (1961), The velocity of compressional waves in rocks to 10 kilobars (Part II), *J. Geophys. Res.*, 66, 2199-2224.

- Blöcher, M. G., G. Zimmermann, I. Moeck, W. Brandt, A. Hassanzadegan, and F. Magri (2010), 3D numerical modeling of hydrothermal processes during the lifetime of a deep geothermal reservoir, *Geofluids*, 10(3), 406-421, doi:10.1111/j.1468-8123.2010.00284.x.
- Block, L. V., C. H. Cheng, M. C. Fehler, and W. S. Phillips (1994), Seismic imaging using micro earthquakes induced by hydraulic fracturing, *Geophysics*, 59, 102-112.
- Boerner, D. E., R. D. Kurtz, J. A. Craven, G. M. Ross, and F. W. Jones (2000), A synthesis of electromagnetic studies in the Lithoprobe Alberta basement transect: Constraints on Paleoproterozoic indentation tectonics, *Canadian Journal of Earth Sciences*, 37(11), 1509-1534, doi:10.1139/cjes-37-11-1509.
- Boness, N. L., and M. D. Zoback (2004), Stress-induced seismic velocity anisotropy and physical properties in the SAFOD Pilot Hole in Parkfield, CA, *Geophys Res Lett*, 31(15), L15S17, doi:10.1029/2003gl019020.
- Bonner, S., M. Fredette, J. Lovell, B. Montaron, R. Rosthal, J. Tabanou, P. Wu, B. Clark, R. Mills, and R. Williams (1996), Resistivity while drilling—images from the string, *Oilfield Review*, 4-19.
- Bourbie, T., O. Coussy, and B. Zinszner (1987), *Acoustics of Porous Media*, 352 pp., Gulf Publishing Company, Houston, Texas.
- Bram, K., J. Draxler, G. Hirschmann, G. Zoth, S. Hiron, and M. Kuhr (1995), The KTB borehole - Germany's superdeep telescope into the Earth's crust, *Oilfield Review*, 4-22.
- Bremer, M. H., J. Kulenkampff, and J. R. Schopper (1992), Lithological and fracture response of common logs in crystalline rocks, in *Geological Applications of Wireline Logs II*, edited by A. Hurst, C. M. Griffiths and P. F. Worthington, pp. 221-234, Geological Society Special Publications, London, UK.
- Broggi, A., A. Lazzarotto, D. Liotta, G. Ranalli, and C. W. Group (2005), Crustal structures in the geothermal areas of southern Tuscany (Italy): Insights from the CROP 18 deep seismic reflection lines, *Journal of Volcanology and Geothermal Research*, 148(1-2), 60-80, doi:10.1016/j.volgeo.2005.03.014.
- Bruno, F., and F. Martillier (2000), Test of high-resolution seismic reflection and other geophysical techniques on the Boup landslide in the Swiss Alps, *Surv Geophys*, 21(4), 333-348.
- Bruno, P. P. G., V. Di Fiore, and A. Rapolla (2002), Seismic reflection data processing in active volcanic areas: an application to Campi Flegrei and Somma Vesuvius offshore (Southern Italy), *Annals of Geophysics*, 45(6), 753-768.
- Bruno, P. P. G., V. Paoletti, M. Grimaldi, and A. Rapolla (2000), Geophysical exploration for geothermal low enthalpy resources in Lipari Island, Italy, *Journal of Volcanology and Geothermal Research*, 98(1-4), 173-188, doi:10.1016/S0377-0273(99)00183-3.
- Bücker, C., and L. Rybach (1996), A simple method to determine heat production from gamma-ray logs, *Marine and Petroleum Geology*, 13(4), 373-375, doi:10.1016/0264-8172(95)00089-5.
- Burton, A., and L. Lines (1996), VSP detection of interbed multiples using inside-outside corridor stacking, *Canadian Journal of Exploration Geophysics*, 32(2), 113-120.
- Burwash, R. A. (1979), Uranium and thorium in the Precambrian basement of western Canada. II. Petrologic and tectonic controls, *Canadian Journal of Earth Sciences*, 16(3), 472-483, doi:10.1139/e79-043.

- Burwash, R. A., and R. W. Burwash (1989), Radioactive heat generation map of the subsurface Precambrian of Alberta, Geological Survey of Canada Paper 89-1C, Current Research, Part C, Canadian Shield, 363-368.
- Burwash, R. A., and R. R. Culbert (1976), Multivariate geochemical and mineral patterns in the Precambrian basement of western Canada, Canadian Journal of Earth Sciences, 13(1), 1-18, doi:10.1139/e76-001.
- Burwash, R. A., and G. L. Cumming (1976), Uranium and thorium in the Precambrian basement of western Canada. I. Abundance and distribution, Canadian Journal of Earth Sciences, 13(2), 284-293, doi:10.1139/e76-030.
- Burwash, R. A., A. G. Green, A. M. Jessop, and E. R. Kanasewich (1993), Geophysical and petrological characteristics of the basement rocks of the Western Canada Basin, in Sedimentary Cover of the Craton in Canada, edited by D. F. Stott and J. D. Aitken, pp. 55-77, Geological Survey of Canada.
- Burwash, R. A., C. R. McGregor, and J. A. Wilson (1994), Precambrian basement beneath the Western Canada Sedimentary Basin, in Geological Atlas of the Western Canada Sedimentary Basin, edited by G. D. Mossop and I. Shetsen, pp. 49-56, Canadian Society of Petroleum Geologists and Alberta Research Council, Calgary, Alberta.
- Cameli, G. M., F. Batini, I. Dini, J. M. Lee, R. L. Gibson, and M. N. Toksoz (1995), Seismic delineation of a geothermal reservoir in the Monteverdi area from VSP data, paper presented at Proceedings of the WGC.
- Cameli, G. M., A. Cerccarelli, I. Dini, and A. Mazzotti (2000), Contribution of the seismic reflection method to the location of deep fractured levels in the geothermal fields of Southern Tuscany (Central Italy), paper presented at Proceedings World Geothermal Congress, Kyushu-Tohoku, Japan, May 28 - June 10, 2000.
- Canadian Association of Petroleum Producers (CAPP) (2009), Oil Sands CO2 Statistics, Retrieved on March 12, 2013 from <http://www.capp.ca/library/statistics/basic/Pages/default.aspx>.
- Canadian Association of Petroleum Producers (CAPP) (2013), Statistical Handbook for Canada's Upstream Petroleum Industry, 221 pp., Canadian Association of Petroleum Producers, Calgary, Alberta, Canada.
- Canales, L. L. (1984), Random noise reduction, paper presented at 1984 SEG Annual Meeting, Society of Exploration Geophysicists, Atlanta, Georgia.
- Carrigy, M. A. (1966), Lithology of the Athabasca Oil Sands, Research Council of Alberta Bulletin, 18, 55 pp., Research Council of Alberta, Edmonton, Alberta.
- Castagna, J. P., M. L. Batzle, and R. L. Eastwood (1985), Relationships between compressional-wave and shear-wave velocities in clastic silicate rocks, Geophysics, 50(4), 571-581, doi:10.1190/1.1441933.
- Chacko, T., S. K. De, R. A. Creaser, and K. Muehlenbachs (2000), Tectonic setting of the Taltson magmatic zone at 1.9-2.0 Ga: a granitoid-based perspective, Canadian Journal of Earth Sciences, 37(11), 1597-1609, doi:10.1139/cjes-37-11-1597.
- Chemali, R., S. Gianzero, R. Strickland, and S. M. Tijani (1983), The shoulder bed effect on the dual laterolog and its variation with the resistivity of the borehole fluid, paper presented at SPWLA Twenty-Fourth Annual Logging Symposium, Society of Petrophysicists and Well-Log Analysts, June 27-30, 1983.

- Cholach, P. Y., and D. R. Schmitt (2006), Intrinsic elasticity of a textured transversely isotropic muscovite aggregate: Comparisons to the seismic anisotropy of schists and shales, *Journal of Geophysical Research*, 111(B9), 18, doi:10.1029/2005jb004158.
- Chopra, P., É. Papp, and D. Gibson (2002), Geophysical well logging, in *Geophysical and Remote Sensing Methods for Regolith Exploration*, CRCLEME Open File Report 144, edited by É. Papp, pp. 105-115.
- Christie, P., I. Gollifer, and D. Cowper (2006), Borehole seismic studies of a volcanic succession from the Lopra-1/1A borehole in the Faroe Islands, northern North Atlantic, *Geological Survey of Denmark and Greenland Bulletin*, 9, 23-40.
- Cocherie, C., C. Guerrot, C. M. Fanning, and A. Genter (2004), Datation U-Pb des deux Faciès du granite de Soultz (Fossé rhénan, France), *C. R. Geoscience Géochimie (Géochronologie)*, 336, 775-787.
- Combs, J., and D. Hadly (1977), Microearthquake investigation of the Mesa geothermal anomaly, Imperial Valley, California, *Geophysics*, 42, 17-33.
- Cotterill, D. K., and W. N. Hamilton (1995), *Geology of Devonian limestones in northeast Alberta* (Prepared for Canada-Alberta MDA Project M92-04-14), Alberta Geological Survey, Alberta Research Council, Open File Report 1995-07(March), 91 pp.
- Crampin, S. (1981), A review of a wave motion in anisotropic and cracked elastic media, *Wave Motion*, 3, 343-391.
- Crampin, S. (1990), Alignment of near surface inclusions and appropriate crack geometries for hot dry rock experiments, *Geophys. Prospect*, 38, 621-631.
- Crickmay, C. H. (1957), *Elucidation of Some Western Canada Devonian formations*, 14 pp., E. de Millie Books, Calgary, Alberta.
- Cuenot, N., C. Dorbath, and L. Dorbath (2008), Analysis of the microseismicity induced by fluid injections at the EGS site of Soultz-sous-Forêts (Alsace, France): Implications for the characterization of the geothermal reservoir properties, *Pure appl. geophys.*, 165, 797-828, doi:10.1007/s00027-008-0335-7.
- Dahle, A., H. Gjoystdal, G. Grammeltvedt, and T. Soyland Hansen (1985), Application of seismic reflection methods for ore prospecting in crystalline rocks, *First Breaks*, 3(2), 9-16.
- Davis, C. E., and H. Y. Tammemagi (1982), A case history of a deep borehole in the Reynard Lake pluton, Saskatchewan-Manitoba border, 53 pp., Whiteshell Nuclear Research Establishment, Pinawa, Manitoba.
- de Parscau, J. (1991), P- and SV-wave transversely isotropic phase velocities analysis from VSP data, *Geophys J Int*, 107(3), 629-638, doi:10.1111/j.1365-246X.1991.tb01422.x.
- Dehghannejad, M., C. Juhlin, A. Malehmir, P. Skytta, and P. Weihed (2010), Reflection seismic imaging of the upper crust in the Kristineberg mining area, northern Sweden, *J Appl Geophys*, 71(4), 125-136, doi:10.1016/j.jappgeo.2010.06.002.
- Drury, M. J. (1988), Tectonothermics of the North-American Great Plains basement, *Tectonophysics*, 148(3-4), 299-307, doi:10.1016/0040-1951(88)90136-9.
- Du, Z., G. R. Foulger, and W. Mao (2000), Noise reduction for broad-band, three-component seismograms using data-adaptive polarization filters, *Geophys J Int*, 141, 820-828.

- Duncan, G., and G. Beresford (1994), Slowness adaptive F-K filtering of prestack seismic data, *Geophysics*, 59(1), 140-147, doi:10.1190/1.1443525.
- Dyer, B. C., U. Schanz, F. Ladner, M. O. Häring, and T. Spillman (2008), Microseismic imaging of a geothermal reservoir stimulation, *The Leading Edge*, 856-869.
- Eaton, D. W., B. Milkereit, and M. Salisbury (eds.) (2003), *Hardrock Seismic Exploration*, 275 pp., Society of Exploration Geophysicists, Tulsa, Oklahoma.
- Eisenmann, P., M.-T. Gounot, B. Juchereau, J.-C. Trouiller, and S. J. Whittaker (1994), Improved Rxo measurements through semi-active focusing, *SPE Annual Technical Conference and Exhibition*, paper SPE 28437, 781-794.
- Ellis, D., C. Flaum, E. Marienbach, C. Roulet, and B. Seeman (1985), Litho-density tool calibration, in *58th SPE Annual Technical Conference and Exhibition*, paper SPE12048, pp. 515-520.
- Ellis, D. V., C. R. Case, and J. M. Chiaramonte (2003), Tutorial - porosity from neutron logs I: Measurement, *Petrophysics*, 44(6), 383-395.
- Ellis, D. V., and J. M. Singer (2007), Gamma ray devices, in *Well Logging for Earth Scientists*, pp. 267-288, Springer, Dordrecht, The Netherlands.
- Energy Resources Conservation Board (ERCB) (2009), *Table of Formations, Alberta*, ERCB Information Services, Calgary, Alberta, Canada.
- Farag, S., C. Mas, P. D. Maizeret, B. Li, and V. H. Le (2010), An integrated workflow for granitic-basement-reservoir evaluation, *SPE Reserv Eval Eng*, 13(6), 893-905.
- Fehler, M., L. House, and H. Kaieda (1987), Determining planes along which earthquakes occur - method and application to earthquakes accompanying hydraulic fracturing, *J Geophys Res-Solid*, 92(B9), 9407-9414, doi:10.1029/Jb092ib09p09407.
- Fehler, M. C. (1989), Stress-control of seismicity patterns observed during hydraulic fracturing experiments at the Fenton Hill hot dry rock geothermal-energy site, New-Mexico, *Int J Rock Mech Min*, 26(3-4), 211-219, doi:10.1016/0148-9062(89)91971-2.
- Fenton, M. M., and J. G. Pawlowicz (2000), Quaternary geology northern Alberta: Information sources and implications for diamond exploration, *EUB Geo-Note* 2000-04, 19 pp.
- Fenton, M. M., B. T. Schreiner, E. Nielsen, and J. G. Pawlowicz (1994), Quaternary geology of the Western Plains, in *Geological Atlas of the Western Canada Sedimentary Basin*, edited by G. D. Mossop and I. Shetsen, pp. 413-420, Canadian Society of Petroleum Geologists and Alberta Geological Survey - Alberta Research Council, Calgary.
- Fenton, M. M., E. J. Waters, S. M. Pawley, N. Atkinson, D. J. Utting, and K. McKay (2013), *Surficial Geology of Alberta*, Alberta Energy Regulator, AER/AGS Map 601, scale 1: 1,000,000.
- Flinn, E. A. (1965), Signal analysis using rectilinearity and direction of particle motion, *Proceedings of the IEEE*, 53, 1874-1876.
- Fordjor, C. K., J. S. Bell, and D. I. Gough (1983), Breakouts in Alberta and stress in the North America Plate, *Canadian Journal of Earth Sciences*, 20, 1445-1455.
- Gadallah, M. R., and R. L. Fisher (2005), *Applied Seismology: A Comprehensive Guide to Seismic Theory and Application*, 1st American ed., 473 pp., PennWell Corporation, Tulsa, Oklahoma.

- Galbraith, M. (2002), 3D geometry for demultiple and noise cancellation, *The Leading Edge*, 838-851.
- GEDCO (2010), VISTA 2D/3D Seismic Data Processing Tutorial Manual Version 10.0, 452 pp., Geophysical Exploration & Development Corporation, Calgary, Alberta.
- Georgsson, L. S. (2010), Geophysical methods used in geothermal exploration, paper presented at UNU-GTP, GDC and KenGen, Lake Bogoria and Lake Naivasha, Kenya, Oct. 29 - Nov. 19, 2010.
- Geoscience Data Repository (2012a), Aeromagnetic Data, Retrieved on April 10, 2013 from http://gdrdap.agg.nrcan.gc.ca/geodap/index_e.html.
- Geoscience Data Repository (2012b), Gravity Data, Retrieved on April 10, 2013 from http://gdrdap.agg.nrcan.gc.ca/geodap/index_e.html.
- Ghomshei, M. M., and T. Sadler-Brown (1996), Direct use energy from the hot springs and subsurface geothermal resources of British Columbia, 33 pp., Canadian Geothermal Energy Association, Richmond, British Columbia.
- Goldberg, D., C. Broglia, and K. Becker (1991), Fracturing, alteration and permeability: *In-situ* properties in hole 735B, paper presented at Proceedings of the Ocean Drilling Program, Scientific Results, College Station, Texas.
- Goldberg, D., and K. Burgdorff (2005), Natural fracturing and petrophysical properties of the Palisades dolerite sill, in *Petrophysical Properties of Crystalline Rocks*, edited by P. K. Harvey, T. S. Brewer, P. A. Pezard and V. A. Petrov, pp. 25-36, Geological Society, London.
- Gosnold, W., J. Majorowicz, R. Klenner, and S. Hauck (2011), Implications of post-glacial warming for northern hemisphere heat flow, *GRC Transactions*, 35, 795-799.
- Gough, D. I., and J. S. Bell (1982), Stress orientations from borehole wall fractures with examples from Colorado, east Texas, and northern Canada, *Canadian Journal of Earth Sciences*, 19(7), 1358-1370.
- Grasby, S. E., *et al.* (2011), Geothermal energy resource potential of Canada, Geological Survey of Canada Open File 6914, 1-322, doi:10.495/288745.
- Green, A. G., and J. A. Mair (1983), Subhorizontal fractures in a granitic pluton: their detection and implication for radioactive waste disposal, *Geophysics*, 48, 1428-1449.
- Green, A. S. P., R. Baria, A. Madge, and R. Jones (1987), Fault plane analysis of microseismicity induced by fluid injections into the Carnmellis granite, in *Eng. Geol. Underground Movements 15*, edited by F. G. Bell, M. G. Culshaw, J. C. Cripps and M. A. Lovell, pp. 415-422, Geological Society (London) Eng. Geol. Spec. Pub., London, UK.
- Gritto, R., T. M. Daley, and E. L. Majer (2003), Estimating subsurface topography from surface-to-borehole seismic studies at the Rye Patch geothermal reservoir, Nevada, USA, *Geothermics*, 32(3), 275-295, doi:10.1016/S0375-6505(03)00022-1.
- Guerrero-Lemus, R., and J. M. Martínez-Duart (2013), Geothermal energy, in *Renewable Energies and CO2: Cost Analysis, Environmental Impacts and Technological Trends - 2012 Edition*, pp. 199-214, Springer-Verlag, London, doi:10.1007/978-1-4471-4385-7_10.
- Gulunay, N. (1986), FX decon and the complex Weiner prediction filter for random noise attenuation on stacked data, paper presented at SEG 56th Annual International Meeting, Houston, Texas.

- Gunasekera, R. C., G. R. Foulger, and B. R. Julian (2003), Reservoir depletion at The Geysers geothermal area, California, shown by four-dimensional seismic tomography, *J Geophys Res-Sol Ea*, 108(B3), 1-11, doi:10.1029/2001jb000638.
- Gupta, H. K., and S. Roy (2007), *Geothermal Energy: An Alternative Resource for the 21st Century*, 1st ed., 279 pp., Elsevier Science & Technology.
- Gupta, H. K., R. W. Ward, and T. L. Lin (1982), Seismic-wave velocity investigation at the geysers - Clear Lake geothermal field, California, *Geophysics*, 47(5), 819-824, doi:10.1190/1.1441349.
- Haimson, B. C., and F. H. Cornet (2003), ISRM suggested methods for rock stress estimation - part 3: hydraulic fracturing (HF) and/or hydraulic testing of pre-existing fractures (HTPF), *International Journal of Rock Mechanics and Mining Sciences*, 40, 1011-1020.
- Hallenburg, J. K. (1984), *Geophysical Logging for Mineral and Engineering Applications*, 254 pp., Pennwell Corp.
- Hardage, B. A. (1985), *Vertical Seismic Profiling*, 2nd ed., 509 pp., Geophysical Press, London, UK.
- Hardage, B. A. (2000), *Vertical Seismic Profiling: Principles*, 3rd updated and revised ed., 552 pp., Pergamon, Amsterdam.
- Harvey, P. K., T. S. Brewer, P. A. Pezard, and V. A. Petrov (eds) (2005), *Petrophysical Properties of Crystalline Rocks*, 351 pp., Geological Society, London, UK.
- Hearst, J. R., P. H. Nelson, and F. L. Paillet (2000), *Well Logging for Physical Properties*, 2nd ed., 483 pp., John Wiley & Sons Ltd., West Sussex, UK.
- Hedin, P., C. Juhlin, and D. G. Gee (2012), Seismic imaging of the Scandinavian Caledonides to define ICDP drilling sites, *Tectonophysics*, 554, 30-41, doi:10.1016/j.tecto.2012.05.026.
- Heffer, K. J., and J. Lean (1993), Earth stress orientation - a control on, and a guide to, flooding directionality in a majority of reservoirs, in *Reservoir Characterisation III*, edited by W. Linville, pp. 799-822, PennWell Books, Tulsa, Oklahoma.
- Heinonen, S., P. Heikkinen, J. Kousa, I. T. Kulkkonen, and D. B. Snyder (2013), Enhancing hardrock seismic images: Reprocessing of high resolution of seismic reflection data from Vihanti, Finland, *J Appl Geophys*, 93, 1-11.
- Henderson, J. B., P. H. McGrath, D. T. James, and R. T. Macfie (1987), An integrated geological, gravity and magnetic study of the Artillery Lake area and Thelon tectonic Zone, District of Mackenzie, in *Current Research, Part A*, pp. 803-814, Geological Survey of Canada, Paper 87-1A.
- Henkel, H., and M. Guzman (1977), Magnetic features of fracture zones, *Geoexploration*, 15(3), 173-181, doi:10.1016/0016-7142(77)90024-2.
- Henley, D. C. (2000), Wavefield separation and other useful applications in the radial trace domain, paper presented at SEG Annual Meeting, Society of Exploration Geophysicists, Calgary, Alberta, August 6 - 11, 2000.
- Henley, D. C. (2001), Revisiting the radial trace transform, *CSEG Recorder*, 21-29.
- Henley, D. C. (2003), Coherent noise attenuation in the radial trace domain, *Geophysics*, 68(4), 1408-1416, doi:10.1190/1.1598134.

- Hesselbo, S. P. (1996), Spectral gamma-ray logs in relation to clay mineralogy and sequence stratigraphy, Cenozoic of the Atlantic margin, offshore New Jersey, in Proceedings of the Ocean Drilling Program, Scientific Results, edited by G. S. Mountain, K. G. Miller, P. Blum, C. W. Poag and D. C. Twitchell, pp. 411-422.
- Hill, D. P. (1976), Structure of Long-Valley Caldera, California, from a seismic refraction experiment, *Journal of Geophysical Research*, 81(5), 745-753, doi:10.1029/Jb081i005p00745.
- Hinds, R. C., N. L. Anderson, and R. D. Kuzmiski (1996), *VSP Interpretative Processing: Theory and Practice*, 214 pp., Society of Exploration Geophysicists, Tulsa, Oklahoma.
- Hoffman, P. F. (1989), Precambrian geology and tectonic history of North America, in *The Geology of North America - Overview*, pp. 447-512, The Geological Society of America.
- Hooijkaas, G. R., A. Genter, and C. Dezayes (2007), Deep-seated geology of the granite intrusions at the Soultz EGS site based on data from 5 km-deep boreholes, *Geothermics*, 35, 484-506.
- Hope, J., and D. Eaton (2002), Crustal structure beneath the Western Canada Sedimentary Basin: constraints from gravity and magnetic modelling, *Canadian Journal of Earth Sciences*, 39(3), 291-312, doi:10.1139/E01-060.
- Hornby, B. E., and W. F. Murphy (1987), Vp/Vs in unconsolidated oil sands - shear from Stoneley, *Geophysics*, 52(4), 502-513, doi:10.1190/1.1442320.
- Hunt, C. W., L. G. Collins, and E. A. Skobelin (1992), *Expanding Geospheres: Energy and Mass Transfers from Earth's Interior*, 436 pp., Polar Publishing, Calgary, Alberta.
- Isaacs, A. J., J. P. Evans, P. T. Kolesar, and T. Nohara (2008), Composition, microstructures, and petrophysics of the Mozumi fault, Japan: *In-situ* analyses of fault zone properties and structure in sedimentary rocks from shallow crustal levels, *J Geophys Res-Sol Ea*, 113(B12), 17, doi 10.1029/2007jb005314.
- Iyers, H. M. (1978), Status of seismic methods in geothermal exploration, paper presented at APSMAGS Workshop, Taos, NM, pp. 11-26.
- Jackson, P. D., S. Shedlock, J. Willis-Richards, and A. S. P. Green (1992), Enhanced resolution resistivity logging for fracture studies, Geological Society, London, Special Publications, 65(1), 265-274, doi:10.1144/gsl.sp.1992.065.01.20.
- Jones, F. W., and J. A. Majorowicz (1987), Regional trends in radiogenic heat-generation in the Precambrian basement of the Western Canadian Basin, *Geophys Res Lett*, 14(3), 268-271, doi:10.1029/G1014i003p00268.
- Jongmans, D., and S. Garambois (2007), Geophysical investigation of landslides: a review, *Bulletin De La Societe Geologique De France*, 178(2), 101-112, doi:10.2113/gssgfbull.178.2.101.
- Juhlin, C. (1995), Imaging of fracture-zones in the Finnsjon area, Central Sweden, using the seismic-reflection method, *Geophysics*, 60(1), 66-75, doi:10.1190/1.1443764.
- Jurkevics, A. (1988), Polarization analysis of 3-component array data, *Bulletin of the Seismological Society of America*, 78(5), 1725-1743.
- Kashubin, A. S., and C. Juhlin (2010), Mapping of crustal scale tectonic boundaries in the Ossa-Morena Zone using reprocessed IBERSEIS reflection seismic data, *Tectonophysics*, 489(1-4), 139-158, doi:10.1016/j.tecto.2010.04.010.

- Kebaili, A., and D. R. Schmitt (1996), Velocity anisotropy observed in wellbore seismic arrivals: Combined effects of intrinsic properties and layering, *Geophysics*, 61(1), 12-20, doi:10.1190/1.1443932.
- Kebaili, A., and D. R. Schmitt (1997), Ultrasonic anisotropic phase velocity determination with the Radon transformation, *J Acoust Soc Am*, 101(6), 3278-3286, doi:10.1121/1.418344.
- Keys, W. S. (1979), Borehole geophysics in igneous and metamorphic rocks, in *SPWLA Twentieth Annual Logging Symposium*, June 3-6, 1979, 26 pp.
- Keys, W. S. (1990), Borehole geophysics applied to ground-water investigations, in *Techniques of Water-Resources Investigations of the United States Geological Survey*, U.S. Geological Survey, 150 pp.
- Krammer, K. (1990), 19. Magnetic susceptibility log measured in Hole 395A, Leg 109, in *Proceedings of the Ocean Drilling Program, Scientific Results*, Vol. 106/109, edited by R. Detrick, J. Honnorez, W. B. Bryan and T. Juteau, pp. 231-235.
- Kuzmiski, R. D., B. Charters, and M. Galbraith (2009), Processing considerations for 3D VSP, *CSEG Recorder*, 30-40.
- Langenberg, C. W., F. J. Hein, D. Lawton, and J. Cunningham (2002), Seismic modeling of fluvial-estuarine deposits in the Athabasca oil sands using ray-tracing techniques, *Steepbank River area, northeastern Alberta*, *Bulletin of Canadian Petroleum Geology*, 50(1), 178-204.
- Langmuir, D., and J. S. Herman (1980), The mobility of thorium in natural-waters at low-temperatures, *Geochim Cosmochim Acta*, 44(11), 1753-1766, doi:10.1016/0016-7037(80)90226-4.
- Li, X. P., and S. Richwalski (1996), Seismic attenuation and velocities of P- and S-waves in the German KTB area, *J Appl Geophys*, 36(2-3), 67-76, doi:10.1016/S0926-9851(96)00036-5.
- Li, Y. D., W. Rabbel, and R. Wang (1994), Investigation of permeable fracture-zones by tube-wave analysis, *Geophys J Int*, 116(3), 739-753, doi:10.1111/j.1365-246X.1994.tb03294.x.
- Liberty, L. (1998), Seismic reflection imaging of a geothermal aquifer in an urban setting, *Geophysics*, 63(4), 1285-1294, doi:10.1190/1.1444430.
- Louie, J. N., S. K. Pullammanappallil, and W. Honjas (2011), Advanced seismic imaging for geothermal development, paper presented at *New Zealand Geothermal Workshop 2011 Proceedings*, Auckland, New Zealand, November 21-23, 2011.
- Luo, M. A., and H. P. Pan (2010), Well logging responses of UHP metamorphic rocks from CCSD main hole in Sulu Terrane, Eastern Central China, *J Earth Sci-China*, 21(3), 347-357, doi:10.1007/s12583-010-0098-9.
- Lüschen, E., K. Bram, W. Söllner, and S. Sobolev (1996), Nature of seismic reflections and velocities from VSP-experiments and borehole measurements at the KTB deep drilling site in southeast Germany, *Tectonophysics*, 264, 309-326.
- Luthi, S. M. (2005), Fractured reservoir analysis using modern geophysical well techniques: Application to basement reservoirs in Vietnam, in *Petrophysical Properties of Crystalline Rocks*, edited by P. K. Harvey, T. S. Brewer, P. A. Pezard and V. A. Petrov, pp. 95-106, Geological Society, London.
- Lyatsky, H., D. Pana, and M. Grobe (2005), Basement structure in central and southern Alberta: Insights from gravity and magnetic maps, *EUB/AGS Special Report*, 72, 76 pp.

- Lyatsky, H., and D. I. Pană (2003), Catalogue of selected regional gravity and magnetic maps of northern Alberta, EUB/AGS Special Report, 56, 40 pp.
- Machel, H. G., P. A. Cavell, B. E. Buschkuehle, and K. Michael (2000), Tectonically induced fluid flow in Devonian carbonate aquifers of the Western Canada Sedimentary Basin, *Journal of Geochemical Exploration*, 69, 213-217, doi:10.1016/S0375-6742(00)00093-5.
- Mah, M. (1999), Experimental determination of the elastic coefficients of anisotropic materials with the slant-stack method, M.Sc. thesis, University of Alberta, Edmonton, Alberta, Canada.
- Majer, E. L., R. Baria, M. Stark, S. Oates, J. Bommer, B. Smith, and H. Asanuma (2007), Induced seismicity associated with enhanced geothermal systems, *Geothermics*, 36(3), 185-222, doi:10.1016/j.geothermics.2007.03.003.
- Majer, E. L., and T. V. McEvilly (1979), Seismological investigations at the Geysers geothermal field, *Geophysics*, 44(2), 246-269, doi:10.1190/1.1440965.
- Majer, E. L., and J. E. Peterson (2005), Application of microearthquake monitoring for evaluating and managing the effects of fluid injection at naturally fractured EGS sites, *Geotherm. Resour. Counc. Trans.*, 29, 103-107.
- Majorowicz, J., W. Gosnold, A. Gray, J. Safanda, R. Klenner, and M. Unsworth (2012), Implications of post-glacial warming for Northern Alberta heat flow - Correcting for the underestimate of the geothermal potential, *GRC Transactions*, 36, 693-698.
- Majorowicz, J. A., and M. C. Moore (2008), Enhanced geothermal systems (EGS) potential in the Alberta Basin, 50 pp, University of Calgary, Calgary, Alberta.
- Malin, P. (1994), The seismology of extensional hydrothermal systems, *Geothermal Resources Council Transactions*, 18, 17-22.
- Mandler, H. A. F., and R. M. Clowes (1997), Evidence for extensive tabular intrusions in the Precambrian shield of western Canada: A 160-km-long sequence of bright reflections, *Geology*, 25(3), 271-274, doi:10.1130/0091-7613(1997)025<0271:Efetii>2.3.Co;2.
- Mandler, H. A. F., and R. M. Clowes (1998), The HSI bright reflector: further evidence for extensive magmatism in the Precambrian of Western Canada, *Tectonophysics*, 288(1-4), 71-81, doi:10.1016/S0040-1951(97)00284-9.
- Manning, C. E., and S. E. Ingebritsen (2010), Permeability of the continental crust: Implications of geothermal data and metamorphic systems, *Review of Geophysics*, 37(1), 127-150.
- Manzella, A. (2000), *Geophysical Methods in Geothermal Exploration*, 40 pp., Italian National Research Council, International Institute for Geothermal Research, Pisa, Italy.
- March, D. W., and A. D. Bailey (1983), A review of the two dimensional transform and its use in seismic processing, *First Breaks*, 1(1), 9-21.
- McEwen, T. J., D. M. McCann, and S. Shedlock (1985), Fracture-analysis from borehole geophysical techniques in crystalline rocks, *Q J Eng Geol*, 18(4), 413-436, doi:10.1144/Gsl.Qjeg.1985.018.04.13.
- McNeill, J. D., J. A. Hunter, and M. Bosner (1996), Application of a borehole induction magnetic susceptibility logger to shallow lithological mapping, *Journal of Environmental and Engineering Geophysics*, 1(B), 77-90.

- Medeiros, W. E., and O. A. L. De Lima (1990), A geoelectrical investigation for ground-water in crystalline terrains of Central Bahia, Brazil, *Ground Water*, 28(4), 518-523, doi:10.1111/j.1745-6584.1990.tb01707.x.
- Melosh, G., W. Cumming, J. Casteel, K. Niggemann, and B. Fairbank (2010), Seismic reflection data and conceptual models for geothermal development in Nevada, paper presented at Proceedings World Geothermal Congress, Bali, Indonesia, April 25-29, 2010.
- Meyer, M. T., M. E. Bickford, and J. F. Lewry (1992), The Wathamun batholith: An early Proterozoic continental arc in the Trans-Hudson orogenic belt, Canada, *Bulletin Geological Society America*, 104, 1073-1085.
- Milkereit, B., E. Adam, A. Barnes, C. Beaudry, R. Pineault, and A. Cinq-Mars (1992), An application of reflection seismology to mineral exploration in the Matagami area, Abitibi belt, Quebec, *Current Research, Part C., Geological Survey of Canada, Paper 92-1C*, 13-18.
- Milkereit, B., and D. Eaton (1998), Imaging and interpreting the shallow crystalline crust, *Tectonophysics*, 286(1-4), 5-18, doi:10.1016/S0040-1951(97)00251-5.
- Miller, R. D. (1992), Normal moveout stretch mute on shallow-reflection data, *Geophysics*, 57(11), 1502-1507, doi:10.1190/1.1443217.
- Mjelde, R. (1992), Reflection and polarization of tube waves as seen in VSP data, *Geophysical Prospecting*, 40(6), 605-617, doi:10.1111/j.1365-2478.1992.tb00544.x.
- Montalbe, J. F., and E. R. Kanasewi (1970), Enhancement of teleseismic body phases with a polarization filter, *Geophysical Journal of the Royal Astronomical Society*, 21(2), 119-129, doi:10.1111/j.1365-246X.1970.tb01771.x.
- Moon, W., A. Carswell, R. Tang, and C. Dilliston (1986), Radon-transform wave field separation for vertical seismic profiling data, *Geophysics*, 51(4), 940-947, doi:10.1190/1.1442151.
- Mwenifumbo, C. J., B. E. Elliott, C. W. Jefferson, G. R. Bernius, and K. A. Pflug (2004), Physical rock properties from the Athabasca Group: designing geophysical exploration models for unconformity uranium deposits, *J Appl Geophys*, 55(1-2), 117-135, doi:10.1016/j.jappgeo.2003.06.008.
- Mwenifumbo, C. J., and A. L. Mwenifumbo (2012), Borehole geophysical logging in the Flin Flon Mining Camp, Geological Survey of Canada, Open File, 1-75, doi:10.4095/291534.
- Nagano, K., H. Moriya, H. Asanuma, M. Sato, H. Niitsuma, and H. Kaieda (1994), Downhole AE measurement of hydraulic fracturing in Ogachi HDR model field, *J. Geotherm. Res. Soc. Japan*, 16, 85-108.
- Nakagome, O., T. Uchida, and T. Horikoshi (1998), Seismic reflection and VSP in the Kakkonda geothermal field, Japan: Fractured reservoir characterization, *Geothermics*, 27(5-6), 535-552, doi:10.1016/S0375-6505(98)00032-7.
- Nedimović, M. R., and G. F. West (2003), Crooked-line 2D seismic reflection imaging in crystalline terrains: Part 1, data processing, *Geophysics*, 68(1), 274-285, doi:10.1190/1.1543213.
- Nickerson, B. (2007), *Seismic Methods for Summer Students*, 210 pp., Global Geosolutions Inc., Calgary, Alberta.
- Niitsuma, H., *et al.* (1999), Current status of seismic and borehole measurements for HDR/HWR development, *Geothermics*, 28, 475-490.

- Nishizawa, O., C. Pearson, and J. Albright (1983), Properties of seismic-wave scattering around water injection well at Fenton Hill hot dry rock geothermal site, *Geophys Res Lett*, 10(1), 101-104, doi:10.1029/G1010i001p00101.
- Ogunsuyi, F., and D. R. Schmitt (2011), Integrating seismic-velocity tomograms and seismic imaging: Application to the study of a buried valley, in *Near-surface Seismology and Ground Penetrating Radar*, edited by R. D. Miller, J. D. Bradford and K. Holliger, pp. 361-378, Society of Exploration Geophysicists, Tulsa, Oklahoma.
- Okaya, D., W. Rabbel, T. Beilecke, and J. Hasenclever (2004), P wave material anisotropy of a tectno-metamorphic terrane: An active source seismic experiment at the KTB super-deep drill hole, southeast Germany, *Geophys Res Lett*, 31(L24620), 1-4, doi:10.1029/2004GL020855.
- Olhoeft, G. R., and J. G. R. (1989), *Densities of rocks and minerals*, CRC Press, Boca Raton, FL.
- Paillet, F. L., and A. E. Hess (1986), *Geophysical well-log analysis of fractured crystalline rocks at East Bull Lake, Ontario, Canada*, 37 pp, U.S. Dept. of the Interior, Geological Survey, Denver, Colorado.
- Pálmason, G. (1975), *Geophysical methods in geothermal exploration*, paper presented at Proceedings of the 2nd U.N. Symposium on the Development and Use of Geothermal Resources, National Energy Authority, San Francisco, U. S. A., May 20-29, 1975.
- Paná, D. I. (2003), *Precambrian basement of the Western Canada Sedimentary Basin in Northern Alberta*, 39 pp, Alberta Geological Survey, Edmonton, Alberta.
- Paulen, R., R. Rice, and M. Gingras (2004), *Geology of the Fort McMurray Area, Northeast Alberta*, 68 pp, Edmonton Geological Society, Edmonton, Alberta.
- Pawlowicz, J. G., and M. M. Fenton (1995), *Bedrock Topography Map of Alberta (1:2000,000 scale)*, Map 226, Alberta Geological Survey, Edmonton, Alberta.
- Pechinig, R., H. Delius, and A. Bartetzko (2005), Effect of compositional variations on log responses of igneous and metamorphic rocks. II: acid and intermediate rocks, in *Petrophysical Properties of Crystalline Rocks*, edited by P. K. Harvey, T. S. Brewer, P. A. Pezard and V. A. Petrov, pp. 279-300, Geological Society Special Publications, London, UK.
- Pechinig, R., S. Haverkamp, J. Wohlenberg, G. Zimmermann, and H. Burkhardt (1997), Integrated log interpretation in the German Continental Deep Drilling Program: Lithology, porosity, and fracture zones, *J Geophys Res-Sol Ea*, 102(B8), 18363-18390, doi:10.1029/96jb03802.
- Pezard, P. A., and S. M. Luthi (1988), Borehole electrical images in the basement of the Cajon Pass Scientific Drillhole, California - fracture identification and tectonic implications, *Geophys Res Lett*, 15(9), 1017-1020, doi:10.1029/G1015i009p01017.
- Pezard, P. A. (1990), Electrical properties of mid ocean ridge basalt and implications for the structure of the upper oceanic crust in hole 504B, *Journal of Geophysical Research*, 95, doi:10.1029/90JB00268.
- Pilkington, M., W. F. Miles, G. M. Ross, and W. R. Roest (2000), Potential-field signatures of buried Precambrian basement in the Western Canada Sedimentary Basin, *Canadian Journal of Earth Sciences*, 37(11), 1453-1471, doi:10.1139/cjes-37-11-1453.
- Place, J., J. Sausse, J. M. Marthelot, M. Diraison, Y. Geraud, and C. Naville (2011), 3-D mapping of permeable structures affecting a deep granite basement using isotropic 3C VSP data, *Geophys J Int*, 186(1), 245-263, doi: 10.1111/j.1365-246X.2011.05012.x.

- Platou, S. W. (1968), On the petrophysical properties of granitic rocks, *Geologiska Foreningens i Stockholm Forhandlingar*, 90, 427-433.
- Rabbel, W. (1994), Seismic anisotropy at the continental deep drilling site (Germany), *Tectonophysics*, 232(1-4), 329-341, doi:10.1016/0040-1951(94)90094-9.
- Rabbel, W., *et al.* (2004), Superdeep vertical seismic profiling at the KTB deep drill hole (Germany): Seismic close-up view of a major thrust zone down to 8.5 km depth, *Journal of Geophysical Research*, 109(B09309), doi:10.1029/2004JB002975.
- Rabbel, W., and W. D. Mooney (1986), Seismic anisotropy of the crystalline crust: what does it tell us?, *Terra Nova*, 8, 16-21.
- Reinecker, J., M. Tingay, and B. Müller (2003), Borehole breakout analysis from four-arm caliper logs, *World Stress Map Project*, 1-5.
- Rio, P., T. Mukerji, G. Mavko, and D. Marion (1996), Velocity dispersion and upscaling in a laboratory-simulated VSP, *Geophysics*, 61(2), 584-593, doi:10.1190/1.1443984.
- Robinson, E. A., and S. Treitel (1964), Principles of digital filtering, *Geophysics*, 29(3), 395-404, doi:10.1190/1.1439370.
- Robinson, R., and H. M. Iyer (1981), Delineation of a low-velocity body under the Roosevelt Hot Springs geothermal area, Utah, using teleseismic P-wave data, *Geophysics*, 46, 1456-1466.
- Rogers, S. F. (2003), Critical stress-related permeability in fractured rocks, in *Fracture and In-Situ Stress Characterization of Hydrocarbon Reservoirs*, edited by M. Ameen, pp. 7-16, Geological Society of London, Special Publications, London, UK.
- Ronen, J., and J. F. Claerbout (1985), Surface-consistent residual statics estimation by stack-power maximization, *Geophysics*, 50(12), 2759-2767, doi:10.1190/1.1441896.
- Rose, P., J. Sheridan, J. McCulloch, J. N. Moore, K. Kovac, R. Weidler, and S. Hickman (2005), An enhanced geothermal system at Coso, California – Recent accomplishments, paper presented at *Proceedings World Geothermal Congress*, 5 pp., Antalya, Turkey.
- Ross, G. (2000), Introduction to special issue of *Canadian Journal of Earth Sciences*: The Alberta basement transect of Lithoprobe, *Canadian Journal of Earth Sciences*, 37(11), 1447-1452, doi:10.1139/cjes-37-11-1447.
- Ross, G. M. (2002), Evolution of Precambrian continental lithosphere in Western Canada: results from Lithoprobe studies in Alberta and beyond, *Canadian Journal of Earth Sciences*, 39(3), 413-437, doi:10.1139/E02-012.
- Ross, G. M., J. Broome, and W. Miles (2008), Tectonic Domains for the Basement of WCSB (GIS data, polygon features), Digital Data DIG 2008-0007, Retrieved on March 19, 2013 from http://www.ags.gov.ab.ca/publications/DIG/ZIP/DIG_2008_0007.zip.
- Ross, G. M., and D. W. Eaton (1997), Winagami reflection sequence: Seismic evidence for post-collisional magmatism in the Proterozoic of western Canada, *Geology*, 199-202.
- Ross, G. M., and D. W. Eaton (1999), Basement reactivation in the Alberta Basin; Observational constraints and mechanical rationale, *Bulletin of Canadian Petroleum Geology*, 47(4), 391-411.
- Ross, G. M., R. R. Parrish, M. E. Villeneuve, and S. A. Bowring (1991), Geophysics and geochronology of the crystalline basement of the Alberta Basin, Western Canada, *Canadian Journal of Earth Sciences*, 28(4), 512-522.

- Rudnick, R. L., and S. Gao (2003), Composition of the continental crust, in *The Crust*, edited by R. L. Rudnick, pp. 1-64, Elsevier-Pergamon, Oxford, UK.
- Rutqvist, J., C. F. Tsang, and O. Stephansson (2000), Uncertainty in the maximum principal stress estimated from hydraulic fracturing measurements due to the presence of the induced fracture, *International Journal of Rock Mechanics and Mining Sciences*, 37(1-2), 107-120, doi:10.1016/S1365-1609(99)00097-0.
- Rybach, L. (1986), Amount and significance of radioactive heat sources in sediments, in *Thermal modeling in sedimentary basins*, edited by J. Burrus, pp. 311-322, Éditions Technip, Paris, France.
- Rybach, L., and V. Cermak (1982), Radioactive heat generation in rocks, in *Landolt-Börnstein Numerical Data and Functional Relationships in Science and Technology, New Series, Group V. Geophysics and Space Research, vol. 1, Physical Properties of Rocks, subvol. B*. Springer-Verlag, Berlin, edited by K. Hellwege, pp. 433-481.
- Sams, M. S., J. P. Neep, M. H. Worthington, and M. S. King (1997), The measurement of velocity dispersion and frequency-dependent intrinsic attenuation in sedimentary rocks, *Geophysics*, 62(5), 1456-1464, doi:10.1190/1.1444249.
- Sato, H., and M. Fehler (1997), *Seismic wave propagation and scattering in the heterogeneous Earth*, 494 pp., Springer, New York.
- Sausse, J., M. Fourar, and A. Genter (2006), Permeability and alteration within the Soultz granite inferred from geophysical and flow log analysis, *Geothermics*, 35(5-6), 544-560, doi:10.1016/j.geothermics.2006.07.003.
- Schijns, H., D. R. Schmitt, P. J. Heikkinen, and I. T. Kukkonen (2012), Seismic anisotropy in the crystalline upper crust: observations and modelling from the Outokumpu scientific borehole, Finland, *Geophys J Int*, 189(1), 541-553, doi:10.1111/j.1365-246X.2012.05358.x.
- Schlumberger (1982), *Natural gamma ray spectrometry: Essentials of N.G.S. Interpretation*, 69 pp., Sugar Land, Texas.
- Schlumberger (1991), *Log Interpretation Principles/Applications*, Sugar Land, Texas.
- Schlumberger (2002), *Borehole geology, geomechanics and 3D reservoir modeling*, Schlumberger Education Services, SMP-5822, Sugar Land, Texas.
- Schlumberger (2009), *Log Interpretation Charts*, Sugar Land, Texas.
- Schmelzbach, C., A. G. Green, and H. Horstmeyer (2005), Ultra-shallow seismic reflection imaging in a region characterized by high source-generated noise, *Near Surface Geophysics*, 3(1), 33-46.
- Schmelzbach, C., H. Horstmeyer, and C. Juhlin (2007), Shallow 3D seismic-reflection imaging of fracture zones in crystalline rock, *Geophysics*, 72(6), B149-B160, doi:10.1190/1.2787336.
- Schmitt, D. R., J. Mwenifumbo, K. A. Pflug, and I. L. Meglis (2003), Geophysical logging for elastic properties in hard rock: a tutorial, in *Hardrock Seismic Exploration*, edited by D. W. Eaton, B. Milkereit and M. H. Salisbury, pp. 20-41.
- Schmitt, D. R., B. Milkereit, T. Karp, C. Scholz, S. Danuor, D. Meillieux, and M. Welz (2007), *In-situ* seismic measurements in borehole LB-08A in the Bosumtwi impact structure, Ghana: Preliminary interpretation, *Meteoritics & Planetary Science*, 42(4-5), 755-768.

- Schmitt, D. R., C. A. Currie, and L. Zhang (2012), Crustal stress determination from boreholes and rock cores: Fundamental principles, *Tectonophysics*, 580, 1-26, doi:10.1016/j.tecto.2012.08.029.
- Schneider, C. L., S. Mei, M. Grobe, and K. Haug (2012), Beneath the oil sands: Stratigraphy and structural features of the Devonian of Northeast Alberta, paper presented at Geoconvention 2012, Calgary, Alberta.
- Schon, J. H. (1996), *Physical Properties of Rocks: Fundamentals and Principles of Petrophysics*, 592 pp., Pergamon Press, Oxford, UK.
- Schön, J. H. (2011), *Physical Properties of Rocks - A Workbook*, *Handbook of Petroleum Exploration and Production*, Vol. 8, 481 pp., Elsevier, Oxford, UK.
- Schutter, S. R. (2003), Hydrocarbon occurrence and exploration in and around igneous rocks, *Geol. Soc. Lond. Spec. Publ.*, 214(1), 7-33, doi:10.1144/Gsl.Sp.2003.214.01.02.
- Scotti, O., and F. H. Cornet (1994), *In-situ* evidence for fluid-induced aseismic slip events along fault zones, *Int J Rock Mech Min*, 31(4), 347-358, doi:10.1016/0148-9062(94)90902-4.
- Sheriff, R. E. (2002), *Encyclopedic Dictionary of Applied Geophysics*, 4th ed., 429 pp., Society of Exploration Geophysicists, Tulsa, Oklahoma.
- Shipboard Scientific Party (1998), Introduction, in *Proceedings of the Ocean Drilling Program 174B Initial Reports*, edited by K. Becker and M. J. Malone, pp. 3-9, Ocean Drilling Program, College Station, Texas (Ocean Drilling Program), doi:10.2973/odp.proc.ir.174b.101.1998.
- Skinner, B. J., S. C. Porter, J. Park, and T. Freeman (2006), *The Dynamic Earth: An Introduction to Physical Geology*, 5th revised ed., 584 pp., John Wiley & Sons Incorporated, Hoboken, New Jersey.
- Sibbit, A. M. (1995), Quantifying porosity and estimating permeability from well logs in fractured basement reservoirs, paper presented at PetroVietnam, Society of Petroleum Engineers, Ho Chi Minh City, Vietnam, March 1-3, 1995.
- Steeple, D. W., and H. M. Iyer (1976a), Low-velocity zone under long-valley as determined from teleseismic events, *Journal of Geophysical Research*, 81(5), 849-860, doi:10.1029/Jb081i005p00849.
- Steeple, D. W., and H. M. Iyer (1976b), Teleseismic P-wave delays in geothermal exploration, paper presented at Proc. 2nd U.N. Sympos. on the Development and Use of Geoth. Res., San Francisco, California.
- Steingrimsson, B. (2011), Geothermal well logging: Geological wireline logs and fracture imaging, in *Short Course on Geothermal Drilling, Resource Development and Power Plants*, pp. 1-11, Santa Tecla, El Salvador.
- Stewart, R. R. (1985), Median filtering: Review and a new F/K analogue design, *Journal of the Canadian Society of Exploration Geophysicists*, 21(1), 54-63.
- Stewart, R. R. (2001), VSP: An in-depth seismic understanding, *CSEG Recorder*, 79-83.
- Stewart, R. R., P. D. Huddleston, and T. K. Kan (1984), Seismic versus sonic velocities - a vertical seismic profiling study, *Geophysics*, 49(8), 1153-1168, doi:10.1190/1.1441745.
- Stoffa, P. L., J. B. Diebold, and P. Buhl (1981), Inversion of seismic data in the t-p plane, *Geophys Res Lett*, 8(8), 869-872.

- Telford, W. M., L. P. Geldart, and R. E. Sheriff (1990), *Applied Geophysics*, 2nd ed., 770 pp., Cambridge University Press, Cambridge, UK.
- Tester, J. W., *et al.* (2006), *The future of geothermal energy: Impact of enhanced geothermal systems (EGS) on the United States in the 21st Century*, 372 pp., Massachusetts Institute of Technology.
- Thomsen, L. (1986), Weak elastic-anisotropy, *Geophysics*, 51(10), 1954-1966, doi:10.1190/1.1442051.
- Tingay, M., J. Reinecker, and B. Muller (2008), Borehole breakout and drilling-induced fracture analysis from image logs, *World Stress Map Project Guidelines: Image Logs*, 1-8.
- Tiwari, G. N., and R. K. Mishra (2012), Geothermal energy, in *Advanced Renewable Energy Resources*, pp. 359-393, Royal Society of Chemistry, London, UK.
- Treitel, S. (1974), The complex Weiner filter, *Geophysics*, 39(2), 169-173.
- Tsvankin, I. (2001), *Seismic Signatures and Analysis of Reflection Data in Anisotropic Media*, 1st ed., 436 pp., Elsevier, Oxford, UK.
- Tsvankin, I., J. Gaiser, V. Grechka, M. van der Baan, and L. Thomsen (2010), Seismic anisotropy in exploration and reservoir characterization: An overview, *Geophysics*, 75(5), A15-A29, doi:10.1190/1.3481775.
- Unruh, J., S. Pullammanappallil, W. Honjas, and F. Monastero (2006), New seismic imaging of the Coso Geothermal Field, Eastern California, paper presented at Twenty-Sixth Workshop on Geothermal Reservoir Engineering, Stanford, California, January 29-31, 2001.
- Unsworth, M., J. Majorowicz, and G. Nieuwenhuis (2012), Is it feasible to use engineered geothermal systems to produce heat for oil sands processing in Northern Alberta, *CanGRC Review*, Winter(2), 5-6.
- Verdon, J. P., J. M. Kendall, and A. Wüstefeld (2009), Imaging fractures and sedimentary fabrics using shear wave splitting measurements made on passive seismic data, *Geophys J Int*, 179(2), 1245-1254, doi:10.1111/j.1365-246X.2009.04347.x.
- Vernik, L., S. Hickman, D. Lockner, and M. Rusanov (1994), Ultrasonic velocities in cores from the Kola superdeep well and the nature of subhorizontal seismic reflections, *J Geophys Res-Sol Ea*, 99(B12), 24209-24219, doi:10.1029/94jb01236.
- Vidale, J. E. (1986), Complex polarization analysis of particle motion, *Bulletin of the Seismological Society of America*, 76(5), 1393-1405.
- Walsh, N. J. (2013), *Geochemistry and geochronology of the Precambrian basement domains in the vicinity of Fort McMurray, Alberta: A geothermal perspective*, M.Sc. thesis, 194 pp, University of Alberta, Edmonton, Alberta.
- Wamalwa, A. M., K. L. Mickus, L. F. Serpa, and D. I. Doser (2013), A joint geophysical analysis of the Coso geothermal field, south-eastern California, *Physics of the Earth and Planetary Interiors*, 214, 25-34.
- Ward, P. L. (1972), Microearthquakes: Prospecting tool and possible hazard in the development of geothermal resources, *Geothermics*, 1(1), 3-12.
- Ward, P. L., and K. H. Jacob (1971), Microearthquakes in the Ahuachapan geothermal field, El Salvador, Central America, *Science*, 173(3994), 328-330, doi:10.1126/science.173.3994.328.

- Welford, J. K. (2004), Deep 3-D seismic reflection imaging of Precambrian sills in the Crystalline Crust of Alberta, Canada, Ph.D. thesis, Department of Earth and Ocean Science, University of British Columbia, Vancouver, British Columbia, Canada.
- West, F. G., and A. W. Laughlin (1976), Spectral gamma logging in crystalline basement rocks, *Geology*, 4(10), 617-618, doi:10.1130/0091-7613(1976)4<617:SGlicb>2.0.Co;2.
- Wikipedia (2006), Athabasca Oil Sands, Retrieved on April 4, 2013 from http://en.wikipedia.org/wiki/File:Athabasca_Oil_Sands_map.png.
- Wright, P. M., S. H. Ward, H. P. Ross, and R. C. West (1985), State-of-the-art geophysical exploration for geothermal resources, *Geophysics*, 50(12), 2666-2696, doi:10.11920/1.1441889.
- Wu, J. (1996), Short note: Potential pitfalls of crooked-line seismic reflection surveys, *Geophysics*, 61(1), 277-281.
- Wu, J. J., R. F. Mereu, and J. A. Percival (1992), Seismic image of the Ivanhoe Lake fault zone in the Kapuskasing uplift of the Canadian Shield, *Geophys Res Lett*, 19(4), 353-356, doi:10.1029/91gl03180.
- Wyllie, M. R. J., A. R. Gregory, and G. H. F. Gardner (1958), An experimental investigation of factors affecting elastic wave velocities in porous media, *Geophysics*, 23, 459-493.
- Yilmaz, O. (2001), *Seismic data analysis: processing, inversion, and interpretation of seismic data*, Rev. ed., 2027 pp., Society of Exploration Geophysicists, Tulsa, Oklahoma.
- Zhou, R., D. McAdow, C. Barberan, D. Dushman, and F. Doherty (2004), Seismic anisotropy estimation in TTI media using walkaway VSP data, paper presented at SEG International Exploration and 74th Annual Meeting, SEG, Denver, Colorado.
- Zoback, M. D., D. Moos, L. G. Mastin, and R. N. Anderson (1985), Well bore breakouts *and in-situ* stress, *J. Geophys. Res.*, 90, 5523-5530.

Appendix A

History of Hunt Well

Event	Date	Remarks
Drilling Session #1		UWI: 00/07-32-089-10W4/0 Company: Archean Corporation KB: 409.3 m TVD: 1649.0 m
Spud date	Sept. 1, 1994	
Rig on site	Early Sept., 1994	
Drilling began	Early Sept., 1994	
Casing #1	Sept. 1, 1994	Casing liner outside diameter 339.7 mm Shoe set depth: 94 m
Casing #2	Sept. 10, 1994	Casing liner outside diameter: 244.5 mm Shoe set depth: 598.2 m
Drilling completed	Oct. 8, 1994	At 1649.0 m
Service rig released	Oct. 8, 1994	
Rig on site	Oct. 8, 1994	For Schlumberger logging
Logging (Schlumberger)	Oct. 8, 1994	Run #1: DLL, MSFL Run #2: CNL, LDT, NGT Run #3: FMI
Drilling operations suspended temporarily	Oct. 9, 1994	
Rig released	Oct. 10, 1994	
Suspended drilling operations	Nov. 2, 1994	Suspended indefinitely (cash flow) as reported by company; bridge plug set at 540 m

Archean Corporation renamed to Anhydride Corporation on June 10, 1996.
Director: Mr. C. Warren Hunt

Purpose: Drill out permanent bridge plugs and test intervals in granite formation

Rig on site	Sept. 25, 2002	
Drill out cement	Sept. 27, 2002	From 533.55 to 539.59 m
Drill out bridge plug 1	Sept. 27, 2002	At 539.59 m
Drill out bridge plug 2	Sept. 28, 2002	At 596.23 m
Clear tight spots	Sept. 29 – 30, 2002	From 1187.48 to 1216.16 m, and possibly a few other tight spots between 1283.29 to 1640 m)
RIH with inflate straddle packer	Oct. 2, 2002	
Swab tests	Oct. 2 – 8, 2002	
Packer test	Oct. 7, 2002	Bottom of top packer at 873.0 m, pressurized

		at different feed rates. ISIP reported at 7 MPa dropping to 5.5 MPa in 13 minutes
Packer test	Oct. 11, 2002	Bottom of top packer at 1370 m, pressurized at 11.5 MPa, held pressure for long time without dropping
Rig released	Oct. 15, 2002	

Drilling Session #2		UWI: 00/07-32-089-10W4/2 KB: 409.3 m TVD: 2363.3 m
Spud date	Dec. 13, 2002	
Drill out cement and bridge plug	Dec. 16, 2002	
Drilling began	Dec. 17, 2002	Bit size: 222 mm, TVD: 1649 to 1654 m Bit size: 200 mm, TVD: 1656.4 m to 2347 m Bit size: 199 mm for coring
Coring #1	Dec. 20, 2002	Recovered 1.22 m core between 1656.4 to 1657.82 m
Coring #2	Jan. 5-6, 2003	Recovered 2.17 m core between 2347.52 to 2350.21 m
Coring #3	Jan. 7, 2003	At 2351 m
Logging (Schlumberger)	Jan. 7, 2003	Run #1: FMI and DSI logs from 2351 m to 1600 m Run #2: TLD, CNL, NGT, HRLA, CAL logs from 2351 m to 1600 m
Coring #4	Jan. 8-9, 2003	Recovered 11.92 m core from 2351.42 m to 2363.34 m
Drilling completed	Jan. 9, 2003	At 2363.3 m
DST #1	Jan. 9-10, 2003	From 1755 m to 1800 m
DST #2	Jan. 10-11, 2003	From 2345 m to 2363 m
DST #3	Jan. 11-12, 2003	From 1640 m to 1664 m, miss run
DST #4	Jan. 12, 2003	From 1645 m to 1670 m, miss run
DST #5	Jan. 13, 2003	From 1640 m to 1683 m, bottom hole sample showed ground-up granite and small speckles of metal of unknown source
DST #6	Jan. 13-14, 2003	At 2363 m
Set bridge plug	Jan. 15, 2003	At 590 m
Rig released	Jan. 15, 2003	

Completion and Workover

Purpose: Drill out permanent bridge plug at 590 m KB, swab and evaluate open hole

Rig on site	Jan. 30, 2003	
Production tubing running in hole (RIH)	Feb. 8, 2003	Tubing size: 89 mm Tubing collar: 0.15 m Tubing bottom: 2329.06 m
Hole camera	Feb .24-25, 2003	Fluid entry found at 632.09 to 640.0 m, 647.94 to 754.81 m, 769.64 to 788.56 m. Possible

		inflow at 1646 m, 1550 m. No inflow at intervals tested below 1645 m.
Casing #3	Feb. 28, 2003	Casing liner outside diameter: 177.8 mm Shoe set depth: 1005.7 m
Run in production tubing	Mar. 5, 2003	
Rig released	Mar. 14, 2003	
Swab rig in	Mar. 17, 2003	Continued swabbing but little additional fluids produced
Swab tests	Feb. 9 – Mar. 20, 2003	Extensive swabbing, could not recover any additional fluids on last runs, total fluid swabbed is 66.71 m ³ of salt water with no signs of oil or gas
Swab rig out	Mar. 20, 2003	

2004 – 2008: Temperature measurements were made by GeoPos but these proprietary data are not accessible.

Purpose: Open hole logging in the basement requested by University of Alberta

Temperature logging #1	Dec. 7-9, 2010	Pumped 51-52 m ³ of water over two days and logged from surface to 2333.7 m Standard logging package included pressure, gamma ccl, temperature and lightning unit including travel time. LSAT Lonkar spectral log Fluid level dropped. Measured water level at 928 m on Dec. 12, 2010.
Temperature logging #2	Jun. 14-15, 2011	Repeat temperature log to check on the thermal stability of the well, well was topped up ~2 weeks before logging date Logging as above Fluid level was observed at ~ 65 m.
Rig on site	Jul. 8, 2011	
Removal of production tubing	Jul. 8-9, 2011	248 tubings removed prior to open hole logging
Rig released	Jul. 9, 2011	
Logging (ICDP-OSG)	Jul. 13-16, 2011	<i>Refer to Appendix B</i>

Phase 1
Environmental Site Assessment October 22, 2012 Done by WorleyParsons

Appendix B

ICDP-OSG Logging List

GFZ participants: Christian Carnein, Jochem Kück, Matxalen Rey Abasolo.

U of A participants: Greg Nieuwenhuis (Research scientist), Dr. Douglas Schmitt (Professor), Judith Chan (M.Sc. Student), Elahe Poureslami (Ph.D. Student), Brendan Snow (Summer Student), Brendan DeMilliano (Summer Student), Lucas Duerksen (Geophysics technician), Dr. Pratap Sahay (Visiting professor).

Run/File #	Log type	Parameters	Acquisition date	Start depth (m)	End depth (m)	Remarks
001	TS1-SGR-MS	GR, K, Th, U, MSUS	07/13/2011	1879	492	Casing: 0-1005 m Chart-based correction done for MSUS
002	FAC40	Acoustic borehole images	07/14/2011	1355	1314	Main
003				1324	990	Main
004				1050	1042	Repeat
005	TS1-DLL	Resistivity		1880	997	Main
006				1050	990	Repeat
007	TS1-DIP	CALI orientation, dipmeter, FTOT			1875	1000
-	SlimWave™ 4 Geophones	VSP zero-offset	07/14 – 07/15/2011	1880	5	186 positions, seismic source: U of A Minivib™
-		VSP walk-away	07/15 – 07/16/2011	1780	800	seismic source: U of A Minivib™
008	TS1-BS	Vp, Vs, FWS	07/16/2011	1880	1775	Logging in several sessions because sonde dropped out several times (if speed > 8 m/min), depth error ≈ 4.5 m
009				1810	1790	
010				1800	1735	
011				1745	1616	
012				1626	1396	
013				1406	998	

Depth reference:	Top of annular preventer
Elevation depth reference above ground:	2.90 m
Type of fluid in hole:	Water, well was filled up one week before logging
Cable type/owner:	3/16" 4-conductor Rochester/ICDP
Winch type/owner:	MW2000/ICDP
Other remarks:	<ul style="list-style-type: none"> • No drill rig, logged with car crane (boom truck), winch was tied on the load floor of a small truck, borehole size(s) initially unknown, later measured with DIP sonde, narrow section, 20 cm long at 1362 m with CAL2 \approx 60 mm. • The manufacturer gives an instrument accuracy of 10 % for the elements (U, Th, and K) and 5 % for the total GR. Additionally, natural variations occurred.

Appendix C

Logs Measured in Hunt Well To-Date

#	Method	Tool provider	Measured interval (m)*	Remarks
1	Natural gamma ray (GR)	Schlumberger	570 - 1652	
		ICDP-OSG	492 - 1879	
2	Spectral gamma ray (SGR)	Schlumberger	582 - 1652	Data was acquired by three separate logging companies (Schlumberger, ICDP-OSG, Lonkar), interpretations were made on the latest logging runs by ICDP-OSG
		Lonkar	Surface to 2329	
		ICDP-OSG	492 - 1879	
3	Compensated neutron (CNL)	Schlumberger	582 - 1652	Neutron porosity (NPOR), Unknown porosity unit measurements
4	Density porosity (DPHI)	Schlumberger	582 - 1652	
5	Self potential (SP)	Schlumberger	570 - 1652	Also known as spontaneous potential
6	Resistivity (Laterolog, DLL)	Schlumberger	85 - 602 570 - 1652	Schlumberger: includes deep laterolog (LLD), shallow laterolog (LLS)
		ICDP-OSG	997 - 1880	
7	Micro-Resistivity (MSFL)	Schlumberger	570 - 1652	
8	Sonic (DT)	Schlumberger	13 - 602	Velocity of sound propagation
9	Full waveform sonic (FWS)	ICDP-OSG	998 - 1880	1 transmitter, 2 receivers Tool top - 0.7 m - T - 2.5 m - R _{near} - 0.5 m - R _{far} - 0.75 m - Tool bottom
10	Dipole shear sonic imager (DSI™)	Schlumberger	1559 - 2357	
11	Acoustic borehole images (FAC40)	ICDP-OSG	990 - 1355	Images are oriented to north Unsuccessful due to problems with tool centralization
12	Formation MicroImager (FMI™)	Schlumberger	433 - 602 600 - 1651	Poor quality in the open hole section
			1559 - 2357	
13	Magnetic susceptibility (MSUS)	ICDP-OSG	492 - 1879	
14	Total magnetic field (FTOT)	ICDP-OSG	1000 - 1875	
15	Caliper (CALI, C)	Schlumberger	82 - 1652	Tight zone at 1362 m
		ICDP-OSG	1000 - 1875	
16	Litho-Density (TLD)	Schlumberger	445 - 602 582 - 1652	Includes RHOB, DRHO and PEF
17	Temperature (TEMP, T)	Lonkar	Surface to 2334	

* Measured intervals for logs measured by Schlumberger are based on the IHS Canada database. Not all data were used for this project since they were unavailable in digital format.

Appendix D

Swab Report

This table is compiled from the 13 pages of swab report for the Hunt well. Details of the individual swab can be found in the original swab report.

Date	Number of swabs taken	Load fluid to recover (m ³)	Total Fluid			Fluid level		Swab depth		Remarks
			Daily Recovery (m ³)	Recovered to date (m ³)	Water Cut (%)	Initial (m)	Final (m)	Initial (m)	Final (m)	
03/06/2003	21	63	29.54	29.54	100	99	1421	650	1772	pH 6-7, Vis 31, Sal 22.5 – 23.5, MW 1198 ; some swabs recovered wax-like material on the swab cup
03/07/2003	24	63	31.13	60.67	100	1420	2181	1617	2326	pH 7, Vis 31, Sal 22-23, MW 1168-1174
03/08/2003	8	63	3.42	64.09	100	2100	?	2326	2326	pH 7, Vis 31, Sal 22, MW 1174; No sign of oil or gas
03/09/2003	6	63	0.44	64.53	100	2266	?	2326	2326	pH 7, Vis 31, Sal 22, MW 1162-1174; No signs of oil or gas
03/10/2003	3	63	0.15	64.68	100	2266	?	2326	2326	pH 7, Vis 33, Sal 22, MW 1186; Salt water with 4.5 % BS
03/11/2003	4	63	0.45	65.13	100	2266	?	2326	2326	pH 6, Vis 33-35, Sal 22, MW 1174; Salt water with 4 % BS
03/12/2003	2	63	0	65.13	100	?	?	2326	2326	Couldn't feel fluid level; No recovery
03/13/2003	6	63	0.90	66.03	100	2266	?	2326	2326	pH 6, Vis 34-37, Sal 21-22, MW 1150-1174; BS 4-17; Trace of wax on swab cups
03/14/2003	6	63	0.68	66.71	100	2266	?	2326	2326	pH 6, Vis 33-34, Sal 15-23, MW 1126-1174, BS 3-19%; Trace of wax on swap cups
03/17/2003	7	63	0.18 Water 0.04 Oil	66.93	58-90	2266	2294	2326	2326	pH 5, Vis 32-37, Sal 21-22, MW 1162-1174, BS 10-43%

Date	Number of swabs taken	Load fluid to recover (m ³)	Total Fluid			Fluid level		Swab depth		Remarks
			Daily Recovery (m ³)	Recovered to date (m ³)	Water Cut (%)	Initial (m)	Final (m)	Initial (m)	Final (m)	
03/18/2003	7	63	0.04 Water 0.088 Oil	67.057	35-62	2267	2310	2326	2326	pH 5, Vis 32-34, Sal 22, MW 1168-1198, BS 35-60
03/19/2003	5	63	0.046 Water 0.024 Oil	67.127	65-75	2293	2307	2326	2326	pH 5, Vis 32-34, Sal 21-23, MW 1186-1198, BS 25-35; Trace of wax
03/20/2003	4	63	0	67.127	50-60	2290	2315	2326	2326	pH 5, Vis 34-36, Sal 22-23, MW 1198-1210, BS 40

Acronyms

Vis – viscosity (s) – The expected value for water according to the Marsh funnel method is 26 ± 0.5 s.

Sal – salinity (%)

MW – mud weight (kg/m³)

BS – base sediments (%) in salt water, the more usual notation seen in swab reports is bs&w for basic sediment and water

Comments

No definitions have been provided with the swab reports. The borehole was swabbed dry and it remained dry until the borehole was filled with water for temperature logging in 2010.

Appendix E

Seismic Anisotropy of Metamorphic Core Sample from the Hunt Well

(This was the term paper submitted for the GEOPH 620 course – Rock Physics and Mechanics, taught by Dr. Douglas R. Schmitt, Fall 2011).

1. Overview

Laboratory measurements of compressional- and shear-wave phase velocities were carried out on a metamorphic rock using the pulse transmission technique up to a confining pressure of 60 MPa. The rock sample used was a metamorphic rock from a deep borehole in Fort McMurray, Alberta, Canada. This project is part of a subsurface characterization study of Northeastern Alberta based on seismic reflection profiles and borehole logging results. Processed seismic data near the deep borehole reveals a number of anomalous strong reflectors and it is currently unclear whether the strong reflectors could be resulting from foliated, regionally metamorphosed rocks, fault-zone anisotropy, sharp velocity/density contrasts between materials, or poor seismic processing workflow. A core sample near the bottom of the deep borehole was used to study the anisotropic properties of the rocks. Velocities were measured in three different directions with respect to the identified foliation plane in the sample. Transverse isotropy is one of the simplest anisotropic cases useful for the understanding of the anisotropic behavior of the material. This symmetry was assumed for the calculation of the five independent elastic stiffness constants related to its hexagonal symmetry. Results show that the selected rock sample is slightly anisotropic with the measured values for P- and S-wave anisotropy averaging at 12% and 9% respectively.

2. Background

A suite of geological and geophysical measurements were carried out at a deep borehole in Fort McMurray, Alberta, Canada, for the detailed subsurface characterization of the sedimentary basin and crystalline basement rocks of the

Canadian Shield. The anisotropic effects of rocks should be considered in the processing of geophysical data in order to remove the anomalies caused by the directional variations of seismic velocities. Most geological materials are considered as elastically anisotropic resulting from the foliations and/or lineations of the rocks. To assess the deformability characters of these rocks, laboratory measurements are required to measure the compressional and shear wave velocities at different pressure states. The behavior of elastic waves in the rocks allows us to describe the elastic properties of the materials by calculating their elastic constants. One of the simpler cases of anisotropy is transverse isotropy, which has a hexagonal symmetry and is described using five independent elastic constants. They can be determined by measuring the compressional and shear wave velocities from the metamorphic rock sample of the deep borehole using the pulse transmission technique. This paper presents the results of the velocity measurements and the anisotropic behavior of the metamorphic rock sample from Fort McMurray based on the assumption that the sample is transversely isotropic.

3. Theory

3.1. Elasticity

According to the theory of linearized elasticity, a linear relation (Equation 1) between stress and strain can be applied to characterize the material properties at a particular point by the generalized Hooke's Law (Bos *et al.*, 2004). In an elastic medium, the stress-strain relationship is written as:

$$\sigma_{ij} = c_{ijkl}\epsilon_{kl} \quad (1)$$

where σ_{ij} , ϵ_{kl} denote variables of stress and strain as second-rank tensors, respectively, c_{ijkl} are the components of the elastic stiffness tensor C (or elastic constants) as fourth-rank tensor with 81 components, and $i, j, k, l = 1, 2, 3$ indicates one of the three orthogonal axes. Einstein summation convention applies here for each instance of a repeated index on the same side of the equation. The finding of the complete elasticity tensor c_{ijkl} can fully describe the elastic

properties of anisotropic crystals or solids (Cholach *et al.*, 2005). Equation 1 can be further reduced from 4 indices $ijkl$ down to 2 indices mn using the reduced Voigt notation (Nye, 1985):

$$C_{ijkl} = C_{mn} \quad (i, j, k, l = 1, 2, 3; m, n = 1, \dots, 6) \quad (2)$$

And the generalized Hooke's Law may be simplified to a matrix equation:

$$\sigma_I = c_{IJ}\varepsilon_J \quad (3)$$

where σ_I and ε_J are 6 x 1 vectors containing independent components of stress and strain tensors respectively (Cholach *et al.*, 2005). Each c_{IJ} is one of the components of a 6 x 6 symmetric matrix of 21 independent elastic stiffnesses that is symmetric about the diagonal:

$$\begin{bmatrix} \sigma_1 \\ \sigma_2 \\ \sigma_3 \\ \sigma_4 \\ \sigma_5 \\ \sigma_6 \end{bmatrix} = \begin{bmatrix} C_{11} & C_{12} & C_{13} & C_{14} & C_{15} & C_{16} \\ C_{12} & C_{22} & C_{23} & C_{24} & C_{25} & C_{26} \\ C_{13} & C_{23} & C_{33} & C_{34} & C_{35} & C_{36} \\ C_{14} & C_{24} & C_{34} & C_{44} & C_{45} & C_{46} \\ C_{15} & C_{25} & C_{35} & C_{45} & C_{55} & C_{56} \\ C_{16} & C_{26} & C_{36} & C_{46} & C_{56} & C_{66} \end{bmatrix} \begin{bmatrix} \varepsilon_1 \\ \varepsilon_2 \\ \varepsilon_3 \\ \varepsilon_4 \\ \varepsilon_5 \\ \varepsilon_6 \end{bmatrix} \quad (4)$$

3.2. Anisotropy

The anisotropy in rocks is primarily due to the preferred orientations of the constituent minerals, textural-structural features such as bedding and foliation, and pores and cracks. The value of anisotropy can be calculated according the following equation (Birch, 1960, 1961):

$$A = \frac{V_{par} - V_{perp}}{V_{par}} \quad (5)$$

where V_{par} and V_{perp} are velocities parallel and perpendicular to the bedding respectively. Despite the fact that many of the constituent minerals in most rocks are highly anisotropic, these rocks are still considered as “weakly anisotropic” for $A \ll 1$ (Thomsen, 1986). Elastic constants are used to quantify the anisotropy of the transversely isotropic material when it is weakly anisotropic. Since measurements parallel to the bedding cannot always be made from the surface,

Thomsen (1986) suggested three other parameters to quantify the weak anisotropic behavior of transversely isotropic materials:

$$\gamma = \frac{C_{66} - C_{44}}{2C_{44}} \quad (6)$$

$$\varepsilon = \frac{C_{11} - C_{33}}{2C_{33}} \quad (7)$$

$$\delta = \frac{(C_{13} + C_{44})^2 - (C_{33} - C_{44})^2}{2C_{33}(C_{33} - C_{44})} \quad (8)$$

where ε is a measure of the P-wave anisotropy showing the fractional change in P-wave velocity, γ is a measure of S-wave anisotropy, δ is an expression related to the curvature of the P-wave wavefront, and C_{ij} indicates elements in the stiffness matrix. ε , γ , δ are dimensionless and have values smaller than 0.5, but frequently much smaller (Sheriff, 2002). These three parameters are useful in quantifying anisotropy when simple inspection of the elastic moduli do not present obvious indications of anisotropy. More details about transverse isotropy will be discussed in Section 3.3.

It is important to note the difference between group (ray) and phase velocities in a homogenous anisotropic media (Figure A-1). Ray velocity is the velocity of energy propagation along a ray path, whereas phase velocity is the velocity of the plane wave. These two velocities are equivalent for an isotropic material, but will need to be considered separately for an anisotropic material in order to properly relate velocities to elastic constants. *Christoffel* equation is an eigenvalue problem in which known elastic constants can be used to calculate the phase velocities of the elastic waves. Detailed derivations are beyond the context of this paper but can be found in the paper published by Musgrave (1970). The formula for linking velocities and elastic constants simplify substantially when wave behaviors are discussed within planes of symmetry and along principal axes (Cholach *et al.*, 2005).

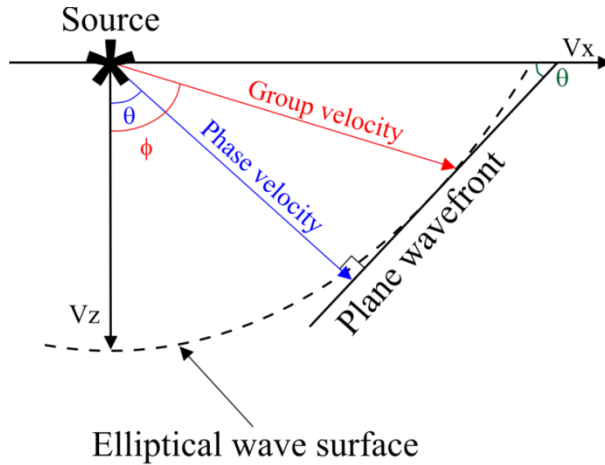


Figure A-1. The relationship between group (ray) and phase velocities when energy propagates in the shape of an elliptical wave surface. The symmetry axis is parallel to the z-direction.

3.3. Transverse Isotropy

Foliated rock type in the absence of any other anisotropy parameter could be described by transverse isotropy. Many low- to medium-grade metamorphic rocks often have well-developed bedding or foliation and behave as transversely isotropic elastic solids (Gupta, 2011). This form of anisotropy involves elastic properties that are the same in any direction perpendicular to a symmetry axis (*i.e.* z-axis) but different parallel to the x-axis (Sheriff, 2002). The hexagonal symmetry axis is normal to the bedding or layering. Figure A-2 illustrates the symmetry of a transverse isotropic medium. The subscripts 0 and 90 correspond to the propagation direction relative to the axis of symmetry. For example, V_{SH90} refers to the S-wave propagating and polarized 90° to the symmetry axis (Hemsing, 2007). Velocities measured within the symmetry plane will be constant, while velocities measured perpendicular to this plane will be different. This form of symmetry is similar to a crystal and hence transverse isotropy possesses hexagonal symmetry that can be described using five independent elastic constants (C_{11} , C_{13} , C_{33} , C_{44} and C_{66}). The stiffness matrix C is expressed by (Musgrave, 1970):

$$C_{IJ} = \begin{bmatrix} C_{11} & C_{11} - 2C_{66} & C_{13} & 0 & 0 & 0 \\ C_{11} - 2C_{66} & C_{11} & C_{13} & 0 & 0 & 0 \\ C_{13} & C_{13} & C_{33} & 0 & 0 & 0 \\ 0 & 0 & 0 & C_{44} & 0 & 0 \\ 0 & 0 & 0 & 0 & C_{44} & 0 \\ 0 & 0 & 0 & 0 & 0 & C_{66} \end{bmatrix} \quad (9)$$

The determination of the five independent elastic constants requires five independent wave measurements. Compressional and shear wave travel times across the rock sample are measured in the laboratory. The elastic constants are then calculated from the velocity measurements and density by the following expressions:

$$C_{11} = \rho V_{P90}^2 \quad (10)$$

$$C_{33} = \rho V_{P0}^2 \quad (11)$$

$$C_{44} = \rho V_{SH0}^2 \quad (12)$$

$$C_{66} = \rho V_{SH90}^2 \quad (13)$$

$$C_{12} = C_{11} - 2C_{66} \quad (14)$$

where ρ is the density of the rock sample, C_{ij} are elastic constants, V_{P90} , V_{P0} , V_{SH0} , and V_{SH90} are P- and S-wave velocities in different directions as indicated in Figure A-2. In a transversely isotropic medium, the S-wave propagating parallel to the symmetry axis does not split and does not need to be labeled according to its polarization. Hence, the velocities of S-waves can be related by $V_{SV0} = V_{SH0} = V_{SV90}$. SH refers to the shear wave with particle motions perpendicular to the z-axis and is the component vibrating along the foliation plane. Using velocity measurements taken at 45° from the foliation plane, C_{13} can be obtained using the following equation:

$$C_{13} = -C_{44} + \left[4\rho^2 V_{P45}^4 - 2\rho V_{P45}^2 (C_{11} + C_{33} + 2C_{44}) + (C_{11} + C_{44})(C_{33} + C_{44}) \right]^{1/2} \quad (15)$$

In this experiment, five different measured velocities were used to calculate the stiffness constants. Specifically, V_{P90} was used to determine C_{11} in equation (10);

V_{P0} for C_{33} in equation (11), V_{SH0} for C_{44} in equation (12), V_{SH90} for C_{66} in equation (13), and V_{P45} for C_{13} in equation (15).

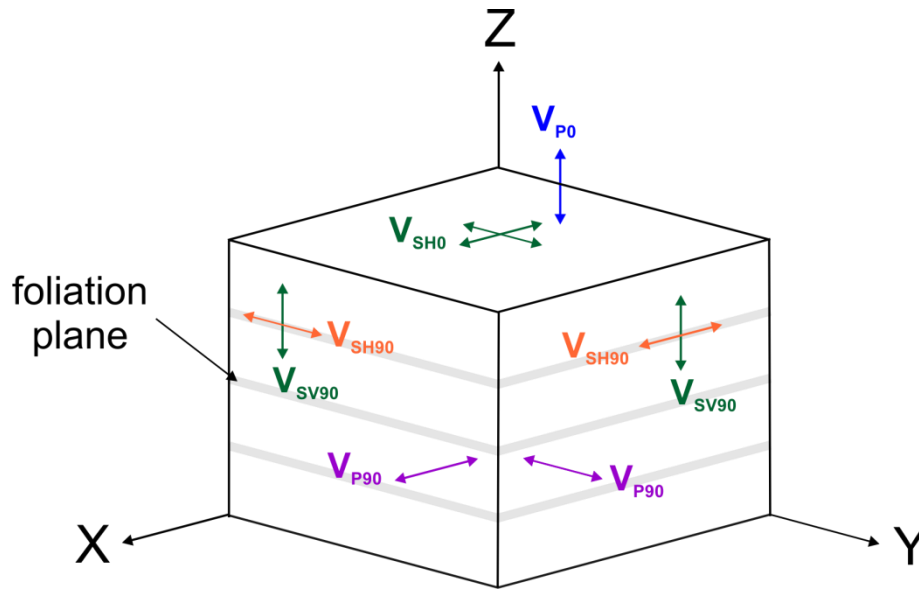


Figure A-2. Symmetry of a transversely isotropic medium where elastic properties are symmetric about the z-axis. Velocities are measured parallel, perpendicular and at 45° relative to the foliation plane in the laboratory. Arrows of the same color indicate waves that propagate at the same speed.

4. Experimental Procedure

4.1. Sample Preparation

Limited core samples were available from ERCB/AGS at two different depth intervals: 1656.5 – 1657.8 meters and 2347.5 – 2364.25 meters in a 2.4-km deep borehole located west of Fort McMurray. For the purpose of this project, rock sample with an identifiable foliation plane was selected from a depth of 2350.3 – 2350.45 m. It is a metamorphic granitic rock sample composed of unknown percentages of schist, mica, and quartz. P- and S-wave velocities will be measured at three different orientations: parallel, perpendicular and at 45° to the foliation plane. The sample was cut, grinded flat and parallel, on a diamond grinding disk at three different angles relative to the apparent direction of the foliation plane to ensure good surface contacts for the transducers. The final sample size was 8.15

cm (length) x 7.0 cm (width) x 4.5 cm (height) with the 45° surfaces at 3.8 cm apart (Figure A-3). After grinding, the sample was placed in the oven to vacuum dry for over 12 hours at approximately 45°C. Bulk density of the sample was measured in the laboratory using a mercury porosimeter and a value of 2.62 g/cm³ was reported at 0.0036 MPa. A bulk density log was also available for this deep borehole and density was reported to be 2.65 g/cm³ at 2350.4 meters which closely agrees with the density value measured in the laboratory.

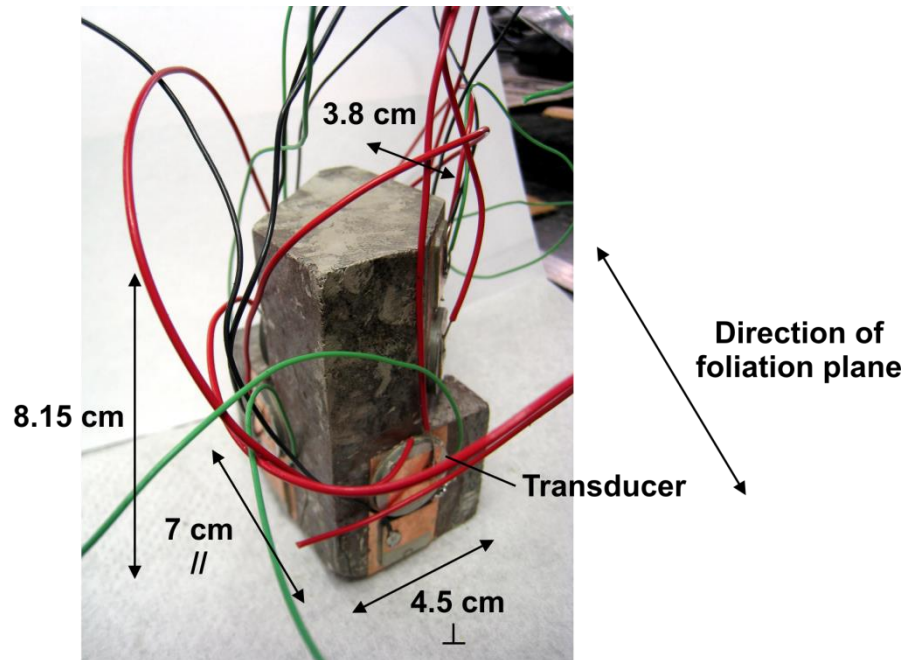


Figure A-3. Dimensions of metamorphic rock sample for velocity measurements. Sample was cut and grinded to ensure that surfaces are flat and parallel to one another for accurate measurements.

The main component for transmitting and receiving elastic waves in the laboratory are the transducers. The transmitting transducer converts the electrical pulse to a mechanical signal, which is transmitted through the rock. The receiving transducer changes that wave back into an electrical pulse, which is then amplified and displayed on the oscilloscope screen (Gupta, 2011). For this project, ultrasonic transducers composed of longitudinally and transversely polarized piezoelectric ceramics and copper foil electrodes are used. The type of vibration

generated is determined by the polarization of the piezoelectric crystal. Longitudinal wave (P-wave) piezoelectric ceramics were circular disks with a diameter of 20 mm whereas the ones for transverse wave (S-wave) were square disks with a diameter of 15 mm. Both were made from APC's 851 material (APC International Ltd., 2011). The piezoelectric material is a ceramic made from lead zirconate titanate with a resonant frequency of 1 MHz, and this material is capable of producing an electrical potential with applied stress such as a mechanical vibration.

A total of six pairs of piezoelectric transducers were mounted on the aforementioned surfaces relative to the foliation plane for the recording of P- and S-waves. Copper foils were glued beneath and on top of the transducers as electrodes using CircuitWorks® CW2400 conductive epoxy. The copper foil attached to the underside of the transducer acted as a ground for the transducers. Insulated electrical wires were soldered to the electrodes, and the entire sample was then sealed in a flexible urethane compound (Flexane® 80 Putty) to protect the rock from the hydraulic oil inside the pressure vessel used as a confining medium. This assemblage was then placed in the pressure vessel for travel time measurements.

4.2. Data Acquisition

The ultrasonic pulse transmission technique was used to determine the elastic constants of the rock sample. A Quizix™ Q5000 pump system was used to control the confining pressure of the pressure vessel. The transmitted signal of the elastic waves was generated using a JSR-PR35 pulse generator that is connected to the electrical wires of the transmitting transducers and the propagated signal is recorded by a digital oscilloscope made by National Instrument (Yam, 2011) (Figure A-4). Velocity measurements were taken in 3.0 MPa increments between 0 to 15 MPa, and in 5.0 MPa increments between 15 to 60 MPa during both pressurization and depressurization cycles conducted at room temperature. There was a five-minute waiting period between after reaching the target confined pressure and the recording of waveforms to allow pressure condition to stabilize

in the pressure vessel, and also to allow any cracks or pores in the sample to open or close. The *in-situ* peak pressure for the sample can be determined based on the density of the sample and the depth from which it was extracted from using the following equation:

$$P = \rho gh \quad (16)$$

where ρ is the density of the sample, g is the acceleration due to gravity (9.81 m/s²), and h is the depth that the sample was originated from. Using the measured density values from the mercury porosimeter, the *in-situ* peak pressure for the sample is at approximately 60 MPa. It is also good to note that this was only based on the assumption that the density at the surface is equivalent to the density of the sample at 2350.4 m depth (Hemsing, 2007). The travel time and amplitude of the wave were recorded at each pressure interval and the final waveform trace was constructed from at least 300 progressively stacked records to minimize the random noise effects (Figure A-5). Travel time was picked from the first extreme value of the waveform on each stacked record. Signals were expected to become stronger with pressure due to better surface contact.

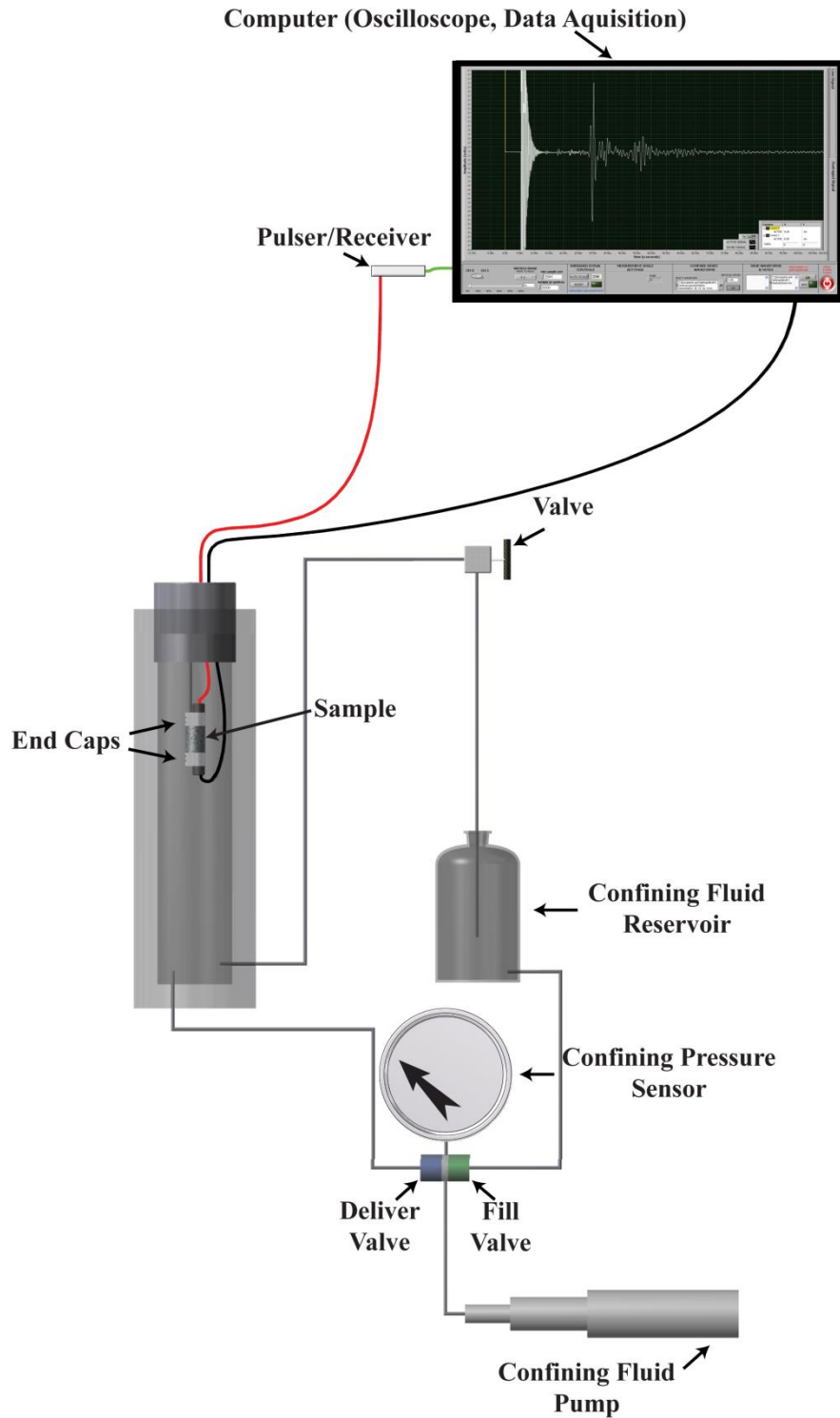


Figure A-4. A schematic diagram of the experimental setup. Sample was prepared and placed in the pressure vessel and confined pressure was applied to the sample from 0 to 60 MPa (Image courtesy of Randy Kofman).

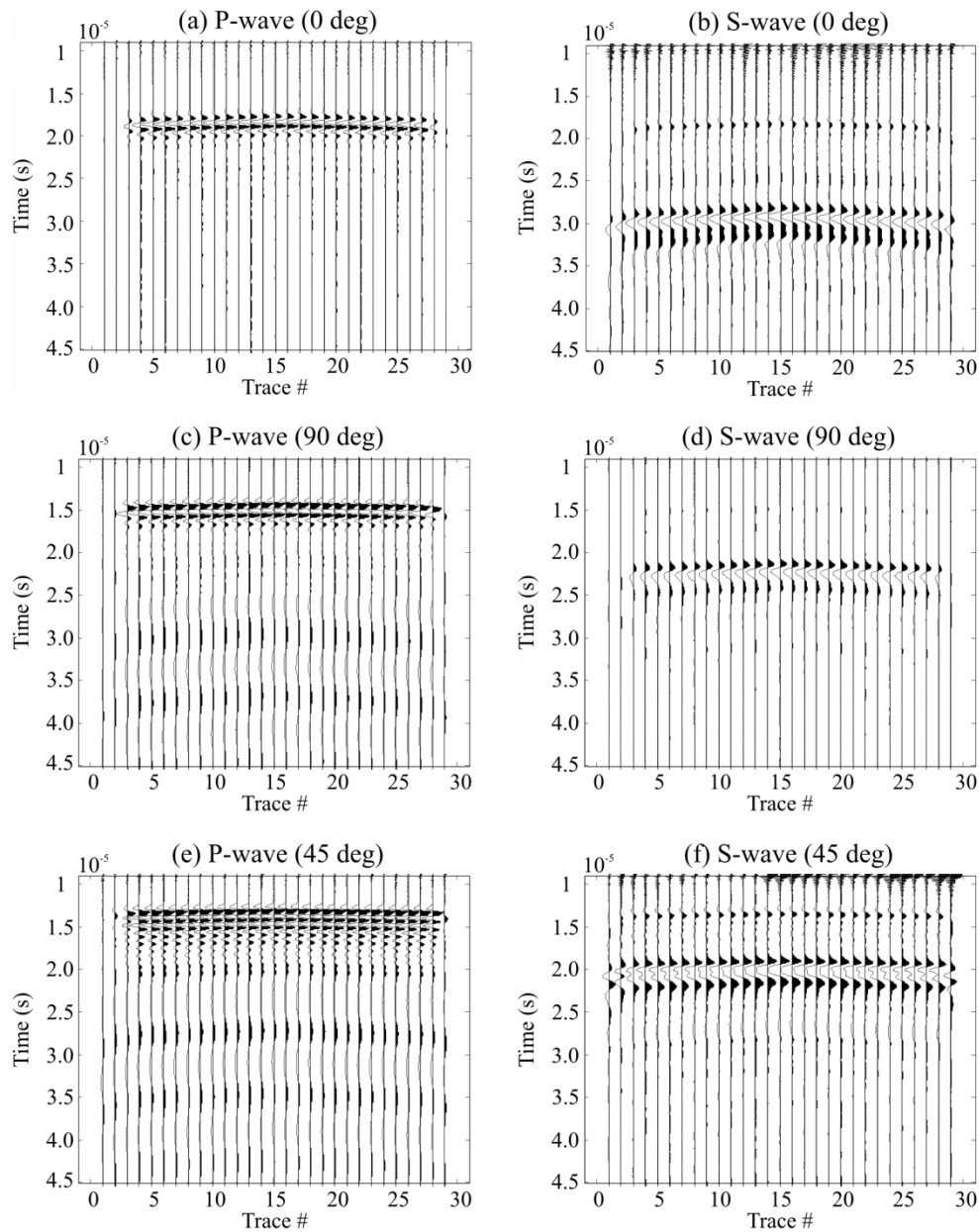


Figure A-5. Variable-area wiggle displays of P- and S-waves propagating (a)-(b) along foliation plane, (c)-(d) across foliation plane, and (e)-(f) at 45° to foliation plane. Angle in bracket of title denotes the wave propagation direction with respect to foliation plane. 29 traces are displayed in each figure indicating the 29 different pressure measurements listed in Tables A-2 and A-3 from 3 to 60 MPa (pressurization) and 60 to 3 MPa (depressurization).

5. Data Analysis

To investigate the anisotropic properties of a rock sample from a deep borehole in Fort McMurray, compressional (P-) and shear (S-) wave phase velocities were measured at confining pressure up to 60 MPa in three different directions with respect to the visible foliation plane. Velocities were measured during both pressurization and depressurization on the rock sample. The effects of cracks and pores in the anisotropic nature of the rocks should decrease as the applied confining pressure increases due to the closing of the cracks (Walsh, 1965). This would also result in the increase of P- and S-wave velocities.

The arrival times for P- and S- waves were picked from the first extreme values of the stacked waveforms. The waveforms for S-waves at 0 to 3 MPa for both the pressurization and depressurization processes were relatively noisy compared to all other waveforms at higher confining pressures. Velocities were calculated using the measured distances between the pulsing and receiving surfaces of the sample. P- and S- wave velocities. The data are reported in Tables A-2 and A-3, and changes are plotted as a function of confining pressure in Figure A-6. The propagating velocity as a function of pressure is primarily dependent upon mineralogy and porosity (Gupta, 2011). In general, waves propagate relatively faster when they encounter fewer low-rigidity materials along the foliation plane, and waves that propagate at 90° from the foliation plane are likely to encounter more low-rigidity materials than waves propagating at 45° to the foliation plane (Lo *et al.*, 1986). The fastest P-wave velocities were measured parallel to the foliation plane from 5.16 to 5.78 km/s, whilst the slowest was measured at 45° to the foliation plane from 4.53 to 4.99 km/s. These were not the expected outcome since the slowest velocities are generally perpendicular to the foliation plane. During the sample preparation stage, it was found that the foliation plane within the rock was not entirely flat. There was a slight tilt of the foliation plane from one end to another. This could be a possible justification for the resulting $V_{\text{perpendicular}} > V_{45^\circ}$ as the sample might have a symmetry that is not perfectly transversely isotropic.

As the confining pressure increases, velocities also increase at a relatively lower velocity gradient that reflects the intrinsic effects of pressure on the mineralogical velocities of the sample. The velocity gradient is significantly higher at lower confining pressure (0 to 12 MPa) and gradually decreases as the pressure also increases. The initial velocity increase with pressure can be attributed to the closing of the cracks and pores. Microcracks can be originated from various sources such as stress relief during coring and are present in many rocks (Hemsing, 2007). The velocity measurements obtained at increasing confining pressure are slightly lower than the velocities measured at decreasing confining pressure. This is related to the hysteresis phenomenon in which a property that has been changed does not return to its original state after the cause of the change has been removed (Sheriff, 2002). The cracks that were closed during the pressurization process will open at a lower pressure than the original closing pressure associated with frictional adjustment of crack faces and grain boundaries. Alternatively, it is also possible that some cracks or pore spaces do not re-open during the depressurization cycle. The hysteresis effect is usually smaller if sufficient time is allowed for measurements between pressure increments (Gupta, 2011).

Preliminary inspection of the sample shows that it composes of unknown percentages of quartz, micas, feldspars, and a few other unidentified minerals. In the Canadian Shield of Northeastern Alberta, the mineral composition of a north-south exposed belt of Granite Gneiss appears to have a close resemblance to the rock sample in this current study (Goff *et al.*, 1986). The compressional wave velocity for granite gneiss at 200 MPa was reported by Christensen (1996) as 6.010 km/s with a density value of 2.643 kg/cm³. This reported density value is within 1% difference from the measured density value for the rock sample in this project. Moreover, a linear extrapolation of the velocity gradient of P-wave velocity as a function of confined pressure matches the reported compressional velocity value by Christensen (1996) at 200 MPa (Figure A-6c).

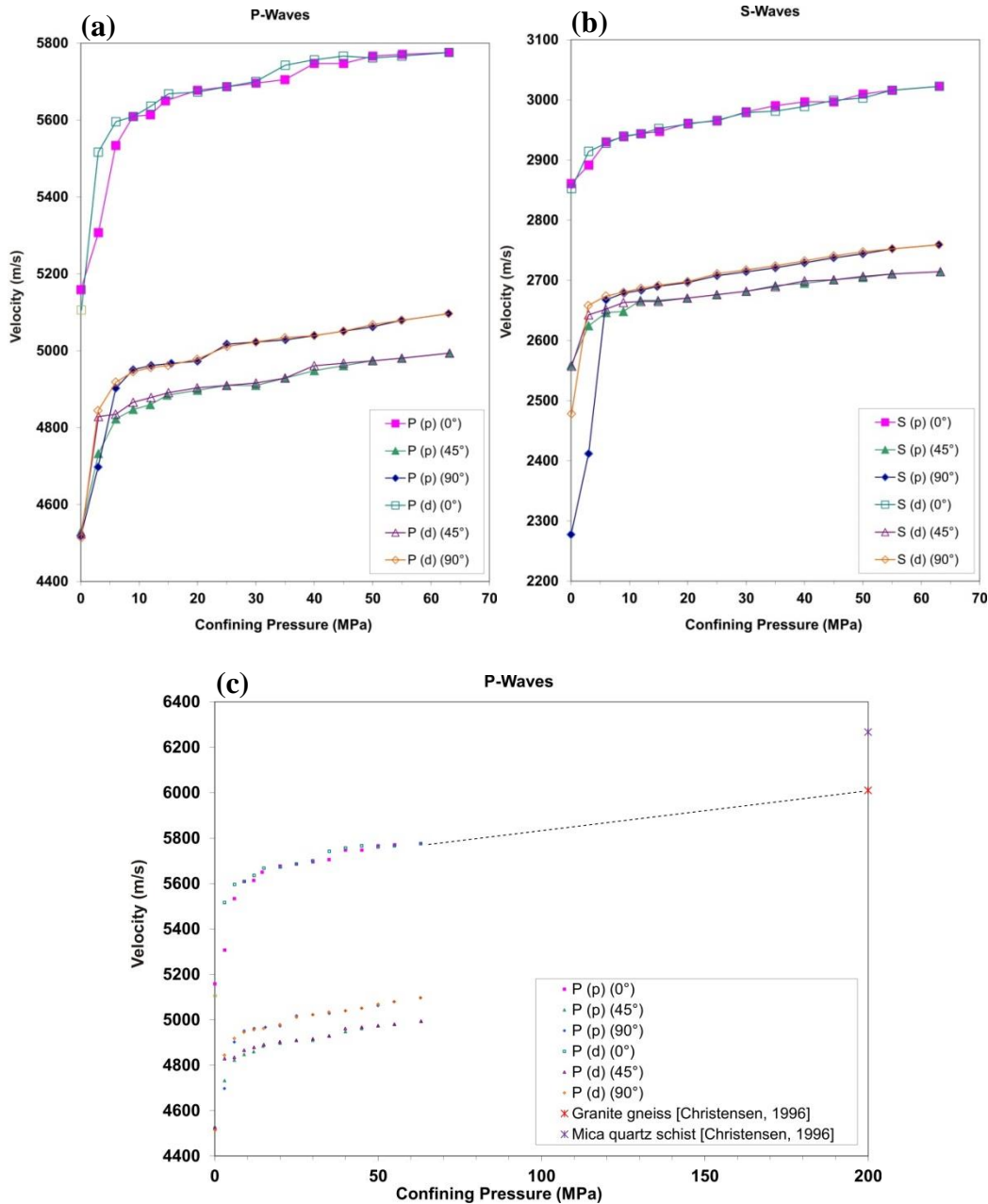


Figure A-6. Comparison of (a) P- and (b) S-wave velocities as a function of confining pressure ranging from 0 to 60 MPa. (c) The extrapolated velocity gradient for P-waves to confining pressure with 200 MPa. This extrapolation also appears to correlate with the reported value (red marker) for granite gneiss at 200 MPa by Christensen (1996).

P-wave velocity anisotropy of the most common metamorphic rocks is typically almost orthorhombic or transversely isotropic (Barberini *et al.*, 2007). The anisotropy in rocks is primarily due to the preferred orientation of the constituent minerals, textural-structural features, pores, and cracks. As the confining pressure increases, the effect of microcracks on anisotropy is expected to lessen, and the remaining anisotropy is more likely to be resulting from layering and preferred orientation of minerals, *i.e.* intrinsic anisotropy. The averaged values for P- and S-wave anisotropy are 12% and 9% respectively calculated using Equation 5 which indicates that the sample is slightly anisotropic.

Figure A-7 shows the change in the anisotropic parameters under pressure. The anisotropic parameters ϵ and γ were obtained from the P- and S-wave velocities (Equations 6 and 7) in the axial directions and have reported values of 15% and 10% respectively. The third anisotropic parameter δ contains an off-diagonal element of elastic constant and has a value of 20% which is also related to the short-spread normal moveout velocities in transversely isotropic media (Hemsing, 2007). These three anisotropic parameters remain relatively stable beyond 9 MPa. It was also observed that $\epsilon > \gamma > \delta$. There is a 6% difference for the S-wave anisotropy at low confining pressures and this sudden sharp decrease could be caused by an erroneous travel time picks in the noisy waveforms as mentioned earlier for confining pressure between 0 to 3 MPa. All three anisotropic parameters are relatively constant beyond 9 MPa. At higher pressures, layering and the preferred orientation of minerals will have greater effects on the anisotropic behavior of the rock as opposed to the cracks.

The five independent elastic stiffnesses C_{11} , C_{13} , C_{33} , C_{44} and C_{66} were calculated from the phase velocities in a transversely isotropic medium. The results indicate that $C_{11} > C_{33} > C_{66} > C_{44} > C_{13}$. The hysteresis phenomena are also noticeable in the elastic constants as a result of the hysteresis in the velocities. Elastic constants are gradually increasing as confining pressure increases. The calculated C_{11} and C_{33} are dependent on the P-wave velocities whereas C_{44} and C_{66} are dependent on the S-wave velocities. The uncertainties for these four elastic stiffnesses should be

lower compared to that for C_{13} due to the possible buildup of uncertainties from the propagation of errors (Equation 15). Figure A-7 is useful in demonstrating whether the sample of interest is isotropic. If a sample is isotropic, it is expected that $C_{11} = C_{33}$, and $C_{44} = C_{66}$. This was not the case of this sample which demonstrates its anisotropic behavior. As the cracks close under the influence of increasing pressure, the velocity gradients of the propagative waves also decrease as they encounter less low-rigidity material (air) and cracks. This also increases the elastic stiffnesses which eventually approached the constant level when all the cracks are closed at high confining pressure. It is also possible that the stiffnesses of the sample can be affected by other minerals in smaller proportions.

6. Conclusions

To determine the elastic properties of a metamorphic rock over a range of confining pressures, P- and S-wave velocities were measured using the ultrasonic pulse transmission technique on a core sample from a deep borehole in Fort McMurray. Under the assumption of transverse isotropy, velocities were measured parallel, perpendicular, and at 45° to the foliation plane. The results are presented in graphs as a function of confining pressure. The sharp velocity gradients at low pressures were observed and can be attributed to the closing of microcracks. The Thomsen's anisotropic parameters and elastic constants were also calculated which reveal the closure of microcracks at low confining pressures. At higher confining pressures, the anisotropic behavior of the rocks is more dependent on layering and the preferred alignment of minerals when the microcracks are closed. These would also lead to the decrease in the calculated anisotropy values. According to the current graphical results, the measured velocities increased linearly as a function of pressures. If higher pressures are applied to the rock sample, it might be possible to observe the decrease in anisotropic parameters as a result of the complete closure of microcracks, layering and preferred alignment of mineral combination. The overall results of the laboratory measurements confirm the anisotropic behavior of the metamorphic rock and could be useful in the construction of velocity models in the seismic

processing workflow. This could help to remove the anomalies caused by the directional dependence in the seismic velocities. Mineral compositions of the sample could also have an effect on the directional velocities. Hence, x-ray diffraction could be performed on the sample to relate the effects of different mineral compositions to the velocities of wave propagations.

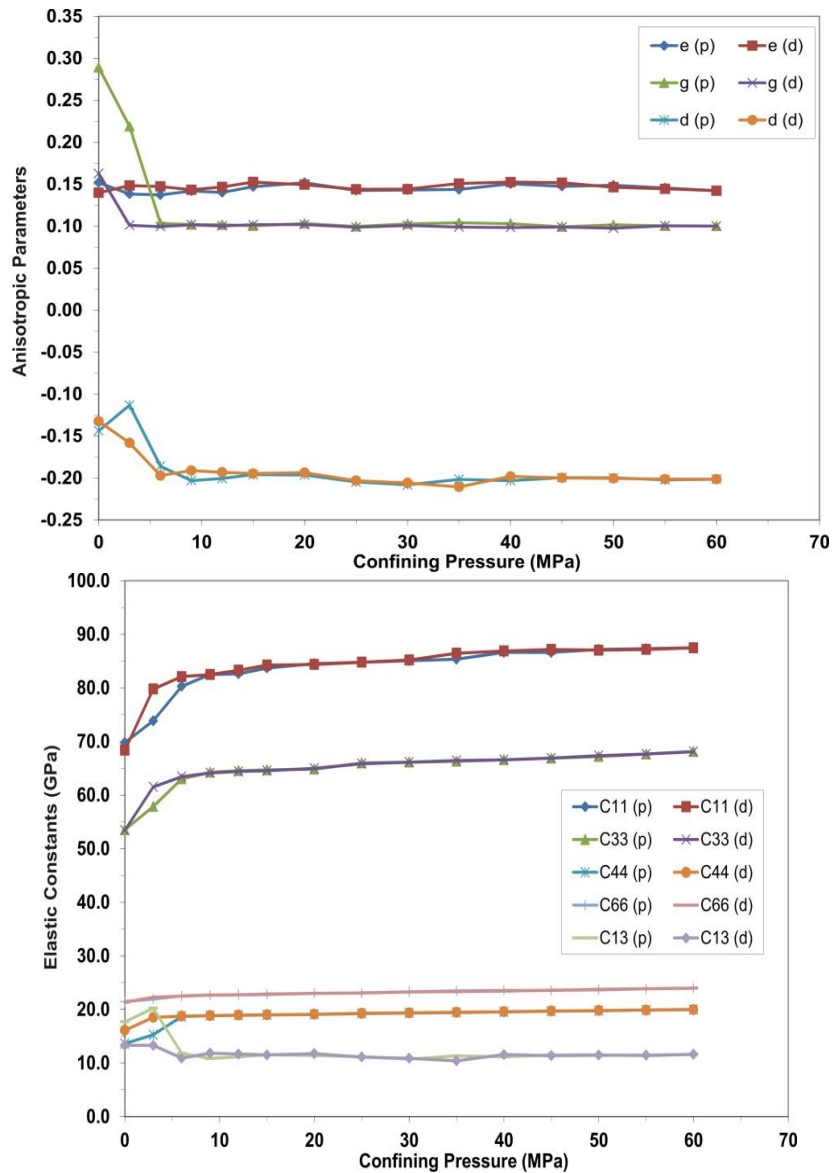


Figure A-7. Comparison of **(top)** anisotropic parameters and **(bottom)** elastic constants assuming transversely isotropic (TI) medium as a function of confining pressure. The e, g and d in (a) corresponds to the anisotropic parameters ϵ , γ , and δ respectively.

Table A-1. Parameters used for velocity and elastic constant calculations.

Direction relative to foliation plane	Distance between surfaces (m)
Parallel	0.070
45°	0.038
Perpendicular	0.045

Table A-2. Measured velocities, calculated elastic constants and anisotropic parameters during the pressurization cycle.

Pressure (MPa)	V_p (m/s)			V_s (m/s)			Elastic Constants (MPa)						Anisotropic Parameters				
	Along	Across	45°	Along	Across	45°	C_{11}	C_{33}	C_{44}	C_{66}	C_{12}	C_{13}	ϵ	γ	δ	A_p	A_s
0	5158	4518	4529	2861	2277	2559	69.8	53.5	13.6	21.5	26.9	17.7	0.15	0.29	-0.14	0.12	0.20
3	5307	4697	4732	2891	2412	2624	73.9	57.9	15.3	21.9	30.0	20.2	0.14	0.22	-0.11	0.11	0.17
6	5534	4902	4822	2930	2667	2646	80.3	63.0	18.7	22.5	35.3	11.8	0.14	0.10	-0.19	0.11	0.09
9	5609	4950	4847	2939	2679	2648	82.5	64.3	18.8	22.6	37.2	10.8	0.14	0.10	-0.20	0.12	0.09
12	5613	4961	4859	2944	2683	2667	82.6	64.6	18.9	22.7	37.2	11.2	0.14	0.10	-0.20	0.12	0.09
15	5650	4967	4884	2947	2690	2667	83.7	64.7	19.0	22.8	38.1	11.5	0.15	0.10	-0.20	0.12	0.09
20	5677	4972	4897	2961	2696	2670	84.5	64.8	19.1	23.0	38.5	11.4	0.15	0.10	-0.20	0.12	0.09
25	5686	5017	4910	2965	2708	2676	84.8	66.0	19.2	23.1	38.7	11.2	0.14	0.10	-0.20	0.12	0.09
30	5696	5022	4910	2980	2714	2682	85.1	66.1	19.3	23.3	38.5	10.7	0.14	0.10	-0.21	0.12	0.09
35	5705	5028	4929	2990	2721	2691	85.4	66.3	19.4	23.4	38.5	11.3	0.14	0.10	-0.20	0.12	0.09
40	5747	5039	4948	2997	2729	2695	86.6	66.6	19.5	23.5	39.5	11.1	0.15	0.10	-0.20	0.12	0.09
45	5747	5051	4961	2997	2737	2701	86.6	66.9	19.6	23.5	39.5	11.5	0.15	0.10	-0.20	0.12	0.09
50	5766	5062	4974	3009	2744	2705	87.2	67.2	19.7	23.8	39.7	11.5	0.15	0.10	-0.20	0.12	0.09
55	5771	5079	4980	3016	2752	2710	87.3	67.6	19.9	23.9	39.6	11.4	0.15	0.10	-0.20	0.12	0.09
60	5776	5096	4993	3022	2759	2714	87.5	68.1	20.0	24.0	39.6	11.6	0.14	0.10	-0.20	0.12	0.09

↓

V_{P90} V_{P0} V_{P45} V_{SH90} V_{SH0}

Table A-3. Measured velocities, calculated elastic constants and anisotropic parameters during the de-pressurization cycle.

Pressure (MPa)	V _P (m/s)			V _S (m/s)			Elastic Constants (MPa)						Anisotropic Parameters				
	Along	Across	45°	Along	Across	45°	C ₁₁	C ₃₃	C ₄₄	C ₆₆	C ₁₂	C ₁₃	ε	γ	δ	A _p	A _s
0	5106	4514	4524	2852	2478	2557	68.4	53.4	16.1	21.3	25.7	13.3	0.14	0.16	-0.13	0.12	0.13
3	5516	4844	4828	2914	2658	2643	79.8	61.5	18.5	22.3	35.3	13.3	0.15	0.10	-0.16	0.12	0.09
6	5596	4918	4835	2928	2674	2652	82.1	63.4	18.7	22.5	37.2	10.9	0.15	0.10	-0.20	0.12	0.09
9	5609	4945	4866	2940	2680	2663	82.5	64.1	18.8	22.7	37.2	11.8	0.14	0.10	-0.19	0.12	0.09
12	5636	4956	4878	2944	2687	2665	83.3	64.4	18.9	22.7	37.9	11.7	0.15	0.10	-0.19	0.12	0.09
15	5668	4961	4891	2952	2691	2665	84.2	64.6	19.0	22.9	38.5	11.5	0.15	0.10	-0.19	0.12	0.09
20	5673	4978	4903	2960	2698	2670	84.4	65.0	19.1	23.0	38.4	11.7	0.15	0.10	-0.19	0.12	0.09
25	5686	5011	4910	2966	2711	2676	84.8	65.9	19.3	23.1	38.7	11.1	0.14	0.10	-0.20	0.12	0.09
30	5700	5022	4916	2979	2717	2682	85.2	66.1	19.4	23.3	38.7	10.9	0.14	0.10	-0.21	0.12	0.09
35	5742	5034	4929	2981	2724	2689	86.5	66.4	19.5	23.3	39.9	10.4	0.15	0.10	-0.21	0.12	0.09
40	5757	5039	4961	2989	2732	2699	86.9	66.6	19.6	23.4	40.0	11.6	0.15	0.10	-0.20	0.12	0.09
45	5766	5051	4967	2999	2741	2701	87.2	66.9	19.7	23.6	40.0	11.4	0.15	0.10	-0.20	0.12	0.09
50	5761	5068	4974	3003	2747	2707	87.0	67.3	19.8	23.6	39.7	11.5	0.15	0.10	-0.20	0.12	0.09
55	5766	5079	4980	3016	2752	2710	87.2	67.6	19.9	23.9	39.5	11.5	0.14	0.10	-0.20	0.12	0.09
60	5776	5096	4993	3022	2759	2714	87.5	68.1	20.0	24.0	39.6	11.6	0.14	0.10	-0.20	0.12	0.09

V_{P90} V_{P0} V_{P45} V_{SH90} V_{SH0}

Bibliography (Appendix E)

- APC International Ltd. (2011), Physical and piezoelectric properties of APC materials, Retrieved on December 17, 2011 from <http://www.americanpiezo.com/apc-materials/piezoelectric-properties.html>.
- Barberini, V., L. Burlini, and A. Zappone (2007), Elastic properties, fabric and seismic anisotropy of amphibolites and their contribution to the lower crust reflectivity, *Tectonophysics*, 445(3-4), 227-244, doi:10.1016/j.tecto.2007.08.017.
- Birch, F. (1960), The velocity of compressional waves in rocks to 10 kilobars (Part I), *J. Geophys. Res.*, 65, 1083-1102.
- Birch, F. (1961), The velocity of compressional waves in rocks to 10 kilobars (Part II), *J. Geophys. Res.*, 66, 2199-2224.
- Bos, L., P. Gibson, M. Kotchetov, and M. Slawinski (2004), Classes of anisotropic media: A tutorial, *Stud Geophys Geod*, 48(1), 265-287, doi:10.1023/B:Sgeg.0000015596.68104.31.
- Cholach, P. Y., J. B. Molyneux, and D. R. Schmitt (2005), Flin Flon Belt seismic anisotropy: elastic symmetry, heterogeneity, and shear-wave splitting, *Canadian Journal of Earth Sciences*, 42(4), 533-554, doi:10.1139/E04-094.
- Christensen, N. I. (1996), Poisson's ratio and crustal seismology, *J Geophys Res-Sol Ea*, 101(B2), 3139-3156, doi:10.1029/95jb03446.
- Goff, S. P., J. D. Godfrey, and J. G. Holland (1986), Petrology and geochemistry of the Canadian Shield of Northeastern Alberta, *AGS Bulletin 051*, 65 pp., Alberta Geological Survey, Edmonton, Alberta.
- Gupta, H. K. (ed.) (2011), *Encyclopedia of Solid Earth Physics (Volume 1)*, Springer, The Netherlands.
- Hemsing, D. B. (2007), Laboratory determination of seismic anisotropy in sedimentary rock from the Western Canadian Sedimentary Basin, M.Sc. thesis, 208 pp, University of Alberta, Edmonton, Alberta, Canada.
- Lo, T. W., K. B. Coyner, and M. N. Toksoz (1986), Experimental-determination of elastic-anisotropy of Berea sandstone, Chicopee shale, and Chelmsford granite, *Geophysics*, 51(1), 164-171, doi:10.1190/1.1442029.
- Musgrave, M. J. P. (1970), *Crystal Acoustic*, Holden-Day, San Francisco, California.
- Nye, J. F. (1985), *Physical Properties of Crystals*, 329 pp., Oxford University Press, London, UK.
- Sheriff, R. E. (2002), *Encyclopedic Dictionary of Applied Geophysics*, 4th ed., 429 pp., Society of Exploration Geophysicists, Tulsa, Oklahoma.
- Thomsen, L. (1986), Weak elastic-anisotropy, *Geophysics*, 51(10), 1954-1966, doi:10.1190/1.1442051.
- Walsh, J. B. (1965), The effects of cracks on the compressibility of rock, *J. Geophys. Res.*, 70, 381-389.
- Yam, H. (2011), CO₂ rock physics: A laboratory study, M.Sc. thesis, 265 pp, University of Alberta, Edmonton, Alberta, Canada.

Appendix F

Thin Sections

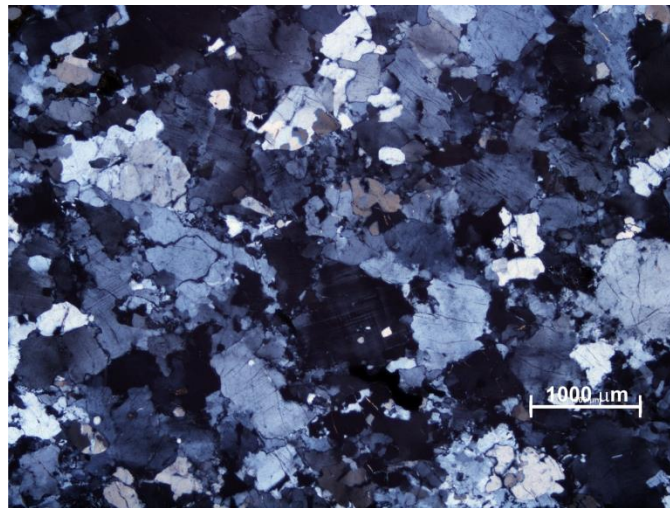
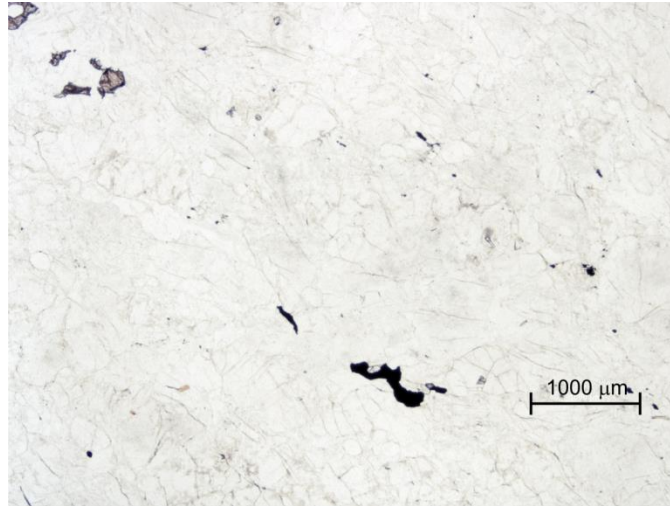


Figure A-8. (Top) Plane and (Bottom) cross-polarized light images of Hunt well sample at 2350.3 to 2350.5 m depth. The sample consists of dominantly quartz and feldspar. Evidence of weak metamorphism and undulatory extinction in quartz were observed. There is no evident foliation and no apparent alignment of minerals in these thin sections (Photo and interpretations done by Randy Kofman).

Appendix G

Photos of Hunt Well Logging

July 2011



(Upper left) Rig setup and the removal of tubings from the borehole prior to logging.

(Upper right) Hunt well

(Lower left) Logging in progress

(Lower right) GFZ personnel Jochem Kuck setting up the logging tool.